Università degli Studi di Palermo

AREA RICERCA E TRASFERIMENTO TECNOLOGICO
SETTORE DOTTORATI E CONTRATTI PER LA RICERCA
U. O. DOTTORATI DI RICERCA

Dottorato di Ricerca in Scienze Fisiche e Chimiche
Dipartimento di Fisica e Chimica – Emilio Segrè
Settore Scientifico Disciplinare PHYS/05B

MHD MODELLING OF ENERGY RELEASE IN CORONAL CLOSED MAGNETIC FLUX TUBES

IL DOTTORE
GABRIELE COZZO

IL COORDINATORE
PROF. MARCO CANNAS

IL TUTOR
PROF. FABIO REALE

IL CO-TUTOR
PROF. PAOLO PAGANO

CICLO XXXVII
ANNO CONSEGUIMENTO TITOLO 2024

Abstract

In this thesis I address the release of magnetic energy into heating in the million degrees solar corona, through detailed MHD modelling of single or interacting closed magnetic flux tubes. According to a commonly accepted scenario, these tubes are stressed by progressive twisting at their footpoints driven by slow photospheric motions. Particular attention is devoted to the observational implications and therefore to the plasma response to the energy release in a realistic solar atmosphere.

As a detailed mechanism to convert the magnetic energy into heat I explore the reconnection events triggered by the kink instability of continuously twisted flux tubes. I performed time-dependent 2.5D and 3D MHD simulations to model the evolution of closed magnetic tubes, the coronal loops, subjected to footpoint motions and eventually MHD instabilities. Our model includes a stratified, magnetised atmosphere extending from the chromosphere to the corona, and accounts for key physical processes such as thermal conduction, optically thin radiation, and transitions from high- to low-beta regions, including magnetic field expansion from the footpoints. I use the stat-of-art MHD numerical code PLUTO, tailored to describe solar coronal conditions. As a preliminary step, which allowed me to tune up the numerical tool, I explored the effect of asymmetric heating release in coronal loop, and found that the high Alfvén speed in the corona levels out possible asymmetries and explain the observed symmetry of coronal loops, even under prolonged asymmetric footpoint motions.

Most of the work is devoted to study twisted interacting flux tubes subject to kink instability. The study confirms that kink instabilities can lead to MHD avalanches, even in a realistic solar atmosphere, driving significant heating up to microflare temperatures ($\sim 10\,\mathrm{MK}$) and inducing chromospheric evaporation. As a next step, spectral data in extreme-ultraviolet (EUV) lines are synthesized for comparison with the anticipated observational capabilities of the forthcoming MUltislit Solar Explorer (MUSE) NASA

mission. Footpoints EUV emission in the MUSE Fe IX 1 MK channel will mark early plasma responses to heating, while Fe XV 2.5 MK will track denser plasma at intermediate heights, and Fe XIX 10 MK will reveal hot plasma within current sheets. Further effort was devoted to possible signatures of magnetic reconnection. A nanojet — a small, high-velocity reconnection outflow — was identified as key observable signature of this impulsive energy release, with temperature reaching 8 MK, outflow velocity of several hundred $\mathrm{km\,s^{-1}}$, and duration of less than one minute. The simulations suggest that MUSE will be able to detect these features, providing crucial insights into the heating mechanisms of the solar corona.

As a final step, which is an initial step for future developments, we addressed the effects of prolonged footpoints rotation, until a statistical energy balance is achieved, to investigate DC coronal heating in multi-stranded coronal loops. A machine-learning based algorithm for automatic detection of nanojets is presented as promising tool to investigate the nanoflare phenomenon and its observational signatures, based on physical assumptions.

Contents

1 Introduction

1.1 Units and constants

In this work, most physical quantities are written in the Centimetre-Gram-Second (CGS) system of units. The exceptions are typical coronal length and velocities, more conveniently described in Mm $= 10^8$ cm (Megameters), and km s^{-1} $= 10^5$ cm s^{-1}, respectively. The following constants are also used:

$R_\odot = 6.96 \times 10^{10}$ cm	(solar radius)
$M_\odot = 1.99 \times 10^{33}$ g	(solar mass)
$L_\odot = 3.83 \times 10^{33}$ g cm^2 s^{-3}	(solar luminosity)
$m_p = 1.67 \times 10^{-24}$ g	(proton mass)
$m_e = 9.11 \times 10^{-28}$ g	(electron mass)
$c = 3.00 \times 10^{10}$ cm s^{-1}	(speed of light)
$e = 4.80 \times 10^{-10}$ cm$^{3/2}$ g$^{1/2}$ s^{-1}	(electron charge)
$G = 6.67 \times 10^{-8}$ g^{-1} cm^3 s^{-2}	(constant of gravitation)
$k_B = 1.38 \times 10^{-16}$ g cm^2 s^{-2} K^{-1}	(Boltzmann constant)

1.2 The solar atmosphere

The magnetic field has an important role in the solar atmosphere. Convective plasma motions power the dynamics of the outermost layers of the solar interior, where the plasma beta (i.e. the ratio of gas and magnetic pressures) is high ($\beta \gg 1$), as shown in

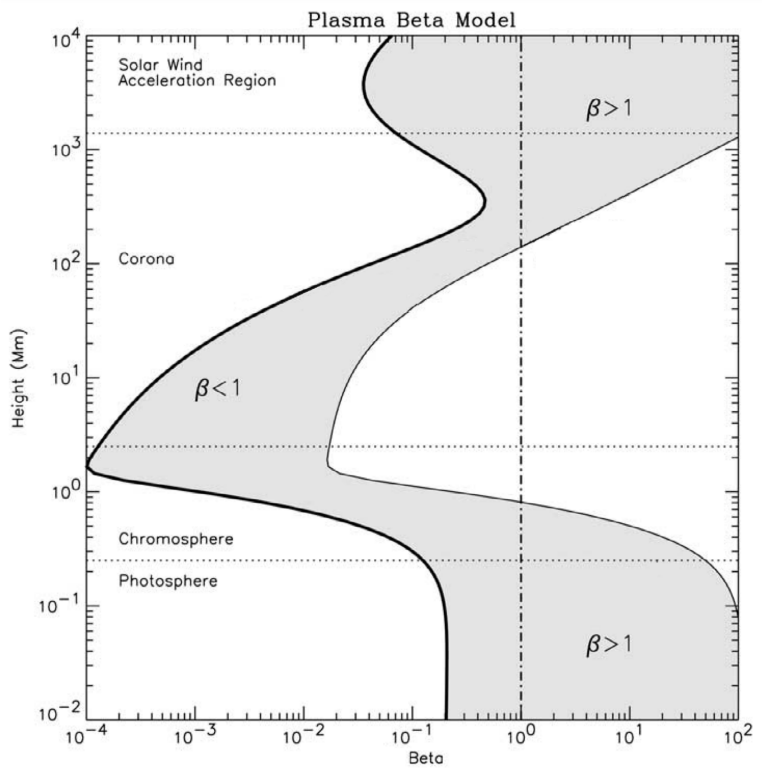

Figure 1.1: Plasma beta stratification as function of height. Credit Gary (2001).

Fig. 1.1. This underlying, at first glance smooth, medium propels and hosts the electric currents upholding the magnetic, multi-scale phenomena observed readily above the solar surface. There, plasma β rapidly decreases and reaches a minimum up in the solar atmosphere, where the magnetic field forces drive plasma motion. Therefore, in the solar atmosphere there is a transition from a gas dominated by hydrodynamic forces ($\beta \ll 1$) to a magnetised plasma ($\beta \gg 1$). Plasma physics, and specifically 'magnetohydrodynamics' (MHD, Alfvén 1942 and Sec. 1.3), is necessary to exhaustively describe it.

1.2.1 The VAL model

The solar atmosphere (Priest 2014) can be generally divided into three parts with different physical and optical properties. In the lower shell of the solar atmosphere, the 'photosphere', extending for some hundreds of kilometres, the plasma is dense ($\sim 10^{18}\mathrm{cm}^{-3}$), cold ($T \sim 6 \times 10^3$ K) and opaque ($\tau \lesssim 1$ from near infrared, *NIR*, to near ultraviolet, *NUV*, $\tau \gg 1$ in most spectral lines). Above the photosphere, in the 'chromosphere' the

plasma crosses the temperature minimum to get hotter ($T \sim 10^4$ K) and more tenuous ($n \lesssim 10^{15}\,\mathrm{cm}^{-3}$), and becomes optically thin in the NIR to NUV continuum (but still optically thick in strong lines). Across a very thin layer (just $\lesssim 100$ km average) called 'transition region' the temperature rises by about two orders of magnitude while the density decreases proportionally to $\sim 10^9\,\mathrm{cm}^{-3}$. The outermost layer of the solar (stellar) atmosphere is the 'corona', extending from few thousands of kilometres above the photosphere to few tens of solar radii (virtually unlimited), where it fills the 'heliosphere'. It is optically thin in the whole electromagnetic spectrum with very few exceptions.

The approximate standard model shown in Fig. 1.3, also known as 'VAL model' (Vernazza et al. 1981; Avrett & Loeser 2008), assumes average plasma properties, such as temperature and density, only as a function of height. Nevertheless, the solar atmosphere is made by non-homogeneous and dynamic plasma out of equilibrium, and to address its complexity a multi-dimensional and time-dependent description is needed.

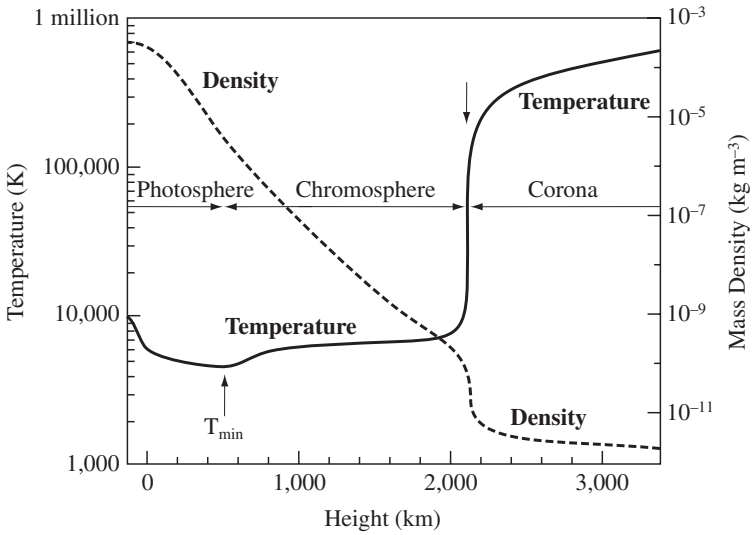

Figure 1.3: The VAL model (Vernazza et al. 1981). The plot shows the variation of averaged plasma temperature (solid line) and density (dashed line) as function of height, from the photosphere to the corona. Credit: Lang (2001).

1.2.2 Sub-corona atmospheric layers

The photosphere (Rutten 2012, top-right panel of Fig. 1.2) is approximately uniform on a large scale (except for sunspots), but on small scales it is entirely covered by ~ 1 Mm convective cells called 'granules', where plasma flows at a speed of $\sim 1\,\mathrm{km\,s}^{-1}$. In the photosphere, the strength of the emerging magnetic field (top-left panel of Fig. 1.2) varies from few kG to $5 - 10$ G for ambient/quiet Sun magnetic fields. In particular,

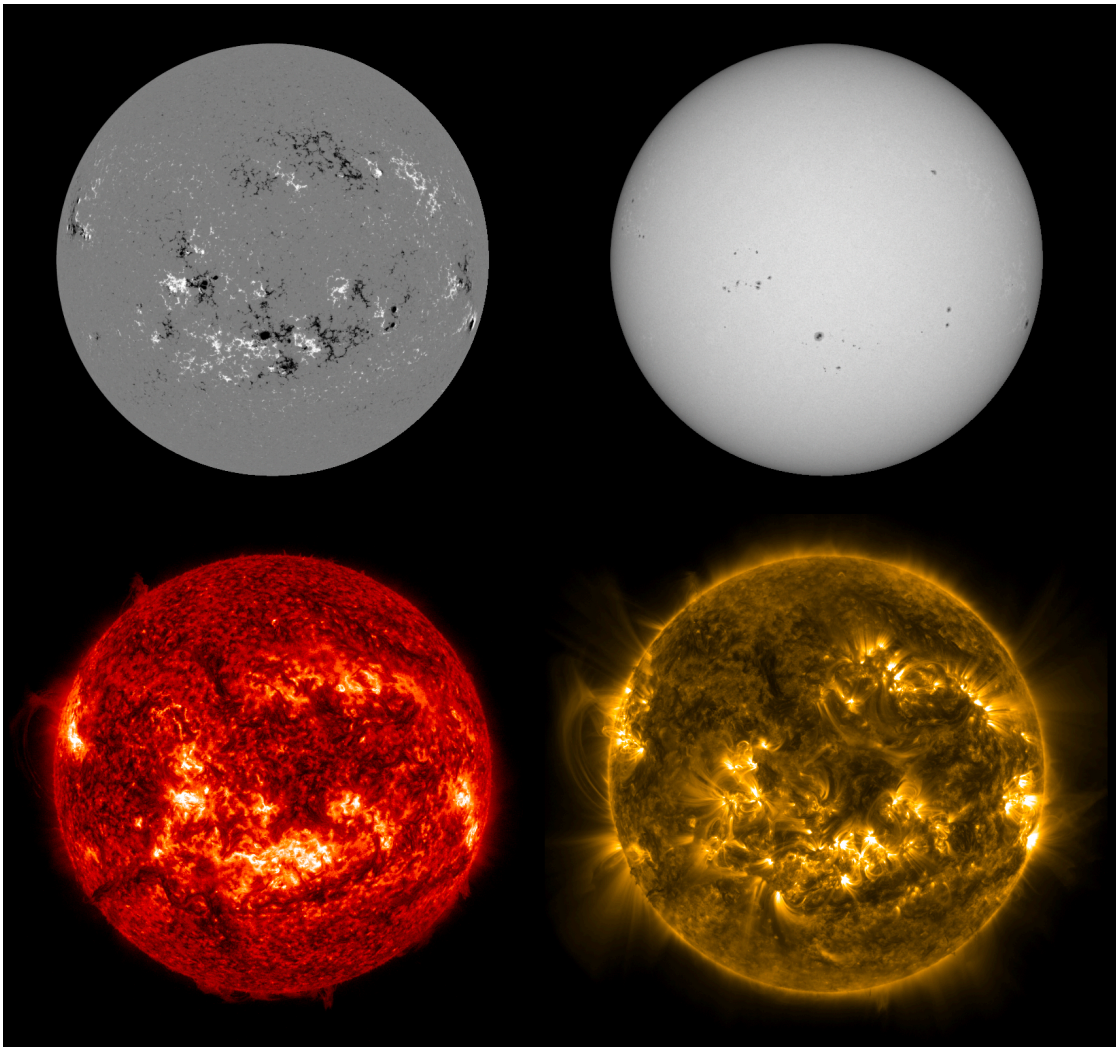

Figure 1.2: Top-left: full disk magnetogram of the Sun observed by SDO/HMI on 30th june 2023. Top-right: photospheric SDO/HMI continuum. Down-left: chromospheric emission with 304 $\mathring{A}$ SDO/AIA channel. Down-right: coronal emission with 171 $\mathring{A}$ SDO/AIA channel. Images extracted from Helioviewer (Garcia Briseno & Ireland 2023).

the strong magnetic field emerges from elemental flux tubes 100 km wide, expanding upward and with typical field strength of 200-500 G at the temperature minimum. In the photosphere, the plasma β is high ($\gg 1$). As a consequence, the magnetic field is most of the time passively advected by photospheric motions.

Chromosphere (bottom-left panel of Fig. 1.2, Vernazza et al. 1981) and transition region (TR, Gabriel 1976a) are very inhomogeneous and dynamically evolving with time. Multi-scale flows, waves, shocks, and heating phenomena in those layers are the response to photospheric convection in the underling atmosphere.

Across the TR, temperature suddenly increases from few thousands to millions K. Such a steep increase with height is formally constrained by the radiative losses and thermal conduction mutual relationship. Indeed, in steady-state conditions, the energy lost by (optically thin) radiative processes (whose efficiency peaks across the TR) must be supplied by the thermal conduction from above. In particular, the steep temperature dependence of the thermal conduction (conductive flux: $F(z) \propto T^{\frac{5}{2}} \frac{dT}{dz}$) determines the abrupt temperature inflation across the transition region, i.e. between 10^4 and 10^6 K, where the radiative losses temperature-spectrum peaks (see Fig. 1.4). The energy drained from the corona by thermal conduction and radiated away in the TR must be in turn supplied by coronal heating process(es) maintaining this external layer in the million K regime and preventing the tenuous plasma from cooling down to photospheric/chromospheric temperatures.

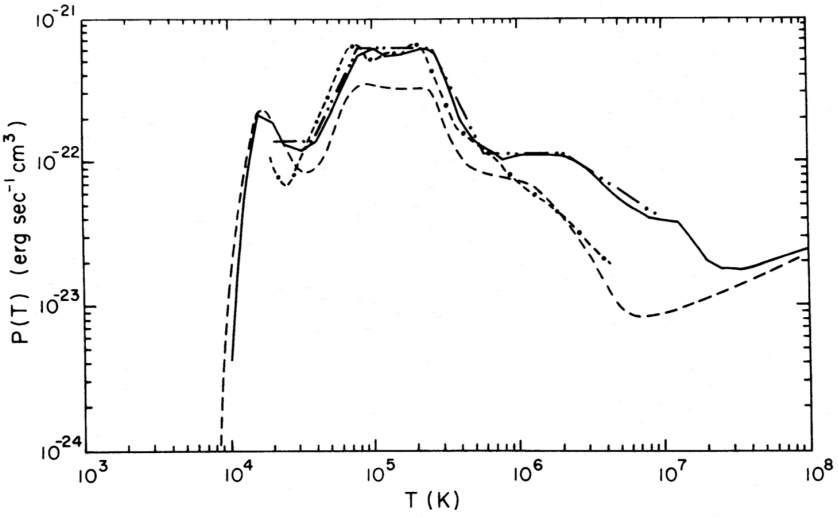

Figure 1.4: Frequency integrated optically thin radiative losses rate peaking at transition region temperatures (around 10^5 K). Credit: Rosner et al. (1978b)

1.2.3 The corona: active regions

The solar corona (Golub & Pasachoff 2010, bottom-right panel of Fig. 1.2) is the outermost layer of the Sun, extending from a few thousands of km above the photosphere to several solar radii and beyond. It is visible in the optical band as a faint white crown

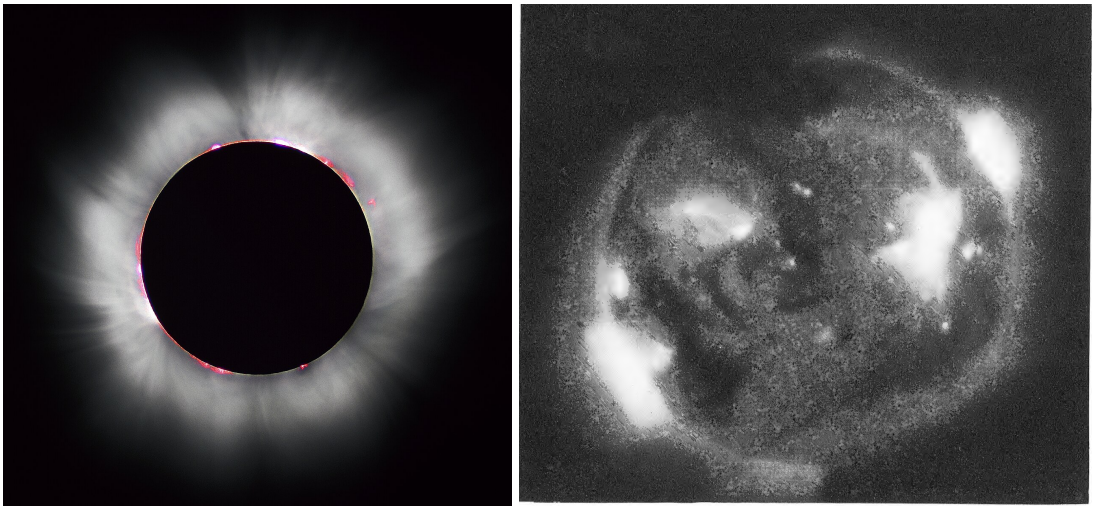

Figure 1.5: Left: image of the solar corona during the total solar eclipse on Monday, August 21, 2017 above Madras, Oregon. Credit: NASA/Aubrey Gemignani. Right: an X-Ray image of the Sun corona emphasizing the highly inhomogeneous nature of the coronal plasma. Credit: Vaiana et al. (1973b)

surrounding the moon disk during total solar eclipses (left-hand side of Fig. 1.5). It is made of almost fully ionized gas, heated to millions K. The highly-ionized coronal plasma strongly interacts with the magnetic field which confines and funnels it along the field lines.

Looking at the Sun in the X-ray band (Testa & Reale 2024), it is possible to recognise a complex scenario of closed structures linking regions of opposite magnetic field polarity (right-hand side of Fig. 1.5). These 'coronal loops' (Reale 2014) are arch-like magnetic tubes filled with relatively dense ($n \sim 10^9$ cm^{-3}), hot ($T \sim 10^6$ K) and bright plasma, as shown on the right-hand side of in Fig. 1.6. They are acknowledged as the "building blocks" of the bright corona where the emergent magnetic field is typically organised into a network of topologically closed structures.

In active regions (van Driel-Gesztelyi & Green 2015) a large-scale and coherent magnetic flux (in contrast with the mixed-polarity quiet corona magnetic field) breaks through the solar surface and organises into photospheric 'sunspots' (Borrero & Ichimoto 2011), chromospheric 'plages', 'filaments'/'prominences' (Parenti 2014), and a forest of coronal loops (Reale 2014), bright in the EUV/X-ray, 10 Mm to 100 Mm long (see the e.g., in the left panel of Fig. 1.6). Generally, active regions span over and between bipolar magnetic fields. Density and temperature are higher than in the quiet Sun, with hot cores reaching $n \sim 10^{10}$ cm^{-3} and $T \sim 3 - 5$ MK.

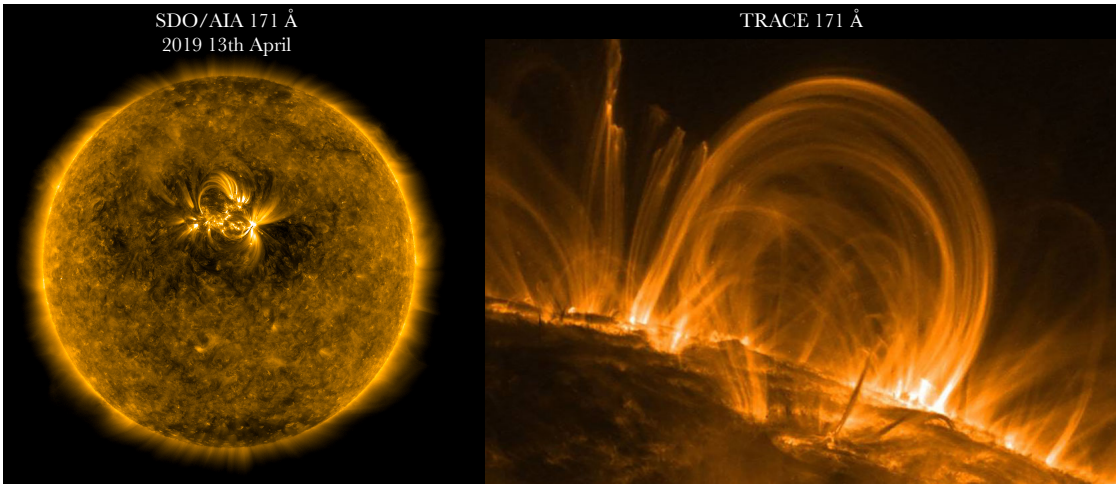

Figure 1.6: Left: AIA observation of an active region in the 171 $\mathring{A}$ channel on April 13th 2019. Right: TRACE observation of a coronal loop in the 171 $\mathring{A}$ line.

1.2.4 Historical keynotes of coronal observations

The solar corona is made by optically thin plasma with temperatures exceeding 1 MK. Emission from this region primarily arises from highly ionized atoms (such as iron), which radiate in the X-ray (5–50 Å), soft X-ray (50–150 Å), extreme ultraviolet (EUV, 150–900 Å), and far ultraviolet (FUV, 900–2000 Å) regions of the electromagnetic spectrum (Fawcett et al. 1968). Since radiation in these wavelengths does not penetrate Earth's atmosphere, most observational data and spectral diagnostics have been acquired through space-based XUV (5–2000 Å) observations.

X-ray and ultraviolet (UV) spectroscopy of the solar corona has been employed for decades to derive key plasma parameters, including electron densities, electron temperatures, differential emission measure (DEM), and relative elemental abundances. Remote-sensing XUV spectroscopy enables precise measurement of plasma conditions, providing insights into parameters such as electron temperature, density, DEM, chemical abundances, Doppler shifts, and non-thermal motion characteristics (Del Zanna & Mason 2018).

In the following paragraph, some of the principal XUV solar missions of the past 70 years are synthetically covered, as also schematically shown in the time-line representation of Fig. 1.7.

Rocket missions

In the late 1960s, grazing incidence optics on board of rockets observed for the first time the X-ray solar corona with arc-min angular resolution (Giacconi et al. 1965). This allowed for temperature diagnostics, the study of magnetic confinement (Reidy et al. 1968), observation of flares (Vaiana et al. 1968), and the first morphological classification of coronal structures (Vaiana & Rosner 1978; Peres & Vaiana 1990).

First orbiting X-ray telescopes

In the 70s, X-ray telescopes on board orbiting missions, such as the Orbiting Solar Observatory-IV (OSO-IV) mission (Krieger et al. 1972) or Skylab (Compton & Benson 1983), monitored the evolution of active regions, thus investigating the lifetime and shape of bright coronal loops with arcsec angular resolution.

X-ray spectroscopy

Between 80s and the early 90s, time-resolved diagnostics of flaring coronal loops was addressed by means of X-ray spectroscopy with the Solar Maximum Mission (SMM, Bohlin et al. 1980; Acton et al. 1980), Hinotory (Tanaka 1983), and Yohkoh (Ogawara et al. 1991). The soft X-ray telescope on board of Yohkoh (SXT, Tsuneta et al. 1991) captured $5-6$ MK plasma in active regions.

Normal incident optics and EUV observations

With the development of normal incidence optics in coronal instruments (e.g., NIXT, Golub & Herant 1989) 90s solar missions focused on the EUV coronal plasma below 2 MK. In particular, the Solar and Heliospheric Observatory (SoHO, Domingo et al. 1995) and the Transition Region and Coronal Explorer (TRACE, Handy et al. 1999), allowed for wide-band diagnostics at subarcsec angular resolution and sub-minute temporal resolution.

State of the art

Gen-Z, still operating, solar corona telescopes include:

- Hinode (Kosugi et al. 2008): by combining its optical instrument, EUV imaging spectrometer (EIS), and X-ray/EUV telescope (XRT), its main goal is to measure strength and direction of the photospheric magnetic field and to understand the causes of solar eruptions.
- Solar TErrestrial Relations Observatory (STEREO, e.g., Kaiser et al. 2008): consisting of two twin spacecraft, it studied in particular the 3D structure and evolution

of solar storms, but also allowed for the first 3D reconstruction of coronal loops (Aschwanden et al. 2009; Kramar et al. 2009). One spacecraft is still operating.

- The Atmospheric Imaging Assembly (AIA, Lemen et al. 2012; Boerner et al. 2012) on board of the Solar Dynamics Observatory (SDO, Pesnell et al. 2012) provides a continuous monitoring of the full solar disk in seven EUV channels, from the 20 kK chromosphere to the flaring 20 MK hot corona, with 12 s cadence and 1 arcsec angular resolution.

- The Interface Region Imaging Spectrograph (IRIS, De Pontieu et al. 2014) obtains UV spectra and images of the solar chromosphere and transition region with high resolution in space (0.33 arcsec) and time (1 s).

- Solar Orbiter (Müller et al. 2020) is a space mission developed by the European Space Agency (ESA) in collaboration with NASA. It consists of a spacecraft equipped with ten instruments designed to observe the Sun up close. The mission's main goal is to study the Sun's outer layers, by capturing high-resolution images and in situ measurements from unique vantage points, including its first-ever close-up views of the Sun's poles during the mission extension.

Forthcoming missions

- The MUltislit Solar Explorer, (MUSE, De Pontieu et al. 2020; De Pontieu et al. 2022; Cheung et al. 2022), is an upcoming NASA MIDEX mission, featuring a multislit EUV spectrometer and an EUV context imager, with planned launch in 2027. MUSE is designed to offer high spatial and temporal resolution for spectral and imaging observations of the solar corona. Its primary goal is to advance our understanding of the heating mechanisms in the corona of both the quiet Sun and active regions, and of the physical processes governing dynamic phenomena like flares and eruptions. MUSE will provide fine spatiotemporal coverage of coronal dynamics, as well as wide field-of-view observations, offering valuable insights into the physics of the solar atmosphere. In particular, it will obtain high resolution spectra ($\approx$ 0.38"), with wide angular coverage ($\approx$ 156" $\times$ 170"; resembling the typical size of an active region), and 12 s cadence. With its 35-slit spectrometer, MUSE will provide spectral observations, with an unprecedented combination of cadence and spatial coverage, in different EUV passbands dominated by strong lines formed over a wide temperature range.

- The EUV High-throughput Spectroscopic Telescope (Shimizu et al. 2019, EUVST - Solar C), developed by JAXA, is a solar observation mission designed to study the Sun's atmosphere in extreme ultraviolet wavelengths. The mission aims to capture high-resolution spectroscopic data to understand the dynamics of solar

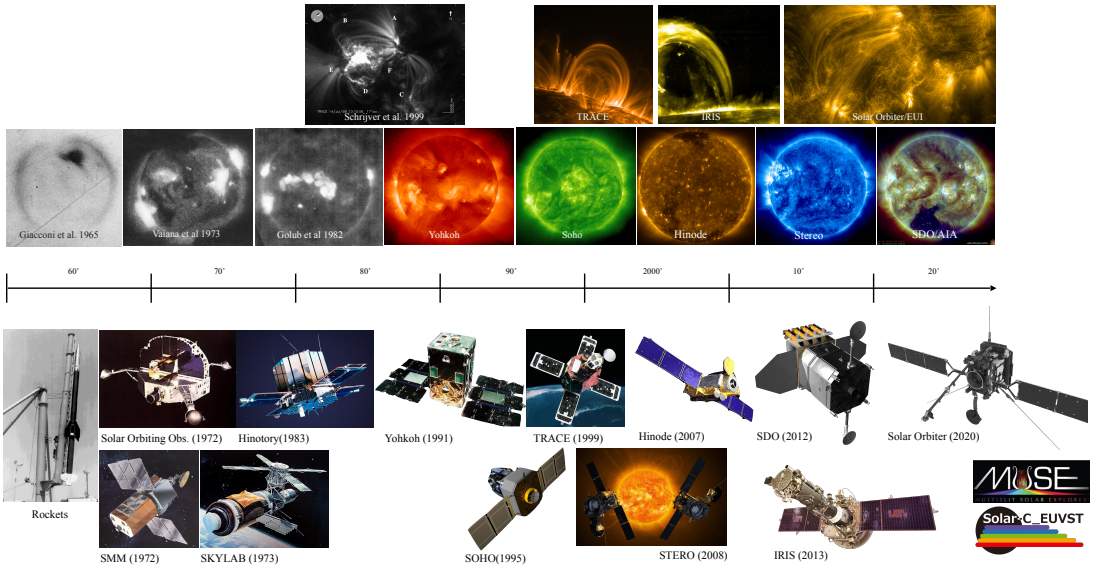

Figure 1.7: Time line of past, current and forthcoming solar missions, including grazing-incidence X-ray telescopes on board of rockets (60s) and spacecraft (70s), X-ray spectrometers (80s), normal incidence UV-EUV images/spectrometers (>90s).

phenomena, by observing the interactions between different layers of the Sun's atmosphere, from the surface to the corona.

1.3 The MHD framework

A 'plasma' is a ionized fluid characterized by long-range collective motions. Plasmas can host strong electric currents inducing and interacting with magnetic fields. Magnetohydrodynamics (Alfvén 1942) describes magnetized matter behavior, under the conditions of (1) fluid-approximation (the collisions time scale are shorter than the system characteristic times: the particle distribution is close to Maxwellian); (2) charge macroscopic neutrality; (3) non-relativistic velocities. The plasma in the solar corona strongly interacts with the solar magnetic field. Under certain assumptions, it is possible to describe it as a single, electrically neutral, and nearly perfectly conducting fluid. Magnetohydrodynamics accurately describes its evolution (Chiuderi & Velli 2012; Priest 2014).

1.3.1 Basics

The Maxwell's equation in c.g.s. units are:

$$c\,\nabla \times \mathbf{E} = -\frac{\partial B}{\partial t}, \tag{1.1}$$

$$\nabla \cdot \mathbf{B} = 0, \tag{1.2}$$

$$\nabla \cdot \mathbf{E} = 4\pi q, \tag{1.3}$$

$$c\,\nabla \times \mathbf{B} = 4\pi \mathbf{j} + \frac{\partial \mathbf{E}}{\partial t}, \tag{1.4}$$

where $\mathbf{E}$ and $\mathbf{B}$ are the electric and magnetic fields, q and $\mathbf{j}$ are the charge and current densities, and c is the speed of light. Combined with the Lorentz force:

$$\mathbf{F}_L = q\,\mathbf{E} + \frac{1}{c}\mathbf{j} \times \mathbf{B}, \tag{1.5}$$

they form the basis for classical electromagnetic phenomena (Jackson 2021).

According to Lorentz transformations, electric field and the current density in a co-moving, conducting medium (primed) frame, have strength:

$$E'_{\parallel} = E_{\parallel} \qquad \mathbf{E}'_{\perp} = \gamma(\mathbf{E}_{\perp} + \beta \times \mathbf{B}), \tag{1.6}$$

$$\mathbf{j}'_{\parallel} = \mathbf{j}_{\parallel} \qquad \mathbf{j}'_{\parallel} = \gamma(\mathbf{j}_{\parallel} - qc\mathbf{v}), \tag{1.7}$$

where β is the fluid velocity in the laboratory (unprimed) frame in units of c and $\gamma = (1-\beta^2)^{-\frac{1}{2}}$ is the Lorentz factor. If the fluid has finite electric conductivity σ', then the Ohm's law for a neutral ($q = 0$), conductive fluid, in the laboratory frame is:

$$\mathbf{E} = \frac{\mathbf{j}}{\sigma} + \beta \times \mathbf{B}. \tag{1.8}$$

Charge neutrality in a ionized plasma is guaranteed when the number of particles in a sphere of Debye radius:

$$\lambda_D = \sqrt{\frac{k_B T}{4\pi n e^2}}, \tag{1.9}$$

is very large ($n\lambda_D^3 \gg 1$, Braus 2019).

By neglecting second-order terms in β, Eq. 1.4 reduces to:

$$\mathbf{j} = \frac{c}{4\pi}\nabla \times \mathbf{B}, \tag{1.10}$$

The current density in Eq. 1.10 is divergence-free ($\nabla \cdot \mathbf{j} = 0$): in non-relativistic MHD, currents have no sources nor sinks. From source term in vacuum electrodynamics, the current density is now denoted as a secondary variable whose values depend on $\mathbf{B}$, by

the Ampere's law (Eq. 1.10). By combining Eq. 1.3 with the divergence of Eq. 1.4, we obtain the charge conservation law:

$$\frac{\partial q}{\partial t} + \nabla \cdot \mathbf{j} = 0, \tag{1.11}$$

that reduces to:

$$\frac{\partial q}{\partial t} = 0, \tag{1.12}$$

in non-relativitic MHD. If the plasma is initially neutral, no charge displacement will further develop, consistently with the assumption of a charge-neutral plasma.

We can combine Eqs. 1.8, 1.1 and the divergence of Eq. 1.10 to infer the magnetic induction equation:

$$\frac{\partial \mathbf{B}}{\partial t} = \nabla \times (\mathbf{v} \times \mathbf{B}) + \eta \nabla^2 \mathbf{B}, \tag{1.13}$$

where $\eta = \frac{c^2}{4\pi\sigma}$ is the electric diffusivity. According to equation 1.13, the rate of change of the magnetic field depends on both the fluid motion ($\nabla \times (\mathbf{v} \times \mathbf{B})$) and some diffusion processes ($\eta \nabla^2 \mathbf{B}$). The second term on the right-hand side of Eq. 1.13 has the same form as, e.g., diffusion of heat (by thermal conductivity) and momentum (by viscosity) in parabolic equations. Moreover, it can be proved that

$$\nabla \cdot \frac{\partial \mathbf{B}}{\partial t} = \frac{\partial}{\partial t} \nabla \cdot \mathbf{B} = 0, \tag{1.14}$$

namely, provided $\nabla \cdot \mathbf{B} = 0$ at $t = 0$, then, the soleinodal condition holds at any time. The first term on the right-hand side of Eq. 1.13 can be expanded using the standard vector identities to:

$$\frac{\partial \mathbf{B}}{\partial t} = -\mathbf{B}\, \nabla \cdot \mathbf{v} - (\mathbf{v} \cdot \nabla)\, \mathbf{B} + (\mathbf{B} \cdot \nabla)\, \mathbf{v}, \tag{1.15}$$

where the first term on the right hand side describes the effect of the fluid expansion or compression. The second term instead describes the effects of advection.

If we integrate Eq. 1.13 on a surface $\mathbf{S}(t)$ whose points are passively advected with the plasma elements ($d\mathbf{S} = d\mathbf{l} \times \mathbf{v}\, \delta t$), we obtain:

$$\frac{d}{dt} \int_{S(t)} \mathbf{B}(t) \cdot d\mathbf{S} = \int_{S(t)} \eta\, \nabla^2 \mathbf{B} \cdot d\mathbf{S}. \tag{1.16}$$

If the plasma is a perfect conductor ($\eta = 0$), then the magnetic flux is always conserved (Alfvén theorem Alfvén 1942).

The Lorentz force is shown in Eq. 1.5 and can be expanded into:

$$\mathbf{F}_L = \frac{1}{4\pi} (\nabla \times \mathbf{B}) \times \mathbf{B} = -\frac{1}{8\pi} \nabla B^2 + \frac{1}{4\pi} (\mathbf{B} \cdot \nabla)\, \mathbf{B} = -\frac{1}{8\pi} \nabla_\perp B^2 + \frac{B^2}{4\pi} \nabla_\parallel \hat{b} \tag{1.17}$$

where $\nabla_{\parallel} = \hat{b} \cdot \nabla$ and $\nabla_{\perp} = \nabla - \nabla_{\parallel}$ are the parallel and perpendicular projection of gradient operator to $\hat{b}$, the **B** orientation. Both terms are oriented perpendicular to the field lines. The first term is the force exerted by the gradient of the magnetic pressure $p_B = B^2/8\pi$. The second term, called magnetic tension, contains the effects of field line curvature:

$$R_c = \frac{1}{|\nabla_{\parallel} \cdot \hat{b}|} \tag{1.18}$$

and acts as a restoring force straightening bent magnetic field lines.

1.3.2 Conservation equations

The equations of conservation of mass and momentum in their conservative (eulerian) form are, respectively (Chiuderi & Velli 2012; Priest 2014):

$$\frac{\partial \rho}{\partial t} + \nabla \cdot (\rho \mathbf{V}) = 0, \tag{1.19}$$

$$\frac{\partial \rho \mathbf{v}}{\partial t} + \nabla \cdot (\rho \mathbf{v}\mathbf{v}) = -\nabla p + \frac{1}{c}\mathbf{j} \times \mathbf{B} + \mathbf{F}_{\text{ext}}. \tag{1.20}$$

The momentum equation (Eq. 1.20) accounts for pressure force ($-\nabla p$), Lorentz force ($\frac{1}{c}\mathbf{j} \times \mathbf{B}$), and external (e.g., gravity) forces ($\mathbf{F}_{\text{ext}}$).

The temporal evolution of magnetic, kinetic, internal, and gravitational energies is driven by energy sources and sinks (e.g., external heating and radiative losses, respectively) and several energy fluxes at the boundaries of the domain (such as thermal conduction, Poynting flux, enthalpy flux, and kinetic and gravitational energy fluxes). In addition, energy transfer terms may link two different forms of energy. This is the case for Ohmic heating, which converts magnetic energy into heat, and work done per unit time by the Lorentz force, the pressure gradient, and gravity, which respectively convert kinetic energy into magnetic, thermal, and gravitational energy. The respective equations governing the evolution of magnetic, kinetic, internal, and gravitational energy are as follows in their conservative form:

$$\frac{\partial}{\partial t}\frac{B^2}{8\pi} + \nabla \cdot \left[-\frac{1}{4\pi}\mathbf{B}\,(\mathbf{v} \cdot \mathbf{B}) + \frac{B^2}{4\pi}\mathbf{v} + \frac{\eta}{c}\mathbf{j} \times \mathbf{B} \right] = -\frac{j^2}{\sigma} - \frac{\mathbf{v}}{c} \cdot (\mathbf{j} \times \mathbf{B}), \tag{1.21}$$

$$\frac{\partial}{\partial t}\left(\frac{1}{2}\rho v^2\right) + \nabla \cdot \left(\frac{1}{2}\rho v^2\,\mathbf{v}\right) = -\mathbf{v} \cdot \nabla P + \frac{\mathbf{v}}{c}\,(\mathbf{j} \times \mathbf{B}) + \rho\,\mathbf{v} \cdot \mathbf{g}, \tag{1.22}$$

$$\frac{\partial(\rho\epsilon)}{\partial t} + \nabla \cdot \left[\frac{\gamma}{\gamma - 1} P\,\mathbf{v} + \nabla \cdot \mathbf{F}_c\right] = \mathbf{v} \cdot \nabla P + \frac{j^2}{\sigma}, \tag{1.23}$$

$$\frac{\partial(\rho g h)}{\partial t} + \nabla \cdot (\rho g h\,\mathbf{v}) = -\rho\,\mathbf{v} \cdot \mathbf{g}. \tag{1.24}$$

The sum of the four equations gives the equation of conservation of the total energy. Terms on the left-hand sides include rates of change in energy (the derivatives with respect to time) and energy fluxes (i.e. surface terms, which appear here as divergences). External sources, and sinks may be added on the right-hand sides.

$$\frac{\partial}{\partial t}\left(\frac{B^2}{8\pi}+\frac{1}{2}\rho v^2+\rho\epsilon+\rho g h\right)+\nabla\cdot\left[-\frac{1}{4\pi}\mathbf{B}(\mathbf{v}\cdot\mathbf{B})+\frac{B^2}{4\pi}\mathbf{v}+\frac{\eta}{c}\mathbf{j}\times\mathbf{B}+\right.$$
$$\left.+\frac{1}{2}\rho v^2\mathbf{v}+\frac{\gamma}{\gamma-1}P\mathbf{v}+\mathbf{F}_c+\rho g h\mathbf{v}\right]=$$
$$=H_{\text{ext}}. \quad (1.25)$$

1.3.3 Dimensionless parameters

Consider the momentum equation (Eq. 1.20) and the induction equation (1.13):

$$\rho\frac{d\mathbf{v}}{dt}=-\nabla p+\frac{1}{4\pi}(\nabla\times\mathbf{B})\times\mathbf{B} \quad (1.26)$$

$$\frac{\partial\mathbf{B}}{\partial t}=\nabla\times(\mathbf{v}\times\mathbf{B})+\eta\nabla^2\mathbf{B}. \quad (1.27)$$

The first equation returns the rate of change of the velocity field as a consequence of magnetic (and pressure) forces; the second equation, complementary, gives the rate of change of the magnetic field due to the velocity field (and diffusion).

We define the Mach number M, the plasma beta β, and the magnetic Reynolds number R_m, the following dimensionless parameters:

$$M=\frac{v_0}{c_i}, \qquad \beta=\frac{p}{B_0^2/8\pi}, \qquad R_m=l_0 v_0/\eta \quad (1.28)$$

where, l_0 (t_0) is the typical length (time) scale of the system, $v_0=l_0/t_0$ and $c_i=\sqrt{\gamma\, p/\rho}$ are the fluid and the isothermal sound speed, respectively, and $B_0^2/8\pi$ is the magnetic field pressure. The plasma beta can be also defined as the ratio between the (squared) sound speed and the (squared) Alfvén speed.

$$\beta=\frac{c_i^2}{v_A^2} \quad (1.29)$$

where $v_A=\frac{B}{\sqrt{4\pi\rho}}$, is the typical velocity of propagation of a magnetic signal along a file line.

Newton's and induction equations can be written in terms of these adimensional parameters, as follows:

$$M^2 \frac{d\tilde{\mathbf{v}}}{d\tilde{t}} = -\tilde{\nabla} \ln \rho + \frac{2}{\beta} (\tilde{\nabla} \times \tilde{\mathbf{B}}) \times \tilde{\mathbf{B}} \tag{1.30}$$

$$\frac{\partial \tilde{\mathbf{B}}}{\partial \tilde{t}} = \tilde{\nabla} \times (\tilde{\mathbf{v}} \times \tilde{\mathbf{B}}) + \frac{1}{R_m} \nabla^2 \tilde{\mathbf{B}} \tag{1.31}$$

where the tilde signs on the top of $\mathbf{v}$ and $\mathbf{B}$ denote the dimensionless quantities $\mathbf{B}/B_0$ and $\mathbf{v}/v_0$, respectively.

These three parameters determine the several regimes that can rule the evolution of an MHD plasma. M separates highly-subsonic flows ($M \ll 1$) vs. strongly supersonic flows ($M \gg 1$) . β discriminates over gas-pressure-dominated ($\beta \gg 1$) v.s. magnetic-field-dominated ($\beta \ll 1$) plasmas. Finally, R_m determines the efficiency of magnetic dissipation and diffusion ($R_m \ll 1$) as compared with the ideal, field lines dragging of frozen-in magnetic fluxes ($R_m \gg 1$).

1.3.4 Force-free fields

$M = 0$ and $\beta \ll 1$ defines a regime of MHD equilibrium that can be guaranteed by neglecting the Lorentz force term in Eq. 1.20:

$$(\nabla \times \mathbf{B}) \times \mathbf{B} = 0 \tag{1.32}$$

This can be achieved in two independent ways, providing two different classes of 'force free fields':

- Potential fields: if $\nabla \times \mathbf{B} = 0$, then the vector field $\mathbf{B}$ can be written in therms of the divergence of a scalar field ϕ i.e. the magnetic field potential;

- (non-potential) Force free fields: when the term $\nabla \times \mathbf{B} \neq 0$ but its everywhere parallel to $\mathbf{B}$, then the vector product in Eq. 1.32 is zero. We call "linear" the force-free fields when $\mathbf{B} = \alpha \nabla \times \mathbf{B}$, with α a constant parameter. In a "non-linear" force-free field, α is a function of space but is always constant along each field line ($\mathbf{B} \cdot \nabla \alpha = 0$).

It can be easily demonstrated that, in a volume with fixed boundaries, a force-free magnetic field is a relative minimum-energy state, while the absolute minimum is a potential field.

1.3.5 Helicity

Being **A** the vector potential of **B**:

$$\mathbf{B} = \nabla \times \mathbf{A}, \tag{1.33}$$

the magnetic helicity H is defined as the volume integral:

$$H = \int_V \mathbf{A} \cdot \mathbf{B}\, dV. \tag{1.34}$$

Such a quantity measures the global degree of twisting and kinking of a single flux tube (self- helicity), as well as the linkage between different flux tubes (mutual helicity). Since the vector potential, **A**, is gauge dependent, the (gauge independent) helicity, H, must depend not only on the local field lines twisting, but also on their global 'linking' within the overall magnetic configuration i.e. it is a topological quantity.

In perfectly conducting and isolated plasmas, the helicity is a global topological invariant, i.e. is a conserved quantity, as no changes in field line topology are allowed without breaking of magnetic field lines i.e. without reconnection. On the other hand, in a resistive medium, it decays over the global magnetic diffusion time:

$$\frac{dH}{dt} = -\int_V 2\eta\, (\nabla \times \mathbf{B}) \cdot \mathbf{B}\, dV. \tag{1.35}$$

Therefore, the rate of change in magnetic helicity scales as $\mathbf{j} \cdot \mathbf{B}$. In dissipative plasmas, relaxation of a magnetic configuration can quickly induce the development of small-scale current sheets, where reconnection takes place, dissipating energy though not necessarily causing the decrease of helicity.

A potential magnetic field ($\nabla \times \mathbf{B} = 0 \rightarrow \mathbf{B} = \nabla\phi$) i.e. a field with zero energy in excess, has also zero magnetic helicity. Therefore, an out-of-equilibrium, ideal, magnetic field with nonzero helicity cannot decay to a potential field. In general, the minimum energy state of an isolated system corresponds to a linear force-free field.

1.3.6 Reconnection

An ideal plasma (magnetic Reynols number $R_m \gg 1$) preserves the magnetic linkage between the plasma elements. On the other hand, in localised regions where $R_m \gtrsim 1$, non-ideal effects of magnetic diffusion can be significant. "Magnetic reconnection" (Pontin & Priest 2022), in particular, comes into play with a change of connectivity between plasma elements. Generally, it involves several physical effects:

- Change of magnetic topology;
- Strong electric currents and electric fields;

- Shock waves and particles acceleration;
- Ohmic dissipation of magnetic energy into heat;
- Release of magnetic tension accelerating plasma (by Lorentz force).

In an ideal plasma ($\mathbf{E} + \mathbf{v} \times \mathbf{B} = 0$) both magnetic flux and field lines are conserved. If the plasma is not ideal ($\mathbf{E} + \mathbf{v} \times \mathbf{B} = \mathbf{N} \neq 0$), flux conservation ($\nabla \times N = 0$) implies field lines conservation ($\mathbf{B} \times (\nabla \times \mathbf{N}) = 0$), but the reverse is not true. The form of $\mathbf{N}$ also determines whether reconnection occurs in a 2D plane or in 3D. In particular, if it can be written as $\mathbf{N} = \mathbf{u} \times \mathbf{B} + \Phi$, where $\mathbf{u}$ is the "slippage velocity" of the field lines and Φ a potential, then, 2D reconnection occurs only where $\mathbf{u}$ is singular. Otherwise, it is 3D reconnection (Priest 2014; Pontin & Priest 2022).

Giovanelli (1947) suggested that electric fields in magnetic neutral points could accelerate particles and produce heating during solar flares. Cowling (1958) investigated the collapse of a X-type neutral point forming a narrow current sheet and Dungey (1961) applied the same mechanism to the Earth's magnetosphere. Sweet (1958) and (Parker 1957) independently modelled steady-state reconnection in a thin current sheet. According to Furth et al. (1963), the instability of the tearing mode instability in current sheet may trigger resistive reconnection. A reconnection regime fast enough to propel flares on the Sun was first proposed by Petschek (1964), then extended to a family of "Almost-Uniform models" for fast reconnection by Priest & Forbes (1986).

Magnetic reconnection in the Sun (Zweibel & Yamada 2009; Pontin & Priest 2022) is supposed to commonly occur in localized regions with strong, ideally infinitely sharp, magnetic field gradients, where magnetic field lines converge and then break apart, releasing energy. These regions are typically found, e.g., at the boundaries of active regions, where intense magnetic activity can create complex magnetic field structures. Key areas of interest include 'null points', 'separatrices', and 'quasi-separatrix layers'. A linear 2D or 3D null point locates the place where the magnetic field vanishes and further increases linearly with distance, creating a topological configuration that can facilitate reconnection. In a planar magnetic field, a separatrix curve is a field line that divides the plane into two topologically, magnetically unlinked regions. In 3D, separatrix surfaces track discontinuities in the field lines mapping as well. Specifically, separatrices are surfaces that divide regions of differing magnetic connectivity, acting as potential sites for reconnection due to the sharp contrast in field lines. For example, they can spread out from the fans of null points. These boundaries are generated by the highly fragmented photospheric magnetic flux, concentrated in the lower, high-β atmosphere within kilogauss flux tubes. As such tubes, separated in the photosphere, expand in the low-β corona, they become space filling and develop contact boundaries known as quasi-separatrix layers (Klimchuk & Antiochos 2021).

2D reconnection

In 2D reconnection, the following basic features are present:

- An X neutral point -namely a point where field lines are locally hyperbolic- surrounded by a localised non-ideal diffusion region;
- Pairs of field lines joining, breaking, and changing their connectivity at the X-point;
- A non-null electric field perpendicular to the plane.

The Sweet-Parker model for slow, steady-state, 2D reconnection (Sweet 1958; Parker 1957, see also left hand side of Fig. 1.8) involves a nonideal region localised in a current sheet (where reconnection occurs), $2L$ long and $2l$ wide, approached by two parallel though oppositely directed magnetic fields. The plasma mass inflow must be equal to mass outflow driven by reconnected field lines:

$$Lv_i = lv_o \tag{1.36}$$

where $v_i = \eta/l$ is the diffusion speed and $v_o = B/\sqrt{(4\pi\rho)}$ the Alfvén inflow speed (the plasma is accelerated along the current sheet by the Lorentz force). The reconnection rate estimated with the Alfvén Mach number $M = v_i/v_o$ therefore is:

$$M = R_m^{-\frac{1}{2}} \tag{1.37}$$

where the magnetic Reynolds number ($R_m = \frac{Lv_o}{\eta}$) is typically of the order of 10^8-10^{12}, leading to an outflow velocity 10^4-10^6 times smaller than the Alfvén velocity. Petschek (1964) demonstrated that faster recollection rates (tens of the Alfvén speed) can be achieved if the diffusion region is small compared to L (right side of Fig. 1.8). However, the existence of a stable, stationary Petschek reconnection was disputed (Biskamp 1986; Forbes & Priest 1987). According to numerical simulations (e.g., Biskamp 1982, 1994), long current sheets undergo resistive magnetic reconnection in a time-variable fashion, with quasi-periodic development and coalescence of magnetic islands ('second tearing reconnection', Priest 1985). Fast reconnection regimes are also produced by plasmoids-mediated tearing instabilities, creating coherent flux ropes (Shibata & Tanuma 2001) as well as in turbulent reconnection, where field lines in turbulent plasmas are rapidly dispersed, thus increasing the aspect ratio of the reconnection layer (Lazarian et al. 2015).

3D reconnection

3D magnetic reconnection occurs within intense electric current concentrations. They can lay within null points separators but also in quasi-separators and braids where the

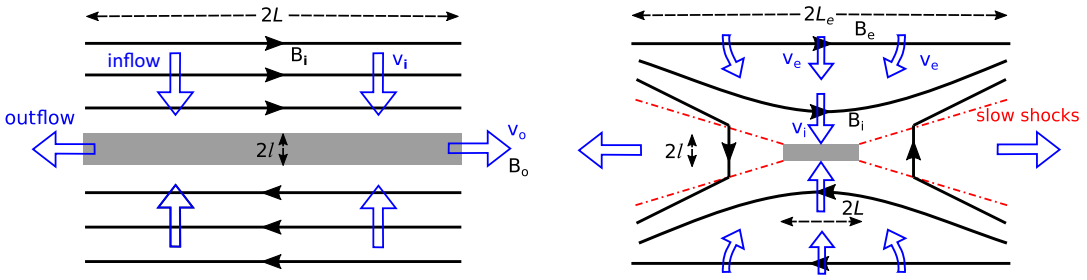

Figure 1.8: A schematic picture of the Sweet–Parker (left hand side) and the Petschek's (right hand side) mechanisms of reconnection. The plasma flow (blue arrows, v_i) squeezes magnetic field lines (black curves, B_i) into the diffusion region (grey rectangle) of dimensions $2L \times 2l$, where they reconnect (B_0) and accelerate outflows (v_o). In regimes of fast reconnection (Petschek's included), plasma inflows v_e at larger distances L_e transport the external magnetic field (B_e) towards the diffusion region. After reconnection four shock waves (red, dashed lines) form as the heated plasma is expelled (to the left and right, on the diagram). Credit Pontin & Priest (2022)

magnetic field does not vanish completely: the occurrence of magnetic reconnection in 3D is not generally restricted to the cases where the magnetic field vanishes somewhere in a non-ideal diffusion region. In 3D magnetic configurations, the formation of localised current sheets is the precondition for reconnection to occur. Indeed, nulls, separators, quasi-separators, and braids are the natural locations where strong currents can develop: at these locations, the field-line mapping can be either discontinuous (null points and separatrices) or exhibits steep gradients (quasi-separatrices or braids), where stress naturally accumulate driving the growth of intense electric currents.

Figure 1.9 schematically shows the different regimes of 3D magnetic reconnection, as also outlined by Schindler et al. (1988). In particular, if the magnetic field vanishes where the plasma is not ideal, namely at the dissipation region D_R, then, "0-B" magnetic reconnection occurs. On the other hand, "finite-B" reconnection evolves within a non-vanishing guide field. Hesse & Schindler (1988) showed that in finite-B, global reconnection (i.e. where the breakdown of magnetic connection occurs for plasma elements that lies beyond the non-ideal region), the electric field component parallel to the magnetic field ($E_\parallel$) plays a crucial role. In particular they demonstrated that, defined

$$U_{\mathrm{fl}} = -\int_{\mathrm{fl}} E_\parallel ds, \tag{1.38}$$

with s denoting the arc length of the field line (fl), a finite-B reconnection process is global if and only if U_{fl} is different than zero on a measurable set of field lines inside the

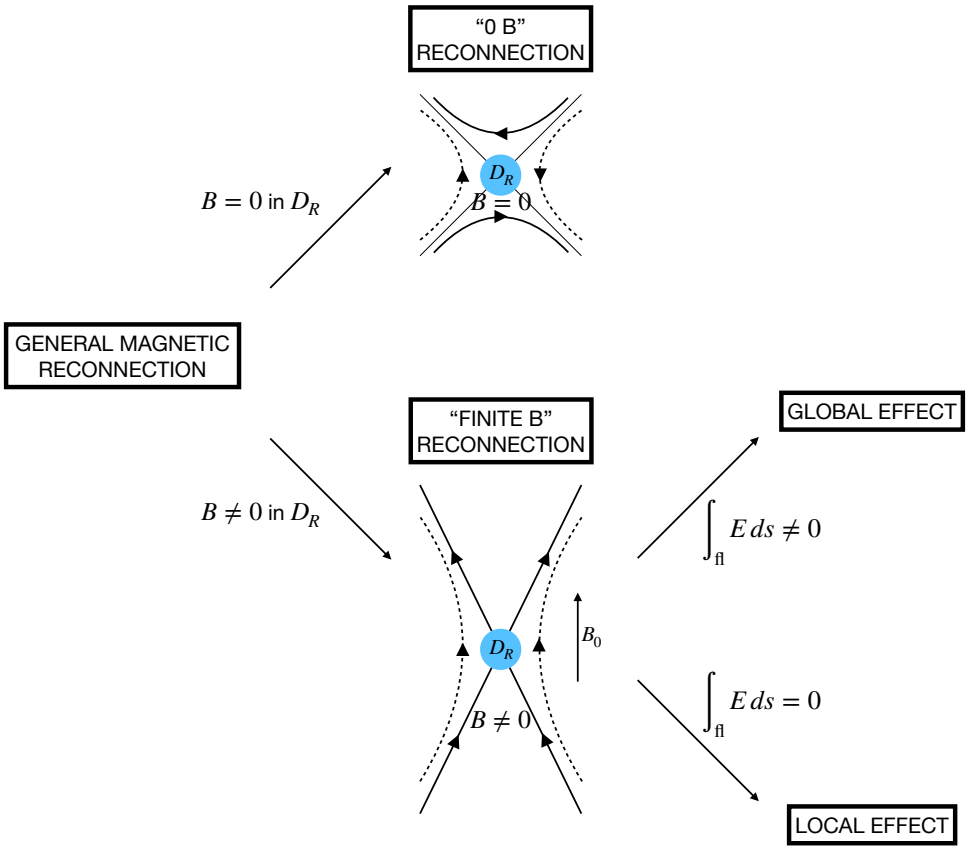

Figure 1.9: General classification of the regimes of 3D magnetic reconnection. "0-B" reconnection occurs when the magnetic field vanishes at the dissipation region D_R. Otherwise, "finite-B" reconnection occurs. A finite-B reconnection is defined "global" if U_{fl} in Eq. 1.38 is zero, otherwise the process is "local". Adapted from Schindler et al. (1988).

diffusion region D_R, defined as the region where the following condition holds:

$$\begin{cases} \mathbf{R} = \mathbf{E} + \mathbf{v} \times \mathbf{B}, \\ \mathbf{B} \times (\nabla \times \mathbf{R}) \neq 0. \end{cases} \tag{1.39}$$

In other words, three-dimensional reconnection occurs when the parallel electric field is non-zero ($\mathbf{E} \cdot \mathbf{B} \neq 0$) within the diffusion region D_R. Outside of this region, the electric field is perpendicular to the magnetic field ($\mathbf{E} \cdot \mathbf{B} = 0$). Although general reconnection includes cases of magnetic diffusion by field lines slippage, it is possible to restrict the definition to a "X-type singular reconnection", where the magnetic field projected onto the plane perpendicular to the field lines forms an X-point, likewise 2D reconnection

(Priest & Forbes 1989; Hornig & Rastätter 1998).

The occurrence of magnetic reconnection is associated with a change in magnetic helicity (H) over time. The rate of change of magnetic helicity can be expressed (from Eq.s 1.35, and 1.8) as:

$$\frac{dH}{dt} = -2\int_{D_R} \mathbf{E}\times\mathbf{B}dV = -2\int_{D_R} E_{\parallel}BdV \sim -2E_{\parallel}B_0V_R \tag{1.40}$$

where V_R is the volume of the diffusion region. Since magnetic reconnection and diffusion only occur within the limited volume of D_R, which in turn is small because at high R_m the current layers are very thin, the total magnetic helicity is approximately conserved. However, the process of three-dimensional reconnection is directly tied to the small but significant changes in magnetic helicity that occur in this region.

1.4 Energisation and heating of the solar corona

Activity in the solar (and stellar, Testa et al. 2015) atmosphere, and especially in the solar corona, is the response to the evolution of the underlying magnetic field. On global scale, the emerging magnetic flux is modulated by an 11-year cycle (Hathaway 2015), during which many characteristics of the solar activity, such as the sunspot number, variate. The solar cycle is regulated by a solar dynamo mechanism (Charbonneau 2020), sustained in turn by convective motions, differential rotation, and magnetic buoyancy. Besides MHD theory is not needed to describe the solar interior (indeed hydrodynamics together with radiative transfer rules plasma behaviour in the convective zone), is there that plasma flows sustain currents, bring and generate magnetic flux and drive it to the solar surface, resulting into a periodic change in magnetic field polarity and topology, on a global scale, and on flux emergence, Sunspots formation, etc. on smaller scales (Hudson 2010).

1.4.1 Flares, microflares, and nanoflares

In solar physics, the term ‘flare’ is generally ascribed to a “syndrome” of observed phenomena, supposedly related by the same underlying mechanism of impulsive energy release by magnetic reconnection (Hudson 2010). However, this definition is based on a specific, although widely accepted, interpretation of the observations. The flare phenomenon is defined as a brightening on the solar (stellar) atmosphere across the electromagnetic spectrum that evolves over time scales of minutes to hours (Benz 2017), and in particular in the chromospheric Hα line and X-rays. The strength of a flare can be determined by both the extent of the Hα area and its X-ray brightness (Svestka & Cliver 1992). In the last case, the energy flux in the 1-8 $\mathring{A}$ range is measured at the brightening peak (Tanaka et al. 1983; Ohki et al. 1983; Tsuneta et al. 1984) using, e.g., GOES data

(Warmuth & Mann 2016). The weakest flare (A class) must exceed $10^{-8}\,\mathrm{W\,m^{-2}}$, while the strongest flare (X class) can reach $10^{-4}\,\mathrm{W\,m^{-2}}$.

From a physical perspective, flares are the most outstanding aftermath of magnetic energy released in coronal loops guaranteed by the existence of multiple force-free states as equilibrium solutions of the MHD equations in response to photospheric motions. The evolution of a flare involves the reorganization of the loop's magnetic field, acceleration of non-thermal particles, chromospheric plasma ablation, and coronal flows (Hudson 2010).

In a commonly accepted scenario, coronal loops act as magnetic energy reservoirs. They gain and store the energy injected as Poynting flux by photospheric motions at the footpoints. The magnetic structure on the corona passively readjusts to slow photospheric motions exploring a series of force-free equilibrium states on time scales much longer than the loop's Alfvén travel-time. As they reach the physical conditions prior to a flare, coronal loops can store a highly twisted or sheared magnetic field with energy in excess of the potential energy. The release of this excess can be accomplished by magnetic reconnection. For instance, MHD catastrophes and instabilities (e.g., torus, kink), reconnection breakout between sheared or oppositely directed collection of field lines, and flux emergence can trigger a flare. Growing magnetic stresses lead to the breakdown of field lines and, consequently, plasma and particle acceleration and, ultimately, heating, at the expense of the magnetic energy (Priest 2014).

The evolution of a flare can be modelled by different phases (Jakimiec et al. 1992; Reale 2007; Hudson 2011). The initial phase of a flare denotes the duration of impulsive energy release, accompanied by intense non-thermal outcomes. Indeed, energy released in the reconnection site initially propels high-energy particles and directly heats the plasma by Ohmic dissipation. Heat conduction and non-thermal particles rapidly transfer the released energy down to the lower atmosphere and transition region, brightening HXR footpoints and, for example, Hα ribbons. As soon as the magnetic energy is released into heat, the gas pressure in the corona increases, as well as its hydrostatic scale height: $\lambda_p = 2k_BT/\mu g_\odot$ (where k_B is the Boltzmann constant, T the temperature, μ the mean molecular weight, and $g_\odot$ gravity acceleration). At typical flaring temperatures ($> 10^7$ MK), λ_p is much larger than loop the structures by factors. As a consequence, the corona drains mass from the chromosphere, which acts as a mass reservoir.

The manifestations of a flare as coronal loop brightening in the EUV band lag behind the chromospheric gleaming. This is due to the delay in time between the swift energy release and the time requested to increase the coronal density by chromospheric evaporation. In this gradual phase, thermal emission (bound–bound transitions from plasma with Maxwellian distribution) from the now dense ($\sim 10^{12}\,\mathrm{cm^{-3}}$) and hot coronal plasma dominates. In the meantime, strong chromospheric and transition-region emission drives cooling, as thermal conduction leads to an excess of radiation at transition-region and chromospheric temperatures (Hudson 2010).

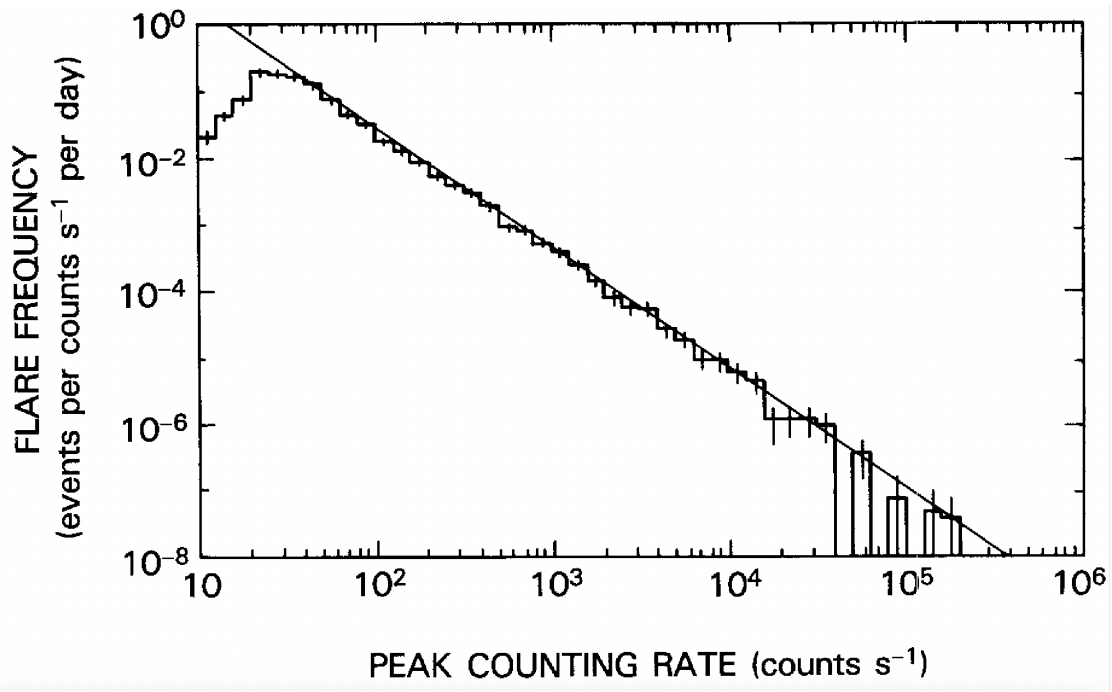

Figure 1.10: Peak rate distribution function for hard X-ray bursts, based upon the complete HXRBS dataset of events detected from the Solar Maximum Mission launch to February 1985. The straight line corresponds to the power-law with a spectral index of ~ 1.8. Credit: Dennis (1985).

Solar flares show similar properties (such as the peak flux of the burst) scaling systematically with the energy released (*big flare syndrome*, Kahler 1982). In particular, flare frequency scales with energy as a power-law distribution:

$$\frac{dN}{dE} = A \times E^{\alpha} \tag{1.41}$$

in terms of the flare energy (E), the power-law index (α), and a normalization factor (A), dependent of the level cof activity of the sun (star). The power-law index $\alpha \sim 1.7$, (Drake 1971; Dennis 1985; Crosby et al. 1993), extends over several orders of energy magnitude, as shown in Fig. 1.10. This is in line with the scale invariance expected from self-organized criticality models.

The total energy of the strongest flares exceed 10^{32} ergs, while the weakest observed feature-like flares, called 'microflares', are around 10^{26} ergs (Lin et al. 1984). Small impulsive events, ascribed to microflares, have also been observed in the EUV band since the 70s (e.g., Kahler 1982; Lites & Hansen 1977; Brueckner & Bartoe 1983).

The observed spectrum has been hypothesised to scale down to nano-flare energies $\sim 10^{24}$ ergs. Those 'nanoflares' could arise from impulsive and localised bursts of magnetic energy release via magnetic reconnection (Parker 1988), as a result of the continuous shuffling of coronal loop strand footpoints (Parker 1983).

The relative contribution to the total energy power between small and large flares critically depends on the power-law index α. In particular, the flatness ($\alpha < 2$) of the energy distribution radiated during a flare implies that the less energetic events, such as micro- and nanoflares, contribute negligibly to the overall energy power, dominated instead by the most energetic ones. Indeed, the total energy released over a given energy range (from $E_{\rm min}$ to $E_{\rm max}$) is (by integration of Eq. 1.41):

$$W(E_{\rm min}, E_{\rm max}) = \int_{E_{\rm min}}^{E_{\rm max}} \frac{dN}{dE}\, E\, dE = \frac{A}{2-A}[E_{\rm max}^{-\alpha+2} - E_{\rm min}^{-\alpha+2}]. \tag{1.42}$$

Enough energy to steadily power chormospheric and coronal heating, as well as the acceleration of the solar wind, can be attained by nanoflare activity only with the power law-index $\alpha > 2$ (Hudson 1991). Recent studies based on SDO/AIA data have found a value of $\alpha > 2$ (e.g., Ulyanov et al. 2019; Purkhart & Veronig 2022; Bogachev & Erkhova 2023), although the total energy released by nanoflares was estimated to be less than the requirements for coronal heating.

Statistical analysis of decayless transverse oscillations (Nakariakov et al. 2021) observed by SDO/AIA and SolO/EUI, as documented, e.g., in Lim et al. (2023), were conducted. These oscillations were found to generate energies ranging from approximately 10^{20} to 10^{25} erg. Lim et al. (2023) demonstrated that high-frequency oscillations, which produce significant energy flux and total energy, dominate the overall heating contribution from oscillations. This result, grounded in the nanoflare heating theory, emphasizes the vital role of high-frequency oscillations. Specifically, it was shown that high-frequency transverse oscillations could play a key role in coronal heating compared to their low-frequency counterparts. Moreover, the total energy flux generated by decayless oscillations was sufficient to heat the quiet Sun and was comparable to the heating requirements of active regions.

1.4.2 The coronal heating problem

The coronal heating problem emerged after Grotian (1939) and Edlén (1943) found that the emission lines observed during the 1869 total solar eclipse were not caused by a newly proposed element, the 'coronium', but by highly ionized iron, thus demonstrating that corona has a temperature of one or more millions K as compared with the underlying, 6000 K hot, photosphere. It is now widely accepted that the solar atmosphere experiences a soft temperature rising across the chromosphere and a dramatic temperature enhancement across the transition region. Afterwards, Vaiana (1981) showed that

most of the stars share the same soft X-ray coronal emission (Testa et al. 2015, for a review).

Combining the energy loss rates by radiation and thermal conduction, the heat flux required to power the corona is about 1-3 $\times 10^5$ erg cm^{-2} s^{-1} for the quiet Sun and a factor of 100 more in active regions, scaling up by an order of magnitude in the chromosphere (Withbroe & Noyes 1977; Katsukawa & Tsuneta 2002). As hotter active regions often involve stronger magnetic fields, it is widely accepted that the magnetic field is the dominant storage of energy heating the solar corona. The energy originates from the convective turbulence of plasma occurring at and beneath the photosphere. These motions constantly displace the footpoints of the pervasive magnetic fields.

In ideal-MHD ($\mathbf{E} = -\mathbf{v} \times \mathbf{B}$, where $\mathbf{E}$ is the electric field, $\mathbf{B}$ is the magnetic field and $\mathbf{v}$ is the plasma velocity), the Poynting flux:

$$\mathbf{\Phi}_B = \frac{c}{4\pi}\mathbf{E} \times \mathbf{B}, \tag{1.43}$$

can be written in terms of the horizontal and vertical magnetic field components (B_h and B_v, respectively), the driver velocity v_h and the up/down-flows velocity v_v, oriented horizontally and vertically, respectively (Parnell & De Moortel 2012):

$$\Phi_B = -\frac{c}{4\pi} v_h B_h B_v + \frac{c}{4\pi} v_v B_h^2 \tag{1.44}$$

The strength of Φ_B crucially depends on the combination of these four factors.

According to a possible scenario, magnetic fields are hypothesised to be confined within intense kilo-G flux tubes, which are transported at a characteristic local velocity on the order of kilometres per second. Assuming the magnetic field is inclined at an angle of 20 degrees and the filling factor in the quiet Sun is 1% (yielding an average field strength of 10 G), the resulting Poynting flux per unit area is approximately 2.5 $\times$ 10^7 erg cm^{-2} s^{-1} (Parnell & De Moortel 2012). In both scenarios, the energy generated by the displacement of magnetic footpoints appears to be more than sufficient to heat both the chromosphere and the corona. The Poynting flux associated with the emergence of a single kilo-G flux tube is estimated to be 2×10^{12} erg cm^{-2} s^{-1}, assuming an upflow velocity of 2 km s^{-1} and a filling factor of 6×10^{-7} (Thornton & Parnell 2011). Consequently, in the quiet Sun, the Poynting flux due to the emergence of new magnetic flux is approximately 10^6 erg cm^{-2} s^{-1}, which is 25 times lower than the flux generated by the horizontal motion of magnetic footpoints, indicating that footpoint motions serve as the dominant energy source. Furthermore, by comparing the calculated magnitude of Φ_B with radiative losses and thermal conduction rates, we conclude that the Poynting flux generated by horizontal photospheric motions at the magnetic footpoints supplies sufficient energy to power the solar corona (Abbett & Fisher 2012).

Suppose a pure horizontal velocity $\mathbf{v} = v_h \hat{h}$, the sign of the product in the first term on the right-hand side of Eq. 1.44 determines the route of the travel of the energy

flux, which can *a priori*, be positive or negative. Magnetic field lines are frozen into the photospheric plasma and randomly move within convective cells. Field lines are dragged by photospheric motions and tilt in the direction opposite to the plasma velocity at the footpoints. This bending of field lines backward away from the footpoint trail implies that the Poynting flux points always upward, directed to the corona, as shown schematically in Fig. 1.11.

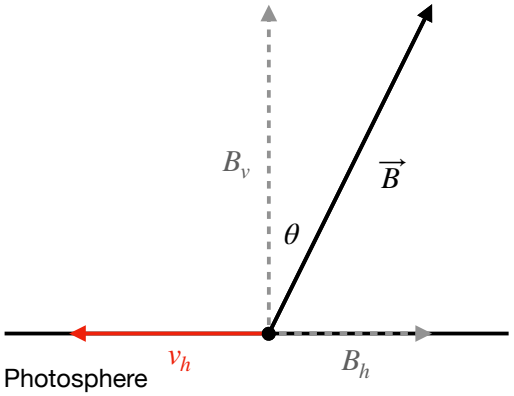

Figure 1.11: Schematic representation of a field line (B_h, B_v) bending in the sense opposite to the velocity driver v_h: the resulting Poynting flux product is positive. Adapted from Priest (2014)

In general, all the tree elements listed above (B_v, v_h, B_h) are determinant for the heating efficiency in the corona, as they all contribute to the Poynting flux product. Specifically, as discussed previously, the strength of the magnetic field in active regions (B_v) generally correlates well with the intensity of the heating itself. However, the convective freedom at the photospheric footpoints of an active region coronal loop appears to be the primary determinant of its brightness (Tiwari et al. 2017). Indeed, braiding of field lines, powering heating by magnetic reconnection, can be quenched if for instance strong umbra fields suppress magnetoconvection at footpoints, while a combination of a strong umbra magnetic field at one footpoint and an intense penumbra convective churning at the other footpoint determines sensibly hotter coronal active regions loops (Tiwari et al. 2021; Venkataramanasastry et al. 2023).

Although typical vertical magnetic fields ($B_v \sim 10\,\mathrm{G}$ in quiet Sun, $B_v \sim 300\,\mathrm{G}$ in active regions) as well as speeds (about $1\,\mathrm{km\,s^{-1}}$) on the solar surface are well constrained by observations, the value of B_h is difficult to determine, as it depends on the nature of the heating mechanism itself. A time-averaged tilting angle of about 10 degrees was predicted by Parker, despite that it may vary depending on the efficiency and frequency of, e.g., magnetic reconnection in the corona. In fact, understanding the nature, location,

and timing of magnetic energy release events is crucial because they can influence the system by affecting the amount of injected Poynting flux and, ultimately, significantly impacting the resulting plasma behaviour and observational results (Klimchuk 2015).

In the resistive-MHD framework ($\mathbf{E} = \sigma\mathbf{j} - \mathbf{v}\times\mathbf{B}$, where σ is the electric conductivity), the Poynting flux across a surface dS can be expressed as volumetric energy source as follows:

$$\frac{c}{4\pi}\mathbf{E}\times\mathbf{B}\cdot d\mathbf{S} = \left[\frac{j^2}{\sigma} + \frac{\mathbf{v}}{c}\cdot\mathbf{j}\times\mathbf{B} + \frac{\partial}{\partial t}\left(\frac{B^2}{8\pi}\right)\right] dV. \tag{1.45}$$

This expression (Priest 2014) suggests that the magnetic energy flux can contribute to Ohmic heating (first term on the right-hand side), acceleration of plasma (second term), and flux emergence (third term).

On the other hand, it is still highly debated on the nature of the mechanisms that might lead the magnetic field to supply energy to the corona in the form of heating. Although several processes have been proposed in the last decades, it is still unclear how they cooperate to arrange the wild, complex behaviour of the solar atmosphere. Today's challenge is indeed to estimate quantitatively the relative importance of current models. In this context, coronal loops appear as fundamental elements of the investigation to grasp important physical aspects of several magnetic-stress-based heating mechanisms.

It is now clear that the coronal heating problem cannot be addressed without treating the whole solar atmosphere as a highly coupled system (Parnell & De Moortel 2012). Indeed, compared with chromospheric heating, coronal heating represents only a small fraction of the energy that powers the solar atmosphere. For this reason, production, transfer, and damping of energy should be treated comprehensively throughout the solar atmosphere. To do that, the perpetual exchange of energy and mass between the various layers and the dynamic plasma heating and cooling across the transition region should be considered systematically.

Slow (long-timescale) motions result in a quasistatic stressing of the field, whilst fast (short-timescale) motions generate waves. Therefore, the solar corona may be heated both by dissipation of stored magnetic stresses (DC heating), resulting from quasi-static stressing of the field by long time-scale motions, and by the damping of waves (AC heating), generated, in turn, by short time-scale movements (Parnell & De Moortel 2012; Zirker 1993). The ultimate cause of heating is the same, i.e. Ohmic or viscous dissipation in narrow regions. Indeed, the actual dissipation is expected to occur on kinetic scales, since the Lundquist number is found to be very large ($> 10^{10}$). It can be generated in different ways, depending on which mechanism is more efficient, according to, for instance, the morphology of the coronal magnetic structure.

1.4.3 AC heating

AC heating is based on the early suggestion of Biermann (1946) and Schwarzschild (1948) that turbulence in the convection zone could produce (sound) waves, steepening

into shocks as they propagate upward to the corona. As the magnetic field is the dominant supply of energy, these waves must have an MHD nature. (Alfvén & Lindblad 1947). In a uniform plasma of infinite extent, three fundamental MHD wave types, fast, slow, and Alfvén waves, play key roles in energy transport and plasma heating (Arregui 2015; Roberts 2000; Nakariakov & Verwichte 2005, for some reviewes). Fast waves (Cooper et al. 2003; Nakariakov et al. 2004; Verwichte et al. 2006a,b) facilitate energy transfer across magnetic surfaces and can resonantly couple with Alfvén and slow waves in nonuniform plasmas, enabling the transfer of energy to smaller spatial scales. Slow magneto-acoustic modes (Wang et al. 2021; Ofman et al. 1999) are essential in the lower solar atmosphere for driving wave dynamics and are critical in nonlinear processes such as shock formation and dissipation. However, slow waves are easily damp because they rapidly turn into shocks, while fast modes are efficiently reflected at the transition region. Alfvén oscillations of coronal loops (Kudoh & Shibata 1999; McIntosh et al. 2011) are closely observed and analysed because they offer a unique method for probing the internal structure of coronal loops through MHD seismology. Observational evidence suggests that transverse MHD waves may carry sufficient energy to sustain the thermal structure of the solar corona. Alfvén waves are therefore likely to be the relevant wave modes carrying energy up to the corona. These waves are capable of transmitting energy over large distances along magnetic field lines, with dissipation occurring primarily through enhanced viscous and resistive effects in nonuniform plasmas. In particular, Alfvén waves can steep into magnetic shocks, generating propagating current sheets, or transverse wave modes can be converted to localised Alfvén modes, that resonate in a loop within narrow frequency bands, (resonant absorption, Okamoto et al. 2015; Antolin et al. 2015a). Phase mixing of Alfvén waves (Heyvaerts & Priest 1983) within the solar corona is considered a viable mechanism for coronal heating, as it generates transverse gradients where magnetic energy can be efficiently converted into thermal energy. This process is highly dependent on the amplitude and period of the transverse oscillations. Only recently has a complete measurement of the power spectrum for transverse oscillations in the corona been obtained (Morton et al. 2016). AC heating may be the dominant heating mechanism for outer corona and coronal holes, although addressing this heating mechanism in nonuniform mediums remains challenging.

1.4.4 DC heating

Considering the remarkable complexity of the chromospheric and coronal magnetic fields, along with the fragmentation and perpetual motion of countless photospheric footpoints, coronal structures are in a state of restless change and interaction. This dynamic environment makes reconnection in nanoflares (namely DC heating) a natural mechanism for heating the solar corona. DC heating must involve both storage and impulsive release of magnetic energy. In solar active regions, the energy is presumably stored over timescales longer than end-to-end Alfvén travel time of closed

magnetic structures. A reasonable general assumption is that the magnetic field evolves quasi-statically through a sequence of equilibria, slowly changing because the coronal footpoints are rigidly line-tied to the low-beta photospheric plasma. As the coronal field moves through these equilibria, energy is injected by the motions and is then stored. Observations and numerical experiments provide evidence that the evolution of coronal loops is strongly influenced by photospheric motions (Chen et al. 2021). For instance, photospheric magnetic field exhibit remarkably complex patterns with clumpy morphology, organized into clusters of elemental flux tubes. It influences the coronal field structuring into several and distinct magnetic strands, bright in the EUV band, reflecting the underlying granular pattern.

The coronal magnetic field must be driven towards a stressed state, which will be a non-potential configuration and then converted into heat by formation and subsequent dissipation of current sheets. Currents sheets may be formed at separatrices, after interaction of topologically distinct magnetic flux tubes (generated, e.g., by magnetic field dragging at footpoints or by flux emergence, Priest et al. 2002). For instance, flux emerging into the photosphere may form new coronal loops linking the new flux footpoint to former ones. The global restructuring of the pre-existing magnetic field is allowed by magnetic reconnection. Flux cancellation on the photosphere also concern magnetic reconnection as antecedently disconnected magnetic filaments must reconnect to cancel. Flux emergence and cancellation can, e.g., explain some flares (Heyvaerts et al. 1977), X-ray bright points (Priest et al. 1994), and jets (Shibata et al. 1992).

Current sheets have key-role during the non linear evolution of MHD instabilities (such as kink instability) in out of equilibrium magnetic systems, as will be widely discussed in the following section. Indeed, since the coronal plasma is a nearly perfect conductor, magnetic reconnection can only occur within narrow sheets of current, allowing for field lines connectivity change and release of magnetic energy.

Currents sheets might also be the inevitable result of braiding of field lines (Parker 1972, 1988, 1994). Parker proposed that the corona must generate infinitely sharp current sheets (tangential discontinuities), even when both the magnetic flux and flow in the photosphere remain continuous. Indeed, footpoints motion can anyway force field lines to reconnect. In simple words, tangling and twisting of the coronal magnetic strands can not be avoided, according to photospheric observations. The field must therefore reconnect in order to prevent an infinite build-up of stress. This produces unavoidable plasma heating (Klimchuk 2015). For example, Close et al. (2004) applied a magnetic feature tracking algorithm to monitor magnetic features observed in high-resolution MDI magnetograms of the quiet Sun. Their findings indicated that all the coronal magnetic flux in the corona is recycled approximately every 1.4 hours, i.e., magnetic field connectivity is continually changed by breaking and reconnection of field lines.

Similarly, current-sheets production can be efficiently enhanced by the presence of

countless, small magnetic sources on the photosphere, contributing to the complexity of the "magnetic carpet" topology in the solar corona. These current sheets, although uniformly spreading over the loops cross-section, fill a small fraction of its volume and evolve over short time scales. Indeed, equating the order-of-magnitude estimate of Ohmic dissipation in a L^3 active region box (left-hand side of Eq. 1.46) with the Poynting flux energy input across the surface L^2 (right-hand side of Eq. 1.46):

$$\frac{j^2}{\sigma} L^3 = \frac{c}{4\pi} v B^2 L^2, \tag{1.46}$$

gives current densities as strong as $10^7\,\mathrm{Fr\,s^{-1}\,cm^{-2}}$, implying concentration of magnetic field gradients in a remarkably tiny region of space.

Reconnection can directly heat the plasma by Ohmic heating or induce the generation of shocks, that indirectly release heat by viscous damping. Some reconnection models (e.g., Petschek 1964) predict that most of the heating is produced after shocks, while in other reconnection scenarios Ohmic heating might dominate (e.g., Fuentes-Fernández et al. 2012). The specific ongoing reconnection regime as well as the plasma properties are believed to determine the specific mechanism of energy conversion.

Active regions with strong magnetic field experience a state of restless micro-flaring (10^{27} erg) or nanoflaring (10^{24} erg) activity where small-scale current sheets are continually generated and dissipated into heat. Reconnecting current sheets as well as propagation/dissipation of waves in the complex coronal environment can also be described in terms of MHD turbulence (Zhdankin et al. 2014; De Moortel & Nakariakov 2012; McIntosh 2012; Rappazzo et al. 2007), as suggested by observations of coronal nonthermal line broadening, indicating the presence of unresolved, turbulent flows of about $30\,\mathrm{km\,s^{-1}}$ (Brooks & Warren 2009). On the other hand, as pointed by Klimchuk & Antiochos (2021), current sheets formation in the corona do not generally involve a traditional turbulent cascade (Kolmogorov 1941). Therefore, the anyway complex structure of the solar coronal do not straightforwardly bears a direct relationship with turbulence.

Polito et al. (2019) investigated high-resolution observations of the Fe XXI line using the Interface Region Imaging Spectrograph (IRIS, De Pontieu et al. 2014). The spectral characteristics of this high-temperature line are critical for distinguishing between different mechanisms responsible for its significant broadening (thereby providing new insights into energy transport processes in solar flares). To explore these mechanisms, they tested various scenarios—such as the superposition of flows from different loop strands—by forward-modeling the FeXXI line profile using hydrodynamic simulations of multithreaded flare loops with the one-dimensional RADYN code Carlsson & Stein (1992, 1997). Their findings indicate that reproducing both broad and symmetric line profiles is challenging when considering only the superposition of flows (Antonucci et al. 1986). This suggests that additional processes may be necessary to explain the observed excess line broadening during solar flares, including the superposition of unresolved

flows with various Doppler-shifted components, acceleration of ions perpendicular to the magnetic field due to Alfvén wave propagation, departures from ionization equilibrium resulting from high temperatures, and isotropic turbulence (McKevitt et al. 2024).

1.5 Physics of coronal loops

1.5.1 General properties

As anticipated in the section 1.2, coronal loops are relatively dense, arc-like magnetic structures that stand out in the EUV and X-ray images of the Sun for their brightness, as compared, e.g., to the quiet-Sun background. They fill the magnetic skeleton of the lower solar corona with a tenuous ($n \sim 10^9$ cm^{-3}) and hot ($T \sim 10^6$ K) plasma. They are also acknowledged as "building blocks" of this layer where the emergent magnetic field is typically organised in a network of topologically closed structures (Reale 2014). Indeed, their semicircular morphology, running aground the photosphere by their footpoints, evoke the typical, topologically close, structuring of magnetic field lines produced by underlying, opposite-polarity, magnetic sources. Moreover, because of the high magnetic field thermal insulation, the fully ionized coronal plasma moves and transports thermal energy mostly along the magnetic field lines. That, in turn, makes these magnetic flux tubes isolated from the surroundings.

Coronal loops are observed in the corona over a wide range of dimensions (from 1-10 Mm bright points to 100 Mm giant arches). The typical, active-region coronal loop length ranges from 10 to 100 Mm. In addition, the density varies from $\lesssim 10^8$ cm^{-3} (difficult to detect) to 10^{12} cm^{-3} in flaring coronal loops. Bright active region coronal loops have a density around 10^{10} cm^{-3} (Reale 2014).

Coronal loops are anchored to the underlying chromosphere and, further down, to the photospheric layer where the plasma beta parameter is high ($\beta \gg 1$). For this reason, the loops footpoints are dragged by photospheric plasma motion, which in turn might be highly structured. The typical strength of the magnetic field in the photosphere is found to be a few hundred G in active regions (Ishikawa et al. 2021). By ascending toward the corona, the pressure decreases, the magnetic field lines progressively expand, and the field intensity decreases, keeping the magnetic flux conserved. The greater expansion rate is expected just below the thin transition region dividing the chromosphere to the upperlying corona (Gabriel 1976b). There, the typical coronal magnetic field strength is about 10 G (Long et al. 2017). Nevertheless, in active regions the magnetic field can exceed 30 G (e.g., Van Doorsselaere et al. 2008; Jess et al. 2016; Brooks et al. 2021) .

Classification

The first X-ray observations of coronal loops suggested an early classification based on their morphology (bright points, active-region loops, and large-scale structures, Vaiana et al. 1973b). Observation of coronal loops in different EUV and X-ray spectral bands showed evidence of three classes of loops (Reale 2014), branched according to the temperature regimes, that might be governed by different physical processes:

- "Cool loops" are primarily observed in UV spectral lines, corresponding to temperatures between 0.1 and 1 MK;
- "Warm loops" are most effectively detected by EUV imagers, confining plasma at temperatures approximately between 1 and 1.5 MK; Their temperature is found to be distributed uniformly along the length while density appears to be higher than expected from hydrostatic equilibrium.
- "Hot loops" are typically identified in the X-ray spectrum and in high-temperature EUV lines, with temperatures reaching or exceeding 2 MK.

Global morphology

Inferring the shape of a corona loop is not a trivial task. Indeed, the reconstruction of their magnetic field skeleton can be done rigorously under a very restrictive set of conditions, such as strong local fields (White et al. 1991). Assuming a semicircular shape can be a useful approach to approximately estimating the length of the loop. By deprojecting the distance between the loop footpoints, the diameter of the arc can be straightforwardly determined. Deviations from circularity have negligible impact on the evolution of the confined plasma as it is channelled along the magnetic field regardless of the shape of the field lines.

Coronal loops cross-section is found to be fairly constant along their length on the corona (while it tapers across the TR, Gabriel 1976a). Indeed, loops typically exhibit only a slight increase in width at their midpoints compared to their footpoints, whereas a bipolar field configuration would predict a more significant expansion factor. This could be explained, e.g., by the presence of significant twisting (or braiding of a bundle of unresolved thin loops) of the magnetic field lines or by certain temperature distributions across the loop, making the loop cross section appear constant in EUV band (Peter & Bingert 2012). Moreover, Klimchuk et al. (1992) found evidence of modest width variations along coronal loops, suggesting an approximately circularly shaped cross section. In particular, TRACE (Aschwanden & Nightingale 2005) and Hi-C (Fuentes et al. 2006; Brooks et al. 2013; Morton & McLaughlin 2013) warm loops, as well as hot loops (Reale et al. 2011) observations suggest a preferred spatial scale near 1500 km.

In general, the presence of distinct loops, rather than homogeneous and fuzzy X-ray/EUV emission, indicates a type of collective behaviour that differs from what is

observed in the diffuse corona. It raises the question: Are all events initiated by a single source, or do they follow an avalanche-like process where one event triggers another, leading to a chain reaction? (Klimchuk 2015).

Fine structuring

Coronal loops are observed to be organised into clusters of numerous strands (Gomez et al. 1993), following a collective behaviour and hosting the elementary processes for loop ignition. The term 'strand' is closely associated with the fragmentation of magnetic flux in the photosphere, but reconnection in the corona can lead to much greater fragmentation of the field. Moreover, the temperature and density (and thus the brightness) of a magnetic strand, which is created through reconnection, are determined by the heating itself. Such strands can also efficiently mix as a consequence of turbulence, generated, e.g., in the presence of Kelvin-Helmholtz instabilities around oscillating coronal loops (Magyar & Van Doorsselaere 2016).

As coronal loops commonly exhibit strong magnetic fields of the order of 10 G or more (Yang et al. 2020; Long et al. 2017; Brooks et al. 2021), and the coronal plasma is nearly ideal, transport of matter across the field is strongly inhibited. In other words, the magnetic field confines the plasma within the flux tubes. For this reason, the plasma that fills each thin fibril may evolve independently from the surrounding environment because of the strong insulation provided by the magnetic field. The plasma is thus strongly funnelled along the field lines and is also thermally isolated from the surroundings (Rosner et al. 1978b; Vesecky et al. 1979). Moreover, since magnetic forces are much stronger than gravity in the corona, the latter will effectively act only along the field lines.

Direct and indirect evidence for loop fine structuring has been inferred over the years. For instance, the different loops fuzziness inferred at different coronal temperatures (Tripathi et al. 2009); optical limb observations of dense and cool, 500 km wide, "coronal rain" (Antolin et al. 2015b) down-falling along field lines (Antolin & van Der Voort 2012); high resolution observations with normal-incidence telescopes (Brooks et al. 2012) as well as the Hi-C sounding rocket (Brooks et al. 2013); the determination of line-of-sight emission measure distributions compatible with loops thermal structuring extending over a broad temperature range of temperatures (Del Zanna 2013), are all signatures of coronal loops fine structuring into many strands.

Coronal loops strands exhibit a range of sizes and magnetic-field strengths, although the exact distribution shapes are not well established. Several studies (Solanki 1993, for a review) indicate a clustering of values around a characteristic size of approximately 150 km or below (Beveridge et al. 2003; Cargill & Klimchuk 2004; Vekstein 2009) and a characteristic strength of about 1500 G ("kilogauss flux tubes") in the photosphere. This component accounts for only about 10% of the coronal magnetic field, since most of the turbulent field closes off in the photosphere or chromosphere. Elemental kG flux

tubes are confined by the dense photospheric plasma but expand rapidly with height, becoming volume-filling in the low-beta corona.

From the modelling side, the magnetic carpet scenario naturally conceives loops substructuring into small-scale flux tubes ("flux tube tectonics model", Priest et al. 2002). Earlier models of monolithic loops in hydrostatic equilibrium failed in reproducing the uniform filter ratio of TRACE warm loops (Lenz et al. 1999). Reale & Peres (1999) tackled the issue superimposing several, static, thin strands at different temperatures, still occurring in inconsistencies with observation, such as larger loop cross sections. As commonly invoked in the framework of coronal heating by nanoflares (Parker 1988), the convolution of hydrodynamic, independent, and impulsively heated coronal loop strands approached TRACE observations, reproducing both the spatial and temporal properties of the observed loops (e.g., Guarrasi et al. 2010).

1.5.2 Loop Scaling Laws

The Skylab mission (e.g., Vaiana et al. 1973a; Tousey et al. 1973), along with subsequent missions, observed that many X-ray-emitting coronal loops remain largely unchanged for duration, significantly exceeding their cooling times by radiation or thermal conduction. This suggests that, for the majority of their lifetimes, these loops can be globally characterised as systems in metastable equilibrium (Rosner et al. 1978b).

In 1D descriptions of monolithic coronal loops in thermal equilibrium, the temperature gradient dramatically increases in the transition region (the temperature suddenly increases from a few thousands to millions of Kelvin degrees), subsequently vanishing at the apex. Thermal equilibrium holds as soon as balance between coronal heating ($H > 0$), radiative losses ($R < 0$), and thermal conduction ($C < 0$) is preserved over the whole coronal loops length:

$$H + R = C. \tag{1.47}$$

In the chromosphere, both R and H are large, but their differences are small, resulting in a gentle change in temperature over space.

Optically thin radiative energy losses are very high in the transition region. Infact, their temperature-spectrum peaks between 10^4 and 10^6 K. Moreover, the relatively high density, as compared with the coronal plasma, makes radiative losses even more efficient. The energy lost in the TR is supplied by thermal conduction. The steep temperature dependence of the Spitzer thermal conduction (conductive flux: $F(z) \propto T^{\frac{5}{2}} \frac{dT}{dz}$) therefore determines the abrupt temperature inflation throughout the transition region.

Up in the corona, thermal conduction efficiently transports heat downward from the temperature maximum, with a small temperature gradient.

Rosner et al. (1978b) developed a model for coronal loops in hydrostatic equilibrium. They considered the steady-state energetics of a coronal loop structure as described by

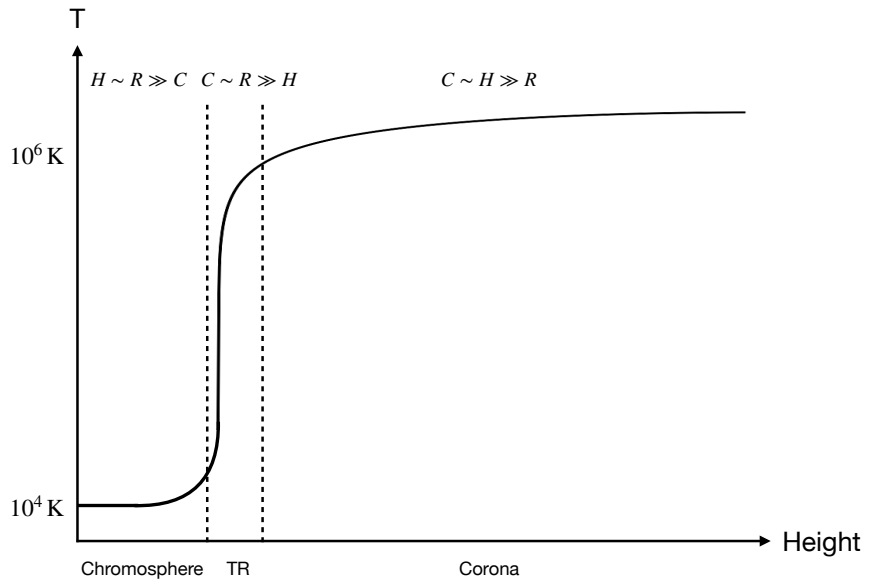

Figure 1.12: Schematic temperature variation with height of a monolithic loop throughout chromosphere, TR, and corona; as also reproduced by Priest (2014). The relative relevance of thermodynamic processes, including thermal conduction (C), radiative losses (R), and heating (Q), changes across the three different layers.

a local energy balance equation of the form:

$$H + R = C + \nabla \left[(E_k + E_h) \cdot v + \rho \cdot v \right] - F_g \cdot v, \tag{1.48}$$

where the second and last terms on the left hand side indicate the enthalpy flux and the work done by gravity, respectively. Assuming several practical simplifying assumptions, such as, symmetry about the apex, a constant cross section, a length much shorter than the pressure scale height, uniform heat distribution along the loop, and minimal thermal flux at the base of the transition region, they integrated the equation over the loop volume and obtained the energy balance relation for the loop as a whole and further derived the following scaling laws (in c.g.s. units):

$$T_6 = 1.4(pL_9)^{1/3}, \tag{1.49}$$

$$H_{-3} = 3p^{7/6}L_9^{-5/6}. \tag{1.50}$$

Although failing in describing, e.g., hot, unstable loops (Wragg & Priest 1981), scaling laws still remain a simple starting reference to interpret equilibrium coronal loop features.

1.5.3 Monolithic loops brightening and dynamics

A key result of 1D hydrodynamic models is the simple description of the plasma behaviour in a magnetic flux tube during an impulsive coronal heating event, starting from an initially cool, low-density, equilibrium state with no EUV or X-ray emission (Cargill & Klimchuk 2004; Klimchuk et al. 2006; Reale 2007). In particular, the evolution of an impulsively heated loop (or strand) can be divided into simple phases (Jakimiec et al. 1992; Reale 2007), listed below, and schematically shown in figure 1.13.

I. Heating

During this phase, the heat from the impulsive event is rapidly conducted along the magnetic field with thermal conduction timescales, raising the temperature of the entire strand to a peak level. Density and emission show instead minimal changes: the strand remains underdense compared to static equilibrium predictions. The plasma in this phase can be hotter than 4 MK (Cargill & Klimchuk 1997). Due to the low plasma density in the loop during this period, the emission is very weak, making the detection of such a hot plasma challenging. Reale et al. (2011) identified thin, high-temperature strands of around 10 MK in coronal active regions using SDO/AIA. Bradshaw & Klimchuk (2011) argued that nonequilibrium ionisation effects may suppress the emission lines from this hot plasma, potentially rendering them invisible.

II. Evaporation

As the impulsive event continues to heat, the temperature remains relatively stable, but the chromosphere becomes overheated and expands, leading to the evaporation of plasma with timescales comparable with the isothermal sound crossing time (τ_{II}, Eq. 1.51).

$$\tau_{II} = \frac{L}{\sqrt{2k_B T/m}}. \tag{1.51}$$

This evaporated plasma rises and fills the strand. During this phase, the emission increases rapidly, and the strand becomes denser, although it still remains underdense.

III. Conductive cooling

Once the impulsive event concludes, the plasma begins to cool down by conduction with the time scale τ_{III}, shown in Eq. 1.52 (Cargill & Klimchuk 2004).

$$\tau_{III} = \frac{3nk_B TL^2}{\frac{2}{7}kT^{\frac{7}{2}}} \tag{1.52}$$

Coronal emission initially peaks but then starts to decline, while the density continues to rise. Radiative cooling effects become more significant until radiative and conductive cooling are balanced. Observations indicate that hot loops (with temperatures greater than 2 MK) are typically underdense (Porter & Klimchuk 1995), which aligns with the model of loops composed of multiple impulsively heated strands in Phases I, II, and III.

IV. Radiative cooling

The loop eventually appears overdense as radiative cooling becomes dominant, causing the density to decrease gradually at first (with a typical timescale τ_{IV}, see Eq. 1.53) until the temperature drops enough to trigger catastrophic cooling.

$$\tau_{IV} = \frac{10^{19} k_B T^{\frac{1}{2}}}{n}. \tag{1.53}$$

Warm EUV loops (with temperatures around 1-2 MK) are observed to be overdense relative to equilibrium models and exhibit a narrow temperature range (Warren et al. 2008). These loops are believed to cool from a hotter state (Warren et al. 2002), and remain overdense (in Phase IV) for an extended period (Klimchuk 2006).

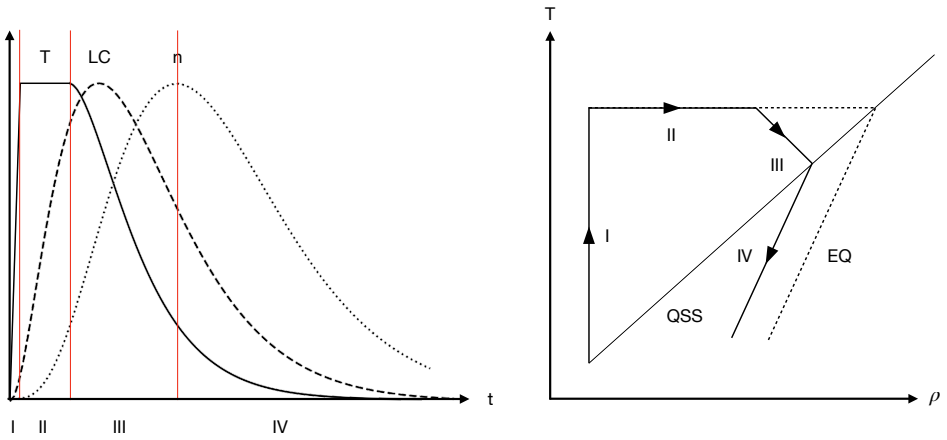

Figure 1.13: Left plot: schematic temperature (T, solid line), X-ray emission (i.e. the light curve, LC, dashed line) and density (n, dotted line) evolution of a loop strand ignited by impulsive heating, as also shown by Reale (2007). The strand evolution is divided into four phases (I, II, III, IV), also described in the diagram on the right-hand side in therms of temperature vs. density variations (Jakimiec et al. 1992), including the case of a long-heated loop (dashed line, Reale 2007).

1.5.4 Coronal loops heating

Observations and numerical experiments provide evidence that the evolution of coronal loops is deeply influenced by photospheric motion. The coronal magnetic field must be driven toward a stressed state, which must correspond to a non-potential configuration. For instance, footpoint rotation may lead the magnetic structure to twist and gain magnetic energy in excess. While magnetic energy is stored, the flux tube could potentially be subject to strong stresses that may eventually trigger fast magnetohydrodynamic instabilities, such as the kink instability (Hood et al. 2009) or the tearing mode instability (Del Zanna et al. 2016), or lead to long-lasting Ohmic heating (Klimchuk 2006).

Heating and brightening of coronal loops may be driven by 'storms' of impulsive events (Klimchuk 2009; Viall & Klimchuk 2011), multiple localised instances of the magnetic field relaxation. The irregular photospheric motions, as well as a wide range of magnetohydrodynamic instabilities, may lead the magnetic structure to develop fast reconnection and to produce heat. A very compelling body of evidence now supports magnetic reconnection as the key element to start the process of large-scale energy release (Hood et al. 2009).

The energy released by several localised reconnection events can be predicted by Taylor's dissipation theory (Taylor 1974), which was first applied to reverse-field pinch devices in plasma laboratories (Taylor 1986) and then extended to the coronal environment (Browning & Priest 1986). According to Taylor's theory, a turbulent, resistive plasma can rapidly reach a minimum-energy state. During the process, the topology of the magnetic field changes via reconnection, but magnetic helicity is conserved.

Magnetic field lines may become braided around each other, creating current sheets whose dissipation leads to nanoflare heating at numerous small locations. If the pattern of small-scale variations is not uniform along a large-scale field, then a force-free equilibrium field must contain current sheets. In simpler terms, a smooth equilibrium is possible only when field variations involve a straightforward twist from one footpoint to the other. However, more complex configurations, like braided tubes, inevitably result in the formation of current sheets, according to (Parker 1972). A broader interpretation of Parker's hypothesis is that when the normal component of the magnetic field is imposed on the boundary, along with the mapping of field lines from one boundary to another, the resulting force-free field generally contains current sheets. (Klimchuk et al. 2023) suggested that such fields, subjected to continuous driving at the boundaries, will initially develop current sheets of finite thickness: only when they reach a critical shear, they spontaneously collapse and reconnect, consistently with the heating requirements estimated for active regions. The subsequent evolution involves resistive relaxation, characterised by decaying turbulence and the formation of a complex array of current sheets dispersed throughout the domain. As the magnetic Reynolds number increases, the global reconnection rate across all diffusion regions continues to grow due to fragmentation, involving multiple or recursive reconnections. Ultimately, this process

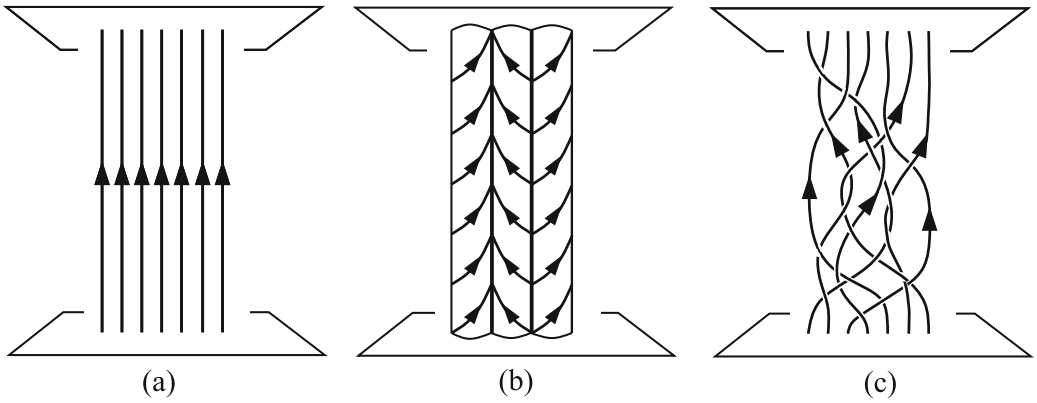

Figure 1.14: Schematic view of the magnetic field evolution, from a uniform, potential state (left picture), by photospheric motions, resulting in twisting (center) or more complicate braiding (right) of field lines. Credit Pontin & Priest (2022)

untangles the field lines, leaving behind two weakly twisted flux tubes with opposite twists.

1.5.5 The nanoflares scenario

In the corona, the magnetic field might become unstable under resistive modes as it is slowly forced by photospheric motions to explore a series of non-linear force-free states. In conditions of high magnetic stress, the field must reconnect and relax towards a linear force-free state, $\nabla \times \mathbf{B} = \alpha \mathbf{B}$, with uniform α (Woltjer 1958; Heyvaerts & Priest 1983). In particular, magnetic energy is found to be released in the corona throughout a widespread range of events that occur from large (flares, $\sim 10^{30}$ erg) down to medium (microflares, $\sim 10^{27}$ erg) scales (e.g., shown by Priest 2014). It has been suggested that the same mechanism, operating on even smaller scales, could be responsible for maintaining the one-million K diffuse corona, through so-called 'nanoflare' activity (Parker 1988). Parker originally conceived nanoflares as bursts of magnetic reconnection, coining the term based on observations of localised brightenings that were estimated to contain approximately 10^{24} erg. Today, the term 'nanoflare' is generally understood to refer to *an impulsive energy release on a small cross-field spatial scale without regard to the physical mechanism* (Klimchuk 2015).

In the original paper, Parker (1972) considered infinitesimal departures from a uniform field between parallel, perfectly conducting plates. He argued that, if the pattern of small-scale variations is not uniform along the large-scale field, then the field cannot be in magnetostatic equilibrium. In other words, equilibrium exists only if the field variations consist of a simple twist extending from one footpoint to another. Counter-arguments

have been presented demonstrating that tangential discontinuities cannot form as a result of smooth boundary motions. For example, Van Ballegooijen (1985) argued that a smooth equilibrium should always be attainable after an infinitesimal perturbation to a uniform magnetic field and demonstrated that discontinuities in the magnetic field, such as current sheets, can only arise if the velocity field at the photospheric boundary itself exhibits discontinuities in space. Similarly, Bineau (1972) proved that smooth force-free fields exist in the vicinity of the potential field. Despite computational studies of the Parker problem not conclusively show the formation of tangential discontinuities, they indicate that as boundary perturbations are progressively increased, the corresponding equilibrium in the domain develops current layers that become increasingly thinner and more intense (Rappazzo & Parker 2013). As noted in Pontin & Hornig (2015), in a force-free field, the parameter α remains constant along the magnetic field lines ($\mathbf{B} \cdot \nabla\alpha = 0$). Therefore, if the field line mapping between two line-tied boundaries contains small perpendicular length scales, so must α. Since $\alpha = \frac{\mathbf{j}\cdot\mathbf{B}}{B^2}$, it follows that $j_{\parallel} = \alpha B$, meaning that $j_{\parallel}$ must exhibit the same perpendicular length scales as α and the field line mapping.

Heating varies significantly over time when viewed from the perspective of individual magnetic field lines. A key aspect of nanoflares is how often they recur on a given strand. This repetition rate greatly impacts both the immediate and the time-averaged properties of the plasma. The crucial factor is the relationship between the heating frequency and the plasma's cooling time. Many coronal loops observations can be interpreted by a "storm" of low-frequency nanoflares. In this scenario, each strand within the loop bundle is heated only once during the loop's lifetime, but the heating occurs at different times for different strands (Schmelz & Winebarger 2015). This low-frequency heating may be responsible for the brightening of distinct coronal loops. Indeed, if the frequency of reconnection events rises sharply, highly energetic nanoflares and a significant increase in temperature occur. As these events extract a high amount of magnetic energy, footpoint driving requires more time to rebuild the stress, resulting in a longer "recharging" time. This allows the plasma to cool completely before the next nanoflare storm occurs. In particular, the shorter storm duration the more nearly isothermal are coronal loops, i.e. they exhibit a narrower temperature distribution compared to those produced by longer-duration storms.

The mechanism of magnetic energy release must remain inactive until significant magnetic stresses have built up. This principle applies not only to coronal heating but also to flares, coronal mass ejections, jets, spicules, and other similar phenomena. This scenario implies that there are critical conditions necessary for energy release. One possibility is that significant energy release does not occur until the magnetic fields are sufficiently misaligned, reaching a critical misalignment angle between adjacent strands. Another possibility involves a critical twist related to the kink instability (Mikic et al. 1990; Galsgaard & Nordlund 1997; Bareford et al. 2011). This could happen at the level of an individual strand or a whole loop. When a twisted loop experiences resistive

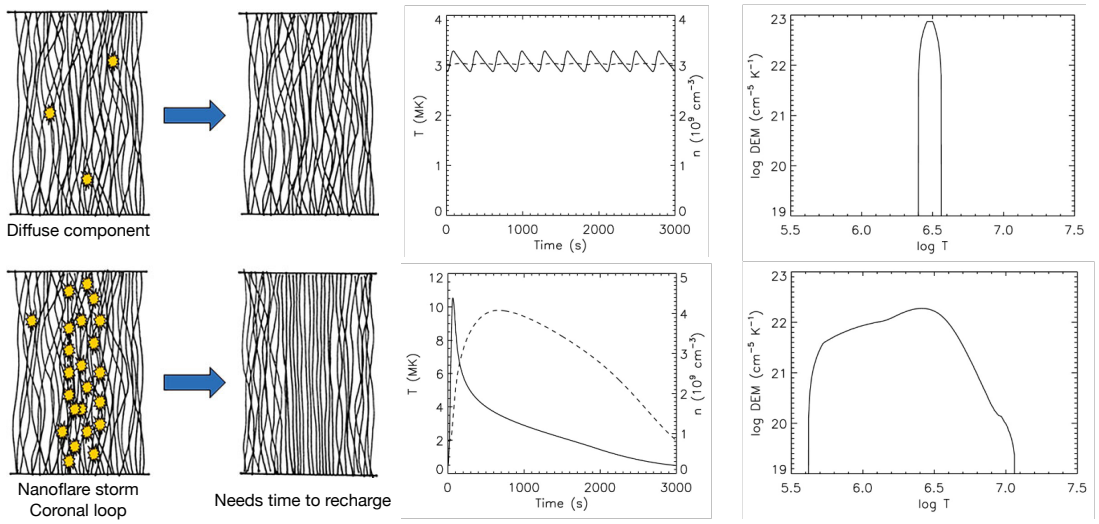

Figure 1.15: Two possible scenarios of solar plasma heated by nanoflares. First row: a diffuse corona heated by high frequency nanoflares (first and second columns). Small and rapid temperature variations (third column) generates a narrow differential emission measure (fourth column, DEM). Second row: a coronal loop heated by a serendipitous nanoflare storm. The strong temperature variation produces a broad DEM spectrum. Credit. Klimchuk (2015, 2017)

internal kinking, the initially smooth distribution of currents rapidly transforms into numerous current sheets scattered throughout the loop volume (Hood et al. 2009). This illustrates a situation where the individual events in a nanoflare storm are triggered by a single source rather than by an avalanche process. Additionally, kinking one loop or strand can potentially trigger the kinking of another nearby, as will be discussed later.

The spatial extent of nanoflares is too small to be clearly observed. Moreover, because of their nature, they must overlap, making them challenging to detect as individual events. Despite that, although undetectable when first proposed (Parker 1988; Antolin et al. 2021), observational evidence of such small events has been growing (Mondal 2021; Vadawale et al. 2021). Although small bursts attributed to nanoflares have been observed at various wavelengths within the upper transition region or lower corona (e.g., Testa et al. 2013, 2014; Tian et al. 2014), and high temperatures of 10 MK have been indirectly deduced from X-ray observations (e.g., Reale et al. 2011; Testa & Reale 2012; Ishikawa et al. 2017), there has been no definitive evidence of the widespread nanoflare activity as hypothesised by Parker. Evidence from EUV and X-ray observations suggests their existence (Reale 2014; Cargill et al. 2015). RHESSI (Lin et al. 2003) hard X-ray

observations observed many thousands of microflares (e.g. Christe et al. 2008; Hannah et al. 2008), with further information provided by instruments with higher sensitivity (e.g., Krucker et al. 2014; Glesener et al. 2017).

1.5.6 Why is coronal heating problem a problem?

Coronal plasma is extremely tenuous as compared to the underlying (chromospheric and photospheric) layers of the solar atmosphere. The low density causes the plasma to be an efficient heating conductor at high temperatures. This leads localised heating events to rapidly spread along the flux tubes, and the plasma to swiftly become almost isothermal inside each magnetic fibril. "Smoking guns" of possible impulsive heating events are therefore difficult to detect.

Direct heating in a tenuous plasma is anyway hard to detect because the coronal EUV emission scales as the square of the density. Density enhancements along loops field lines are driven by chromospheric evaporation, in response to coronal heating. They therefore occur only after thermal energy has been locally deposited and conducted toward loops footpoints. The further longer (sound) time scales involved in the plasma ablation from the chromosphere make the swift reconnection features vanish in post-nanoflare phase.

For the same reason, also the conditions prior to the energy release are poorly observationally constrained, as hidden in a tenuous and faint coronal plasma. For instance, clear evidence of field line braiding is not commonly observed in filamentary coronal loops. Indeed, as ordinarily observed in the 171 $\mathring{A}$ iron line, coronal loops strands show up to be smoothly wandering along a common, overall magnetic field structure, with no obvious indication of twisting, tangling, or more complicate interweaving. This does not cast out the hypothesis of heating by magnetic braiding, as what we observe can be interpreted as the result of the unbraiding process of reconnection, rendered visible in the late stages of the strands evolution. On the top of that, braiding is also believed to occur at relatively small spatial scales that are not yet possible or difficult to resolve by state-of-the-art instruments.

Even if visible, coronal plasma anyway shows up ambiguously, as its optically thin nature makes integrated emission along the line of sight difficult to decompose into elemental sources, presumably heated independently. For instance, a fundamental challenge in the statistical analysis of coronal loops is the difficulty in establishing an objective criterion for loop identification. Loops are seldom isolated; they typically coexist with other loops that may intersect or overlap along the line of sight.

On the modelling side, plasma heating by magnetic reconnection in coronal loop strands, namely the fundamental magnetic process for energy release, has reveled itself as an intrinsically three-dimensional process, making self-consistent coronal loop modelling a computationally demanding task, only recently rendered achieved by state of the art parallel calculus on High Performace Computing (HPC) facilities. In the big picture of ab initio modelling of the solar atmosphere, recent numerical experiments

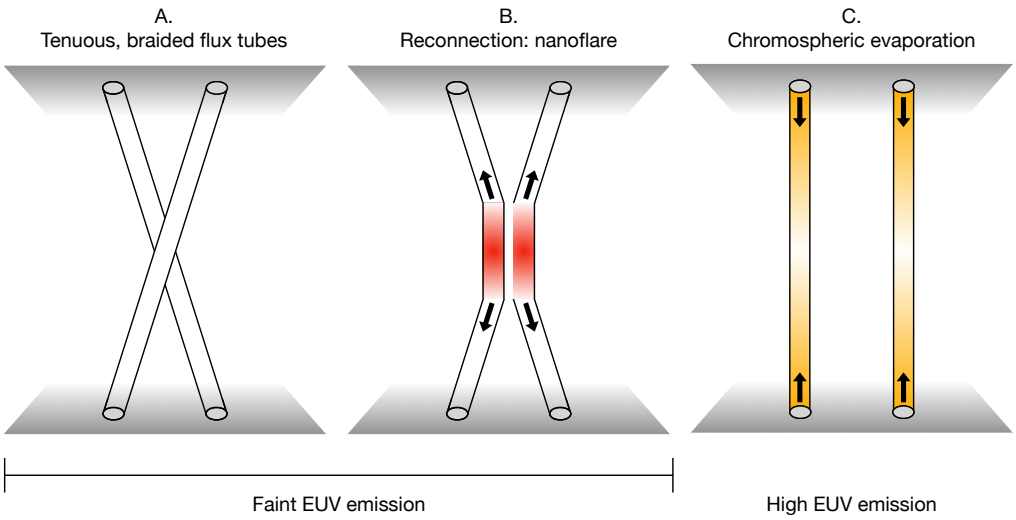

Figure 1.16: Two magnetic flux tubes reconnecting at the mid point. Initially (left picture) the tubes are filled by tenuous plasma, therefore are faint in the EUV. During the reconnection (mid panel) the heat is efficiently conducted towards the footpoints. Only in the post-reconnection phase (right picture), the (untilted) flux tubes becomes EUV bright, as consequence of the chromospheric evaporation.

have highlighted the importance of the interplay between the corona and the underlying layers, for instance, in terms of chromospheric and transition region response to coronal heating; Poynting flux generation by photospheric (down to convection zone) motions; and the reconnection rate feedback on the Poynting flux itself, which makes the overall estimate of the magnetic energy budget a nontrivial, highly nonlinear problem.

1.5.7 Nanojets

The high spatial and temporal resolution observations of the solar atmosphere with IRIS (De Pontieu et al. 2014) and SDO/AIA (Pesnell et al. 2012; Lemen et al. 2012) enabled the discovery of fast and bursty ‘nanojets’ (Antolin et al. 2021), which have been interpreted as a direct evidence of coronal heating by magnetic reconnection in braided magnetic structures, and in particular as outflow jets accelerated by the slingshot effect of magnetic field lines during small-angle reconnection. Such episodic phenomena provide novel and important diagnostics of nanoflare activity, overcoming the general difficulties in directly observing nanoflares.

High resolution observations of active regions (Antolin et al. 2021, Sukarmadji et al. 2022, Patel & Pant 2022, Sukarmadji & Antolin 2024) have revealed a variety of

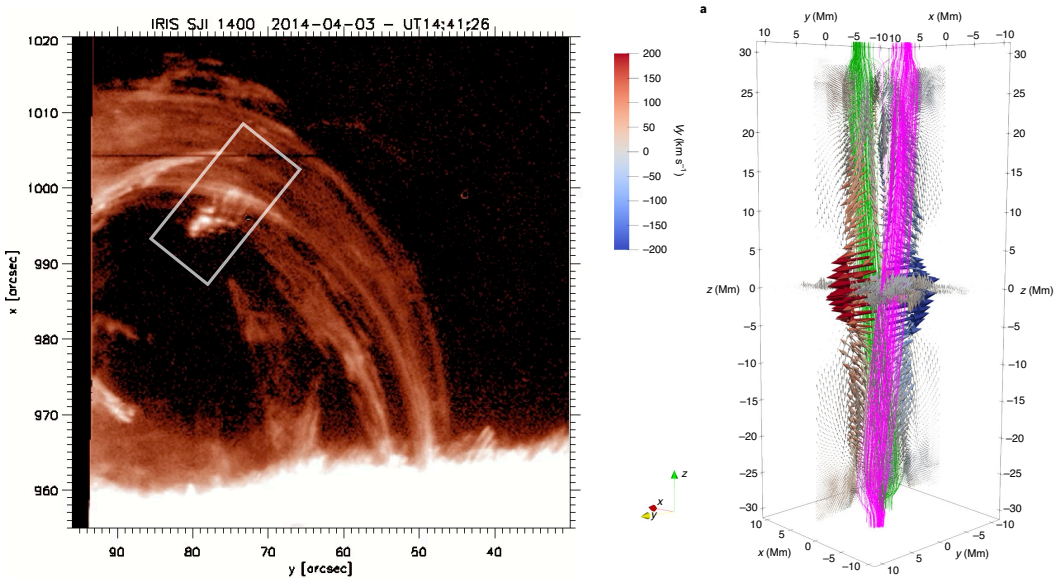

Figure 1.17: Left picture: FOV of IRIS/SJI 1400 Å channel observed on the on 3rd April 2014. A loop-like structure connects the bright prominence on the left to the solar surface. The snapshot captures a small ($\lesssim$ 10 acrsec) jet accelerated inwardly respect to loop curvature. Right picture: Credit: 3D MHD simulation of two reconnecting magnetic strands. After reconnection a bidirectional outflow jet (arrows) is accelerated by the released magnetic field tension. Credit: Antolin et al. (2021).

small (500 – 1500 km), and transient (< 30 s) nanoflare-like EUV bursts followed by collimated nanojets, 100 to 300 km s^{-1} fast, presumably driven by dynamic instabilities such as MHD avalanches (Antolin et al. 2021), Kelvin Helmholtz, and Rayleigh–Taylor instabilities (Sukarmadji et al. 2022) or during catastrophic cooling of coronal loops strands (Sukarmadji & Antolin 2024), often accompanied by the formation of coronal rain (Antolin et al. 2015b). Observation of nanojets at different temperatures supports the hypothesis of multithermal structuring (e.g., Sukarmadji et al. 2022; Patel & Pant 2022). Although bidirectional jets are expected from reconnection, observed nanojets are often strongly asymmetric (e.g., Patel & Pant 2022), possibly due to loop curvature (Pagano et al. 2021) or braiding.

In particular, Antolin et al. (2021) reports on the observation of a multitude of nanojets in a loop structure monitored at the limb of the Sun on April 2014. Such observations were carried out with the Atmospheric Imaging Assembly (AIA, Lemen et al. 2012) on board of the Solar Dynamics Observatory (SDO, Pesnell et al. 2012), the Interface Region Imaging Spectrograph (IRIS, De Pontieu et al. 2014) and the Hinode/Solar Optical Telescope (SOT, Suematsu et al. 2008; Tsuneta et al. 2008). The detected sequence of events ultimately resulted in the creation of a highly heated coronal

loop. The way in which these heating events evolved in space and time, along with the dynamics of the interwoven loop structure, exhibited features that align with the characteristics typically associated with an MHD avalanche. Specifically, the observed nanojets exhibit specific characteristics, including confinement with dimensions typically around 500 km in width and lengths ranging from 1000 to 2000 km. They are short-lived, lasting approximately 15 s or less, and are characterised by rapid plasma flows of 100 to 200 km s^{-1} that move perpendicular to the magnetic field guiding the coronal loop.

Sukarmadji et al. (2022) present IRIS and SDO observations of nanojets found in a blowout jet with ongoing Kelvin–Helmholtz instability, identified as the reconnection driver, and in two coronal loops with coronal rain, whose dynamics is likely driven by Rayleigh–Taylor or Kelvin–Helmholtz instabilities. The nanojets, observed to be accelerated transversely to field line of origin, arise from nanoflare-like intensity UV/EUV bursts and reach velocities between 150 and 250 kms^{-1}. In a subsequent study, Sukarmadji & Antolin (2024) identify, from IRIS and SDO observations of clustered nanojets, transverse coronal loop MHD waves powered by braiding-induced reconnection. In particular, the estimated nanojets kinetic and thermal energy was high enough to induce transverse waves and power the observed coronal loop heating. Observations results supports the small-angle reconnection scenario in braided coronal structures, predicting that reconnected magnetic field lines, driven sideways by the released magnetic tension, can generate small-amplitude transverse MHD waves.

Patel & Pant (2022) report on the observations of 10 nanojets from the High-resolution Coronal Imager 2.1 (Hi-C 2.1 Rachmeler et al. 2019) and AIA. They found both outward and inward directed jets on curved active-region loop filaments, with the former ones having higher averaged speed and longer length and duration than the latter ones. They also argue about the multithermal nature of nanojets, as they can be simultaneously identified in multiple temperature (TR and coronal) passbands.

The properties of such reconnecting plasma outflows were investigated via MHD numerical simulations (e.g., Antolin et al. 2021; Pagano et al. 2021; De Pontieu et al. 2022). Antolin et al. (2021) show a nonideal MHD simulation of two interacting, gravitationally stratified coronal loops, the footpoints of which are slowly moved in opposite directions to create an increasing angle between the loops. As the x-type misalignment increases, the electric current between the loops increases as well, thus leading to reconnection of magnetic field lines at the midplane. The enhanced magnetic tension in the reconnection region drives a transverse displacement of the plasma. A high-velocity (up to 200 km s^{-1}), collimated (widths of the order of a few Mm), bidirectional nanojet also results from the reconnection process.

1.6 HD coronal loop modelling

The field line perspective is crucial because the plasma's response to heating is primarily influenced by processes that align with the magnetic field. Due to the frozen-in flux condition, low plasma beta, and the efficiency of thermal conduction in moving energy along the field rather than across it, flux strands behave like nearly rigid, thermally insulated flow pipes. In particular, the minimal energy transport across field lines allows for the use of 1D hydrodynamic models (e.g., Peres et al. 1982; MacNeice 1986), which can include essential physical processes like thermal conduction, radiation, radiative transfer, and non-equilibrium of ionisation effects. These models can effectively simulate the plasma response within a single strand or a monolithic loop, i.e., a loop composed by a single "fat" strand. Although the evolution of the magnetic field can be important, a one-dimensional hydrodynamic model describes the distribution and evolution of the plasma along the field lines under the effect of an empirical heating function (Klimchuk 2015). One can combine several single-strand simulations to obtain the description of a multi-stranded coronal loop (Klimchuk 2006; Reale 2014).

Monolithic or single-strand coronal loops can be described by the numerical integration of the time-dependent, coupled equations of mass, momentum, and energy conservation in a one-dimensional grid (Peres et al. 1982). In order to adequately describe the brightening of the loop after the heating event, a chromospheric mass reservoir must be included. It can be treated as simply as possible, neglecting heating and cooling below a certain threshold temperature (e.g., 10^4 K), or with detailed radiative transfer (Carlsson & Stein 1992, 1994, 1997, 2002), or energy models (Peres et al. 1982; Reale et al. 2000a). Realistic mechanisms, e.g., for the heating input (that can be either steady, slowly changing, or impulsive, uniform or localised e.g., at footpoints or at the loop apex, Priest et al. 1998), momentum deposition, the time-dependent ionisation, and thermal conduction saturation (Orlando et al. 2008) can be also included at the expense of the numerical simulation complexity.

The steep transition from the cold ($\sim 10^4$ K) chromosphere to the $\gtrsim 10^6$ K hot corona must be carefully addressed, as an appropriate numerical description of the steep transition region (only a few tens of kilometres thick, or even narrower during flares) requires very large (eventually adaptively refining, Betta et al. e.g., 1997) spatial and temporal resolutions. In fact, very large temperature gradients are needed to balance the Spitzer thermal conduction (Spitzer Jr & Härm 1953) and the radiative losses, peaking between 10^5 and 10^6 MK (Serio et al. 1981). Insufficient resolution of the transition region leads to an inaccurate reproduction of the mass transfer after heating (Linker et al. 2001; Lionello et al. 2009; Mikić et al. 2013; Bradshaw & Cargill 2013; Johnston et al. 2020). Relatively small errors in density evolution can turn out to produce large errors in the emission response, as it scales with the density square.

One significant outcome of 1D hydrodynamic models is their ability to clearly illus-

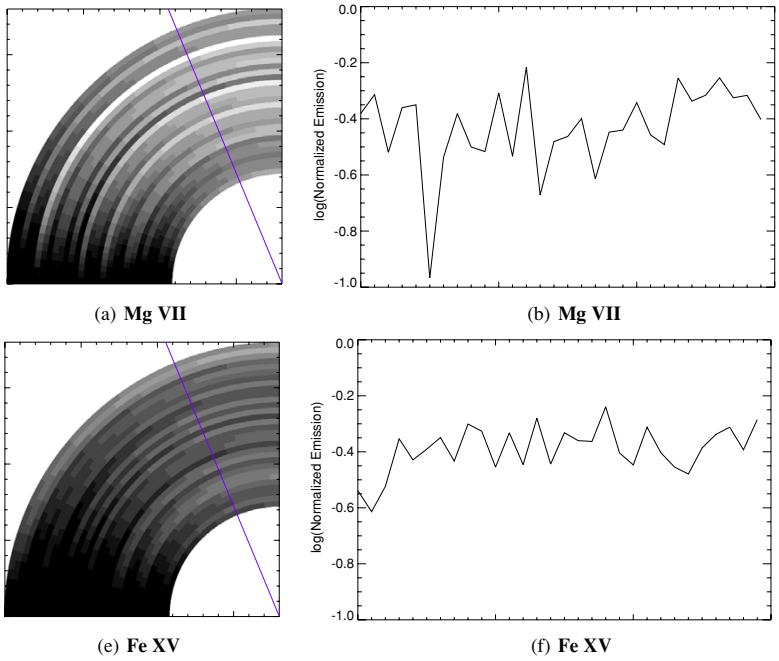

Figure 1.18: Left column: Mg VII cold ($T < 1$ MK) and Fe XV warm ($T \sim 2.5$ MK) loop bundles emission from (Guarrasi et al. 2010) simulation. Right column: emission profiles along marked lines for the same transitions. Flux strands show up in the cooler line, while, in the hot channel, the loop's emission spreads out more uniformly.

trate the behaviour of plasma within a strand during an impulsive coronal heating event (Cargill & Klimchuk 2004; Klimchuk et al. 2006; Reale 2007). Although monolithic (single-strand) coronal loop models fail to reproduce many coronal loop observations (Lenz et al. 1999), but successfully model flares (Cheng et al. 1983; Fisher et al. 1985; Betta et al. 2001; Reale 2007), results from many single, evolving flux tubes can be combined to reproduce the evolution of a multistranded coronal loop. This approach has been used to model both static loops (Reale & Peres 1999) and those impulsively heated by nanoflares (Warren et al. 2002), and it has also been applied to represent entire active regions (Warren & Winebarger 2006). The multistrand approach usefully contributed in (indirectly) testing the hypothesis of coronal heating by nanoflares against observations. For instance, bundles of active region loops appear increasingly diffuse in harder and harder energy bands sensitive up to about 3 MK (Brickhouse & Schmelz 2005; Tripathi et al. 2009). Guarrasi et al. (2010) simulated a 3 MK active region loop made by bundles of thin strands, each heated by a short and evenly intense pulse at a random time up to 10 MK. The model obtains precisely that in lines emitted by 2–3 MK plasma, the emission is more uniform across the loop bundle, while in cooler lines, the loops strands are more

distinct and the region appears less diffuse, as shown in Fig. 1.18. A complementary, effective method to describe loops as ensembles of numerous independent strands with a statistical distribution of heating events is the "0-D" approach, which tracks the temporal evolution of averaged loop properties like temperature, pressure, and density (Klimchuk et al. 2008; Cargill et al. 2012).

1.7 MHD coronal loop modelling

Multi-D MHD models no longer prescribe an ad hoc heating impulse but they treat the heating mechanism self-consistently by including the nonlinear interaction between the plasma and the magnetic field.

The time-dependent, ideal MHD equations are:

$$\frac{\partial \rho}{\partial t} + \nabla \cdot (\rho \mathbf{v}) = 0, \tag{1.54}$$

$$\frac{\partial \rho \mathbf{v}}{\partial t} + \nabla \cdot (\rho \mathbf{v}\mathbf{v} - \mathbf{B}\mathbf{B} + \mathbf{I}p_t) = \rho \mathbf{g}, \tag{1.55}$$

$$\frac{\partial \rho E}{\partial t} + \nabla \cdot [\mathbf{v}(\rho E + P_t) + \mathbf{B}(\mathbf{v} \cdot \mathbf{B})] = \rho \mathbf{u} \cdot \mathbf{g}, \tag{1.56}$$

$$\frac{\partial \mathbf{B}}{\partial t} + \nabla \cdot (\mathbf{v}\mathbf{B} - \mathbf{B}\mathbf{v}) = 0, \tag{1.57}$$

where

$$p_t = p + \frac{B^2}{2}, \qquad E = \epsilon + \frac{u^2}{2} + \frac{B^2}{2\rho} \tag{1.58}$$

are the total pressure and energy density, respectively, and, t is the time, n_H is Hydrogen numerical density, $\mu = 1.28$ is the mean atomic mass, m_H is the Hydrogen mass, $\rho = \mu m_H n_H$ is the mass density, u is the gas velocity, Φ_g is the gravitational potential, $\mathbf{g}$ is the gravity acceleration vector, T is the temperature, $\mathbf{v}$ and $\mathbf{B}$ are the velocity and magnetic fields, p is the gas pressure, ϵ is the internal energy of the gas.

2D Simulations

A limitation of current 1D loop models is their inability to effectively account for the expected magnetically-dependent transition region throat, due to the steep change of pressure from the corona to the chromosphere. In particular, loop's cross-sectional area is expected to adapt in real time depending on the relative equilibrium between magnetic pressure and time-dependent plasma pressure. Using a time-dependent 2D MHD flaring loop model, Guarrasi et al. (2014) examined the area response to gradual changes in coronal heating rates, challenging current steady-heating models. They found that the area could vary significantly with the quasi-steady heating rate, such as a 40%

change at 0.5 MK when loop temperatures range from 1 MK to 4 MK, thus affecting the interpretation of differential emission measure (DEM) curves.

Another obvious limitation of 1D hydrodynamic simulations is their inability to describe self-consistently heating by magnetic field dissipation. For instance, magnetic reconnection needs at least 2D MHD simulations to be addressed numerically. In particular, 2D simulations allow the study of the onset and evolution of magnetic reconnection in infinite current layers with high spatial resolution. For example, Landi et al. (2015) used 2D numerical simulations in compressible resistive MHD to study the tearing instability in thin current sheets. They found that the tearing mode can induce plasmoid formation and reconnection on Alfvénic timescales, which is essential for explaining explosive flaring activity.

Ab-initio simulations with detailed chromosphere/TR physics

In their pioneering work, Gudiksen & Nordlund (2005a,b) first ran 3D MHD models including an energy equation that incorporates field-aligned thermal conduction and radiative losses. They began with a stratified atmosphere and a magnetic field derived from a potential extrapolation of an MDI magnetogram (left image in Fig. 1.19). At the photospheric boundary, they applied a simulated random granular pattern driving the coronal magnetic field into an approximately nonlinear force-free (but close to potential) field configuration. The resulting, Ohmic in nature, coronal heating arises from sporadic, short-duration reconnection events due to numerical diffusion. Coronal loops becomes EUV bright (right images in Fig. 1.19). The transition region is highly variable, both spatially and temporally, while the density and temperature of the coronal plasma fluctuate continuously over space and time. Since then, progresses have been made, by addressing magnetically driven scenarios with multidimensional and multiphysics numerical applications. For example, transition region downflows (Hansteen et al. 2010), as well as type I (Martínez-Sykora et al. 2009) and type II (Martínez-Sykora et al. 2011) spicules, were reproduced by MHD simulations by including the effects of optically thick radiation in the chromosphere using non-LTE radiative transfer (Carlsson et al. 2010; Carlsson & Leenaarts 2012). In these simulations, chromospheric heating is mainly caused by Ohmic dissipation at the edges of magnetic flux concentrations, whereas, in the corona, episodic heating events are identified as the aftermath of magnetic field stressing and flux emergence, although spicules might play a role too (De Pontieu et al. 2017a). The key role of ambipolar diffusion from ion-neutral interactions in the generation of spicules was emphasised by (e.g., Martínez-Sykora et al. 2017; De Pontieu et al. 2017b).

Flux emergence (Heyvaerts et al. 1977) is also self-consistently described by ab initio models with detailed chromosphere and transition region physics. For instance, Archontis & Hansteen (2014) report on the formation of small energy bursts in the micro/nanoflare range produced by the gradual emergence of the magnetic field. Spon-

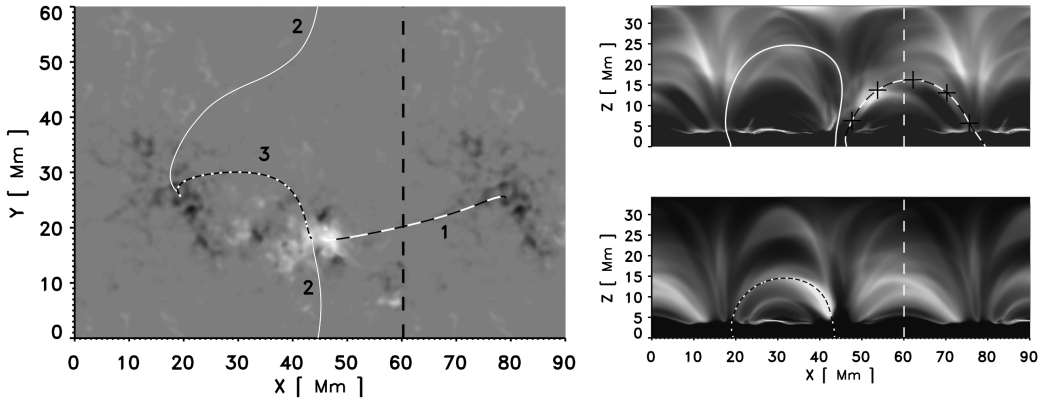

Figure 1.19: Ab-initio, MHD simulations of a large-scale coronal box. The panel on the left shows a simulated magnetogram, while the top (bottom) panel on the right is a synthetic image from TRACE 171 $\mathring{A}$ (195 $\mathring{A}$), showing three bright loops. Credit: Gudiksen & Nordlund (2005a)

taneous formation of small current layers at the interfaces of the resulting network of dynamically interacting loops produces patchy magnetic reconnection and coronal heating, coherently with flux-cancellation-driven nanoflares models, for both solar chromospheric and coronal heating (Priest et al. 2018).

Wave heating

Potential deviations from the purely 1D evolution could be caused by intense oscillations or kinks (Ofman 2009). In such cases, the influence of the three-dimensional loop structure should be considered to accurately describe the interaction with excited MHD waves (McLaughlin & Ofman 2008; Pascoe et al. 2009; Selwa & Ofman 2009; Arregui 2015; Van Doorsselaere et al. 2020).

The generation, propagation, and damping of waves in the solar atmosphere are investigated through various methods (Arregui 2015). Linear wave analysis in simple magnetic configurations provides insights into wave trapping and propagation mechanisms, while nonlinear wave analysis in structured plasmas examines wave transformation, wave-flow interactions, and phenomena such as shock waves and Alfvén wave turbulence. Large-scale numerical models, incorporating boundary conditions and drivers, are employed for global solar seismology and for making observational predictions.

Resonant damping of oscillations (Van Doorsselaere et al. 2004) is a well-established mechanism for transferring energy from large-scale transverse motions to localised small-scale motions, arising from the inhomogeneity of the medium in the direction perpendicular to the magnetic field (Goossens et al. 2006). This mechanism supports multistrands structures (Terradas et al. 2008; Pascoe et al. 2011) and can be modelled

with standing waves (Goossens et al. 2002) and propagating waves (Pascoe et al. 2012), also using simple flux tube models (Ruderman & Erdélyi 2009; Goossens et al. 2011).

Pagano & De Moortel (2017) investigated the conversion of energy into thermal energy through phase mixing of Alfvén waves in a cylindrical coronal flux tube, assessing its implications for coronal heating and thermal structuring. In a subsequent study, Pagano et al. (2018) expanded this analysis by including higher harmonics, in addition to the fundamental harmonic, observed in standing oscillations of coronal loops. However, these higher harmonics were found to hinder the formation of small-scale structures. More realistic numerical simulations, including oscillations based on the observed coronal power spectrum (Pagano & De Moortel 2019), demonstrated a significant role in the development of small-scale structures, while Pagano et al. (2020) evaluated the impact of varying initial density distributions, which were found to significantly affect the evolution of the boundary shell. Across all cases, the authors concluded that phase mixing is unlikely to contribute significantly to the global heating of the solar corona.

Alfvén wave turbulence is another extensively studied mechanism. Supported by an increasing collection of observations (De Moortel et al. 2014), in this process, photospheric foot-points motions are transported along magnetic loops and amplified as they reflect at the transition region boundary. The resulting counterpropagating perturbations interact in complex ways, leading to the formation of small-scale structures and the subsequent dissipation of energy (Van Ballegooijen et al. 2011, 2014; Asgari-Targhi et al. 2013). Originally proposed by Coleman Jr (1968) and later first modelled by Belcher & Davis Jr (1971); Alazraki & Couturier (1971), the concept of Alfvén wave turbulence has been further developed in modern studies. Using three-dimensional models of the solar corona and inner heliosphere, Sokolov et al. (2013) demonstrated that Alfvén waves turbulence can reproduce the overall observable EUV emission, with some exceptions, such as emission near active regions. The Alfvén Wave Solar Model (AWSoM) introduced by van der Holst et al. (2014) addresses both coronal heating and solar wind acceleration through low-frequency Alfvén wave turbulence, eliminating the need for ad hoc heating functions. This approach simulates the three-dimensional magnetic field topology using data from photospheric magnetic field measurements. The injection of Alfvén wave energy at the inner boundary is determined by the Poynting flux, which is taken to be proportional to the strength of the magnetic field.

Finally, transverse MHD oscillations can induce the formation of Kelvin-Helmholtz instabilities that deform loop cross sections and produce small-scale currents (Browning & Priest 1984; **?**). The heating rate produced by these current sheets has been established to be highly dependent on the formation of small spatial scales, which are influenced by numerical resolution, as well as by the values of resistivity and viscosity (Howson et al. 2017). Shestov et al. (2017), using forward modelling of three-dimensional MHD simulations, demonstrated that small-amplitude transverse MHD waves can rapidly induce strand-like structures in long, thin loops within EUV intensity images, often within just

a few wave periods.

Heating in twisted flux tubes

Photospheric motions are easily expected to drive foot-point rotation which in turn may twist the magnetic flux tube to gain magnetic energy (Rosner et al. 1978a). While magnetic energy is stored, the flux tube could be subjected to potentially strong stresses that may lead to impulsive magnetohydrodynamic instabilities (such as the kink instability, Hood et al. 2009) or to widespread Ohmic heating. According to the numerical experiment described in Reale et al. (2016), the gained energy is likely to be widespread released by magnetic dissipation as soon as a current density threshold is exceeded as the twisting progresses. The subsequent evolution resembles usual large scale loop evolution, including significant mass transfer from the chromosphere to the corona, and plausible observables. Random components of the footpoint motion might explain the internal filamentary loop structure.

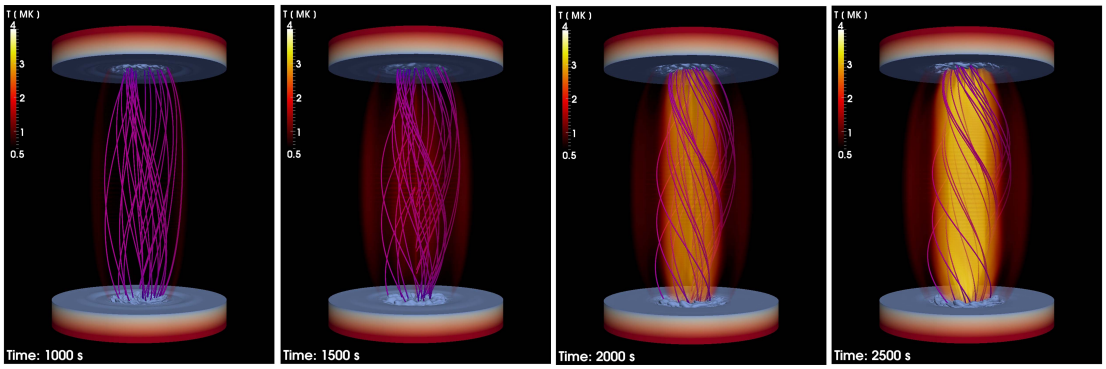

Figure 1.20: Rendering of the temperature evolution in a twisted coronal loop simulation. 3D MHD simulation of a twisted magnetic flux tube. The chromosphere is represented by two solid cylindrical layers at the top and bottom. Twisted magnetic field lines are shown by fuchsia curves. Credit: Reale et al. (2016)

1.7.1 Nanoflares MHD modelling

Models demonstrate that even simple magnetic fields can produce multiple current sheets through random driving motions (e.g., Rappazzo et al. 2007, 2008). The footpoints of an initially straight and uniform magnetic field are slowly shuffled, and the total Ohmic and viscous dissipation over the time is then measured. This experiment is repeated by varying only the resistivity and viscosity, and shows that both the intensity and nature of the heating are highly dependent on the Reynolds number. Specifically,

the time-averaged heating rate increases with higher Reynolds numbers, as reduced dissipation allows stresses to build up to higher levels. Additionally, the heating becomes much more intermittent and resembles nanoflares. Rappazzo et al. (2010, 2013) used reduced MHD to further consider the heating rate for various rotational and shear driving motions. In a following work, Rappazzo et al. (2017) examined the magnetic topology and field line random walk characteristics of a magnetically confined, nanoflare heated corona within the reduced MHD framework. Field lines emerging from current sheets form coherent structures named "current sheet connected regions" (shown in Fig. 1.21). Field line random walk in these regions is highly anisotropic, diffusing mainly along the in-plane length of the current sheets, and the mean square displacements increase due to the stronger magnetic fields. Rappazzo et al. (2018) evaluated heating by random driving motions for different ratios of the photospheric forcing velocity timescale to the Alfvén loop crossing travel time, showing that both the heating rate and the maximum temperature are approximately independent of the two timescales relative amount. The significance of the driving (with associated helicity and topological entropy) was addressed by Ritchie et al. (2016). They showed that heating is crucially dependent on the nature of the photospheric driver with coherent motions typically leading to fewer large energy-release events, whereas more complex motions resulting in more frequent but less energetic heating events.

The multithermal nature of coronal plasma confined in coronal loops has been addressed by Dahlburg et al. (2016). They investigated the evolution of a coronal loop using numerical simulations of fully compressible three-dimensional MHD equations. Random motions at the loop's footpoints energise the magnetic field, leading to turbulent nonlinear dynamics and the continuous formation and dissipation of field-aligned current sheets, and to small-scale heating. The dissipation is unevenly distributed, resulting in the heating of only a fraction of the coronal mass and volume at any time. Temperature and density are highly structured at subobservational scales, making the loop plasma multithermal, with dynamic hot and cool strands scattered throughout. Consequently, coronal heating is found to be highly intermittent, with most of the loop cooling at any given time.

Ab initio simulations with detailed description of the transition region, chromosphere, photosphere, down to convective region physics have been used to investigate how energy generated by photospheric magneto-convection is transported into the upper atmosphere to heat a coronal magnetic loop and form its internal structure. Breu et al. (2022) simulated an isolated coronal loop as a straightened magnetic flux tube rooted in the convection zone, with the MURaM 3D MHD code (Vögler et al. 2005; Rempel 2016). The model incorporates field-aligned heat conduction, grey radiative transfer, and optically thin radiative losses. The loop footpoints interact with surrounding granulation, and heating occurs through Poynting flux generated by small-scale motions within magnetic concentrations in the photosphere. Turbulence arises in the upper atmosphere

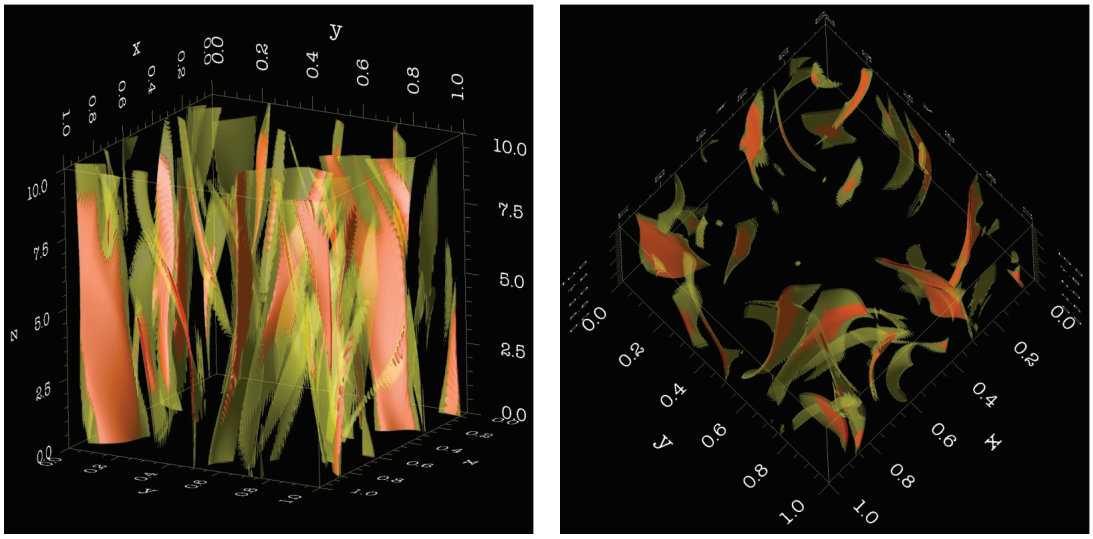

Figure 1.21: Side (left panel) and top (right panel) view of current density isosurfaces from a long-duration, high-resolution (Reduced-) MHD simulation of turbulent plasma in coronal loop. Strong current sheets (red isosurfaces) are always nested inside weaker current layers (yellow). They spread throughout the entire domain with small filling factor. Credit: Rappazzo et al. (2007)

as a result of these footpoint motions, with little evidence of heating from large-scale magnetic braiding. Synthesised emission, as would be observed by instruments like the AIA or the XRT, shows transient bright strands forming in response to heating events. The model effectively replicates the observed properties and evolution of plasma within coronal-loop substructures, providing a coherent picture of energy flux transfer.

Instead of creating multiple forced reconnection events through a complex driving pattern on a initially simple magnetic field, a complex magnetic field undergoing instability can also generate numerous small-scale reconnection events. For example, Pontin et al. (2011) studied the resistive relaxation of a coronal loop with a complex braided magnetic field, where an instability leads to spontaneous reconnection and the formation of many tiny nanoflares. Initially, the magnetic field has large-scale diffuse currents (left panel of Fig. 1.22), but as it evolves, intense current layers naturally form (middle panel, Fig. 1.22) until a resistive instability triggers reconnection, initiating a cascade of energy release to smaller scales. They also observed that the magnetic field does not necessarily follow the quickest or simplest path to untangling itself, but reconnects whenever conditions are suitable for reconnection. This leads to a partial reduction in magnetic stresses but not a complete untangling, requiring a continuous series of reconnection events to fully resolve the field (Parnell et al. 2008). This process, known as ‘multiple’ or

'recursive reconnection', allows the entire loop to be heated, rather than just a few strands within it, potentially releasing significant energy over an extended period. According to Pontin et al. (2016), for every field anchored to perfectly-conducting boundaries, a force free equilibrium state exists and contain current sheets whose thickness is inversely proportional to the topological entropy of the structure, i.e., the complexity of the braid.

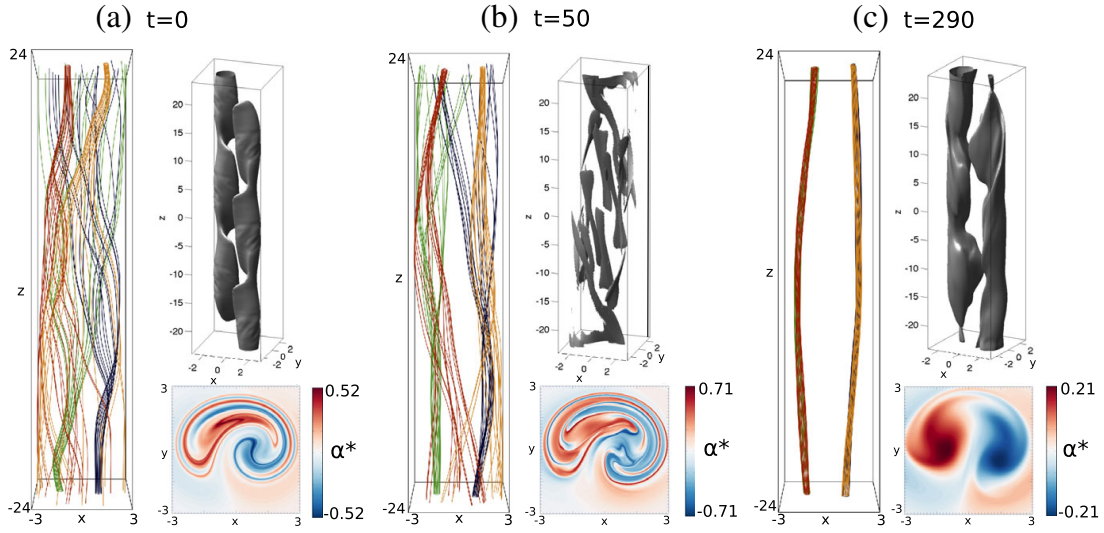

Figure 1.22: Resistive relaxation of a magnetic braid. In the left panel, magnetic field lines are traced from four rings of points at the top (red and orange) and lower (green and black) boundaries of the box. The process of unbraiding is qualitatively appreciable from the field lines evolution (t = 0, 50, and 290 s), but also from the distribution of the $\alpha = \mathbf{j} \cdot \mathbf{B}/B^2$ at the lower boundary (constant along field lines in force-free equilibrium; bottom right panel). Electric currents (gray isosurfaces, top right of each panel) are distributed over many individual layers, narrowing during the turbulent decay of the structure (t = 50 s). Credit: Pontin et al. (2016)

Hood et al. (2016) discuss another example of modelling complex and unstable magnetic structures dissipating into small-scale reconnection events. With their 3D MHD simulation of a loop containing 23 nonpotential, highly twisted magnetic threads, they demonstrate that kink instability of a single thread can trigger an avalanche of reconnection events, even when the remaining threads are below marginal stability. Magnetic energy is released in discrete bursts, with the overall heating pattern characterised by short spikes that resemble the temporal behaviour of nanoflares rather than continuous heating. This has important implications for coronal heating, as it offers a mechanism for energy dissipation through triggered events (explored in more detail in Sec. 1.8.2).

1.8 Flux tube instabilities

Flux ropes play a very important role in eruptions in the solar corona (Liu 2020; Patsourakos et al. 2012). An idealised theoretical flux rope can be modelled by a cylindrically-symmetric magnetic field (Priest 2014). This is an approximation of real magnetic fields, often encountered in magnetically-confined fusion devices, such as twisted magnetic fields bent into tori, and in solar and astrophysical environments, where they are often embedded within complex topological structures.

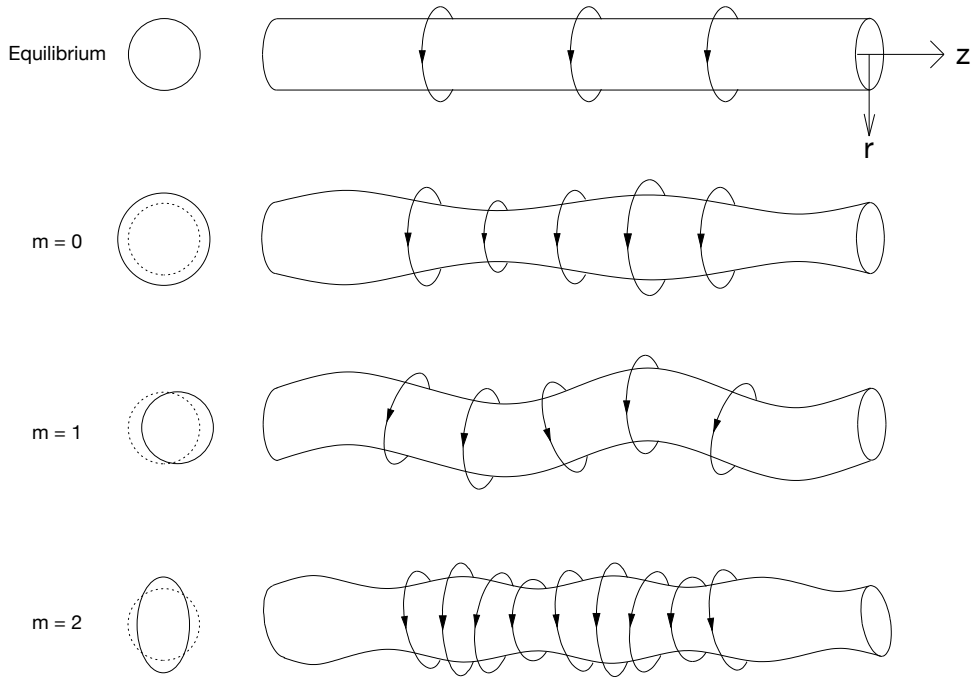

Figure 1.23: Co-moving surfaces of a flux tube perturbed by modes m = 0, m = 1 and m = 2 compared with equilibrium (first column). Magnetic field represented by arrows. Credit: Braithwaite (2006)

Consider an infinite cylindrically symmetric magnetic flux tube, whose equilibrium magnetic field, in cylindrical polar coordinates (r, ϕ, z), is:

$$\mathbf{B} = B_\phi \hat{\phi} + B_z \hat{z}. \tag{1.59}$$

The corresponding electric current density is:

$$\mathbf{j} = -\frac{dB_z}{dr}\hat{\phi} + \frac{1}{r}\frac{drB_\phi}{dr}\hat{z}. \tag{1.60}$$

Suppose the field is force-free, with $\mathbf{j} \times \mathbf{B} = 0$, or equivalently:

$$\frac{d}{dr}\left(\frac{B_\phi^2 + B_z^2}{8\pi}\right) = -\frac{B_\phi^2}{4\pi r} \tag{1.61}$$

As far as pressure force is negligible, equilibrium is completely determined by the magnetic field profile.

Bernstein's energy method (Bernstein et al. 1958, anticipated by Lundquist 1951) can be applied to the system of a magnetic flux tube to infer the relative stability conditions (Newcomb 1960), also under force-free conditions (Anzer 1968; Raadu 1972). It consists of determining the second order change (δW) in potential energy when a plasma element is displaced by a general perturbation ξ from equilibrium. In cylindrical coordinates:

$$\xi = \xi(r) \exp\left[i(lr + m\phi + kz) + i\omega t\right] \tag{1.62}$$

and, assuming force-free conditions, namely $\delta\mathbf{B} = \nabla \times (\xi \times \mathbf{B}_0)$:

$$\delta W \propto \int \left[\delta B^2 + \delta\mathbf{B} \cdot \xi \times (\nabla \times \mathbf{B}_0)\right] dV \tag{1.63}$$

As soon as the equilibrium field components ($B_{\phi,0}$ and $B_{z,0}$) are specified, δW variations are tested for each set of wavenumbers (l, m, k): broadly speaking, if the resulting value of δW is negative (positive), the system is unstable (stable) to that class of perturbations (Priest 2014).

For instance, Hood & Priest (1979a) addressed a force-free coronal tube anchored in the photosphere, considering the uniform-twist force-free field:

$$B_\phi = B_0 \frac{\Phi r L}{1 + (\Phi r L)^2}, \tag{1.64}$$

$$B_z = B_0 \frac{1}{1 + (\Phi r L)^2}. \tag{1.65}$$

where the parameter Φ is the angle of twist of a field line about the axis from one end to the other. They considered a kink-like perturbation: $\xi \propto e^{i\phi + kz}$ (with $l = 0$, and $m = 1$). The resulting stability diagram indicates that the magnetic flux tube is first unstable to kink modes when the twist exceeds about 3.3 π. Therefore, perturbations with wave numbers $l = 0$ and $m = 1$ (second row of Fig. 1.23) can lead to a flux tube instability called 'kink instability'. Fig. 1.24 shows the kink stability diagram of a cylindrical flux tube (of length L, section a, and twisting angle Φ) with fixed footpoints. If we set $m = 0$ (third row of Fig. 1.23), the related instability is called the 'sausage instability'. High-wave-number perturbations (e.g., third row of Fig. 1.23) produce more complex field configurations but are less effective in instigating instability (to dominate is often the kink $m = 1$ mode, Braithwaite 2006).

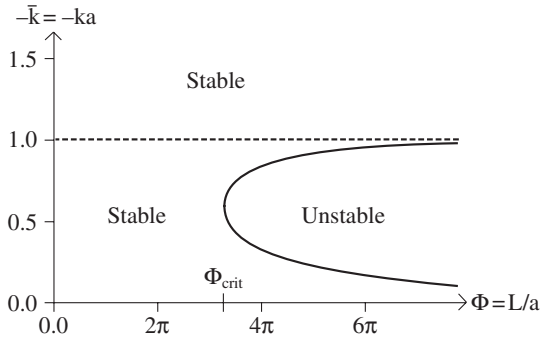

Figure 1.24: The helical kink stability diagram for a force-free, cylindrical flux tube, line-tied at the boundaries and uniformly twisted. The stability of the mode with wave number k depends on the cylinder aspect ratio (Length over cross-section, L/a) and the twisting degree Φ. Credit: Hood & Priest (1979a)

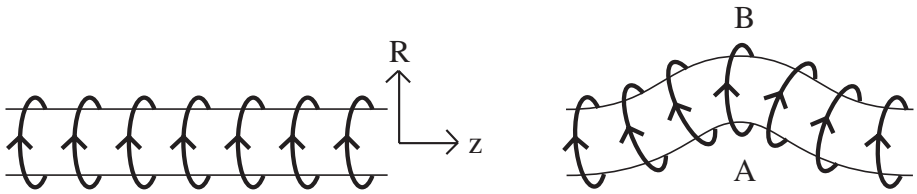

Figure 1.25: Onset of kink instability in a cylindrical magnetic flux. The initial magnetic field is azimuthally directed (left panel). A small perturbation creates a (irreversible) misalignment between points A and B. Credit: Priest (2014)

1.8.1 The kink instability

A possible trigger mechanism for large-scale energy release is the MHD kink instability in a single twisted magnetic flux strand (Hood & Priest 1979b). It typically arises in narrow, strongly twisted magnetic tubes and results in the cross section of the plasma column moving transversely away from its centre of mass, determining an irreversible imbalance between the outward directed force of magnetic pressure and the inward force of magnetic tension (Priest 2014).

A heuristic but intuitive argument for the kink instability in a straight and cylindrical flux tube (Priest 2014) begins by considering a lateral kink-like perturbation, i.e. perturbation proportional to $e^{i\phi}\cos(kz)$, which can be obtained by superposing two oppositely twisted helical perturbations such as: $e^{i\phi+kz}$ and $e^{i\phi-kz}$. For simplicity, we assume that magnetic field lines have only the ϕ component (left panel on Fig. 1.25). The kink-like displacement makes the field lines at A close together and those at B to depart (right panel on Fig. 1.25). The magnetic pressure is therefore stronger at A than at B, so

that the resulting force is directed from A to B. Consequently, the initial perturbation increases further indefinitely. This is a simple argument and implies that flux tubes with purely azimuthal magnetic field are always unstable (i.e. unstable under any small, kink-like perturbation). If extra features, such as an axial magnetic field, a plasma pressure gradient, curvature, or line-tying, are added, equilibrium conditions shall be modified (for instance, axial magnetic field has stabilising effect against kink-like perturbations, Priest 2014).

Browning (2003) proposed that the onset of the ideal kink instability in a twisted magnetic flux rope could serve as a trigger for relaxation. This hypothesis is supported by laboratory spheromak experiments that demonstrate the crucial role of the kink instability in relaxation processes (Duck et al. 1997). Some observations indicate the occurrence of the ideal kink instability in the solar corona, for instance in initiating solar eruptions (e.g., Török et al. 2004; Williams et al. 2005). The development of the kink instability has also been extensively studied in laboratory astrophysics experiments (e.g., Bellan 2018).

As shown over the last decades by several numerical experiments of kink instability in twisted magnetic flux tubes (e.g., Baty & Heyvaerts 1996; Velli et al. 1997; Lionello et al. 1998; Arber et al. 1999; Baty 2000; Gerrard et al. 2001; Gerrard & Hood 2003; Browning et al. 2008; Hood et al. 2009; Kliem et al. 2010; Bareford et al. 2013; Gordovskyy et al. 2013), initially, a helical kink develops and grows in accordance with the linear theory of instability. Subsequently, the initial helical current sheet progressively fragments in a turbulent manner into smaller-scale sheets. During the onset of the instability, kinetic energy increases rapidly, and throughout the nonlinear phase, magnetic energy dissipates. Notably, reconnection events arise within fine-scale structures such as current sheets. The dissipation occurring in these sheets is analogous to a nanoflare storm. As time progresses, the magnetic field reaches a minimum energy state constrained by the conservation of magnetic helicity, as expected in highly conducting plasmas (Browning 2003; Browning et al. 2008), but it is also subject to other topological constraints (e.g., Yeates et al. 2010).

Gibson (1977) interpreted X-ray flares observations on the limb as produced by kink instability. Sakurai (1976) predicted instead that erupting filaments during two-ribbon flares are another example of kink instability. Hood & Priest (1979b) addressed an explanation for flares alternative to the emerging flux model (see e.g., Priest 1976a,b; Heyvaerts et al. 1977). They suggested that small loop flares are induced by unstable, possibly resistive, kink modes developing along the flux tubes. By considering the stability of an infinitely long, cylindrical, twisted, magnetic flux tube, Kruskal et al. (1958) and Shafranov (1963), showed that the kink instability is set when the amount of twist exceeds a critical value $\Phi_{\text{crit.}}$. In a finite flux tube, the threshold depends on its aspect ratio, plasma beta, and the detailed traverse tube structuring. Hood & Priest (1981) estimated a critical threshold of $2.49\,\pi$ for a uniformly twisted force-free

field, by comparison with previous bounds of 3.3 for instability Hood & Priest (1979b). Other different studies have predicted the critical twist in different configurations, e.g., $\Phi_{\text{crit.}} = 4.8\,\pi$ for a localised twisting profile (Mikic et al. 1990); and $\Phi_{\text{crit.}} = 5.15\,\pi$ for a localised, variable twisting profile (Baty & Heyvaerts 1996). Van der Linden & Hood (1998, 1999) used a WKB method (Connor et al. 1979) to estimate the critical length for the onset of the ideal MHD instability in force-free, cylindrical, and line-tied coronal loops, extending earlier approximations.

In order to evaluate the budget of free energy released during a kink instability, the magnetic relaxation theory was initially developed, in the context of laboratory plasmas, by Taylor (1974) and later extensively adapted for the solar corona (e.g., Heyvaerts & Priest 1984; Priest et al. 2005). As anticipated by Woltjer (1958), and shortly discussed in Sec. 1.5.4, Taylor (1974) proposed that in a plasma with small (but finite) resistivity, the only invariant conserved is the total helicity (Berger et al. 1999). In other words, in a highly conducting plasma, where small-scale magnetic reconnection occurs, the global magnetic helicity remains approximately conserved as an invariant, namely, changes in magnetic helicity are significantly less as compared with changes in magnetic energy, which is dissipated through reconnection. Taylor's hypothesis has been successfully employed to account for the formation of the distinctive layer exhibiting a reversed toroidal magnetic field in Reverse Field Pinch devices (Taylor 1974), as well as in various other laboratory plasma settings (Taylor 1986, 2000). Further experimental evidence for helicity conservation was provided by Ji et al. (1995), during relaxation events in a Reverse Field Pinch, and similar applications have been made to spheromaks (Bellan 2000) and tokamaks (Gimblett et al. 2006; Liang et al. 2010). Taylor's theory has also been extensively applied to the solar corona. In this context, for Taylor's hypothesis to hold, the conservation of magnetic helicity in the highly conductive solar corona must be more robust than that of magnetic energy. This condition is met when dissipation is primarily confined to small-scale structures, such as current sheets, that are associated with magnetic reconnection (Browning et al. 2008). Indeed, as heuristically shown by Browning (1988), since in current sheets dissipation occurs in thin layers of width l much smaller than the global length scale L, then j scales with B/l. Moreover, since the magnetic energy and helicity volumetric resistive dissipation rates scale respectively as $\mathbf{j} \cdot \mathbf{B}$ (Eq. 1.35) and j^2 (Eq. 4.16), their ratio will be very small ($\sim l/L$). As a consequence of that, when a non-linear force free magnetic magnetic field is disrupted, it relaxes towards the state of minimum magnetic energy available under the constraint of helicity conservation i.e. toward a linear force-free field:

$$\nabla \times \mathbf{B} = \alpha \mathbf{B} \tag{1.66}$$

with α a constant parameter whose value is constrained by helicity conservation. During the relaxation process, magnetic energy is initially converted into both thermal and kinetic energy, but it ultimately dissipates into heating, e.g., by viscosity. Observations

of this relaxation process in the solar corona have been discussed, e.g., by Nandy et al. (2003). Further constraints on the relative magnitudes of helicity and energy dissipation in the solar corona are provided by Berger (1984), with observational evidence supporting Taylor relaxation in the flaring corona found in studies by, e.g., Nandy et al. (2003) and Murray et al. (2013).

In order to apply these ideas to solar coronal heating, Heyvaerts & Priest (1984) considered that photospheric footpoint motions determine the growth of coronal magnetic field stresses at timescales slower than the loops Alfvén travel time. They presented a 'mixing-time' theory according to heating results from motions that build up stresses at a rate comparable to that at which reconnection relaxes them. As a result, the field generally evolves towards a nonlinear force-free state with excess of magnetic energy. When this state is perturbed, it relaxes to a lower-energy constant-α force-free configuration, releasing any stored free energy as heat. This cycle of energy accumulation and relaxation continuously generates heating, as in a stress-and-relax process.

As previously mentioned, the concept of helicity-conserving relaxation to a minimum energy state can be valuable in predicting the energy released during solar flares or smaller events, such as nanoflares related to coronal heating. The magnetic energy available for release depends on the magnetic field configuration at the onset of relaxation. To release substantial free energy, the magnetic field must deviate significantly from a constant-α state, and relaxation should occur intermittently. Browning (2003) applied this framework to a family of nonlinear force-free field profiles in a cylindrical geometry with piecewise constant $\alpha(r)$. They proposed that heating events in the solar corona may be initiated by the onset of an ideal (rather than resistive) MHD instability. Indeed, in the highly conductive coronal plasma, only ideal instabilities have sufficiently rapid (typically Alfvénic) timescales to be relevant for flare onsets or coronal heating. For instance, evidence from 3D MHD simulations of cylindrical loop models (e.g., Velli et al. 1997) with small, though non-zero, resistivity indicates that, during its nonlinear phase, the ideal kink instability generates strong current sheets that facilitate rapid energy dissipation through fast magnetic reconnection. In the Browning (2003) scenario, the coronal magnetic field, stressed by photospheric footpoint motions, evolves quasi-statically through a series of equilibria until it becomes ideally unstable. This instability triggers a dynamic heating event, after which the field settles into a minimum energy or constant-α state, preserving its helicity but with reduced energy. They apply relaxation theory with linear instability calculations that include line-tying effects to determine the ammount of energy release. The resulting energy release varies considerably based on the specific current profile at the onset of instability. Notably, this model predicts a minimum nanoflare size of approximately 10^{25} erg (10^{18} J), given specific loop parameters (length of 20 Mm, radius of 1 Mm, and longitudinal magnetic field of 30 G), and a maximal energy release up to 10 -100 times bigger, within the same coronal loop. This model was further extended by Bareford et al. (2010, 2011) to explore the distribution of nanoflare

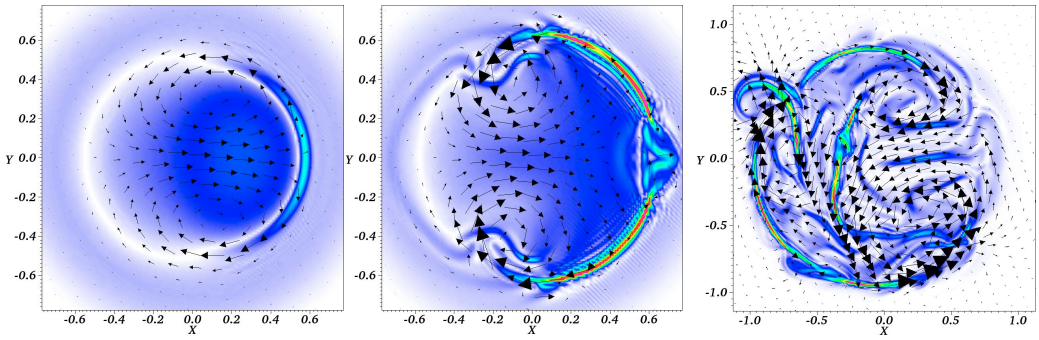

Figure 1.26: MHD simulation of a kink-unstable flux tube with zero net-current with Lare-3D code (Arber et al. 2001). The min plane maps of the current density before (left), during (middle), and after (right) the onset of the instability are shown. The arrows show the velocity components along the plane scaled proportionally to the magnitude of the horizontal velocity. As the flux tube is distorted, a helical current sheet forms and increases at the surface. It further breaks into two and, finally, it chaotically fragments into many sheets. Credit: Hood et al. (2009)

energies resulting from random photospheric twisting motions.

Browning et al. (2008) compared Browning (2003) model outcomes with the results obtained from a three-dimensional numerical MHD simulation of energy release in a cylindrical coronal loop model. The initial magnetic field profiles are chosen to be linearly kink-unstable. The results include line-tying effects and are extended to account for a surrounding potential field layer. The loop initially develops a helical kink, whose structure and growth rate align well with linear stability theory, followed by the formation of a current sheet. During this phase, there is a burst of kinetic energy as the magnetic energy decays. A new relaxed equilibrium, closely resembling a constant-α field, is established. The energy released is evaluated against predictions that the magnetic field will relax to a minimum energy state with conserved magnetic helicity, forming a constant-α force-free field, it is also consistently dependent on the initial current profile.

A 3D magnetohydrodynamic numerical code (Lare-3D, Arber et al. 2001) is used to simulate the evolution of coronal loops which are initially in ideally unstable equilibrium. The initial states have zero net current. The results are interpreted by comparison both with linear stability analysis and with helicity-conserving relaxation theory. The disturbance due to the unstable mode is strongly radially confined when the loop carries zero net current. Strong current sheets are still formed in the nonlinear phase with dissipation of magnetic energy by fast reconnection. The nonlinear development consists first of reconnection in a large-scale current sheet, which forms near the quasi-resonant surface of the equilibrium field. Subsequently, the current sheet extends and then fragments, leading to multiple reconnections and effective relaxation to a constant α field. Magnetic reconnection is triggered in the non-linear phase of kink instability in

loops with zero net current. Initially, reconnection occurs in a single current sheet, which then fragments into multiple reconnection sites, allowing for almost full relaxation to the minimum energy state. The loop is heated to high temperatures throughout its volume.

Hood et al. (2009) further explored coronal heating by magnetic reconnection in kink-unstable loops with zero net current. They show that in loops with zero-net-current, where the instability is more localised, the relaxation remains as effective as in previous studies involving net-current loops. In their 3D MHD simulations, fast magnetic reconnection occurs during the nonlinear phase of the kink instability, effectively dissipating magnetic energy and allowing the loop to relax to a minimum energy state, consistent with relaxation theory predictions. In particular, the kink mode initially exhibits exponential growth, leading to helical deformation of the loop and an internal double-vortex flow. As the deformation increases, a helical current ribbon forms near the surface of the most unstable linear mode (Fig.1.26, left panel). The current sheet grows in both magnitude and length, eventually splitting into two (Fig.1.26, middle panel) and becoming distorted within the loop, forming a complex, fragmented current sheet structure throughout the loop cross section (Fig.1.26, right panel). Reconnection occurs vigorously within this fragmented structure, driving further reconnection and heating the plasma to temperatures exceeding 10^8K. Due to the initial profile containing currents of opposite signs and the involvement of the surrounding potential field layer in the relaxation process, the final α value is nearly zero, resulting in a final field that closely resembles a uniform axial field.

Strong bursts in plasma temperature ($\sim 10^8$K) as well as in kinetic energy are attenuated by an order or magnitude when the effects of thermal conduction along field lines are taken into account (Botha et al. 2011). Such effects play a fundamental role, as they strongly influence the plasma properties, as well as the global timescales of the fast MHD event, with deep consequences also in the forward modelling of such loops.

In contrast to cylindrical models, real coronal loops exhibit field line convergence at the photospheric footpoints, leading to significantly weaker field strength at the loop tops compared to the footpoints (Gordovskyy et al. 2013, 2014). In 3D MHD simulations of confined solar flares within twisted coronal loops, the footpoints are gradually twisted within a dipolar magnetic region and a gravitationally stratified atmosphere until instability occurs. Specifically, Bareford et al. (2016) investigated magnetic reconnection in twisted magnetic flux tubes with different loop configurations, to establish the role of field geometry, heat conduction, and atmospheric stratification on the stability and further heating distribution in twisted coronal loops. For instance, when coronal loops large-scale curvature is taken into account, the current (and thus heating) distribution loses its cylindrical symmetry (as in the straight-cylinder case), with strong currents clustered in a thin shield on the top. Curvature is also demonstrated to systematically reduce the stability of flux tubes. In the loops with strong convergence at footpoints, current sheets and heating are stronger and localised above the footpoints. Stability proves

different for curved and straight flux tubes: in curved loops footpoints convergence has a stabilising effect, the opposite is true for straight tubes. Atmospheric stratification is demonstrated to affect loop stability because of the destabilising effect of waves propagating from the chromosphere to the corona. In agreement with Botha et al. (2011), localised heating is smoothed by thermal conduction, although the temperature distribution remains very structured across field lines. Curved loops typically experience an upward "failed eruption", marked by an initial expansion followed by contraction and large-scale reconnection, eventually relaxing to a lower-energy, weakly twisted state (Bareford et al. 2016; Pinto et al. 2016). Observationally, such failed eruptions are commonly detected as energy release signatures in reconnecting twisted loops (e.g., Leamon et al. 2003; Srivastava & Dwivedi 2010; Kuridze et al. 2013).

Studies have also analysed line-of-sight velocities and velocity dispersions in relaxing twisted loops, linking these to non-thermal spectral broadening (Gordovskyy et al. 2016), with results indicating positive correlations between velocity dispersion and temperature, consistent with observations (Doschek et al. 2008). Work in cylindrical geometries has identified additional soft X-ray signatures (Pinto et al. 2015), such as loop expansion and intensity increases at the loop edges, with potential observables for DKIST (Snow et al. 2018). Other signs of energy release in reconnecting twisted loops include microwave polarization patterns (Sharykin et al. 2018).

1.8.2 MHD avalanches

While much of the discussion has focused on individual twisted loops so far, configurations with multiple twisted flux ropes also contain free magnetic energy that can be released as these flux ropes merge through magnetic reconnection (Browning & Priest 1986). As twisted flux ropes coalesce with each other, they generate a cascade of energy release from smaller to larger scales that has been interpreted as "domino" or "avalanche" mechanism.

The concept of avalanche mechanism (Charbonneau et al. 2001) for energy release in a magnetically complex corona dates back to the works of Lu & Hamilton (1991) and Lu et al. (1993). They suggested that the solar coronal magnetic field exists in a self-organised critical state, which accounts for the observed power-law distribution of solar flare occurrence rates across more than five orders of magnitude in peak flux. This mechanism posits that the clustering of numerous dissipating magnetic discontinuities within a localised area can lead to large-scale explosive events. In their model, the magnetic field is defined over a three-dimensional grid, with "rules" applied at each grid point to determine whether magnetic energy dissipation occurs based on local field stresses. Dissipation at one point can destabilise adjacent points, triggering a chain reaction. This model envisions solar flares as avalanches of numerous small-scale reconnection events.

The cellular automaton (CA) approach has been extensively developed for modelling

solar flares and coronal heating through nanoflares (see review by Charbonneau et al. 2001; Aschwanden et al. 2016), showing that continuous energy release models can be translated into discrete self-organised critical models (Bak 2013). In these models, various rules can be defined to drive the system, determine instability, and relax to a stable state. Typically, the CA models represent the magnetic field using vector or scalar values on a 2D or 3D rectangular grid. Relaxation is triggered when a field value deviates significantly from neighbouring values or when the horizontal field or twist exceeds a critical threshold (e.g., Vlahos & Georgoulis 2004; Fuentes & Klimchuk 2010, 2015). Subsequent research has expanded on this idea using increasingly sophisticated models, including CA to simulate highly inhomogeneous active regions (Vlahos et al. 1995), considering an ensemble of field lines rather than magnetic field strength (Hughes et al. 2003; Morales & Charbonneau 2008), or using deterministic driving to reproduce the slow twisting of a loop (Strugarek et al. 2014). A CA model whose instability criterion recalls kink instability in twisted loops has been proposed by Mendoza et al. (2014), although it does not account for reconnection between neighbouring loops.

An alternative scenario suggests that photospheric motions with vorticity twist individual elements of a magnetic flux tube (e.g., De Moortel & Galsgaard 2006). Consequently, the coronal magnetic field is likely nonpotential, composed of numerous current-carrying threads, simplified as twisted magnetic flux rope, often separated by current sheets. The merging of two or more twisted flux ropes into a single structure has long been considered a potential mechanism for releasing stored magnetic energy, leading to both large-scale flares and, on smaller scales, coronal heating (e.g., Gold & Hoyle 1960; Melrose 1997; Kondrashov et al. 1999). As twisted flux ropes coalesce into fewer, larger structures, the typical field scale-length increases, which can be interpreted as an inverse energy cascade from small to large scales or as a self-organization process. Reconnection and energy release during flux rope mergers have been both modelled (e.g., Linton et al. 2001; Kliem et al. 2014) and observed in various eruptive events (Liu 2020). Merging flux ropes may also contribute to the pre-eruption formation of a large-scale flux rope (Patsourakos et al. 2012, 2020; Kliem et al. 2021). The merging of magnetic flux ropes has been explored in several laboratory reconnection experiments. For example, in the MAST spherical tokamak, two current-carrying plasma tori merge into a single twisted flux rope, resulting in significant heating and forming a hot spherical tokamak plasma through "merging-compression" (Stanier et al. 2013; Browning et al. 2014; Gryaznevich & Sykes 2017). Semi-analytical models have been developed for plasmas within a conducting chamber of rectangular cross-section, using both an infinite-aspect ratio configuration (Browning et al. 2014, 2015) and a tight-aspect ratio cylindrical configuration (Bareford et al. 2016). This models begin with two adjacent flux ropes of rectangular cross-section, determining the values of α and peak magnetic field by imposing constraints of helicity and toroidal flux conservation. This relaxation model is adaptable to simulate coronal loop mergers, where initial configurations could

include multiple loops or oppositely twisted loops (Browning et al. 2015).

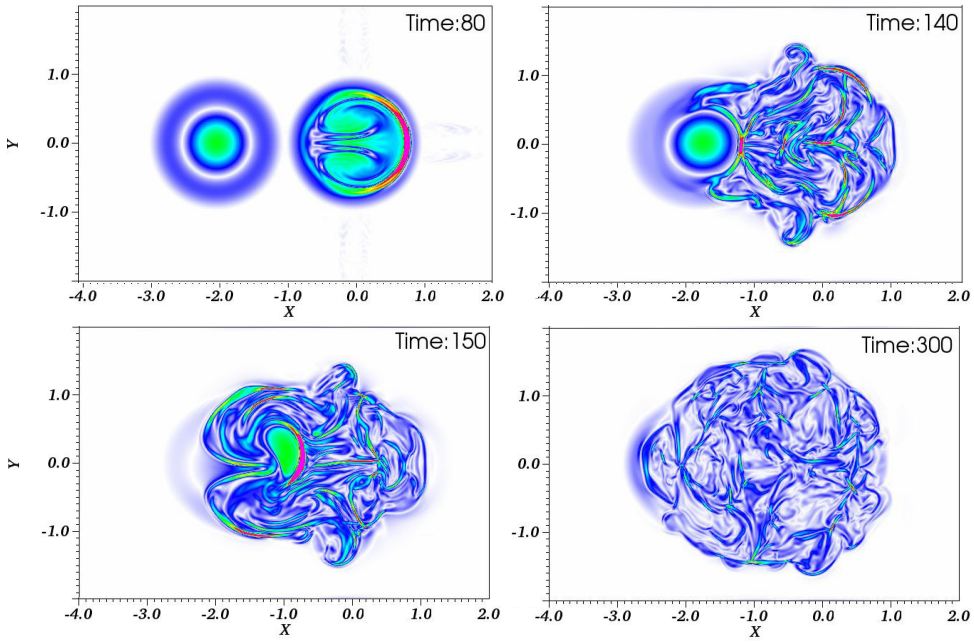

Figure 1.27: MHD simulation of the merging of two twisted flux tube with Lare-3D code (Arber et al. 2001). The maps of the current density at the mid plane are shown at four evolution stages. Initially (top-left panel), the flux tube on the left undergo kink instability. The unstable tube expands and eventually coalesces with the other one (top-right, bottom left panels), the final structure is a single, quasi-circular flux tube (bottom-right panel). As the magnetic structure evolve, the current density tubes breaks and chaotically fragments into many sheets. Credit: Tam et al. (2015)

In general, there are two primary approaches to study the non linear evolution of merging flux ropes: in the first, the twisted flux ropes carry a net current, causing them to attract each other (e.g., Stanier et al. 2013); in the second, the flux ropes are in full equilibrium, necessitating an instability or external driving force to initiate merging. Tam et al. (2015) addressed the second scenario, as an initial step toward the development of MHD avalanche models by propagation of kink instabilities. In a series of numerical experiments, they explored the heating of a coronal loop composed of multiple small magnetic threads. Their study focused on a scenario involving two magnetic threads, in which one thread was rendered unstable to the kink instability. A key finding from these simulations is that a stable magnetic thread can be destabilised by an adjacent unstable thread if they are sufficiently close and share the same twist orientation. In fact, since the unstable loop expands in the radial direction (‘partial relaxation’, Bareford et al. 2013, see also the top panels of Fig. 1.27), during the relaxation process, it can

disrupt the nearby stable loops (bottom-left panel of Fig. 1.27). After both threads become destabilised, the system relaxes into a single, larger loop with reduced twist (bottom-right panel of Fig. 1.27). The characteristic length scales of this weakly twisted field are now greater than those of the original configuration, similarly to the inverse cascade of magnetic helicity observed by Antiochos (2013).

Hood et al. (2016) demonstrate that an MHD avalanche can occur in a nonpotential multithreaded coronal loop. Considering 23 twisted magnetic threads within a loop, they used 3D MHD simulations to show that a single unstable thread can trigger the decay of the entire structure. In particular, as shown in Fig. 1.28, each flux tube coalesces with the neighbouring ones and releases discrete heating bursts. The spiky temporal evolution of heating agrees with the nanoflare-storm scenario for coronal loop heating.

Tam et al. (2015) and Hood et al. (2016) 3D MHD results have been successfully compared with a model for the relaxation and merging of twisted flux ropes, based on a helicity-conserving relaxation hypothesis (Taylor 1974, 1986). Hussain et al. (2017) determined the lowest available energy state under the constraint of total helicity conservation: a linear force-free field α determined by the conservation of the dimensionless helicity-axial-flux ratio (Taylor 1974, 1986). Since the lowest energy is likely achieved imposing circular boundaries, the relaxed field is assumed to be a circular cross-section flux tube, whose extent is constrained by few assumptions on the total flux ropes volume conservation, and magnetic/gas pressure balance. Solar coronal fields have no conducting walls, so the background potential field must remain unchanged as in a free boundary problem (Browning 1988; Dixon et al. 1989).

Simulations with more complex initial states, such as braided magnetic fields, tend to relax to configurations that deviate from a Taylor state, often resulting in two weakly twisted flux ropes with opposite signs of α. Indeed, relaxation theory does not always predict a minimum energy state. For relaxation to proceed, a sufficient level of turbulent reconnection is required to allow field line reconnection across the volume. In cases like two oppositely twisted flux ropes, free magnetic energy may remain unreleased, as reconnection to achieve a minimum energy state (a potential field) is unlikely, due to the alignment of azimuthal fields at the interface. Furthermore, for astrophysical plasmas, which lack the conducting boundaries of laboratory plasmas, relaxation theory must be adjusted to account for partial relaxation, where only a limited volume of the field undergoes relaxation while the surrounding magnetic field remains unchanged (Bareford et al. 2013). The merger of two flux ropes can in general be classified as either "co-helicity" or "counter-helicity" depending on whether the helicities of the ropes are the same or opposite (Yamada et al. 1990). Co-helicity mergers, which are observed in spherical tokamaks, seem more probable in the solar corona. In the counter-helicity scenario, oppositely twisted flux ropes are less likely to relax and release energy since neither toroidal nor poloidal magnetic fields reverse at the interface, making magnetic reconnection initiation difficult without a strong external trigger (Ripperda et al. 2017a,b).

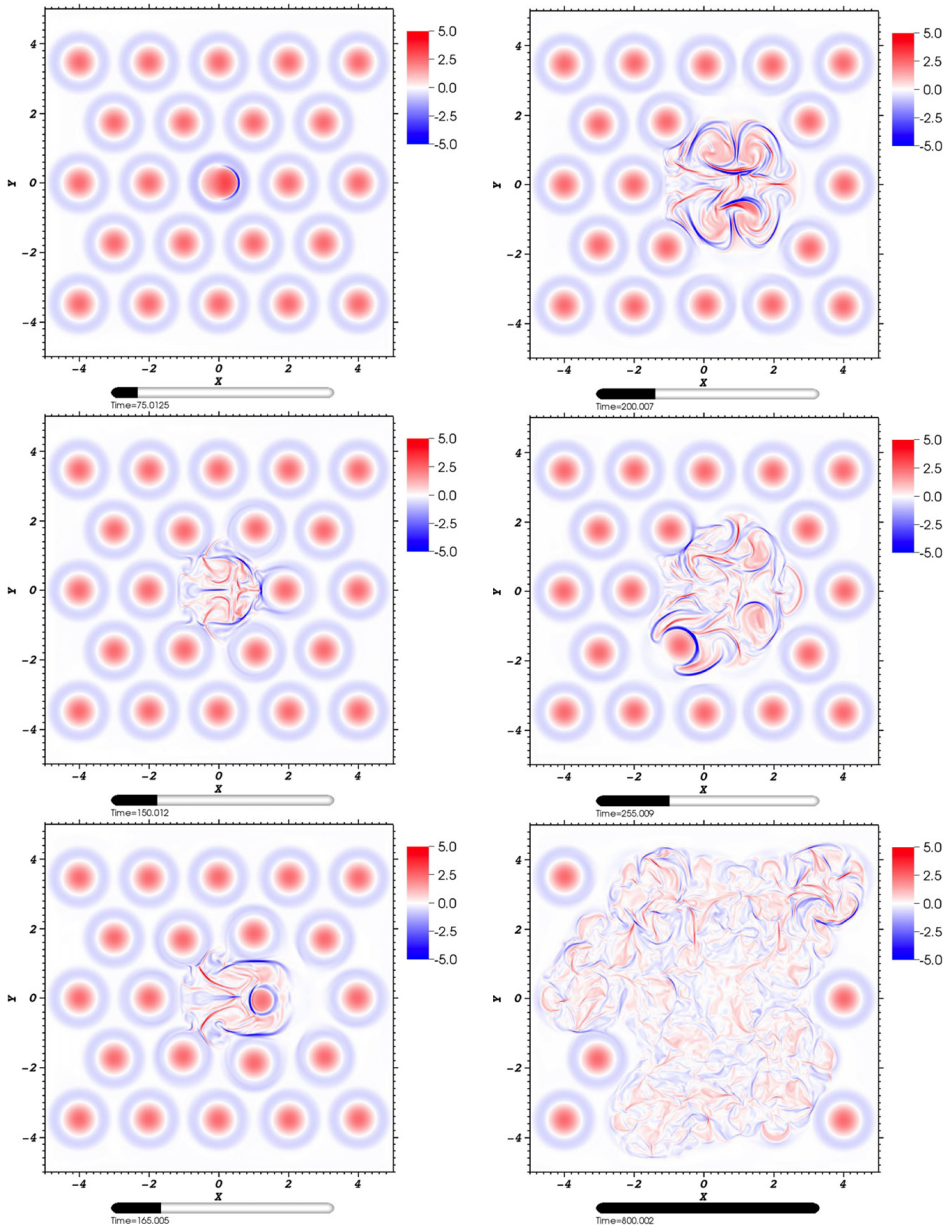

Figure 1.28: MHD simulation of an MHD avalanche in a multi-threaded coronal loop with Lare-3D code (Arber et al. 2001). The maps of the axial current density at the mid plane are shown at six evolution stages. The avalanche process is triggered by a single, kink-unstable coronal loop strand (first panel from the top-left). As the process evolve (following panels), the unstable flux tubes coalesce with nearby stable one, causing widespread current density fragmentation in current sheets. the Credit: Hood et al. (2016)

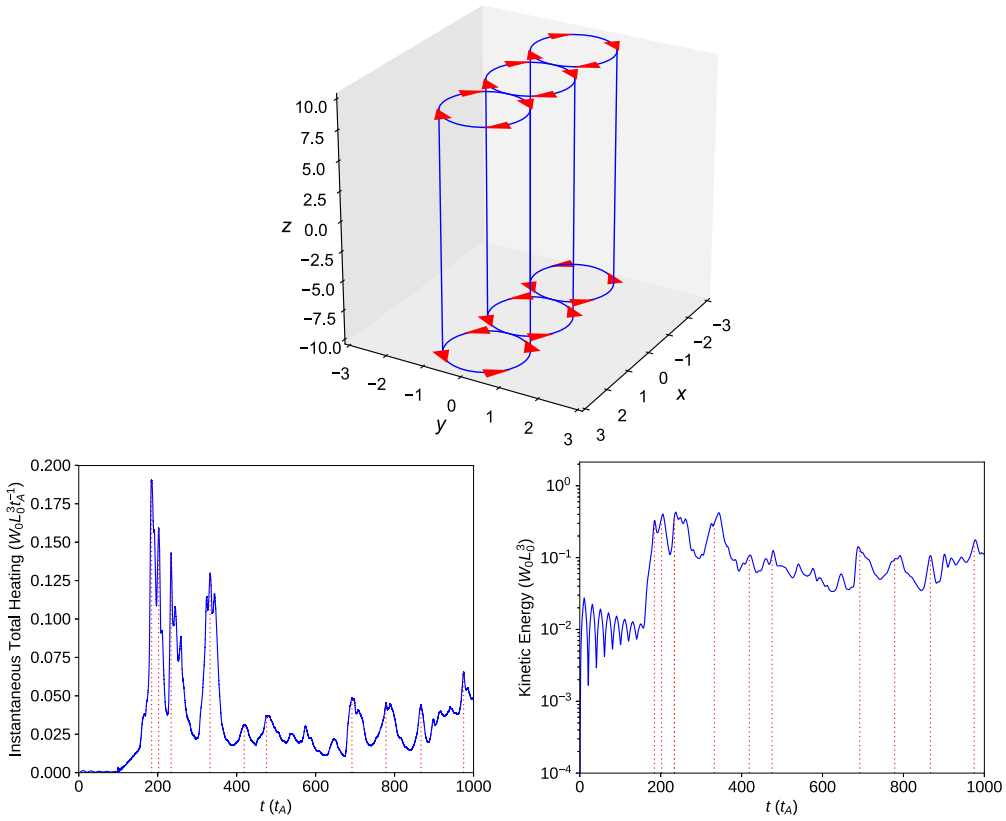

Figure 1.29: Lare-3D (Arber et al. 2001) MHD simulation of an MHD avalanche within a three-stranded coronal loop twisted at the boundaries (as shown on top panel). Bottom-right panel: instantaneous total (Ohmic+viscous) heating over the time. Bottom-left panel: volume-integrated kinetic energy over time. The red dashed lines indicates the times of visibly large heating events. Credit: Reid et al. (2018, 2020)

According to Hussain (2018), relaxation between oppositely twisted threads is unlikely or occurs more slowly, requiring stronger triggers. This is attributed to topological constraints not accounted for in Taylor's hypothesis (Yeates et al. 2015).

In general, the energy stored by photospheric motions can be released via viscous and Ohmic dissipation during a dynamic relaxation process (Reid et al. 2018) and thereafter through a sequence of impulsive, localised, and aperiodic heating events under the action of continuous photospheric driving (Reid et al. 2020). One question is whether repeated episodes of instability and energy release can occur, as the field is continually twisted or the disordering of the field prevents the onset of further kink instabilities (Rappazzo et al. 2013). Reid et al. (2018, 2020) addressed coronal energy release by MHD avalanches considering the driven evolution of three neighbouring threads within a large-scale loop structure, twisted by boundary motions. In agreement with previous investigations (Tam

et al. 2015; Hood et al. 2016) they demonstrated, using full three-dimensional MHD simulations, that the destabilisation of large-scale magnetic fields by a single unstable "node" is feasible: the instability of one of the threads leads to the release of magnetic energy in all three, with burst energy release continuing throughout the simulation. An important outcome of this work is that, while the relatively simple driving of three vortex motions at the photospheric boundaries initially produces three coherent and distinct flux tubes, after the instability and subsequent disruptions, the magnetic field lines are connected to different vortices and the continued photospheric motions begin to braid the magnetic field in a much more complex way. This scenario differs from that proposed by others who argue that current sheets will always form in sufficiently tangled magnetic fields generated by complex motions (Hendrix & Van Hoven 1996; Ng et al. 2012). Here, the current sheets spontaneously form from a highly ordered initial state, with photospheric motions that cause the braiding of the magnetic field, as has often been seen in such driven simulations (Wilmot-Smith 2015). The field then attempts to relax to a lower-energy configuration, but nevertheless the constant imposition of the driving velocity necessitates a departure from the classical theory of Taylor (1974). The perpetual influx of energy by photospheric driving prevents the system from attaining a minimal-energy state. This suggests that the constant-α state will not be reached. The temporal evolution of the total heating shows that after the first few large releases of energy, there is a continued background level of heating and a large number of small heating events. There is no obvious periodicity or size for these events (Reid et al. 2020).

In a recent work, Threlfall et al. (2021) and Reid et al. (2022) demonstrated the feasibility of MHD avalanches within the more physically realistic curved geometry of a coronal arcade. In this configuration, MHD avalanches effectively amplify instabilities across strong solar magnetic fields, leading to widespread plasma disturbances. Unlike in straight-cylindrical models, the curved geometry induces a modified ideal MHD kink mode that occurs more readily and preferentially in the upward direction.

Threlfall et al. (2018) focused on non-thermal particle behavior within 3D MHD simulations of unstable, multi-threaded coronal loops. In particular, they investigated particle acceleration mechanisms under conditions of magnetic reconnection, occurring during the loop magnetic decay. By using a numerical scheme based on the relativistic guiding center approximation (Northrop 1963; Threlfall et al. 2016a,b, 2017), they examined the electron and proton dynamics in Tam et al. (2015) high-resolution MHD simulations, showing the effects of uniform background resistivity against those of anomalous resistivity (Rosner et al. 1978b; Hood et al. 2009). Specifically, they demonstrated that anomalous resistivity can lead to near-identical particle impact sites at the footpoints, while background resistivity results in distinct impact locations. Additionally, when secondary thread instability is triggered, a secondary acceleration event and the emergence of a hardened particle energy spectrum are identified, with energetic particles spreading across both loop strands volumes.

2 Methods

2.1 The numerical tool: PLUTO Code

PLUTO code (Mignone et al. 2007, 2012) is a modular, Godunov-type code (Godunov & Bohachevsky 1959) for the solution of astrophysical plasma flows in up to 3 spatial dimensions, in different system geometries and physical regimes (Newtonian, relativistic, MHD or relativistic MHD). The code provides a multiphysics, multi-algorithmic modular environment particularly oriented toward the treatment of astrophysical flows in the presence of discontinuities. The code is also designed to make efficient use of massive parallel computers using the message passing interface (MPI) library for interprocessor communications. PLUTO code exploits a general framework for integrating the system of conservation laws:

$$\frac{\partial U}{\partial t} + \nabla \cdot \mathbf{F} = S, \tag{2.1}$$

where $\mathbf{F}$ is the (hyperbolic and/or parabolic) flux and S stands for the sources, built on modern Godunov-type, high resolution, shock-capturing schemes (HRSC, Toro et al. 1997; LeVeque et al. 1998) that makes it particularly suitable for the treating fluids discontinuities.

The majority of HRSC codes shares a common discretisation scheme (schematically shown in Fig. 2.1), involving three general steps, discussed below:

- **A piece-wise polynomial reconstruction**. Interpolation routines are designed to reconstruct a piece-wise polynomial approximation of the solution between each cell from the cell values (Toro et al. 1997; LeVeque et al. 1998). In PLUTO many reconstruction methods are available, including flat, linear, parabolic schemes (Mignone 2005), and so forth. For instance, linear interpolation provides second order accuracy in space.

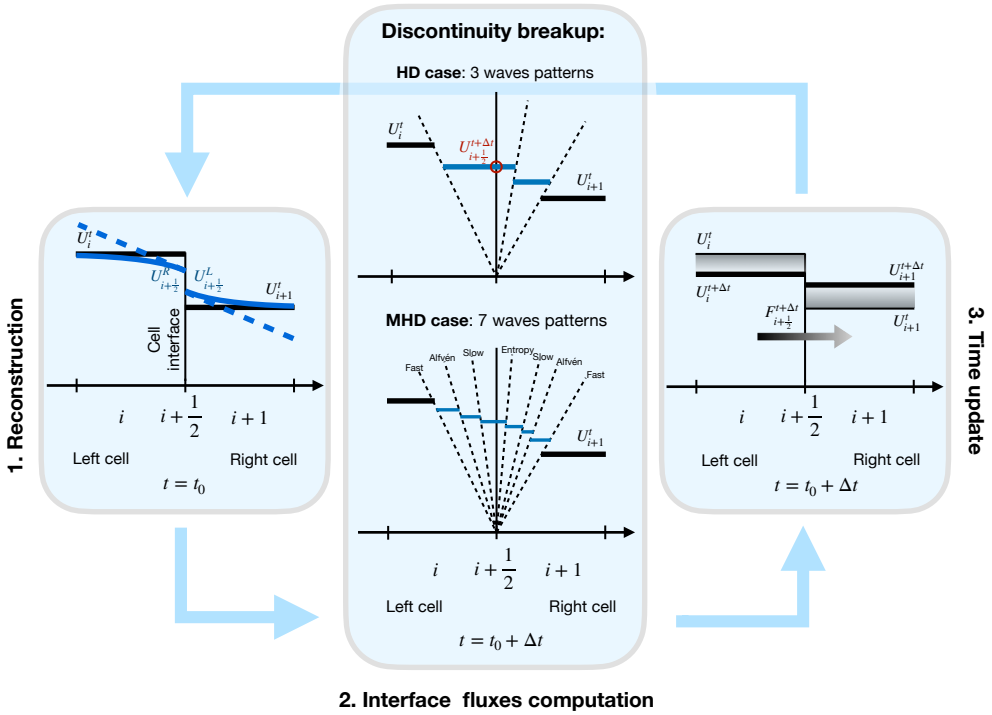

Figure 2.1: HRSC discretisation scheme involving: (1) a piece-wise polynomial reconstruction, (2) computation of fluxes at the cell interfaces, (3) temporal update.

- **The solution of Riemann problems at zone interfaces followed by the computation of fluxes at the cell interfaces**. The discontinuity at each cell interface evolves into a discontinuity breakup. Its exact evolution involves the decay of a set of non-linear waves, according to the Rankine-Hugoniot jump conditions, whose solution in turn requires relatively high computational times (especially within MHD, where seven wave patterns must be taken into account, Li 2005). Linear solvers (such as Roe solvers, Roe 1986) have a small numerical diffusivity, but can easily lead to numerical pathologies. Finally, the HLL family of solvers (Toro et al. 1994; Batten et al. 1997) is based on a guess of the signal speed and on the integral average of the Riemann fan (so fewer weaves are considered). Those methods, although less accurate (numerical diffusive), are numerically robust and preserve the positivity of the solution. Parabolic terms (such as electric resistivity, and thermal conduction) introduce second-order spatial derivatives and their treatment requires the solution of diffusion equations, bringing further time step limitations. The (explicit) super time stepping method (Alexiades et al. 1996), where the solution vector is evolved over a super time step (Δt_{ad}) consisting of N smaller substeps (Δt_{par}), has been proved to be very effective at speeding up

explicit time-stepping schemes for parabolic problems. Indeed, the STS requires $N_{STS} \sim \sqrt{\frac{\Delta t_{ad}}{\Delta t_{par}}}$ substeps rather than $N_{\rm exp} = \frac{\Delta t_{ad}}{\Delta t_{par}}$ as would be the case with explicit classical subcycling schemes. This approach is crucial when high values of plasma temperature are reached (e.g., during flares) the explicit scheme being subject to a rather restrictive stability condition (i.e. $\Delta t \leq (\Delta x)^2/2\eta$, where η is the maximum diffusion coefficient), because the thermal conduction timescale τ_{cond} is shorter than the dynamical one τ_{dyn} (see, e.g., Orlando et al. 2005, 2008 Orlando et al. 2008).

- **A final temporal evolution stage**. PLUTO provides a number of time-marching schemes (Euler, RK2, RK3, RK4, Hancock, Characteristic Tracing) for the explicit discretisation and integration of the (left hand side of) Eq. 2.1.

2.2 MHD modelling of the solar corona

The works presented in the following sections are based on the design, execution, analysis, and forward modelling of numerical experiments aimed at reproducing coronal activity without losing the conceptual effectiveness of ideal MHD modelling. The numerical experiments are based on a solar atmosphere model that includes a chromospheric layer and a magnetised coronal environment crossed by one or multiple coronal loop strands. Each loop is modelled as a straightened magnetic flux tube connecting two far and independent chromospheric layers at the opposite sides of the box, as shown in Fig. 2.2. The length of the tubes is taken to be much larger than their radius. For this reason, the effects of the curvature on their structure are negligible.

The evolution of the plasma and magnetic field in the box is described by solving the full time-dependent MHD equations including gravity (for a curved loop), thermal conduction (Alexiades et al. 1996), also with the effects of heat flux saturation, radiative losses (Raga et al. 1997), and magnetic diffusivity.

$$\frac{\partial \rho}{\partial t} + \nabla \cdot (\rho \mathbf{v}) = 0, \tag{2.2}$$

$$\frac{\partial \rho \mathbf{v}}{\partial t} + \nabla \cdot (\rho \mathbf{v}\mathbf{v}) = -\nabla \cdot (\mathbf{I}P + \mathbf{I}\frac{B^2}{8\pi} - \frac{\mathbf{B}\mathbf{B}}{8\pi}) + \rho \mathbf{g}, \tag{2.3}$$

$$\frac{\partial B}{\partial t} - \nabla \times (\mathbf{v} \times \mathbf{B}) = -\eta \nabla^2 \mathbf{B}, \tag{2.4}$$

$$\frac{\partial}{\partial t}\left(\frac{B^2}{8\pi} + \frac{1}{2}\rho v^2 + \rho\epsilon + \rho g h\right) + \nabla \cdot \left[\frac{c}{4\pi}\mathbf{E} \times \mathbf{B} + \frac{1}{2}\rho v^2 \mathbf{v} + \frac{\gamma}{\gamma - 1} P\mathbf{v} + \mathbf{F}_{\rm c} + \rho g h \mathbf{v}\right] = \\ = Q(T). \tag{2.5}$$

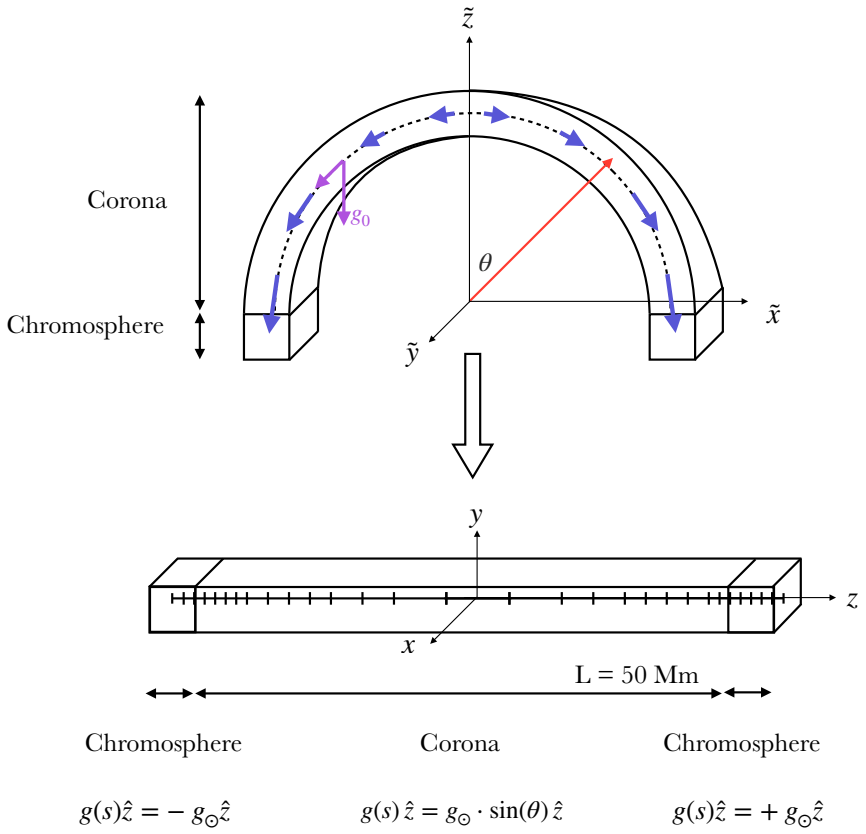

Figure 2.2: The typical semicircular loop geometry v.s. the adopted straight box geometry. Upper picture: a semicircular coronal loop box with straight chromospheric layers at the base. Lower picture: schematic representation of the 3D box containing the computational domain of the simulation. In the corona we adopted a stretched grid and the field aligned gravity of a semicircular coronal loop (blue arrows on the top).

where t is the time; ρ is the mass density; $\mathbf{v}$ is the plasma velocity; P is the thermal pressure; $\mathbf{B}$ is the magnetic field; $\mathbf{E}$ is the electric field; $\mathbf{g}$ is the gravity acceleration vector for a curved loop; $\mathbf{I}$ is the identity tensor; ϵ is the internal energy; $\mathbf{j}$ is the induced current density; η is the magnetic diffusivity; $\sigma = \frac{c^2}{4\pi\eta}$ is the electrical conductivity; T is the temperature; $\mathbf{F}_c$ is the thermal conductive flux; $Q(T)$ includes the radiated energy losses and heating.

The MHD equations (Eq.s 2.2 to 2.5) are solved in the Eulerian, conservative form, using the MHD module available in PLUTO, configured to compute intercell fluxes with the Harten-Lax-Van Leer approximate Riemann solver (Janhunen 2000), while the second order in time is achieved using a Runge-Kutta scheme (Cockburn & Shu 2001). A Van Leer limiter (Van Leer 1974) for the primitive variables is used.

The solution to the MHD equations must fulfil the solenoidal constraint at all times. According to the induction equation (Eq. 1.13 and Eq. 2.4), the magnetic field solenoidal condition ($\nabla \cdot \mathbf{B} = 0$, Eq. 1.2) formally holds at any time t, provided that the initial conditions are well posed (Eq. 1.14). On the other hand, numerical errors can produce non-negligible magnetic field divergence. The monopole control strategies available in PLUTO are 'Divergence cleaning' (Tóth 1996), 'Eight-waves' (Powell 1994; Powell et al. 1999), 'Constrained transport' (Londrillo & Del Zanna 2004; Balsara & Spicer 1999). In this work, we consider the Constrained transport approach that maintains the solenoidal condition at machine accuracy. In particular, with the constrained transport approach, the staggered magnetic field is treated as an area-weighted average on the zone face and Stoke's theorem is used to update it:

$$\int \left(\frac{\partial \mathbf{B}}{\partial t} + \nabla \times \mathbf{E} \right) dS = 0 \Longrightarrow \frac{d\mathbf{B}}{dt} + \frac{1}{S} \oint \mathbf{E} \cdot \mathbf{d}l = 0. \tag{2.6}$$

2.2.1 Supplementary Maxwell equations

Ampère's law in MHD regime (which holds until $v \ll c$) gives the current density in terms of the magnetic field curl:

$$\mathbf{j} = \frac{c}{4\pi} \nabla \times \mathbf{B}, \tag{2.7}$$

In Eq. (2.7), the displacement current has been neglected, provided that the plasma velocity is not relativistic (i.e. $v \ll c$). The electric field $\mathbf{E}$ is defined by Ohm's law:

$$\mathbf{E} = -\frac{\mathbf{v}}{c} \times \mathbf{B} + \frac{\mathbf{j}}{\sigma}, \tag{2.8}$$

From this, the Poynting flux can be decomposed into three terms:

$$\frac{c}{4\pi} \mathbf{E} \times \mathbf{B} = -\frac{1}{4\pi} \mathbf{B}(\mathbf{v} \cdot \mathbf{B}) + \frac{B^2}{4\pi} \mathbf{v} + \frac{\eta}{c} \mathbf{j} \times \mathbf{B}. \tag{2.9}$$

The first term on the right-hand side ($-\frac{1}{4\pi}\mathbf{B}(\mathbf{v} \cdot \mathbf{B})$) is significant for the driving, as it determines the energy injected into the domain by the photospheric driver. The second term ($\frac{B^2}{4\pi}\mathbf{v}$) represents the flow of magnetic energy across the boundaries of the domain. Finally, the third term ($\frac{\eta}{c}\mathbf{j} \times \mathbf{B}$) is related to Ohmic dissipation and field line diffusion at the boundaries of the domain.

We use the ideal gas law for a fully ionized plasma:

$$p = (\gamma - 1)\rho\epsilon = \frac{2k_b}{\mu m_H} \rho T. \tag{2.10}$$

where m_H is the hydrogen mass; k_B is the Boltzmann constant; $\mu = 1.265$ is the mean ionic weight (relative to a proton and assuming metal abundance of solar values: X (H) $\simeq 70.7\,\%$, Y (He) $\simeq 27.4\,\%$, Z (Li – U) $\simeq 1.9\,\%$; Anders & Grevesse 1989);

2.2.2 Thermal conduction

The thermal conductive flux is defined in Eq. 2.11 and accounts also for heat flux saturation.

$$\mathbf{F}_c = \frac{F_{\rm sat}}{F_{\rm sat} + |F_{\rm class}|}\mathbf{F}_{\rm class}, \tag{2.11}$$

where,

$$\mathbf{F}_{\rm class} = k_{\parallel}\hat{b}(\hat{b}\cdot\nabla T) + k_{\perp}\left[\nabla T - \hat{b}(\hat{b}\cdot\nabla T)\right], \qquad F_{\rm sat} = 5\phi\rho c_{\rm iso}^3. \tag{2.12}$$

The subscripts $\parallel$ and $\perp$ denote the parallel and normal components to the magnetic field, $k_{\parallel} = K_{\parallel}T^{\frac{5}{2}}$ and $k_{\perp} = K_{\perp}\rho^2/(B^2T^{\frac{1}{2}})$ are the thermal conduction coefficients along and across the field, $K_{\parallel} = 9.2\times10^{-7}$ and $K_{\perp} = 5.4\times10^{-16}$ (cgs units), c_{iso} is the isothermal sound speed, $\phi < 1$ is a free parameter that we set to 0.9 (Cowie & Mckee 1977), $\hat{b} = \mathbf{B}/B$ is the unit vector pointing along the magnetic field, and $F_{\rm sat}$ is the maximum flux magnitude in the direction of $\mathbf{F}_c$. Specifically, the classical thermal conductivity $F_{\rm class}$ holds when the mean free path is relatively short. Vice versa, when it becomes comparable to the temperature scale height, the heat flux is no longer equal to the classical values: we describe this effect as heat saturation. In this limit (i.e. for large temperature gradients) the flux is assumed to be independent of ∇T. In particular, the flux magnitude approaches $F_{\rm sat}$. The thermal conduction is treated separately from the advection terms through operator splitting. In particular, we adopted the super-time-stepping technique (Alexiades et al. 1996).

2.2.3 Radiative losses

Atmospheric gravitational stratification on the Sun is modulated by radiative and heat transfer. In the corona, collision de-excitation and photon absorption are negligible, generated photons directly escape. Optically thin radiative cooling is important in the corona with a rate per unit volume:

$$Q_{\rm coro} = n_{\rm H}n_{\rm e}\Lambda(T), \tag{2.13}$$

where $\Lambda(T)$ is the plasma emissivity per unit emission measure (integrated over all wavelengths); $n_{\rm H}$ and $n_{\rm e}$ are the hydrogen and electron number density, respectively (assumed equal). PLUTO code includes optically thin radiative losses in a fractional step formalism, which preserves the second-order time accuracy, since the advection and source steps are at least second-order accurate; the radiative loss values ($\Lambda(T)$) are computed at the temperature of interest using a table lookup/interpolation method. In particular, we considered the radiative losses from optically thin plasma per unit emission measure (shown in the plot of Fig. 2.3), derived from the CHIANTI v. 7.0

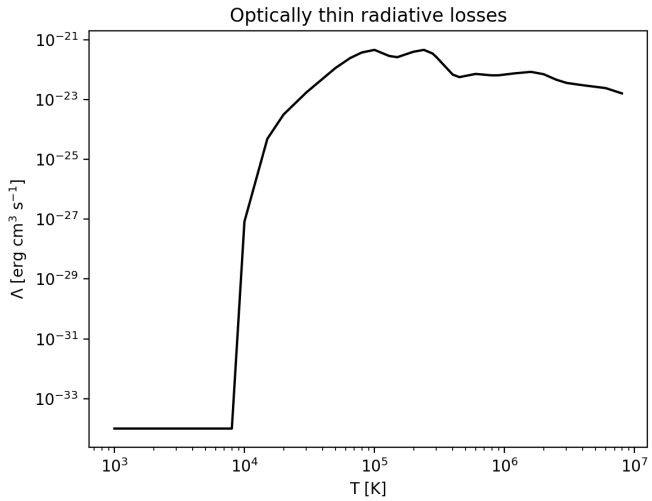

Figure 2.3: Function of optically thin radiative losses per unit emission measure, derived from the CHIANTI v. 7.0 database (Landi & Reale 2013), assuming coronal element abundances (Widing & Feldman 1992).

database (e.g., Landi & Reale 2013) assuming coronal element abundances (Widing & Feldman 1992).

One can also include an accurate description of the radiative losses in the more optically thin chromospheric layers. The chromospheric radiative energy balance is dominated by a small number of strong lines, including neutral hydrogen (H I), singly ionized calcium (Ca II), and singly ionized magnesium (Mg II) (Vernazza et al. 1981). In those lines most of the emitted photons are immediately absorbed in the same transitions as the collisional destruction probability is often very low. Therefore, each photon escapes after large number of scattering events. In particular, the basic cooling process is the electron impact excitation followed by radiative deexcitation. These strong lines are formed out of Local Thermodynamic Equilibrium (LTE) which means that numerical simulations of the dynamic chromosphere need to solve simultaneously the MHD equations, the radiative transfer equations, and the rate equations for all the radiative transitions and energy levels involved. Carlsson & Leenaarts (2012) used detailed radiative transfer calculations from dynamical snapshots to derive simple lookup tables that only use easily obtainable quantities from each single simulation snapshot. They tested these recipes by applying them to several simulation runs, compared the radiative losses from detailed solutions with those from the recipes, and found, in general, good agreement. The net effects of this process on cooling can be approximated as the product of three factors, all dependent on local quantities: $L_{X_m}(T)$, the optically thin radiative loss function for the element X in the ionisation stage m (i.e. the energy loss from generation of photons in absence of absorption); $E_{X_m}(\tau)$, the escape probability

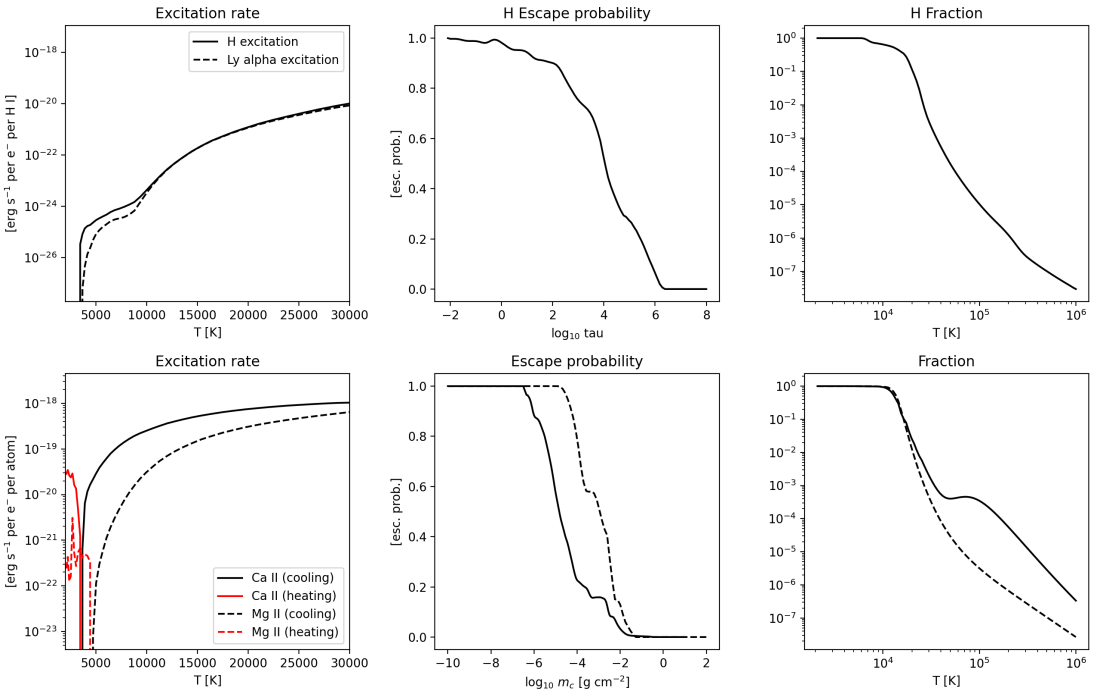

Figure 2.4: Look-up tales for approximated radiative cooling/heating in the chromosphere from lines out of LTE derived by (Carlsson & Leenaarts 2012). First column: Function of total collisional excitation rate (probability density function of the radiative losses, in black, and heating from the same transitions, in red) in the H lines (top, solid), Lyman-continuum (top, dashed), Ca II lines (bottom, solid), and Mg II lines (bottom, dashed), as function of the temperature. Second column: probability density function of the escape probability at Lyman-α line center, as function of the optical depth, and Ca II (bottom, solid) and Mg II (bottom dashed), as function of column mass. Third column: probability density function of the fraction of neutral hydrogen atoms, calcium atoms in the form of Ca II, and magnesium atoms in the form of Mg II, as function of temperature.

(meaning the probability that the photon escapes from the chromosphere); and N_{X_m}/N_X, the ionization fraction for each element. Fig. 2.4 shows the tabulated functions.

$$Q_X = -L_{X_m}(T)\, E_{X_m}(\tau)\, \frac{N_{X_m}}{N_X}(T) A_X \frac{N_H}{\rho} n_e \rho, \tag{2.14}$$

where A_X is the abundance of the element X, and $N_H = 4.407 \times 10^{23}$ is the number of hydrogen (H) particles per gram of solar material.

2.2.4 Heating

Beyond time-dependent heating deriving from conversion of magnetic energy (described in Sec. 2.2.7), other terms are typically included, which allow, for instance, to maintain the system at equilibrium and therefore isolate the effect of impulsive events.

Heating production and transfer can be split into three terms: a background coronal heating H_0; chromospheric heating from incident coronal radiation (as part of the radiative losses in the corona is absorbed by the chromosphere in the continua of helium and neutral hydrogen); heating by photospheric absorption (that is the reverse process of chromospheric cooling, Sec. 2.2.3).

The volumetric heating rate H_0 balances the energy losses to keep the corona static, e.g., at $\sim$ 1 MK. This is taken as a background atmosphere for initial conditions, according to hydrostatic loop models (Serio et al. 1981; Guarrasi et al. 2014). An estimate of this heating rate can be derived from loop scaling laws. According to Rosner-Tucker-Vaiana (RTV) scaling laws ($H_0 \sim 10^{-3} T_6^{3.5} L_9^{-2}$, where T_6 and L_9 are the temperature and the loop half-length in units of 10^6 K and 10^9 cm, respectively, Rosner et al. 1978b, and in Sec. 1.5.2, Eq.s 1.49, 1.50), a volumetric heating rate $H_0 = 4.3 \times 10^{-5}$ erg cm^{-3} s^{-1} is sufficient to keep the corona static with an apex temperature of about 8×10^5 K and a half-length of $L = 2.5 \times 10^9$ cm (25 Mm). This provided a background atmosphere that was adopted as the initial condition, according to the hydrostatic loop models of Serio et al. (1981) and Guarrasi et al. (2014). This heating rate was not scaled similarly for temperatures below the chromospheric cut-off temperature (cf. Johnston et al. 2020)

Part of the emissivity associated to the frequency integrated radiative losses $\eta = Q_{\rm coro}/4\pi$ in the corona ($z_b < z < z_t$) hits the solar surface (z_b) with incoming intensity:

$$I(\mu)_{\rm coro} = \frac{1}{|\mu|} \int_{z_b}^{z_t} \eta(z')\, dz', \tag{2.15}$$

where $\mu = \cos(\theta)$ is the angle of incidence. It is then absorbed mainly after the process of ionisation of neutral helium at the edge of its ground state whose representative opacity χ is:

$$\chi = \alpha N_{He\,I} = \alpha \rho \frac{N_H}{\rho} A_{He} \frac{N_{HeI}}{N_{He}}(T), \tag{2.16}$$

with $\alpha = 2 \times 10^{-18}$ the cross section fo the helium continuum, A_{He} the helium abundance and N_{HeI}/N_{He} the (tabulated) fraction of neutral helium as a function of the temperature. Assuming for each location η or χ be zero the classical, full radiative transfer equations:

$$Q_{\rm chrom} = \chi \int_\Omega I\, d\Omega - \eta, \tag{2.17}$$

$$\frac{dI}{ds} = \eta - \chi I, \tag{2.18}$$

can be simplified and integrated. In particular, chromospheric heating from incident coronal radiation (Eq. 2.17) can be approximated by the product of the opacity by the angle-average intensity (solution of Eq. 2.18):

$$Q_{\text{chrom}} = 2\pi\chi(z)\int_{-1}^{1} I(z,\mu)d\mu, \tag{2.19}$$

where $\tau(z)$ is the optical depth.

Carlsson et al. (2010) argue that the cool parts of the chromosphere can be heated by radiation at the same transitions of chromospheric cooling. In particular they show that full radiative-transfer process of cool pockets chromospheric heating:

$$Q = \int_{0}^{\infty} \chi_\nu(J_\nu - S_\nu)d\nu, \tag{2.20}$$

can be approximated by the same functional form used for cooling (Eq. 2.14, Sec. 2.2.3). In particular, in the two-level atom approximation, the source function S_ν results from the sum of the Planck function B_ν and the mean intensity J_ν:

$$S_\nu = \epsilon B_\nu - (1-\epsilon)J_\nu, \tag{2.21}$$

weighted by the collisional destruction probability $\epsilon \sim f(T)\, n_e$. Assuming the opacity function for the generic ion X_m likewise Eq. 2.16, the resulting heating rate has the following functional form:

$$Q = f(T)\,\alpha_0 \frac{N_{X_{m,j}}}{N_{X_m}} \times \int_{0}^{\infty} \phi_\nu(J_\nu - B_\nu)d\nu \times \frac{N_{X_m}}{N_X}(T) \times A_X \frac{N_H}{\rho} n_e \rho, \tag{2.22}$$

where the first therm of products depends on T and can be interpreted as a (positive) optically thin radiative losses term, while the integral emulates the escape probability $E(\tau)$.

2.2.5 Transition region capturing methods

One of the main difficulties encountered in MHD models is the need to implement a grid that fully resolves the steep gradients in the transition region (Bradshaw & Cargill 2013). Across the transition region, the number density and the temperature change by two orders of magnitude in less than 100 km. Specifically, the temperature scale length $L_T = T/(dT/ds)$ (with s the coordinate along the loop) is generally as small as 1 km, but it can scale down to 100 m or less during strong and impulsive events. Resolving such rapid variation and steep gradients would ordinarily require an extremely high spatial resolution (very small grid cell widths, less than 1 km) and would lead to unfeasible computational times (Bradshaw & Cargill 2013), as it acts, in turn, as a major constraint

on the time step. As pointed out by Bradshaw & Cargill (2013), the main consequence of not properly resolving the transition region when using the standard Spitzer Jr & Härm (1953) conduction description is that the resulting coronal density in response to heating is artificially low (while the TR is, conversely, denser): the heat flux directed downward to the underresolved TR directly jumps over the deeper and denser layers, where the energy is rapidly radiated. Since the emission measure scales with the density squared, underestimating the density leads to inaccurate conclusions when numerical predictions are compared with real observational data.

The Linker–Lionello–Mikić method (Linker et al. 2001; Lionello et al. 2009; Mikić et al. 2013) allows us to artificially broaden the transition region without significantly changing the properties of the loop in the corona, obviating this challenge. In particular, Linker-Lionello–Mikić approach modifies the temperature dependence of the parallel thermal conductivity and radiative emissivity below a fixed temperature threshold, e.g., $T_c = 2.5 \times 10^5$ K:

$$\tilde{k}_{\parallel}(T) = \begin{cases} k_{\mathrm{Spz}}(T) \ , & T > T_c \ , \\ k_{\mathrm{Spz}}(T_c) \ , & T < T_c \ , \end{cases} \tag{2.23}$$

$$\tilde{\Lambda}_{\parallel}(T) = \begin{cases} \Lambda_{\mathrm{Spz}}(T) \ , & T > T_c \ , \\ \Lambda_{\mathrm{Spz}}(T) \left(\frac{T}{T_c}\right)^{5/2} \ , & T < T_c \ . \end{cases} \tag{2.24}$$

In impulsively heated coronal loops, a fixed value of T_c might not be suitable, as the transition region might dramatically change. Johnston & Bradshaw (2019) devised a method that allows the characteristic temperature of the TR, T_c, to change in response to the dynamic coronal loop evolution. As pointed out by Johnston & Bradshaw (2019), modelling the solar Transition Region with the use of an Adaptive Conduction (TRAC) method permits fast and accurate numerical solutions of the field-aligned hydrodynamic equations, capturing the enthalpy exchange between the corona and transition region, when the corona undergoes impulsive heating. The TRAC method eliminates the need for highly resolved numerical grids in the transition region and the commensurate very short time steps that are required for numerical stability. Johnston et al. (2020) and Johnston et al. (2021) presented a highly efficient formulation of the TRAC method for use in multidimensional MHD simulations, thus extending the TRAC method to MHD simulations. It efficiently accounts for the magnetic field evolution, without the need to trace field lines at each time step. The field aligned thermal conduction is modified as

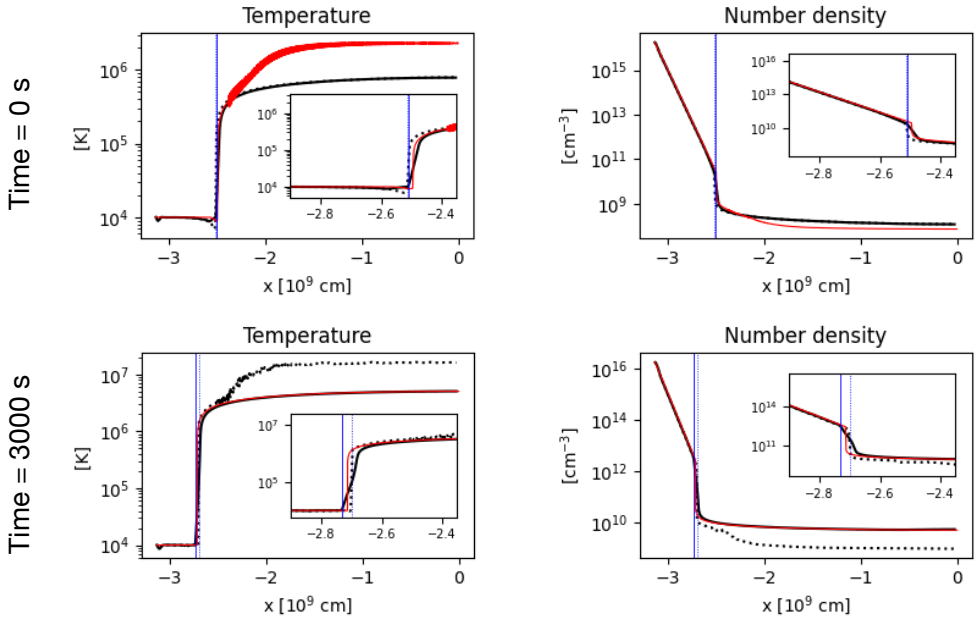

Figure 2.5: 1D simulations of a impulsively heated coronal loop with PLUTO code (Mignone et al. 2007) with high (red line) and low (black, dotted line) spatial resolution. The black, solid line show the results with the modified TRAC thermal conduction/radiative losses. The top row show the initial temperature (left panel) and density (right panel) distributions over the loop length x. The bottom row show the same quantities after 3000 s. HD, Spitzer simulation is numerically unstable at low temperature and (overestimate) underestimate the initial (temperature) density. Inversely, the LD Spitzer simulation (overestimates) underestimates the (temperature) density after the heat pulse. Even at low small resolution TRAC is reproduce reliable, numerically stable results.

follows:

$$\tilde{k}_{\parallel} = \max\left[\frac{5k_B|nv| + \sqrt{25k_B^2(nv)^2 + 4\frac{k_{\mathrm{Spz}}}{T}\left[n^2\Lambda_{\mathrm{Spz}}(T) - Q_{\mathrm{Spz}}(T)\right]}}{\frac{2\delta}{L_R}}, k_{\mathrm{Spz}}\right] \tag{2.25}$$

$$\text{for } L_T < 2L_R/\delta, \tag{2.26}$$

$$\tilde{k}_{\parallel} = \max\left[\frac{\sqrt{4\frac{k_{\mathrm{Spz}}}{T}\left[n^2\Lambda_{\mathrm{Spz}}(T) - Q_{\mathrm{Spz}}(T)\right]}}{\frac{2\delta}{L_R}}, k_{\mathrm{Spz}}\right] \tag{2.27}$$

$$\text{for } L_T > 2L_R/\delta. \tag{2.28}$$

where k_{Spz} is the Spitzer thermal conduction and Λ_{Spz} and Q_{Spz} are the original radiative

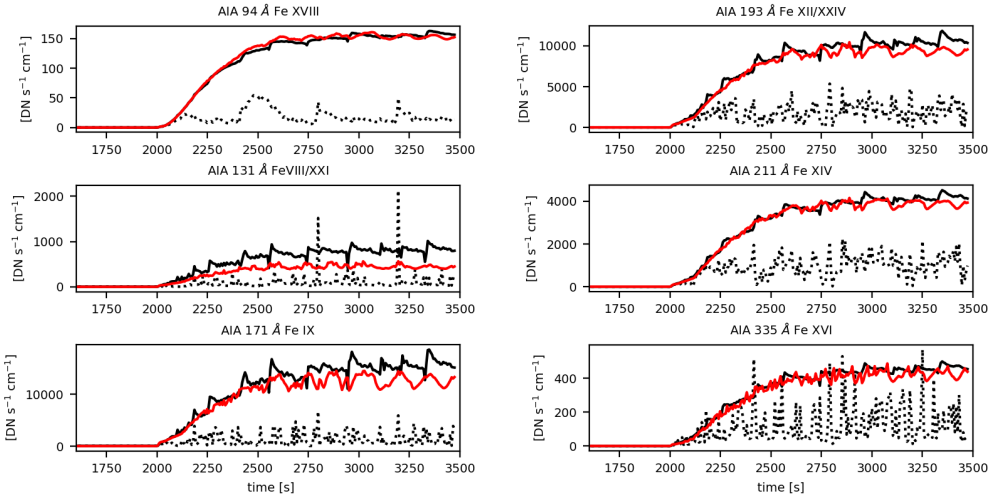

Figure 2.6: SDO/AIA lines light-curves of a impulsively heated coronal loop, forward-modelled from the 1D coronal loop simulation described in figure 2.5. Numerical stability and low spatial resolution affect systemic plasma emission within Spitzer thermal conduction (red and black, dotted lines), as compared with TRAC results (black, solid line).

losses and heating rates, L_R is the pixel resolution and δ is a parameter (set equal to 2). Thermal conduction is thus enhanced in underresolved grid cells of the TR. To broaden the steep temperature and density gradients in the TR, as already proposed by Linker (Linker et al. 2001), Lionello (Lionello et al. 2009), and Mikić (Mikić et al. 2013), heating Q and radiative losses $\Lambda(T)$ rates are modified thus keeping the $\Lambda \times k_{\parallel}$ product constant and, therefore, ensuring that the total radiation and heating, integrated across the TR, remains the same:

$$\Lambda_{\mathrm{Spz}}(T) \rightarrow \Lambda_{\mathrm{Spz}}(T)\frac{k_{\parallel}}{k_{\mathrm{Spz}}} \tag{2.29}$$

$$Q_{\mathrm{Spz}}(T) \rightarrow Q_{\mathrm{Spz}}(T)\frac{k_{\parallel}}{k_{\mathrm{Spz}}} \tag{2.30}$$

2.2.6 Gravity

We assumed that the flux tube is semicircularly curved only in the corona and that it is straight in the chromosphere. Thus, we considered the gravity of a curved loop in the corona:

$$g(z)\,\hat{\mathbf{z}} = g_{\odot}\sin\left(\pi\frac{z}{L}\right)\hat{\mathbf{z}}, \tag{2.31}$$

where $g_\odot = \frac{GM_\odot}{R_\odot^2}$ is constant; G is the gravitational constant; $M_\odot$ is the solar mass; and $R_\odot$ is the solar radius. We note that the gravitational acceleration decreases and becomes zero at the loop apex ($z = 0$) to account for the loop curvature. Below the corona, gravity is uniform and vertical. Gravity orientation is schematically shown in Fig. 2.2.

2.2.7 Anomalous plasma resistivity

The resistivity is critical in constraining rate and amount of magnetic energy converted into heat. Anomalous magnetic resistivity, i.e. much higher than predicted by Spitzer collisional diffusion, is customary in MHD simulations of magnetic reconnection (e.g., Ugai 1992; Yokoyama & Shibata 1994).

Rosner et al. (1978a) showed that the observed high temperature and inhomogeneous structure of the solar corona can be explained by in situ heating via anomalous current dissipation. Duijveman et al. (1981), through the use of a marginal stability analysis, investigate the anomalous character of the current dissipation as caused by ion-cyclotron and/or ion-acoustic instabilities. They show that ion acoustic modes become unstable only when the electron temperature exceeds three times the ion temperature. According to Benford (1983), the electrostatic ion cyclotron instability is the dominant mechanism heating coronal loops, while ion acoustic modes never become unstable ($T_e/T_i < 3$). Heating is ultimately determined by complex interactions of boundary effects and turbulent resistivity.

In the simplified MHD framework, anomalous resistivity is switched on only when the magnitude of the current exceeds a critical value as in the following:

$$\eta = \begin{cases} \eta_0 & |J| \geq J_{cr} \\ 0 & |J| < J_c, \end{cases} \tag{2.32}$$

Kliem et al. (2000) showed how this spatially varying critical resistivity could be derived by matching the local electron drift speed with the local ion sound speed. They also verified that the system dynamics weekly depends on the particular choice of the parameters set for the resistivity. For example Gordovskyy et al. (2014) set a variable resistivity whose critical current density is determined independently in each cell, locally in space and time, by the electron-ion drift velocity $v_D = j/(e\,n)$. In particular, an "anomalous" value for η is set where and when v_D exceed the critical velocity, $v_{cr} = \sqrt{(\frac{p}{\rho})}$, equal to the sound speed; otherwise it is assumed to vanish. The expression for critical current density is therefore:

$$j_{cr} = e\,n\sqrt{\gamma\frac{p}{\rho}}, \tag{2.33}$$

that can be written in normalized units as:

$$\frac{j_{cr}}{j_0} = \sqrt{\frac{\gamma}{2}}\,\beta\,\frac{L_0}{R_p}\,\frac{\rho}{\rho_0} \tag{2.34}$$

where $\beta = \frac{2nk_BT}{B_0^2/8\pi}$ is the plasma beta, and $R_p = \frac{m_p}{eB_0}\sqrt{\gamma\frac{p}{\rho}}$ is the Larmor radius of the thermal proton. The typical thickness of reconnecting current sheets approximates the Larmor radius of the proton ($\sim$ 1 m in the corona). Grid pixel resolution (δx) in (3D)MHD numerical experiments of the solar corona is typically orders of magnitude higher, meaning that the real current densities are underestimated by the same factor $\delta x/R_p$. To overcome this problem, the correcting factor of $\delta x/R_p$ is introduced in Eq. 2.34. This extra factor accounts for finite spatial resolution and depends on local quantities. In particular, since the Larmor proton radius is proportional to $\sqrt{T}/B$, the resulting current density will depend on the local plasma quantities in the following way (Bareford & Hood 2015):

$$\frac{j_{cr}}{j_0} = \sqrt{\frac{\gamma}{2}}\,\beta\,\frac{L_0}{\delta x}\frac{\rho}{\rho_0} \propto \frac{1}{\delta x}\frac{\rho T}{B} \tag{2.35}$$

Hood et al. (2009) assume that an anomalous plasma resistivity with fixed critical current density which brings the critical current just above the current densities before the kink instability. As far as the value for the anomalous resistivity is concerned, it is more difficult to determine a physically justified value. For example, Reale et al. (2016) also sets a fixed threshold value for the switch on of the local magnetic dissipation. They assume $\eta_0 = 10^{14}$ cm^2 s^{-1}, $J_{cr} = 75$ Fr cm^{-3} s^{-1}. With this assumption, the minimum heating rate above switch-on is $H = \eta_0(4\pi|J_{cr}|/c)^2 \sim 0.1$ erg cm^{-3} s^{-1}, which is the equilibrium heating of a loop with a maximum temperature of $\sim$ 6 MK and half length 2.5×10^9 cm, according to the loop scaling laws (Rosner et al. 1978b).

3

Asymmetric twisting of coronal loops

This chapter is structured based on the paper titled "Asymmetric twisting of coronal loops" (Cozzo et al. 2023a).

The bright solar corona entirely consists of closed magnetic loops rooted in the photosphere. Photospheric motions are important drivers of magnetic stressing, which eventually leads to energy release into heat. These motions are chaotic and obviously different from one footpoint to the other, and in fact there is strong evidence that loops are finely stranded. One may also expect strong transient variations along the field lines, but at glance coronal loops ever appear more or less uniformly bright from one footpoint to the other. In this work we aim to understand how much coronal loops can preserve their own symmetry against asymmetric boundary motions that are expected to occur at loop footpoints. We investigate this issue by time-dependent 2.5D MHD modelling of a coronal loop including its rooting and beta-variation in the photosphere. We assume that the magnetic flux tube is stressed by footpoint rotation but also that the rotation has a different pattern from one footpoint to the other. In this way we force strong asymmetries, because we expect independent evolution along different magnetic strands. We found that until the Alfvén crossing-travel time relative to the entire loop length is much lower than the twisting period, the loop's evolution depends only on the relative velocity between the boundaries, and the symmetry is efficiently preserved. We conclude that the very high Alfvén velocities that characterise the coronal environment can explain why coronal loops are capable to maintain a very high degree of symmetry even when they are subjected to asymmetric photospheric motions for a long time.

3.1 Introduction

Coronal loops are relatively dense and bright structures supported by an arch-like magnetic tube. They fill the magnetic skeleton of the lower solar corona with tenuous ($n \sim 10^8$ cm^{-3}) and hot ($T \sim 10^6$ K) plasma. They are acknowledged as "building blocks" of this layer where the emergent magnetic field is typically organized in a network of topologically closed structures (Reale 2014). As coronal loops commonly exhibit strong magnetic fields of the order of 10 G (Yang et al. 2020; Long et al. 2017) it is thought the closed field lines confine the plasma, and make it move and transport energy mostly along them (Reale 2014). Coronal loops are anchored to the underlying chromosphere and, a little further down, to the photospheric layer where the plasma beta parameter exceeds one by few orders of magnitude. For this reason, the loop footpoints are dragged by photospheric plasma motions which in turns might be highly structured. The typical strength of the photospheric magnetic field in active regions is found to be few hundreds of G (Ishikawa et al. 2021). By ascending toward the corona the pressure decreases, the magnetic field lines progressively expand and the field intensity decreases keeping the magnetic flux conserved. The greater expansion rate is expected across the thin transition region dividing the cromosphere to the upperlying corona (Gabriel 1976b).

As coronal loops built up in the lower corona, they go through different phases of twisting, heating and brightening, ultimately cooling back to a tenuous, $\sim$ 1 MK hot atmosphere. Observations and numerical experiments provided evidence that coronal loops evolution is deeply influenced by the photospheric motion. For instance, footpoints rotation may lead the magnetic structure to twist and gain magnetic energy. The transverse-velocity pattern of the photospheric plasma can show an high degree of complexity. Indeed, each foot-point may undergo to an independent evolution. While magnetic energy is stored, the flux tube could subjected to potentially strong stresses that may lead to fast magnetohydrodynamic instabilities (as the kink instability, Hood et al. 2009) or to a long lasting Ohmic heating. According to the numerical experiment described in Reale et al. (2016), in the last case, the gained energy is likely to be released by magnetic dissipation when a current density threshold is exceeded. In particular, when Ohmic dissipation starts, the highly efficient thermal conduction spreads the heat along the whole magnetic tube. The heat pulse reaches also the transition region and drains material from the underling chromospheric layer leading to a sudden enhancement of the coronal loop's density. The loop brightening is associated to the progressive densification of the flux tube which in turns leads the differential emission measure ($DEM(T) = \int n^2(T)dr$) of the loop's optically-thin material to increase. Axisymmetric 2D and 3D MHD simulations (Guarrasi et al. 2014; Reale et al. 2016) have investigated the behaviour of such systems by including gravity as in curved loop, thermal conduction, radiative losses from optically thin plasma, Ohmic heating by magnetic dissipation and

magnetic field expansion across a dense chromospheric layer and a thin transition region. In Reale et al. (2016) the twisting of the magnetic field lines is provided by photospheric motion at the boundaries of the domain. For each foot-point, such a photospheric motion, despite non-uniform at small scales, is assumed to be constrained by the same azimuthal velocity's macroscopic envelope. For this reason the coronal loop is always found to be symmetric with respect to the plane transverse to the tube at its apex (mirror-symmetry).

In this chapter we assess how much the degree of twisting along the tube depends on the specific degree of coherence of the foot-points rotation. Moreover, we investigated how coronal loop's properties could be influenced by asymmetries in the photospheric boundary conditions. In general, we found that coronal loops tend to preserve an high degree of symmetry when subjected to different foot-points velocities as well as by different cross-sections in the rotation patterns. This is deeply related to the high Alfvén speeds that characterise the coronal environment. However, if the coronal density is enhanced by a long-lasting chromospheric evaporation the Alfvén speed may be reduced enough to not ensure fast signal transmission and magnetic field relaxation against asymmetric photospheric motions. We concluded that only long lasting footpoints rotation can lead initially mirror-symmetric coronal loops to evolve into asymmetric configurations.

3.2 Methods

We considered a single, axi-symmetric coronal loop. The loop is modelled as a straightened magnetic flux tube hooked to two chromospheric layers at the opposite sides of the box. The length of the tube is taken much longer that its radius. For this reason, the effects of the curvature on its structure are negligible. Moreover, the two (upper and lower) chromospheric layers can be assumed as independent regions. The domain is a 2.5D box while the geometry of the problem is cylindrical (r, ϕ, z).

The MHD equations (Eq.s 2.2 - 2.5) are solved in the non-dimensional conservative form (Mignone et al. 2007). We use the ideal gas law as equation of state (Eq. 2.10), assuming $\mu = 1.265$ as the mean atomic mass (from typical solar metal abundances, Anders & Grevesse 1989) and assume negligible viscosity. Thermal conductive flux is treated as in Eq.s 2.11, 2.12 with thermal conduction coefficients $K_{\parallel} = 9.2 \times 10^{-7}$ and $K_{\perp} = 5.4 \times 10^{-16}$, in cgs units, and $\phi = 0.9$ (Cowie & Mckee 1977). We account for optically thin radiative losses (see Sec. 2.2.3 and Eq. 2.13) and uniform heating (Sec. 2.2.4):

$$Q(T) = -\Lambda(T) n_e n_H + H_0 \tag{3.1}$$

where $\Lambda(T)$ are the optically thin radiative losses per unit emission measure obtained from the CHIANTI v. 7.0 database (Dere et al. 1997; Reale & Landi 2012; Landi & Reale 2013, e.g.,) assuming typical coronal element abundances (Widing & Feldman

1992). $H_0 = 4.3 \times 10^{-5}$ erg cm $^{-3}$ s^{-1} is a uniform heating rate per unit volume which maintains the corona with a temperature of about 8×10^5 K (Serio et al. 1981; Rosner et al. 1978b; Reale 2014; Guarrasi et al. 2014). Gravity in the corona is treated by taking into account only the component along the (untwisted) flux tube (see Eq. 2.31). By considering an anomalous plasma resistivity, Ohmic dissipation activates only when the current density magnitude exceeds a certain threshold J_{cr} (Eq. 2.32, Hood et al. 2009). Here we assume $\eta_0 = 10^{14}$ cm, and $J_{cr} = 75$ Fr cm^{-3} s^{-1}.

The calculations are performed using the PLUTO code (Mignone et al. 2007, 2012), a modular, Godunov-type code for astrophysical plasmas (see also Reale et al. 2016; Guarrasi et al. 2014, and Sec 2.1 for more details about the numerical setup).

3.2.1 The loop setup

We addressed a typical active region loop of length 5×10^9 cm and initial temperature of $\sim 10^6$ K. The loop's foot-points are anchored at the upper and lower boundaries of the domain through two independent chromospheric layers separated from the coronal environment by a steep transition region. Across this thin layer, temperatures suddenly increase from 10^4 K, typical of the upper cromosphere, to few millions of K in the corona. The magnetic field expands across the chromospheric layer as the plasma beta parameter decreases up to very small values in the corona. Such initial conditions are provided following the same procedure adopted in Guarrasi et al. (2014). Initially, the chromosphere and the corona are treated as two isothermal layers at temperatures of 10^4 K and 8×10^5 K respectively. We assumed an initial vertical, non-uniform magnetic field. It is more intense near the axis, $B(r = 0) \sim 500G$, and it decreases radially down to a background value of 10 G. As we let this configuration relax, the magnetic field expands in the corona, until a horizontal total pressure balance sets in. In contrast, below the transitions region the magnetic field lines remain fundamentally unperturbed as they are rooted in the dense high-β chromospheric plasma. Finally, in the longitudinal direction density and temperature vary until thermal conduction, radiative losses and a background heating balance and the loop relaxes to the steady state configuration described so far. In this new configuration, the magnetic field is more intense in the deep chromosphere where it reaches 300 G. It then decreases in the corona down to 12 G at the loop apex.

The computational domain is 2.5 D cylindrical. The domain range is $-z_M < z < z_M$ (with $z_M = 3.1 \times 10^9$ cm) in the vertical direction and $r_0 \leq r \leq r_M$ (where $r_0 = 7 \times 10^7$ cm and $r_M = 3.5 \times 10^9$ cm) in the radial direction. To properly account for the transition region, high spatial resolution is needed (Bradshaw & Cargill 2013). For this reason, the cell size in the corona decreases from $|z| \sim 2.4 \times 10^9$ cm to $dr \sim dz \sim 3 \times 10^6$ cm in the transition region. The adopted piece-ways uniform and stretched grid is sketched in figure 3.1. We assume reflective boundary conditions (B.Cs.) near the symmetry axis (i.e. at $r = r_0$) and at $r = r_M$; periodic B.Cs. at the azimuthal boundaries; and

equatorial-symmetric B.Cs. at $z = \pm z_M$.

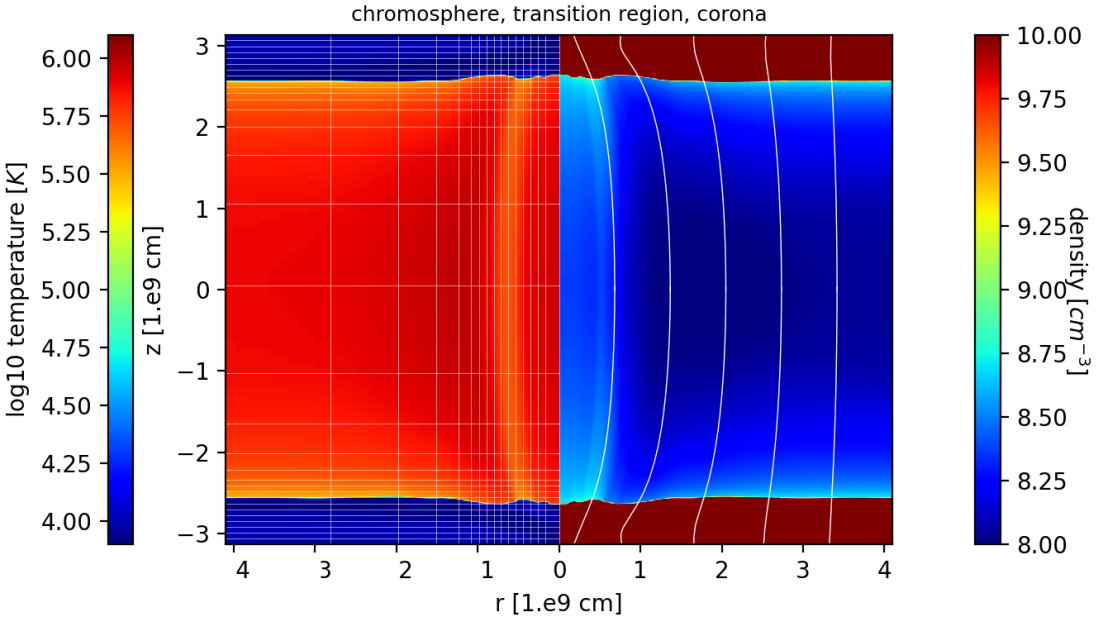

Figure 3.1: Maps of initial temperature (left) and density (right) distributions. For instance, cold colours on the left are representative of the chromospheric layer where temperatures do not exceed 10^4 K. Shades on red instead color the nearby 1 MK hot coronal environment. Chromosphere and corona are separated by a steep transition region where high gradients of temperature and density occurs. On the left, white straight lines highlight the structure of non-uniform grid. Higher resolution is expected across the chromospheric layer and the transition region as well as in the highest magnetised regions of the domain (i.e. near the loop's axis). On the right, solid, white lines trace the shape of the magnetic field. Magnetic field expansion (tapering) is clearly visible at the top and bottom sides of the flux tube.

3.2.2 Loop Twisting

We tested the evolution of a coronal loop under the effects of a footpoint rotation. Rotation at the loop's foot points induces a twisting of the magnetic field lines. As flux tube torsion proceeds the current density is amplified and eventually exceed a critical value triggering magnetic diffusion and heating via Ohmic dissipation. Two rotation profiles have been taken into account. The first one is that of a rigid body around the central axis, i.e., the angular speed is constant in an inner circle and then decreases

linearly in an outer annulus (Reale et al. 2016):

$$v_\phi = \omega(r) r, \tag{3.2}$$

$$\omega = v_{max}/R_{max} \times \begin{cases} 1 & r < R_{max} \\ (2R_{max} - r)/R_{max} & R_{max} < r < 2R_{max} \\ 0 & r > 2R_{max}, \end{cases} \tag{3.3}$$

where v_{max} is the maximum tangential velocity and R_{max} provides a size of the region subjected by photospheric rotation. The second one is a smoother profile (Reid et al. 2018) where the tangential velocity increases almost linearly around $r \sim 0$ cm and becomes zero for $r > 2R_{max}$. The velocity decrease rapidly toward zero at $r \sim R_{max}$ but the profile is differentiable everywhere.

$$v_\phi = \begin{cases} 2v_{max} \frac{r}{a} (1 - \frac{r^2}{a^2})^3 & r < a \\ 0 & r \geq a, \end{cases} \tag{3.4}$$

where $a = 2R_{max}$.

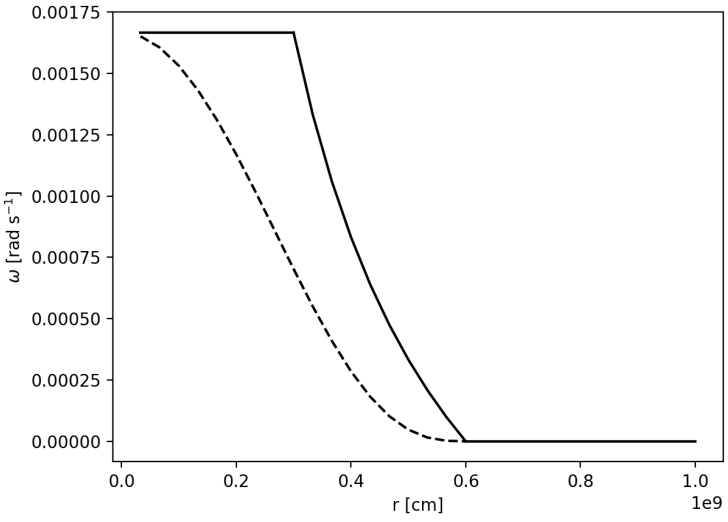

Figure 3.2: The solid and dashed, black lines represent the profiles of two angular velocities implemented at the lower and upper boundaries of the domain. In the first case (solid line), the photosphere initially ($r \leq R_{max}$) rotates as a solid body. Then (for $r > R_{max}$) it linearly decays to zero. There are two discontinuities in the derivative of $\omega(r)$ at $r = R_{max}$ and at $r = 0$. For $r > 2R_{max}$ there is no rotation. In the second case (dashed line) the angular velocity profile is smoother: it is everywhere differentiable. Again, the rotation kindly stops at $r > 2R_{max}$.

Five different configurations of v_{max} and R_{max} where explored. In case a. and b. both foot-points are driven by a coherent photospheric rotation at the same speed and same radius. In case c. only one foot-point rotates under the influence of the photospheric boundary conditions. In case d. different dimensions of the rotation pattern at the loop basis are considered. In the last case, the loop initially evolves symmetrically as in case a. and b. and, after a while (t_0 = 1400 s), one foot-point progressively slows down and stops (after δ = 600 s) while the other one accelerates up to 10 km/s as in configuration c. The time t_0 was chosen so that the loop is already filled by chromospheric plasma when the symmetry at foot-points is broken.

Table 3.1: The table shows the five cases explored to study the loop's behaviour under different photospheric drivers. Each case differs for the maximum speed of the rotation (v_{max}) or its maximum extent (r_{max}). Moreover two different profiles are considered: Reale et al. (2016) and Reale et al. (2016). Each foot point undergoes to an independent evolution. They are labelled as "up" and "down".

Simulation	down		up		
	v_{max} [km/s]	R_{max} [km]	v_{max} [km/s]	R_{max} [km]	Velocity profile
a.	5	3000	5	3000	Reale et al. (2016)
b.	5	3000	5	3000	Reale et al. (2016)
c.	10	3000	0	*	Reale et al. (2016)
d.	5	6000	5	1500	Reale et al. (2016)
e. (for $t < t_0$)	5	3000	5	3000	Reale et al. (2016)
e. (for $t > t_0 + \delta$)	10	3000	0	*	Reale et al. (2016)

* The radius is not defined because no rotation occurs.

The choice of a photospheric rotation with a maximum tangential velocity of $10\,\mathrm{km\,s^{-1}}$ is a compromise to have an effective heating in reasonable computational times still maintaining a velocity in the order of realistic ones, for instance, comparable with typical photospheric swirls and chromospheric vortexes (e.g., Díaz-Castillo et al. 2024; Moll et al. 2011). In this work we are exclusively interested in the coronal evolution of the flux tube, therefore we make simplifying assumptions regarding the photosphere and the chromosphere and we do not study their details.

3.3 Results

Our model presents a coronal loop that is straightened into a vertical magnetic flux tube hooked to two independent chromospheric layers. The magnetic field rapidly expands through the chromosphere while the loop body in the corona has approximately constant cross section. Figure 3.3 shows the initial condition of the simulation. It shows the steep

gradient of the density (ρ) and temperature (T) across the transition region, and the strong change of plasma β by a few orders of magnitude across the domain. The vertical component of the current density (J_z) is initially zero because the loop is untwisted. For completeness, the figure shows the null maps of angular velocity (v_ϕ). Finally, in order to track the plasma upward motions from the chromosphere, we also include the map of a passively-advected tracer of the chromospheric mass, initially identified where $T < 10^4$ K.

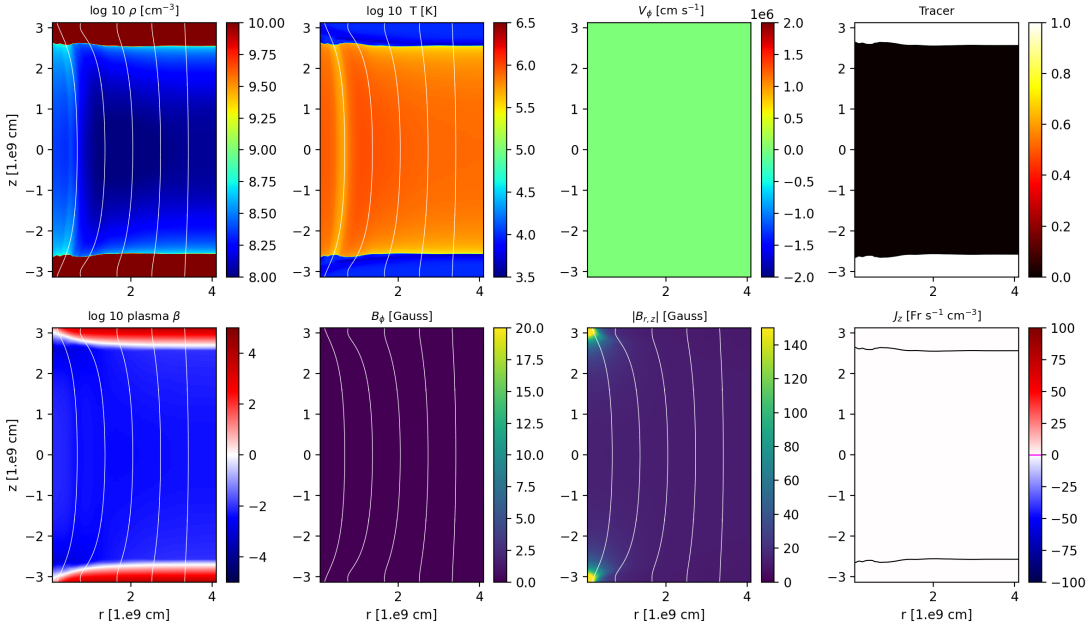

Figure 3.3: First row: maps of the initial plasma density, temperature, azimuthal velocity, and tracer. Second row: maps of the initial plasma beta, azimuthal magnetic field, magnetic field magnitude on the r-z plane, vertical component of the current density. Field lines are marked as white solid lines. Initial conditions are the same for all the simulations discussed below. Black lines in the last panel enclose the region of the domain where $T > 10^4$ K (i.e. transition region and corona).

3.3.1 Mirror-symmetric driver

In simulations a. and b. (see table 3.1) the rotation at both loop footpoints is driven by same but opposite photospheric motions. Figure 3.4 and 3.5 show the maps at $t = 5000$ s for simulations a. and b., respectively.

At the very beginning the rotation propels material just above the photospheric boundary. As the magnetic field is frozen into the plasma, this rotation generates an azimuthal

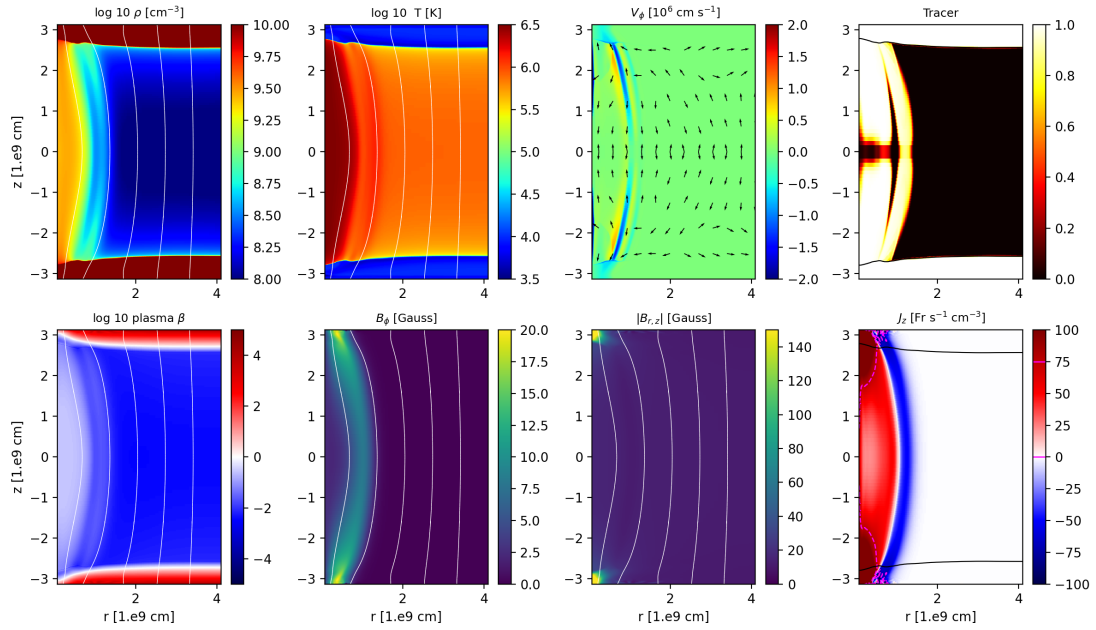

Figure 3.4: Same as Fig. 3.3 for Simulation a. and after 5000 s. Black arrows in the third panel show the orientation of the plasma velocity along the r-z plane. The dashed line in magenta in the last panel encloses the region of the domain where the current density exceeds the current threshold of 75 Fr cm^{-3} s^{-1}.

component of the magnetic field which propagates as perturbation upward to the corona. The same happens to azimuthal component of the velocity, so that the loop is progressively twisted throughout. Figure 3.6 shows the sampled velocity of such magnetic perturbation traveling along the loop compared to the theoretical Alfvén velocity, and the map of the Alfvén speed at t = 0 s. Of course, the propagation speed of the signal is slow in the dense chromosphere and greatly speeds up in the much more tenuous corona. The signal-traveling velocity agrees with what expected from the theoretical value $v_{\rm Alf} = \frac{B}{\sqrt{4\pi\rho}}$.

The vertical component of current density also grows with the twisting. However, its sign reverses at larger radial distance from the centre (i.e. outer ring) where the the radial derivative of the tangential velocity switches its sign (see eqs. 3.3, 3.4). Since outside of the loop no twisted magnetic field is present, according to the Ampere's law the total current flowing across the loop must be zero. Thus an inversion current is present in the outer shells of the loop as shown in figures 4 and 5. In the corona, the z-component of the current density dominates over the other ones. Current perpendicular to z is more concentrated below the transition region where the loop expansion is stronger. Current

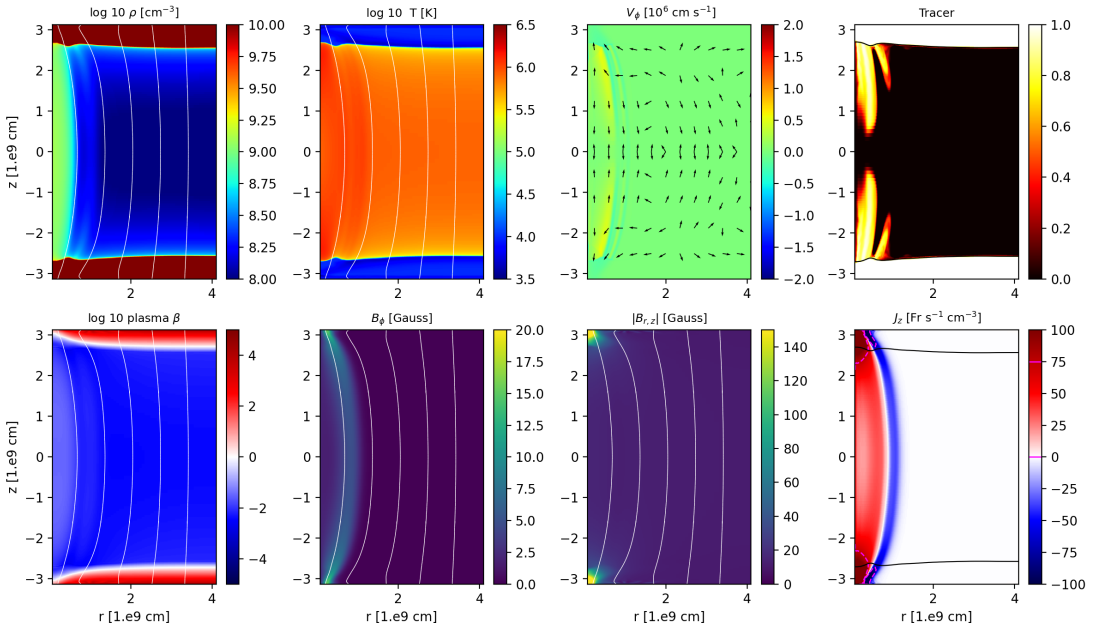

Figure 3.5: Same as Fig. 3.4 for Simulation b.

flows inside and outside of the domain across the upper and lower boundaries as a consequence of the boundary conditions. In the sheared shell between twisting and no twisting, there is some magnetic compression, which makes some dense plasma move upwards from the chromosphere. Indeed the chromosphere is more compressed by the twisting than the corona because the magnetic field is stronger there. As a consequence of that, the chromospheric plasma is forced to rise above in the corona. By looking at the tracers in Fig. 3.4 and Fig. 3.5 we might conclude that the smoother the shearing layer, the slower is this plasma transfer (Fig.3.2). Indeed, the compression experienced by the tube is proportional to the gradient of the tension provided by the twisted magnetic field lines. There is stronger compression when the radial profile of the angular velocity is steeper. A stronger compression in turn drives more upflowing plasma. For this reason, the harsher the velocity profile the more intense will be the ascended material across the outer boundary of the magnetic tube.

The current density first increases in the shell boundary layer between the twisted and untwisted region (i.e., at $r = 6000$ Km, Reale et al. (2016)). It takes some minutes to grow above the critical value in the corona and trigger the heating by Ohmic dissipation. In particular, after 800 s it exceeds the threshold of 75 Fr cm^{-3} s^{-1}, and the enhanced resistivity allows magnetic dissipation to start in the corona and the gained magnetic energy is partially released as heating. The Ohmic dissipation remains mostly localised just above the chromosphere where the current density magnitude is higher, because of

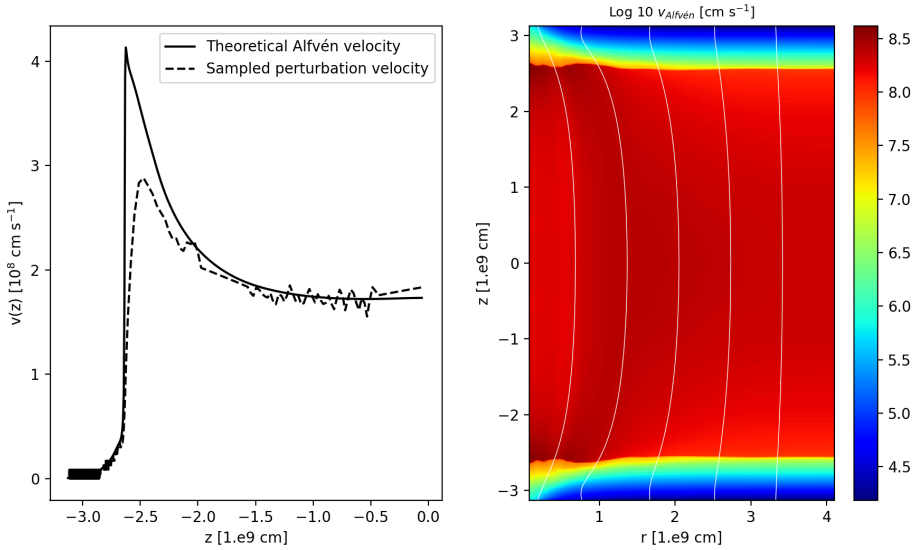

Figure 3.6: Left: theoretical Alfvén velocity (solid line) progressing upwards along the central z-axis, as compared to the velocity of the signal propagating at a certain height and measured in the simulation (dashed line). Right: map of the Alfvén velocity at $t = 0$ s. The logarithmic colour scale emphasizes the deep difference in magnitude between chromosphere and corona.

the tapering of the magnetic field. The density magnitude of the inversion current is close to the direct current in the corona, but mostly below the dissipation threshold and therefore not driving significant plasma evaporation. Because of the efficient thermal conduction the whole magnetic tube almost uniformly heats up to about 4 MK after $t = 1500$ s in the central part of the tube, much less in the outer shell. The heating drives an overpressure which makes chromospheric plasma expand upwards to fill the tenuous coronal part of the tube (chromospheric evaporation). After $t = 2400$ s the coronal loop is filled by a dense and hot plasma and the initial, tenuous coronal plasma is compressed near the loop apex. The plasma is confined in the inner cylindrical region and in a thin and more tenuous shell. In particular, inside the tube, density increases up to $\sim 10^9$ cm^{-3} while in the outer shell only to 3×10^8 cm^{-3}. After $t = 2400$ s evaporation has slowed down and the flow motion is significantly smaller. The evaporating chromospheric plasma moves upward following the orientation of the twisted magnetic field lines as shown by the reversed-signed v_ϕ component inside the flux tube and just above the chromosphere. The coronal part of the loop is not completely empty initially. For this reason, the chromospheric plasma flowing upwards cannot penetrate in the preexisting

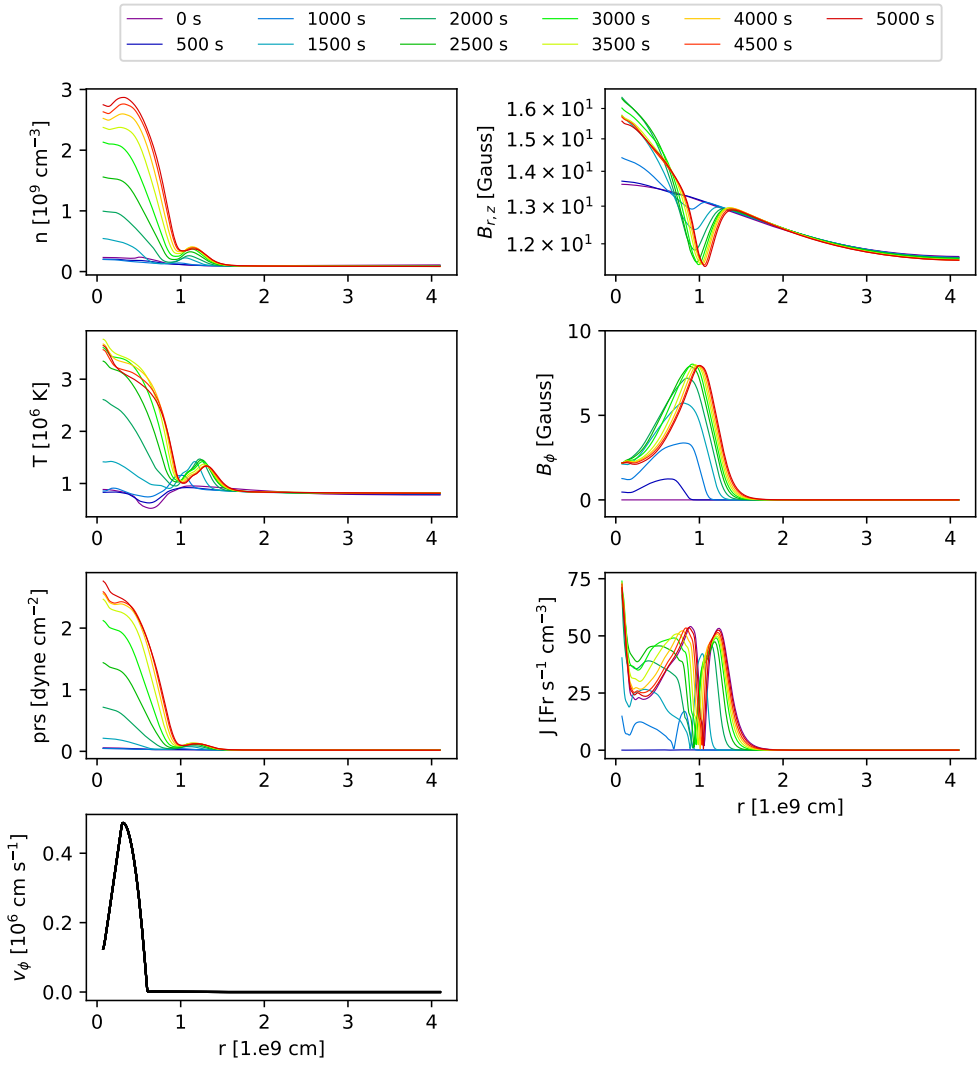

Figure 3.7: Simulation a. First column: radial profiles of density, temperature, pressure at $z = 0$ (loop apex) and velocity at photospheric level. Second column: total magnetic field intensity, azimuthal component of the magnetic field and modulus of the current density. The profiles are spaced by about 200 s and the color coding marks the time progression from purple (0 s) to red (5000 s).

coronal plasma, and remains behind it, thus filling the loop only partially and not reaching the loop apex.

Fig. 3.7 shows the radial profiles of the density, temperature, pressure, magnetic field

intensity, azimuthal component of the magnetic field, and current density at the top of the loop at different times. In the last panel of figure 3.7 the velocity at the photospheric level is shown. The profiles are consistent with those in Reale et al. (2016). In particular, density, temperature and pressure peak at the central axis. Then they decay to ambient values outside the tube cross-section. The secondary peak at $r \simeq 1.2 \times 10^9$ cm is localised in the outer shell which is heated mostly by compression. Each quantity is only slightly perturbed by the twisting and it is left almost unchanged until Ohmic heating is switched on. As shown in figures 3.7, 3.8, and 3.9, the azimuthal component of the magnetic field grows almost linearly in time as expected from ideal induction equation. Indeed, for a straight, cylindrical tube $\frac{\partial B_\phi}{\partial t} = \frac{\partial (v_\phi B_z)}{\partial z}$. Then, taking $v_\phi \sim \omega(r) r \frac{z}{L}$ (we assume the absolute value of the angular velocity decreases almost linearly with height and becomes zero at the loop apex) and B_z uniform along the whole tube's length $2L$, we find: $B_\phi = \frac{\omega(r) r B_z}{L} t$. During the last stages of the simulation, Ohmic diffusion efficiently damps the rise of B_ϕ which settles to a steady value. The radial profile of the azimuthal magnetic field fits, as expected, the shape of the implemented photospheric rotation. The rise of B_ϕ influences the radial profile of the vertical magnetic field since it carries a stronger and stronger magnetic tension that compresses the inner twisted flux tube. For this reason, the vertical component of the magnetic field slightly rises up in a region closed to the loop's axis. On the other hand, since the magnetic field is line tied to the photosphere, magnetic flux is globally kept constant also in the corona. So, B_z must drop just outside the region where magnetic twisting is performed to preserve the magnetic flux. The behaviour of B_z found is these simulations fits the numerical solutions of the Grand-Shafranov equation retrieved in Browning & Hood (1989).

Fig. 3.8 shows the density, temperature, pressure, magnetic field intensity, azimuthal component of the magnetic field, and current density along the vertical direction and near the symmetry axis $r = 0$ at different times. Because of the cylindrical symmetry of the problem (and the solenoidal condition $\nabla \cdot \mathbf{B} = 0$), the magnetic field lines at $r = 0$ are expected to be aligned with the axis. For this reason we probed the physical properties of the plasma along a field line. Temperature, density and pressure do not change until heating starts at $t \simeq 800s$. Then, the temperature suddenly rises and overcomes 3 MK at the end of the simulation. Pressure and density rise as well at a rate that can be traced looking at the evolution of the vertical velocity. In particular, the chromospheric plasma is accelerated in a very sharp region (the transition region) where the density abruptly drops with height. In few 10^7 cm, the velocity reaches values of several 10^6 cm/s. Its maximum is placed just above the transition region. While climbing the thread, the material decelerates as it compresses the over lying plasma. At the loop apex the velocity is zero, as expected from symmetry arguments. B_z and B_r magnetic field components do not seem to change by the twisting (at list, near the loop axis). B_ϕ and consequently the magnitude of the current density grows fast at the beginning of the simulation as photospheric rotation twists the flux tube. Finally, at the end of

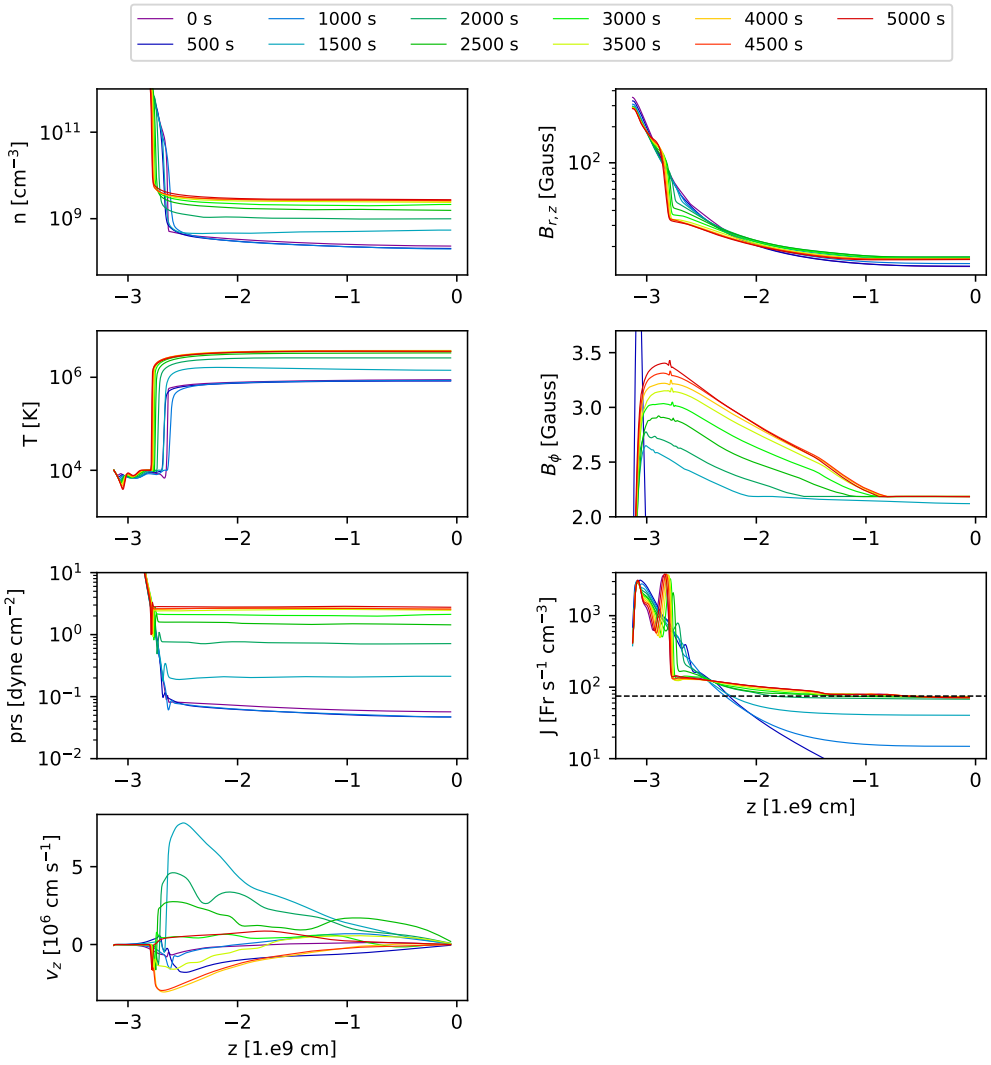

Figure 3.8: Simulation a. First column: vertical profiles of density, temperature, pressure and velocity at $r \simeq 0$ (near the loop axis). Second column: vertical profiles of the total magnetic field intensity, azimuthal component of the magnetic field and modulus of the current density at $r \simeq 0$ (near the loop axis). The profiles are spaced by 500 s and the color coding marks the time progression from purple (0 s) to red (5000 s). In the third panel on the right, the critical current density is marked by a horizontal dashed line.

the simulation, temperature, density and pressure, as well as, the ϕ component of the magnetic field and current density magnitude settle to a stable value, as the magnetic

diffusion balances the growing field stresses. Once again, the results found here are consistent with those shown in previous works (Guarrasi et al. 2014; Reale et al. 2016) as well as with 1D hydrodynamics simulations (Warren et al. 2002).

Fig. 3.9 shows the trend of the maximum (black line) and averaged (red line) temperature, the maximum values of the vertical velocity, the maximum current density magnitude, the maximum and averaged heating rate, and the temporal behaviour of the azimuthal component of the magnetic field in four different locations inside the domain. Space-averaging has been performed inside a cylinder of radius 10^9 cm, entirely contained within the corona ($T > 10^4$ K). The maximum temperature as well the averaged one (top left panel) are initially steady at about 1 MK. The maximum temperature starts to increase at t=800 s and at the end of the simulation it overcomes 3 MK, typical of an active region loop. The average temperature increases significantly only after 1300 s and it reaches $\simeq$ 2.5 MK after 3000 s. Loop heating is provided by the electric current density as soon as it exceeds the threshold of 75 Fr cm^{-3} s^{-1} after 800 s. The maximum vertical speed shows that the plasma evaporation also starts as soon as the maximum current magnitude exceeds the threshold for dissipation in the corona ($t \sim 800s$). It peaks at $t = 1500$ s ($v_{\rm max} \simeq 8 \times 10^6$ cm s^{-1}), approximately when the first impulsive evaporation front reaches the top of the loop, and then settles at $\sim 6 \times 10^6$ cm/s indicating a more gentle evaporation. These values are subsonic and usual for evaporation, driven by a continuous sequence of heat pulses (e.g., **?**). The maximum heating rate is shown in the upper panel on the right. The average heating rate is instead plotted in the middle panel on the right column. It is obtained by averaging only among the effectively heated cells i.e. where $j \geq j_{\rm cr}$. Both quantities keep growing as the squared value of the maximum (averaged) current density. In the last panel of Figure 3.9 the azimuthal magnetic field component B_ϕ is shown at two different heights (along the loop apex and just above the transition region) and at two different radial distances from the central loop axis (close to the axis and 3000 km apart). The twisting initially makes B_ϕ grow linearly at all positions. After $t = 1200$ s B_ϕ stops growing close to the loop's axis and to the chromosphere because of magnetic dissipation.

3.3.2 Asymmetric twisting

We so far have discussed cases a. and b. where photospheric rotation is symmetric at the upper and lower boundary conditions, and the loop evolution is therefore mirror symmetric with respect to the loop apex. We now test how the symmetry of the coronal loop is retained upon the effect of an asymmetric driver. We consider three different cases, already described in sec 2.2 and listed in table 1. In case c., one foot-point rotates while the other one is held fixed. In case d. both foot-points rotate at the same speed but the rotation radius is not the same. Finally, in case e. rotation begins symmetrically but after a while ($t_0 = 1400$ s) one foot-point accelerates and the other one slows down until it stops at $t_0 + \delta = 2000$ s. So in case e. asymmetries are implemented only after

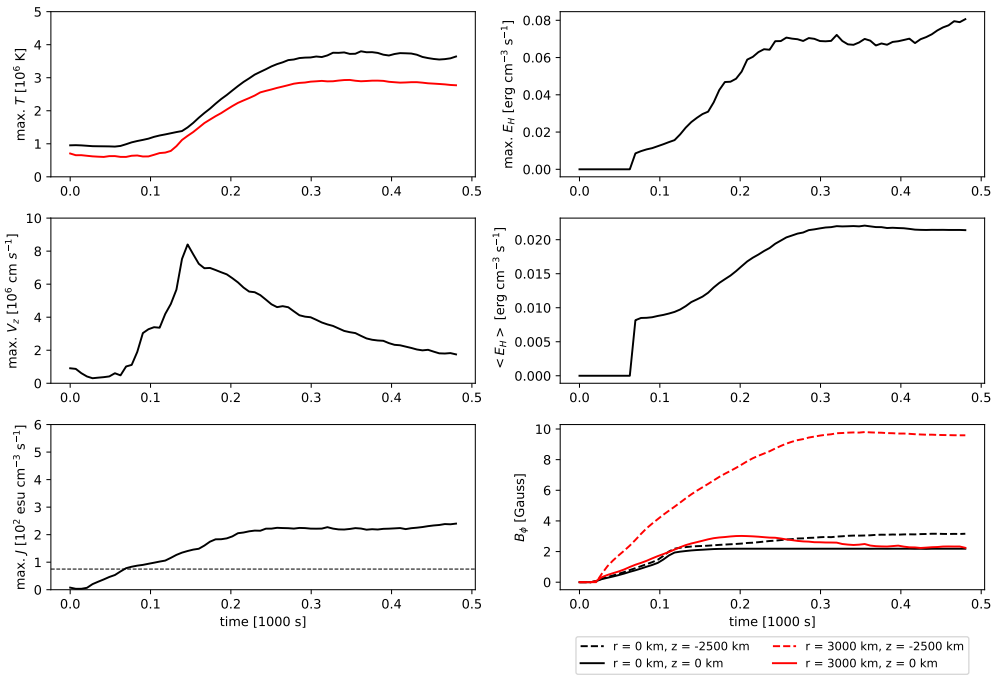

Figure 3.9: Simulation a. Evolution of the maximum temperature, vertical velocity, and coronal maximum current density in the simulation domain, and of the maximum heating rate per unit volume (top), the averaged heating over cells with $E_h > 0$, and of the azimuthal component of the magnetic field B_ϕ, at the two labeled heights z along the loop, i.e., apex (solid) and just above the transition region (dashed) and at the two labeled radial distances r from the central axis, i.e., close to the axis (black) and 3000 km far away (red). In the left panel the averaged temperature (red line) and current threshold for dissipation (horizontal dashed line) are also shown. Space-averaging is performed inside a cylinder of radius 10^9 cm, entirely contained within the corona ($T > 10^4$ K).

plasma evaporation has started filling the tube with dense chromospheric material.

Case c

In case c., one footpoint (the upper one) does not rotate, the other (lower) rotates at a speed twice bigger than in cases a. and b., so that the magnetic stress grows at the same rate. As in the previous experiments, rotation at the photospheric boundary twists the magnetic field lines. Initially, the twisting is localised near the rotating footpoint. Then, the azimuthal component of the magnetic field grows and propagates upwards reaching

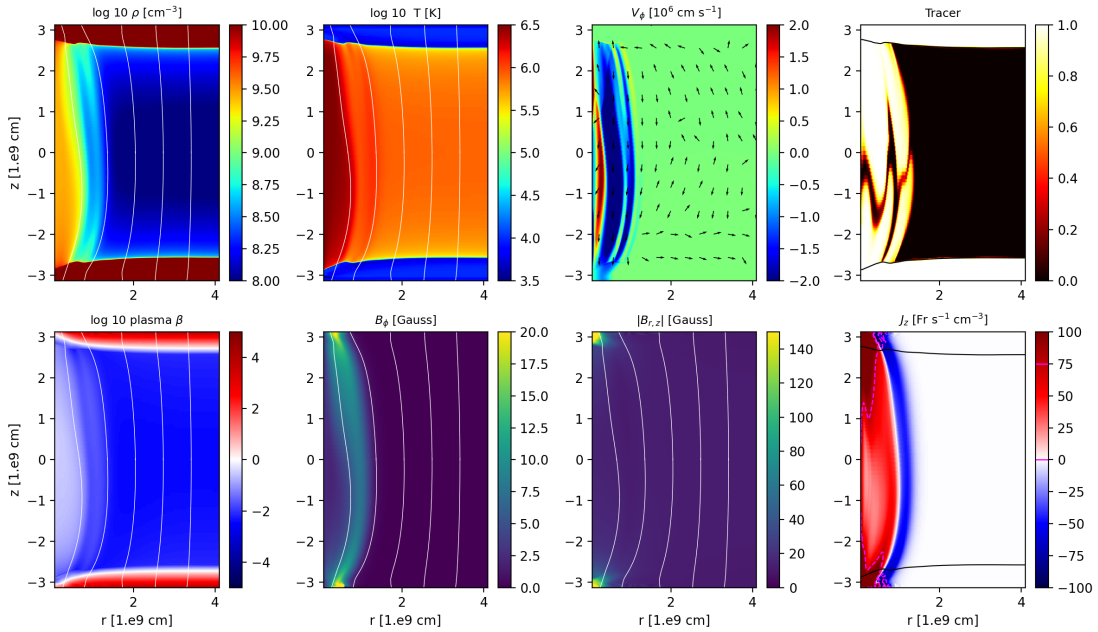

Figure 3.10: Same as Fig. 3.4 for Simulation c.

the corona in the expected Alfvén time. Rotation never involves the upper chromospheric layer. Nevertheless, except that there is a certain time delay, the current density equally grows fast on both sides of the domain. It exceeds the threshold value after about 800 s, almost simultaneously in both upper and lower layers above the transition region. The loop evolution then continues very similar to the symmetric cases, for about 3800s. Then the magnetic structure starts to warp. The final state of the simulation is shown in Fig. 3.10. It represents the maps of density, temperature, azimuthal velocity, plasma beta, chromospheric tracer and current density at t = 5000 s. The dense, hot part of the loop fits the shape of the field lines. The azimuthal components of the plasma velocity is significantly higher where chromospheric evaporation fills the tube with dense material. There, the plasma β is about one order of magnitude larger than in the surrounding environment because of the higher pressure, enhanced both by heating and compression. The tube expands on its lower half and it is squeezed on the upper side. It is clearly visible, looking at the evolution of the tracer, that the upper lying chromospheric material pushes down the underlying plasma. The same dynamics signature is visible in the orientation of the velocity in the r-z plane (black arrows in the third panel). This is because in the upper side of the domain more heating is released. Consequently, more plasma is injected from the upper side than the lower part. This is shown in eighth panel of Figure 3.10. The dashed line in magenta encloses the region where the current density exceeds

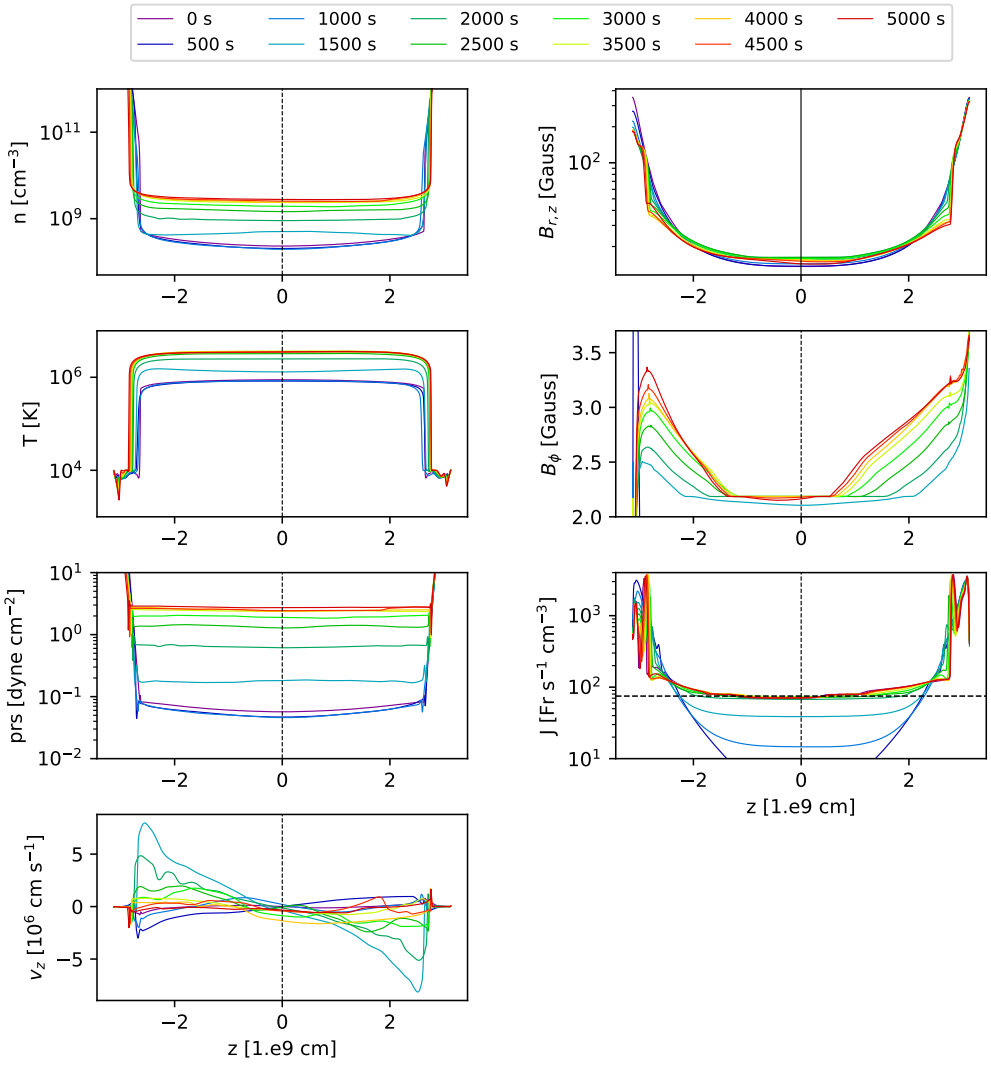

Figure 3.11: Same as Fig. 3.8 for Simulation c.

75 Fr cm^{-3} s^{-1} i.e. where magnetic reconnection dissipates magnetic energy into heat. The heated region looks bigger in the upper side of the domain than in the lower part.

Figure 3.11 shows the density, temperature, pressure, magnetic field intensity, azimuthal component of the magnetic field, and current density probed long the vertical direction and near the symmetry axis at different times. During the first 2500 s the loop's evolution is closely symmetric. The profiles shown in figure 3.11 are similar to those depicted in figure 3.8. In the last 2500 s of the numerical experiment, temperature, den-

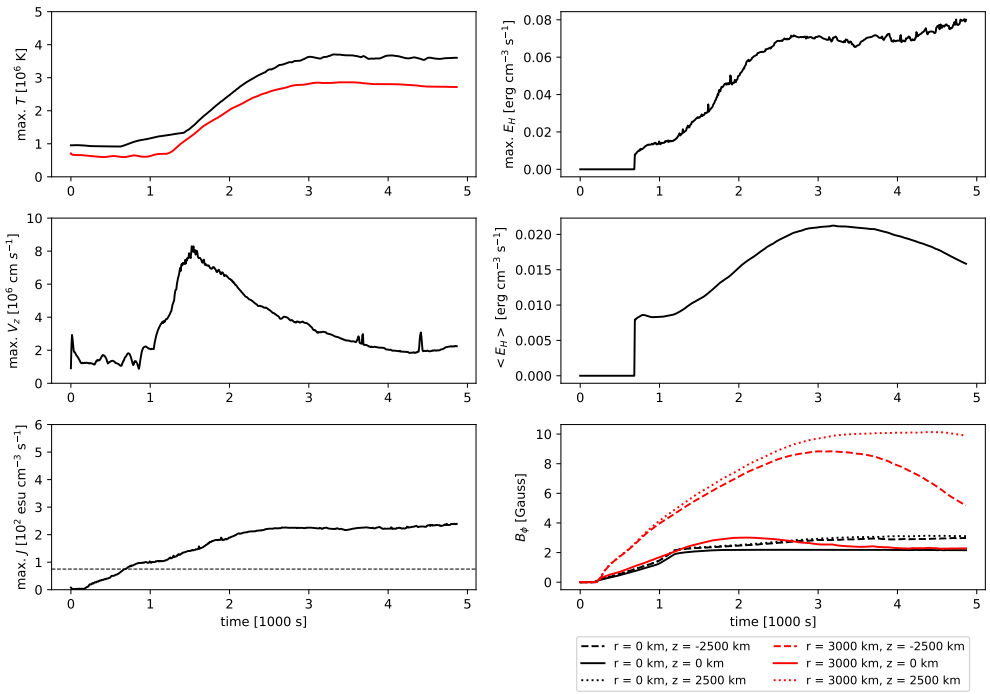

Figure 3.12: Same as Fig. 3.9 for Simulation c. We represented in the last panel (bottom left) the azimuthal component of the magnetic field B_ϕ at the three labeled heights z along the loop i.e., apex (solid) and just above the transition region $z = -2.5 \times 10^9$ cm (dashed) and $z = 2.5 \times 10^9$ cm (dotted) and at the two labeled radial distances r from the central axis, i.e., close to the axis (black) and 3000 km far away (red). The current threshold for dissipation (horizontal dashed line) is also shown. Space-averaging is performed inside a cylinder of radius 10^9 cm, entirely contained within the corona ($T > 10^4$ K).

sity and pressure are only slightly evolved. For instance, the tube appears to warm up at slower and slower rates. The vertical velocity displays the same profile discussed before but its peak decays in time as evidence of the reduced chromospheric evaporation. The height at which the velocity reverses its sign is not exactly the loop apex but displaced by few hundreds of kilometres toward the lower part of the domain. Both the magnetic field components and the current density magnitude are clearly distorted from the mirror symmetric initial configuration and the asymmetry appears to grow in time.

Fig. 3.12 shows the trend of the maximum (black line) and averaged (red line) temperatures, the maximum values of the vertical velocity, the maximum current density magnitude, the maximum and averaged heating rates, and the temporal behaviour of the azimuthal component of the magnetic field in six different locations inside the domain.

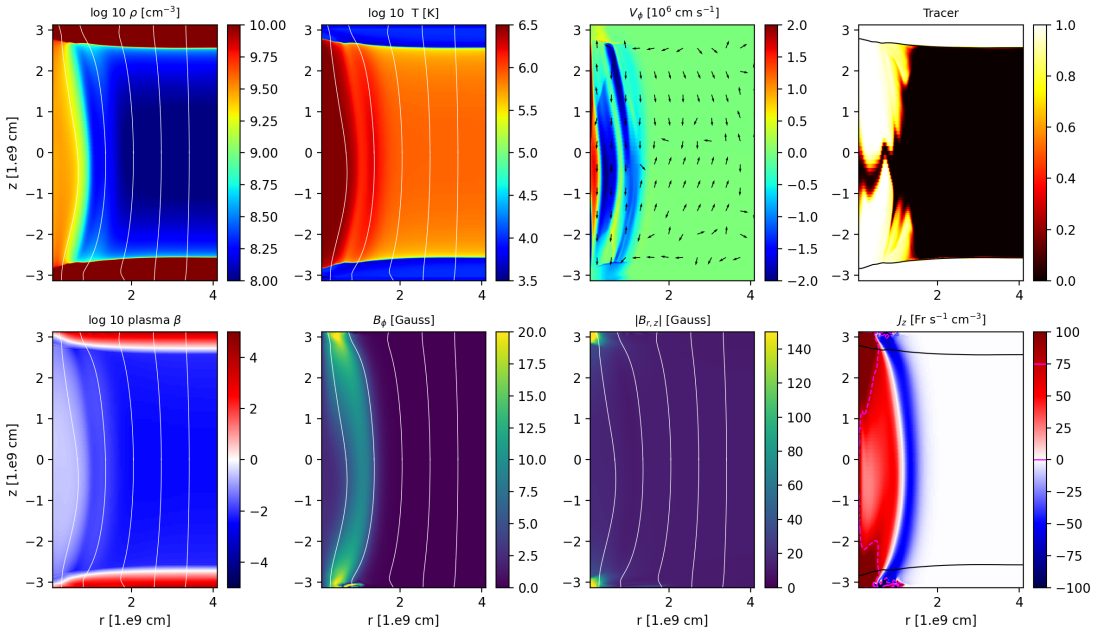

Figure 3.13: Same as Fig. 3.4 for Simulation d.

During the last 2500 s the averaged and maximum temperatures reach a steady state, at 2.5 MK and 3.5 MK, respectively. As before, after the peak at t=1600s the maximum velocity slowly decays to settle at about 20 km/s. Both the maximum current density, and the maximum heating rate settle to about 250 Fr cm^{-3} s^{-2} and 0.07 erg cm^{-3} s^{-2}, respectively during the second half of the simulation. The averaged heating rate instead begins to decrease after t=3000 s. The evolution of the azimuthal magnetic field at different locations along the flux tube (last panel of Figure 3.12) clearly shows the departure from mirror symmetry.

As with the symmetric twisting, the azimuthal magnetic field initially increases everywhere but more rapidly far from the axis where the tangential speed is faster. At $t \sim 1200$ s, the heating rate begins to grow and at the same time B_ϕ saturates close to the loop axis, where the dissipation is stronger. Farther from the axis and at the loop apex, the magnetic field saturates slightly later. Finally, closer to the chromosphere but far from the axis, the azimuthal component keeps increasing with a trend very similar to the heating rate (dashed line) at z = -2.5×10^9 cm, and a flat one (dotted line) at the opposite side, until the end of the simulation. The red dashed and dotted field lines remarkably departure in the final stages of the numerical experiment as a consequence of the broken mirror-symmetry. The black dashed and dotted lines keeps following the same path until the end of the simulation suggesting that asymmetries becomes less pronounced near

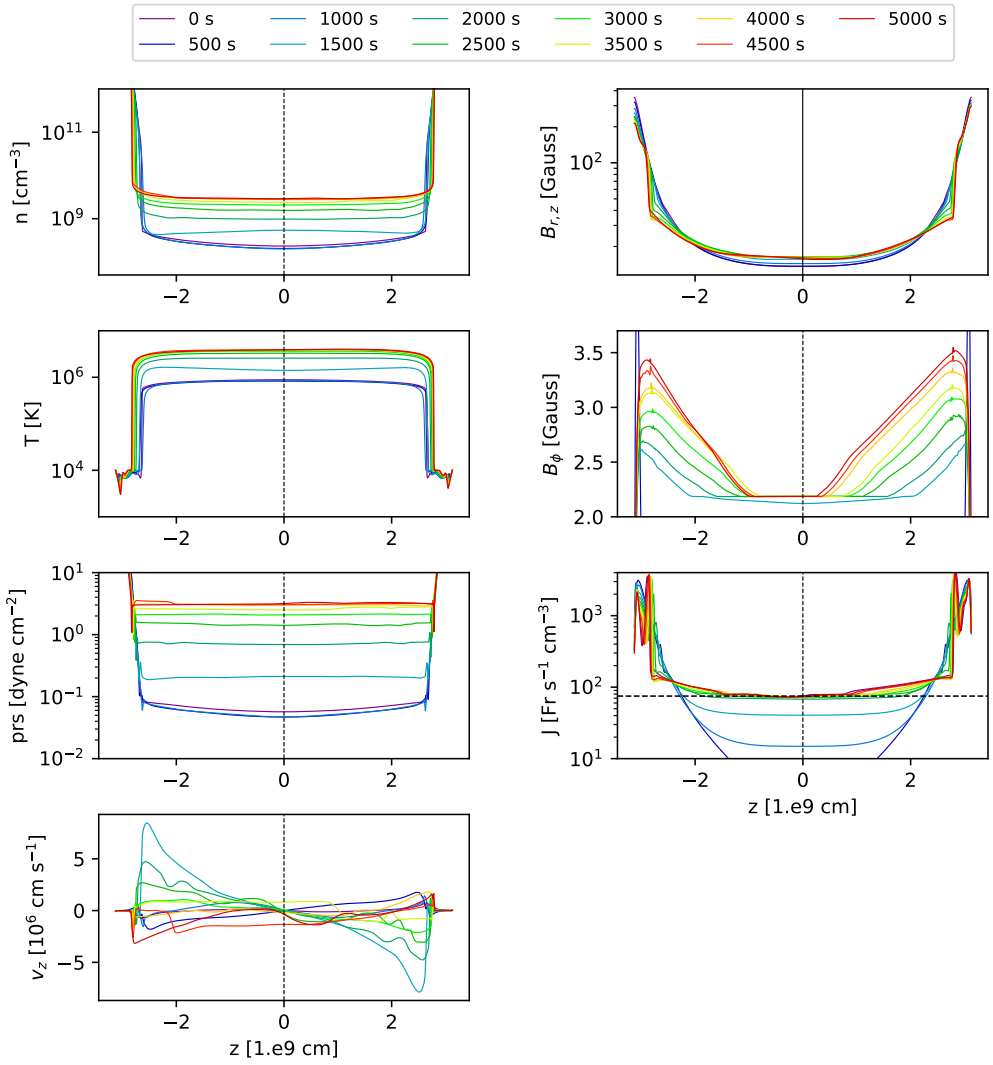

Figure 3.14: Same as Fig. 3.8 for Simulation d.

the loop axis.

Case d

In case d, both foot-points rotate around the symmetry axis at the same maximum tangential velocity $v_{\max}$ but with different extension of the rotating region for the footpoints ($R_{\max}$). The smaller rotating footpoints rotates with faster angular velocity ($\omega = v_{\max}/R_{\max}$), as the paremeter $v_{\max}$ is the same for both. Once again, the loop

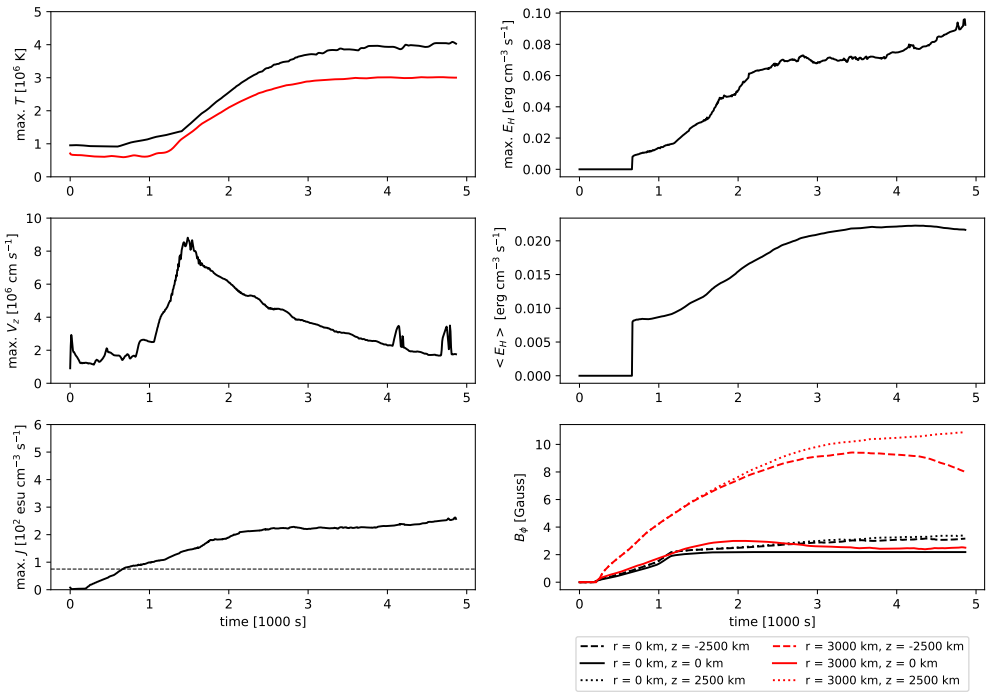

Figure 3.15: Same as Fig. 3.12 for Simulation d.

initially evolves very symmetrically and its behaviour fits quite well with cases a and b, discussed in the previous section. As in case c. the effects of the asymmetric boundary conditions becomes dominant after 3800 s. Figure 3.13 shows the evolved coronal loop at $t = 500$ s0. Figure 3.14 focus on the temporal evolution of several physical quantities sampled along the loop axis. Figure 3.15 finally displays the evolution in time of some maximum and space-averaged quantities. All the results shown in the previous figures agree very much with those shown in figures 3.10, 3.11, 3.12 for case c. Indeed, in both cases asymmetries develops after 3000 s. In particular, the upper side of the loop is squeezed while the lower side of the structure expands. Since velocities and magnetic field strength at the photospheric boundaries are similar to case c. we expected to probe a similar evolution (at least in terms of times scales and orders of magnitude involved).

Case e

With case e. we wanted to test the behaviour of a coronal loop when asymmetries are implemented at the boundaries only after the flux tube has been filled by chromospheric plasma. Indeed, in the previous cases, asymmetric boundary conditions acts from the

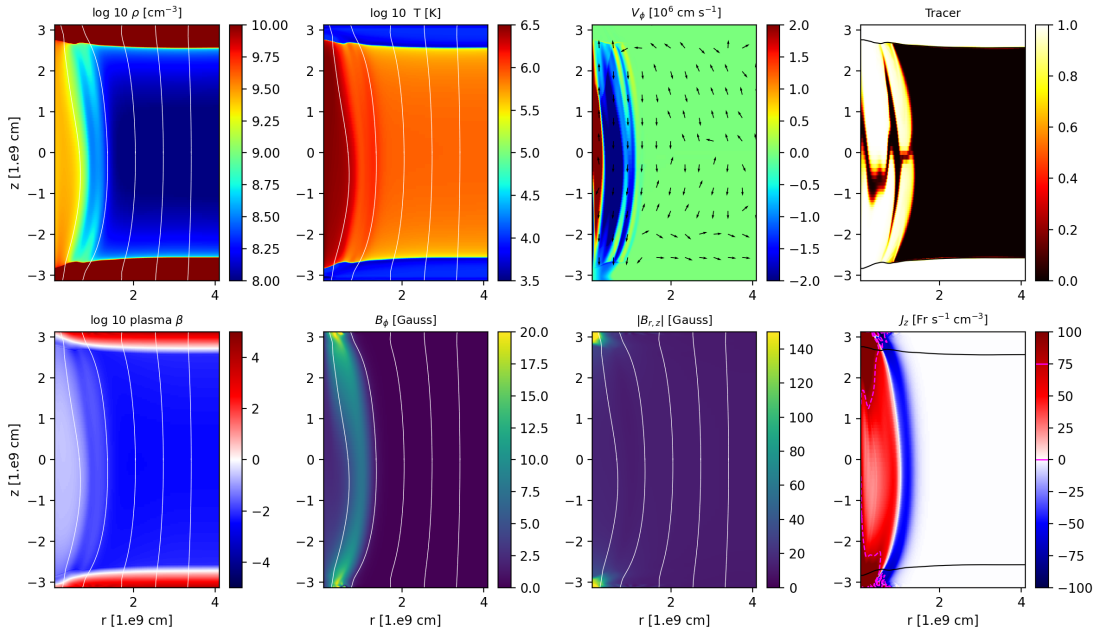

Figure 3.16: Same as Fig. 3.4 for Simulation e.

beginning i.e. when the magnetic structure encloses only a tenuous coronal atmosphere. This time, the flux tube initially evolves under the effect of a symmetric photospheric driver. After 1400 s the lower foot-point accelerates to double its initial velocity. In the meantime the upper foot-point progressively decelerates and it stops after 2000 s. After that time, boundary conditions are the same as in case c. The initial evolution of the loop is exactly the same as in case a. (we performed the simulation deploying the rotation pattern described in Eq. 3.2 and 3.3). Also in this case asymmetries becomes clearly appreciable only after 3800 s from the beginning of the numerical experiment.

Also in this case, the asymmetric evolution of the loop in the latest stages of the simulation remarks very well that described for case c. In particular, figure 3.16 shows the evolved coronal loop at $t = 5000$ s. Figure 3.17 focus on the temporal evolution of several physical quantities sampled along the loop axis. 3.18 finally displays the evolution in time of some maximum and space-averaged quantities. All the results shown in the previous figures agree very much which those shown in figures 3.10, 3.11, 3.12 for case c. This is expected since, after 2000 s, the loop twisting is driven by the same photospheric driver considered for case c.

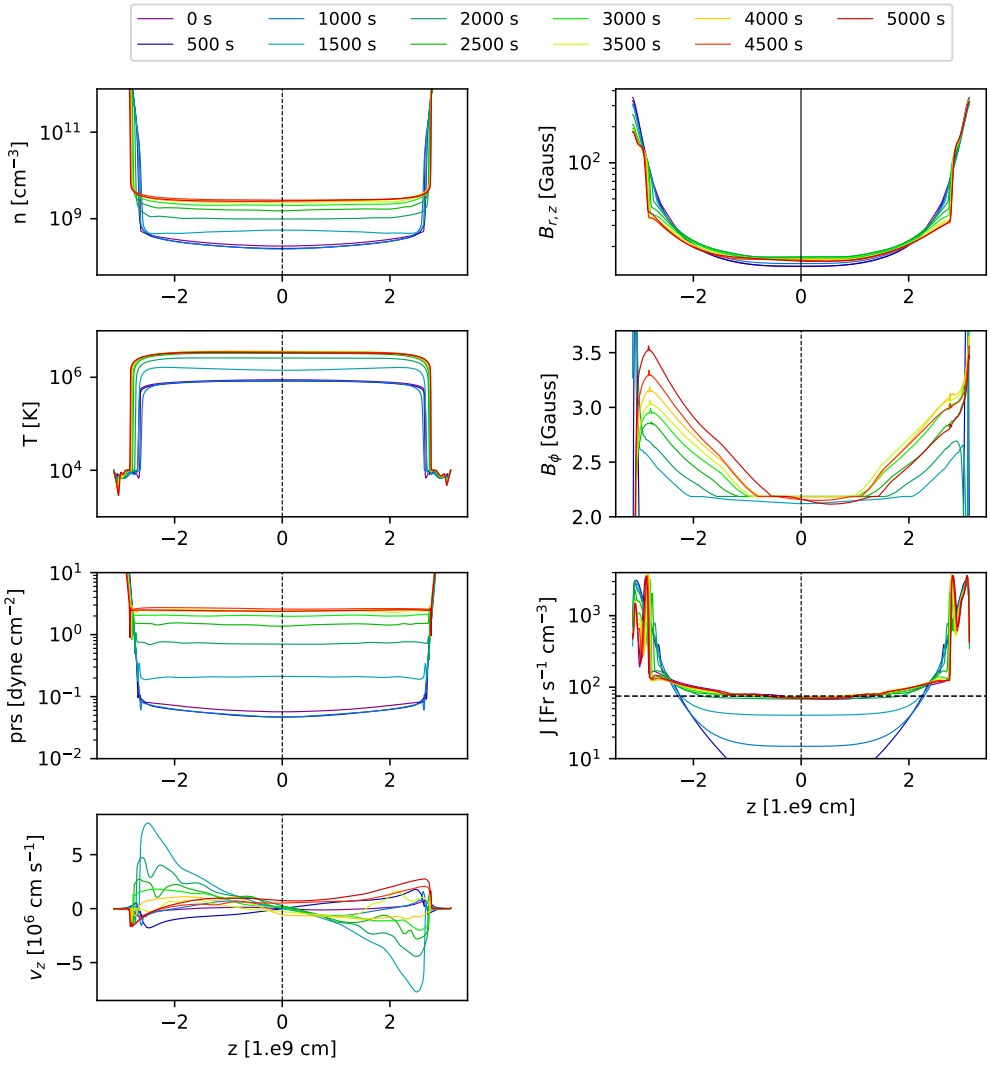

Figure 3.17: Same as Fig. 3.8 for Simulation e.

3.4 Discussion

We have addressed the brightening of a coronal loop hooked to two independent chromospheric layers through their footpoints. We performed a series of 2.5D simulations in cylindrical geometry. The coronal loop is treated as a straightened, cylindrically symmetric flux tube, where the gravity is that of a curved arch. The basic assumption is that the flux tube is progressively twisted by the rotation of the footpoints due to

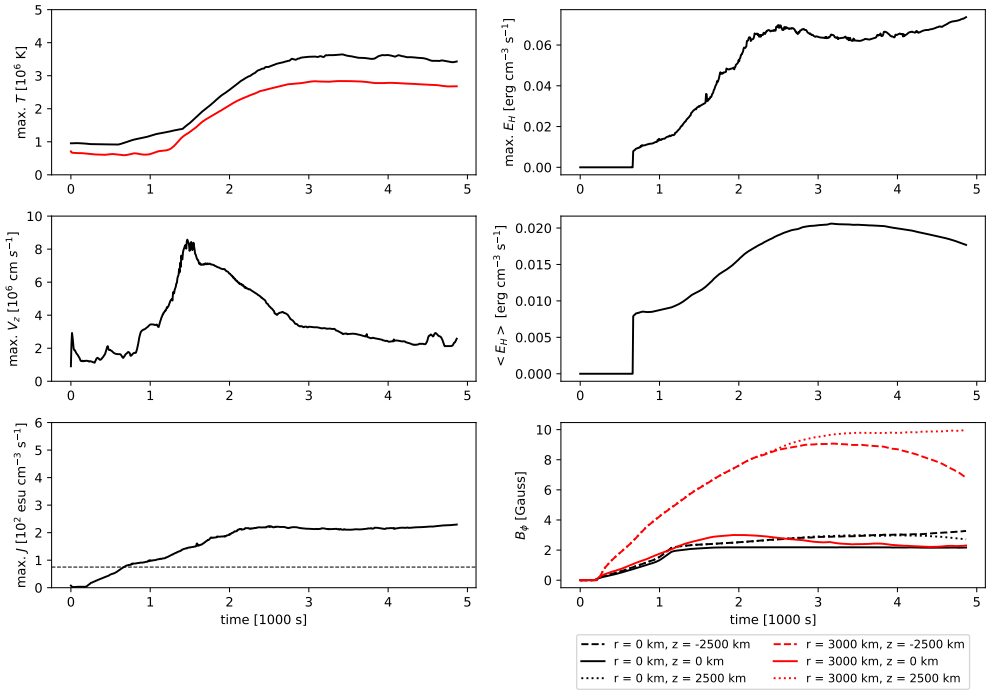

Figure 3.18: Same as Fig. 3.12 for Simulation e.

photospheric motions. The tube is then heated by Ohmic dissipation when the induced current grows above a threshold. Since it is difficult to imagine that the photospheric rotation is exactly identical at the two footpoints, here we study the effect of asymmetric twisting on the evolution of the heated loop. This extends the results presented in Reale et al. (2016) where only coherent photospheric motions are taken into account. We chose to take into account five particular cases to explore the space of the parameters involved in the prescription of the photospheric rotation. For comparison we first consider mirror-symmetric twisting in cases a. and b. which differ only for the radial shape of the angular velocity $\omega(r)$: trapezium-like vs smoother and everywhere differentiable, respectively. In particular, simulations a. and b. resemble the numerical experiments performed in the previous work (Reale et al. 2016). We assured the new results are coherent with the older ones.

In case c. the rotation is driven only at one side of the cylindrical box, in case d. the rotating area is different from one footpoint to the other, maintaining the same maximum speed, in case e. the rotation is mirror symmetric initially and then made different after few thousands of seconds. In the last three cases, the loop evolution is closely symmetric for the first 3800 s. Asymmetries becomes non-negligible after the tube has

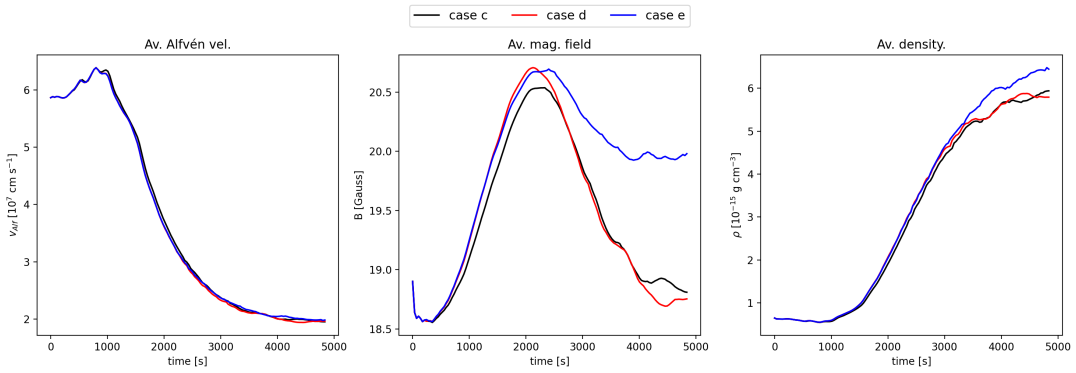

Figure 3.19: Evolution of the pixel-averaged Alfvén velocity v_{Alf} (left). magnetic field B (middle), and density ρ (right). Black, red and blues lines refer respectively to models c, d, and e.Space-averaging is performed inside a cylinder of radius 10^9 cm, entirely contained within the corona ($T > 10^4$ K).

been filled enough by dense chromospheric plasma. All the simulation shows the same qualitative behaviour during the first 2400 s. The azimuthal component of the magnetic field and the current density are tracers of the degree of twisting of the magnetic field lines. Both quantities grow smoothly with the boundary rotation. Photospheric rotation is transmitted by the line tied magnetic field up to the chromosphere and the corona at the expected Alfvén crossing time (see figure 3.6). A quasi-steady coherent twisting settles in the corona after just few Alfvén crossing travel times. Then, both the azimuthal component magnetic field and the maximum current amplitude grow almost linearly with time, as expected from the induction equation (eq. 1.13). Energy is gained by the stressed magnetic field until the current density exceeds the threshold of 75 Fr cm^{-3} s^{-1}. Then Ohmic dissipation of the magnetic field is triggered and the next evolution is similar to that found in previous loop models.

Here our attention focuses on the symmetry of the evolution. We invariably observe that even when the rotation pattern at the footpoints is not symmetric (cases c. d. and e.), the evolution is initially symmetric, i.e., the evolution of the two legs of the tube almost overlaps. The explanation lies in the speed of propagation of the signal from one footpoint to the other. The magnetic twisting driven by the footpoint rotation is transmitted along the tube at the Alfvén speed. This speed is very high in the tenuous initial loop corona ($\langle v_{\mathrm{Alf}} \rangle \sim 6 \times 10^7$ cm s^{-1}), and makes the twisting uniform along the whole loop in a very short time (few Alfvén crossing travel times) and leads to the initially symmetric evolution. The chromospheric evaporation determines a reduction of the Alfvén speed and a slight disequilibrium which makes the heating more effective at first in the lower leg than in the upper one. The higher plasma pressure inflates the

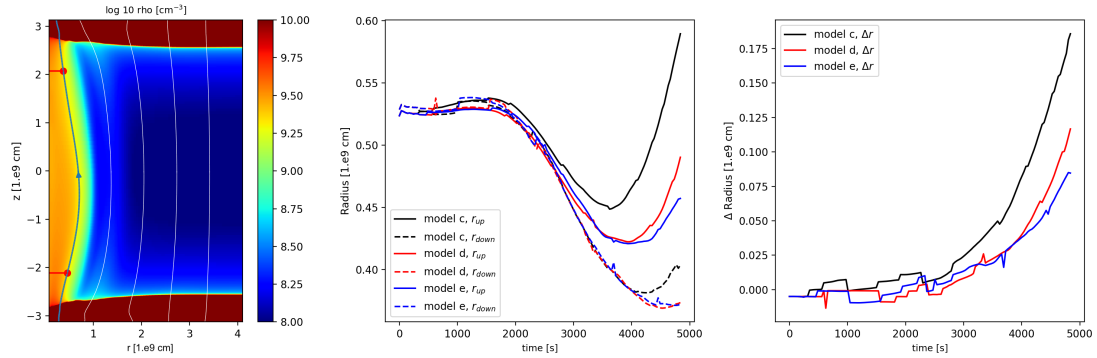

Figure 3.20: Left: Map of the density at time t=3500 s with field lines for simulation c. We selected a specific field line (solid blue line) and two symmetric points along it (red points), and we measured their distance $r_{\rm up}$ and $r_{\rm down}$ from the axis (red lines). Middle: $r_{\rm up}$ and $r_{\rm down}$ vs time for cases c. d. and e. Right: difference $\Delta r = r_{\rm up} - r_{\rm down}$ vs time for cases c. d. and e. Black, red and blues lines refer respectively to models c, d, and e.

loop more, i.e. the magnetic field becomes weaker, and the current density as well, thus eventually making the heating steadily weaker in the low region than in the upper region. A simple model can qualitatively describe the behaviour of the Alfvén velocity at the early stages of the simulation and at the latest.

Initially, the Alfvén speed slightly grows. Indeed, changes in the average magnetic field are relatively small ($\leq 25\%$) and the density stays approximately constant for the first 1500 s. In particular, B_ϕ grows almost linearly with time while B_z and B_r slightly readjust as a consequence of the rising azimuthal stresses. The evolution of B_ϕ is approximately given by solving the induction equation, assuming that B_r is negligible in the corona and B_z can be kept constant throughout the initial part of the evolution.A simple expression for the Alfvén velocity follows from the previous assumptions:

$$v_A = \frac{B}{\sqrt{4\pi\rho}} \sim \frac{\sqrt{B_z^2 + B_\phi^2}}{\sqrt{4\pi\rho}} \sim \frac{B_z}{\sqrt{4\pi\rho_0}} \left[1 + \frac{1}{2}\left(\frac{\omega r t}{L}\right)^2\right]. \tag{3.5}$$

All three components lose strength because of Ohmic dissipation at later times. In particular, after 2400 s the strong current dissipation stops the growth of B_ϕ, which settles to a steady value. At the same time the coronal density increases strongly because of chromospheric evaporation, and reduces the Alfvén speed:

$$v_{\rm Alf} \sim \frac{\langle B \rangle}{\sqrt{4\pi\rho(t)}} \propto \frac{1}{\sqrt{t}}, \tag{3.6}$$

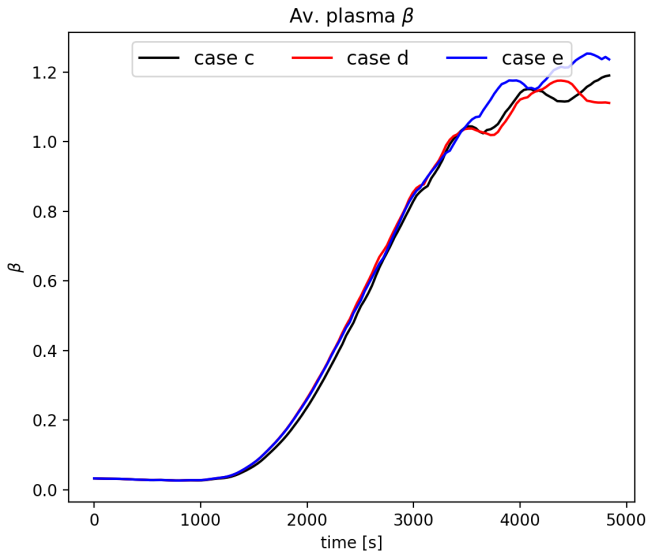

Figure 3.21: Evolution of the pixel-averaged plasma *beta*. Black, red and blues lines refer respectively to models c, d, and e. Space-averaging is performed inside a cylinder of radius 10^9 cm, entirely contained within the corona ($T > 10^4$ K).

where $\langle B \rangle$ is the averaged magnetic field. The left panel of Figure 3.19 shows the evolution of the Alfvén speeds obtained by averaging over the pixels inside the coronal part of the flux tube (i.e. at $T > 10^4$ K). It initially increases linearly. After 1000 s, it reaches a peak and then starts to decrease rapidly because of the increase in the plasma density.

In order to track the evolution of the asymmetries inside the loop, we consider a single magnetic field line at the edge of the flux tube, marked in Fig.3.20. We select two points along this field line, at symmetric distances from the footpoints, and we measure their radial distance from the tube central axis as a function of time. This distance holds the same for mirror-symmetric simulations, but it does not if there are deviations from symmetry; so we are measuring these deviations and we do this for all three simulations c., d. and e. The middle and right panels of Figure 3.20 clearly show that for all three simulations the general trend is that the distance is constant for about 2000 s, then it shrinks until a time between $t = 3500$ s and $t = 4500$ s, and widens again afterwards, showing a clear minimum. However, on all three simulations the distance decreases much more for the lower point than for the other, and this detachment starts at $t \sim 2500$ s, thus remarking the asymmetry since then.

Figure 3.21 shows the evolution of the plasma β over the time. It increases in the corona as a consequence of the magnetic dissipation and the further chromospheric

evaporation. Asymmetries shown in the previous figure occur once the plasma beta has reached relatively high values in the corona. These results suggest that the asymmetries are allowed to occur only in relatively high-β environments. In other words, the detachment from mirror-symmetry is not directly caused by the long-lasting nature of the asymmetric twisting but by its occurrence when the loop density is very high. Indeed, until the loop is not filled with dense plasma, asymmetries can not occur, not even if the foot-points have been dragged for a long time. On the other hand, a relatively rapid evolution of the asymmetries is expected in high beta coronal loops (as in case-e loop at time t=2000 s).

3.5 Conclusions

We have extended the study done in Reale et al. (2016) by addressing a coronal loop twisted by asymmetric photospheric motions. Indeed, the previous work addressed a straightened coronal loop subjected to a symmetric twisting at its footpoints. This time, we consider that independent photospheric motions can drag field lines toward a stressed configuration. We, in particular, investigated the response of these coronal loops to non-coherent photospheric motions by forcing strong asymmetries at the boundary conditions. Our numerical MHD simulations show that coronal loops are capable to maintain a very high degree of symmetry for a relatively long time against asymmetric twisting drivers at their footpoints.

Observations agree with the simulations. As far as isolated coronal loops are concerned, such magnetic flux tubes do not display strong side-by-side asymmetries despite their footpoints are likely driven by different rotation drivers at the photospheric footpoints. Here we only account for coherent drivers but irregular patterns on smaller scales may lead to field braiding, which may make any possible asymmetry unobservable on large scales. In general, the magnetically complex environment in which all coronal loops are embedded can influence each tube shape. For instance, coronal loops can be tangled with each other or may interact with open-field-lines structures. On the other and, their cross sections are widely observed to be almost constant along their length i.e. they would appear symmetric if stretched. In other words, also non-isolated coronal loops possess a hidden symmetry that may be highlighted looking at the uniformity of their physical properties (for instance, temperature, density, emission measure) along their entire length. A plasma β in the corona even smaller than the one implied by our model assumptions could explain why such coronal loops preserve so well such symmetry properties. Moreover, we understand that in order to break the symmetry, high plasma beta values are required. This regimes can be reached by long lasting photospheric twisting. They are unlikely to occur because of the stochastic (turbulent) behaviour of the photospheric plasma. In addition, highly twisted coronal loops would be unstable against kink modes.

4

Coronal heating by MHD avalanches: Effects on a structured, active region coronal loop

This chapter is structured based on the paper titled "Coronal heating by MHD avalanches. Effects on a structured, active region coronal loop" (Cozzo et al. 2023b).

A possible key element for large-scale energy release in the solar corona is a MHD kink instability in a single twisted magnetic flux tube. An initial helical current sheet progressively fragments in a turbulent way into smaller-scale sheets. Dissipation of these sheets is similar to a nanoflare storm. Since the loop expands in the radial direction during the relaxation process, an unstable loop can disrupt nearby stable loops and trigger an MHD avalanche. Exploratory investigations have been conducted in previous works with relatively simplified loop configurations.In this work, we address a more realistic environment that comprehensively accounts for most of the physical effects involved in a stratified atmosphere typical of an active region. The questions we investigate are whether the avalanche process will be triggered, with what timescales, and how will it develop as compared with the original, simpler approach. We used three-dimensional MHD simulations to describe the interaction of magnetic flux tubes, which have a stratified atmosphere with chromospheric layers, a thin transition region to the corona, and a related transition from high-β to low-β regions. The model also includes the effects of thermal conduction and of optically thin radiation. Our simulations address the case where one flux tube amongst a few is twisted at the footpoints faster than its neighbours. We show that this flux tube becomes kink unstable first in conditions in agreement with those predicted by analytical models. It then rapidly affects nearby stable tubes, instigating significant magnetic reconnection and dissipation of energy as heat. In turn, the heating brings about chromospheric evaporation as the temperature

rises up to about 10^7 K*, close to microflare observations. This work confirms, in more realistic conditions, that avalanches are a viable mechanism for the storing and release of magnetic energy in plasma confined in closed coronal loops as a result of photospheric motions.*

4.1 Introduction

Observations and numerical experiments provide evidence that the evolution of coronal loops is strongly influenced by photospheric motions (Chen et al. 2021). The coronal magnetic field must be driven towards a stressed state, which will be a non-potential configuration. For instance, footpoint rotation may lead the magnetic structure to twist and gain magnetic energy. While magnetic energy is stored, the flux tube could potentially be subject to strong stresses that may eventually trigger fast magnetohydrodynamic instabilities, such as the kink instability (Hood et al. 2009) or the tearing mode instability (Del Zanna et al. 2016), or lead to long-lasting Ohmic heating (Klimchuk 2006).

Heating and brightening of coronal loops may occur as a 'storm' of impulsive events (Klimchuk 2009; Viall & Klimchuk 2011). Such heat pulses may be driven by multiple localised instances of the magnetic field relaxing. The irregular photospheric motion, as well as a large range of magnetohydrodynamic instabilities, may lead the magnetic structure to develop fast reconnection and to produce heat.

In the corona, the magnetic field might become unstable under resistive modes as it is slowly forced by photospheric motions to explore a series of non-linear force-free states. In conditions of high magnetic stress, the field must reconnect and relax towards a linear force-free state, $\nabla \times \mathbf{B} = \alpha \mathbf{B}$, with uniform α (Woltjer 1958; Heyvaerts & Priest 1983).

A possible trigger mechanism for large-scale energy release (such as solar flares) is the magnetohydrodynamic (MHD) kink instability in a single twisted magnetic flux strand (Hood & Priest 1979b; Hood et al. 2009). It typically arises in narrow, strongly twisted magnetic tubes and results in the cross-section of the plasma column moving transversely away from its centre of mass, determining an irreversible imbalance between the outward-directed force from magnetic pressure and the inward force of magnetic tension (Priest 2014). During the twisting, a helical current sheet forms that can eventually trigger reconnection along the tube. The condition for the instability to occur can be expressed in terms of a critical amount of twist $\Phi_{\text{crit.}}$. Different studies have predicted the critical twist in different configurations: $\Phi_{\text{crit.}} = 3.3\,\pi$ for a uniform twisting (Hood & Priest 1979a); $\Phi_{\text{crit.}} = 4.8\,\pi$ for a localised twisting profile (Mikic et al. 1990); and $\Phi_{\text{crit.}} = 5.15\,\pi$ for a localised, variable twisting profile (Baty & Heyvaerts 1996). Energy is released after the magnetic field becomes unstable to ideal MHD modes. At the beginning, a helical kink develops and grows according to the linear theory of instability. Afterwards, the initial helical current sheet progressively fragments, in a turbulent way,

into smaller-scale sheets. During the onset of instability, the kinetic energy rapidly increases, and throughout the non-linear phase of the instability, magnetic energy dissipates. In particular, reconnection events arise in fine-scale structures like current sheets. Dissipation of these sheets is similar to a nanoflare storm. As time progresses, the magnetic field reaches an energy minimum constrained by the conservation of magnetic helicity, as expected in highly conducting plasmas (Browning 2003; Browning et al. 2008), but also subject to other topological constraints (e.g., Yeates et al. 2010).

Since the loop expands in the radial direction, during the relaxation process, an unstable loop can disrupt nearby stable loops (Tam et al. 2015) and trigger an MHD avalanche (Hood et al. 2016). For instance, Hood et al. (2016) demonstrates that an MHD avalanche can occur in a non-potential multi-threaded coronal loop. They showed that a single unstable thread can trigger the decay of the entire structure. In particular, each flux tube coalesces with the neighbouring ones and releases discrete heating bursts. In general, the energy stored by photospheric motions can be released via viscous and Ohmic dissipation during a dynamic relaxation process (Reid et al. 2018) and thereafter through a sequence of impulsive, localised, and aperiodic heating events under the action of continuous photospheric driving (Reid et al. 2020).

The earlier works we cited conducted exploratory investigations with relatively simplified loop configurations, with no gravitational stratification and consequently no variation of β with height while also neglecting thermal conduction and optically thin radiation. Separately, others have considered the effect of thermal conduction, but in a purely coronal loop (Botha et al. 2011), and again without stratification in density. Here, we consider a more realistic scenario of flux tubes interacting within a stratified atmosphere that includes chromospheric layers, and the thin transition region to the corona, the associated transition from high-β to low-β regions, as well as including thermal conduction and optically thin radiation (as in Reale et al. 2016). The questions that we investigate are whether the avalanche process will be triggered, with what timescales, and how it will develop in comparison with the evolution in the original, simplified approach.

4.2 The model

The numerical experiment is based on a solar atmosphere model that consists of a chromospheric layer and a coronal environment crossed by multiple coronal loop strands. Each strand is modelled as a straightened magnetic flux tube linked to two chromospheric layers at opposite ends of a box (Fig. 4.1). The length of each tube is much longer than its cross-sectional radius. Though the loop-aligned gravity is that of a curved, untwisted loop, we neglect other effects of the curvature. In our scenario, the two (upper and lower) chromospheric layers are the two loop footpoints and are so distant from each other that they can be assumed independent regions. The evolution of the

plasma and magnetic field in the box is described by solving the full, time-dependent MHD equations including gravity (for a curved loop), thermal conduction (including the effects of heat flux saturation), radiative losses from an optically thin plasma, and an anomalous magnetic diffusivity.

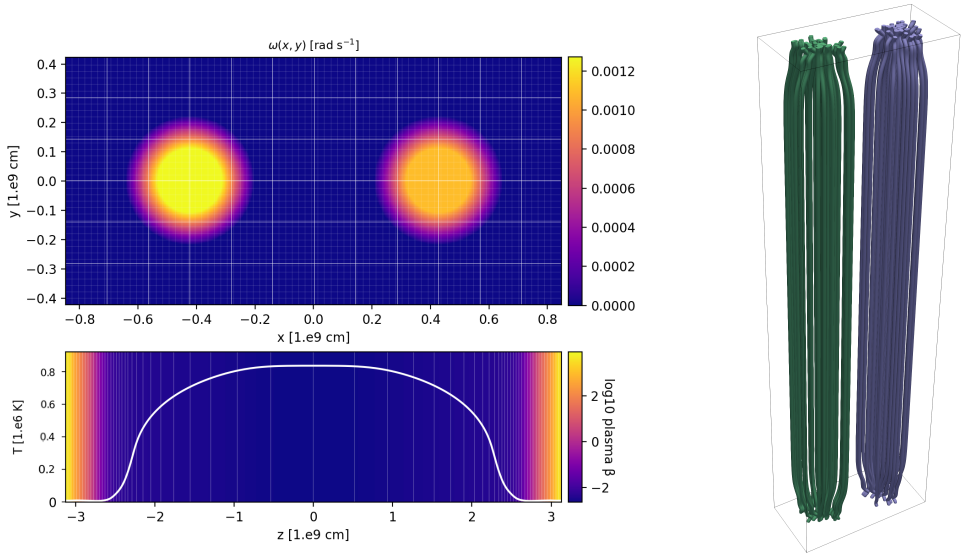

Figure 4.1: The initial conditions used in the numerical simulation. Upper-left panel: Map of the angular velocity at the bottom of the box. The colour scale emphasizes higher angular velocity. The uniform grid is marked. The two rotating regions have the same radius $R_{\max}$. The region on the left has a higher angular velocity ($v_{\max.,\text{left}} = 1.1 \times v_{\max.,\text{right}}$). Lower-left panel: Map of average plasma β as a function of z at $t = 0$ s. The solid curve shows the initial temperature along the z axis. Right panel: Three-dimensional rendering of the initial magnetic field configuration in the box around the two flux tubes. The green field lines are twisted more quickly than the purple ones.

The MHD equations (Eq.s 2.2 - 2.5) are solved in the non-dimensional conservative form (Mignone et al. 2007). We use the ideal gas law as equation of state (Eq. 2.10), assuming $\mu = 1.265$ as the mean atomic mass (from typical solar metal abundances, Anders & Grevesse 1989) and assume negligible viscosity. Thermal conductive flux is treated as in Eq.s 2.11, 2.12 with thermal conduction coefficients $K_{\parallel} = 9.2 \times 10^{-7}$ and $K_{\perp} = 5.4 \times 10^{-16}$, in cgs units, and $\phi = 0.9$ (Cowie & Mckee 1977).

We account for optically thin radiative losses (see Sec. 2.2.3 and Eq. 2.13) and uniform heating (Sec. 2.2.4):

$$Q(T) = -\Lambda(T) n_e n_H + H_0 \tag{4.1}$$

where $\Lambda(T)$ are the optically thin radiative losses per unit emission measure obtained from the CHIANTI v. 7.0 database (Dere et al. 1997; Reale & Landi 2012; Landi &

Reale 2013, e.g.,) assuming typical coronal element abundances (Widing & Feldman 1992). $H_0 = 4.3 \times 10^{-5}$ erg cm $^{-3}$ s^{-1} is a uniform heating rate per unit volume which maintains the corona with a temperature of about 8×10^5 K (Serio et al. 1981; Rosner et al. 1978b; Reale 2014; Guarrasi et al. 2014).

The Linker–Lionello–Mikić method (Linker et al. 2001; Lionello et al. 2009; Mikić et al. 2013) allowed us artificially to broaden the transition region without significantly changing the properties of the loop in the corona, obviating that challenge. In particular, we modified the temperature dependence of the parallel thermal conductivity and radiative emissivity below a temperature threshold $T_c = 2.5 \times 10^5$ K (see E.s 2.23 and 2.24).

We assumed that the flux tube is circularly curved only in the corona and that it is straight in the chromosphere. We note that gravitational acceleration (see Eq. 2.31) decreases and becomes zero at the loop apex ($z = 0$) to account for the loop curvature. Below the corona, gravity is uniform and vertical.

We considered an anomalous plasma resistivity that is switched on only in the corona and transition region (i.e. above $T_{\rm cr.} = 10^4$ K) where the magnitude of the current density exceeds a critical value, as in the Eq. 2.32 (e.g., Hood et al. 2009), where we assumed $\eta_0 = 10^{14}\,{\rm cm}^{-2}\,{\rm s}^{-1}$ and $J_{\rm cr.} = 250\,{\rm Fr\,cm}^{-3}\,{\rm s}^{-1}$. The current threshold was chosen so as to avoid Ohmic heating before the onset of the avalanche process and to permit the ideal build-up to the instability. With this assumption, the minimum heating rate above the threshold is $H = \eta_0(4\pi|J_{\rm cr.}|/c)^2 \approx 0.3\,{\rm erg\,cm}^{-3}\,{\rm s}^{-1}$. Below the critical current, a minimum numerical resistivity is inevitably present, but it does not contribute any heating during the simulation.

4.2.1 The loop setup

The 3D computational domain of our reference simulation contains two flux tubes, each with a length of 5×10^9 cm and an initial temperature of approximately 10^6 K (see lower-left panel of Fig. 4.1). Their footpoints are anchored to two thick, isothermal chromospheric layers at the top and bottom of the box. As the plasma β decreases farther from the boundaries, the magnetic field expands (see Fig. 4.1). The initial atmosphere is the result of a preliminary simulation in which we let a domain with a vertical magnetic field relax to an equilibrium condition until the maximum velocity reached a value below $10\,{\rm km\,s}^{-1}$, as described in Guarrasi et al. (2014).

The computational box is a 3D Cartesian grid, $-x_M < x < x_M$, $-y_M < y < y_M$, and $-z_M < z < z_M$, where $x_M = 2y_M = 8\times10^8$ cm, $y_M = 4\times10^8$ cm, and $z_M = 3.1\times10^9$ cm, with a staggered grid. We adopted the piecewise uniform and stretched grid sketched in Fig. 4.1. In particular, in the corona, we considered a non-uniform grid whose resolution degrades with height. To describe the transition region at sufficiently high resolution, the cell size there ($|z| \approx 2.4 \times 10^9$ cm) decreases to $\Delta r \sim \Delta z \sim 3 \times 10^6$ cm and remains constant across the chromosphere. The boundary conditions are periodic at $x = \pm x_M$

and $y = \pm y_M$. Reflecting boundary conditions were set at $z = \pm z_M$. There, the magnetic field has equatorial-symmetric boundary conditions (i.e., symmetric for the normal component of the magnetic field and anti-symmetric for the tangential components).

We also performed a second numerical experiment, extending the domain in the x-direction ($x_M = 1.5 \times 10^9$ cm) and including a third flux tube. The results of this simulation are discussed in Sect. 5.6.

4.2.2 Loop twisting

We tested the evolution of a coronal loop under the effects of a footpoint rotation. In particular, both strands were driven by coherent photospheric rotations that switch signs from one footpoint to the other. Rotation at the threads' footpoints induces a twisting of the magnetic field lines. As flux tube torsion increases, the current density is amplified. Once the conditions for kink instability are reached, a strong current sheet forms and the critical current is exceeded, triggering magnetic diffusion and heating via Ohmic dissipation. The angular velocity $\omega(r)$ is that of a rigid body around the central axis; that is, the angular speed is constant in an inner circle and then decreases linearly in an outer annulus (Reale et al. 2016):

$$\omega = \omega_0 \times \begin{cases} 1 & r < r_{\text{max.}} \\ (2r_{\text{max.}} - r)/r_{\text{max.}} & r_{\text{max.}} < r < 2r_{\text{max.}} \\ 0 & r > 2r_{\text{max.}} \end{cases}, \tag{4.2}$$

where $\omega_0 = v_{\text{max.}}/r_{\text{max.}}$, $v_{\text{max.}}$ is the maximum tangential velocity ($v_\phi = \omega r$), and $r_{\text{max.}}$ is the characteristic radius of the rotation. In this specific case, the central loop is driven at a speed that is 10% higher than the lateral ones and is equal to $1.1\,\text{km}\,\text{s}^{-1}$. The maximum velocity achieved by twisting is always smaller than the minimum Alfvén velocity $v_{\text{Alf}} = B/\sqrt{4\pi\rho}$ in the domain. Moreover, the characteristic velocity ($\omega_0\, r_{\text{max.}}$) is high enough to avoid field line slippage at the photospheric boundaries caused by numerical diffusion. The choice of a mirror-symmetric photospheric driver does not cause the further system evolution to lack generality: as the relatively high Alfvén velocities lead coronal loops to maintain a very high degree of symmetry, even when they are subjected to asymmetric photospheric motions for a long time (Cozzo et al. 2023a). The $r_{\text{max.}}$ parameter was set to 1200 km for both loops (see top-left panel of Fig. 4.1). For many recent simulations of coronal loops subject to photospheric driving, a significant challenge has been in attaining realistic driving speeds, given that there is a need to drive quickly enough to prevent slippage of field lines, which requires modelling velocities that are much faster than those observed. However, with velocities of the order of $1\,\text{km}\,\text{s}^{-1}$, we approach typical photospheric velocity patterns (Gizon & Birch 2005; Rieutord & Rincon 2010) and benefited from growing computational resources.

4.2.3 Numerical computation

The calculations were performed using the PLUTO code described in Chapter 2.

A Van Leer limiter (Sweby 1985) for the primitive variables was used. The evolution of the magnetic field was carried out adopting the constrained transport approach (Balsara & Spicer 1999). Thermal conduction was treated separately from advection terms through operator splitting. In particular, we adopted the super-time-stepping technique (Alexiades et al. 1996).

4.3 Basic theory

4.3.1 Twisting with expanding magnetic tube

Simple analytical models can predict the initial, steady-state evolution of a system provided that certain assumptions be satisfied (Hood & Priest 1979a; Browning & Hood 1989). Each loop is modelled as a cylindrically symmetric magnetic structure not interacting with the neighbouring ones. The initial magnetic field is not uniform: magnetic field lines expand from the photospheric boundaries (where $B \approx 300\,\mathrm{G}$) to the upper corona (where $B \approx 10\,\mathrm{G}$). As the field lines expand, the magnetic field decreases by an order of magnitude because of conservation of magnetic flux. The expansion of the field corresponds to a height that is roughly equal to the distance between the chromospheric sources, so it involves a small fraction of a coronal loop length, and thus the loop is of mostly uniform width in the corona. Field line tapering is strong in the chromosphere, where changes in the plasma beta are steeper, but weaker in the corona. In typical coronal conditions, such as high ($T \approx 1\,\mathrm{MK}$) and uniform temperature, the pressure scale height is large compared with the loop length. Therefore, density and pressure can be assumed to be uniform and constant in the corona. Averaged values can be constrained from the RTV scaling laws (Rosner et al. 1978b) once the total length of the loop $2L$ and the uniform heating rate H_0 are given. At the boundaries, the photospheric driver twists the magnetic field, causing the azimuthal component to increase. Perfect line-tying to the photospheric boundaries is assumed and no field line slippage is taken into account. The driver is much slower than the Alfvén velocity so that the magnetic torsion can be assumed to be instantaneously transmitted along the whole tube.

Under these assumptions, it is possible to express the magnetic field of a single thread in cylindrical coordinates in terms of the flux function ψ as a generalized parameter:

$$\mathbf{B} = \frac{1}{R}\left(-\frac{\partial\psi}{\partial z}, G(\psi), \frac{\partial\psi}{\partial R}\right), \tag{4.3}$$

where $\psi(R,z) = \int_0^R B_z(r',z)r'\,\mathrm{d}r'$. In Eq. (4.3), the azimuthal magnetic field com-

ponent is given by a function, G, of the flux function, ψ. The function G is related to the radial profile of the twisting velocity. In the following, R denotes the radius in the corona, and r is the radius in the photosphere. Under typical coronal conditions (i.e. low plasma beta), the force-free condition,

$$(\nabla \times \mathbf{B}) \times \mathbf{B} = 0 \,, \tag{4.4}$$

holds. Using Eq. (4.3), the force-free equation is satisfied by the Grad-Shafranov equation (Grad & Rubin 1958; Shafranov 1958):

$$\frac{\partial^2 \psi}{\partial R^2} - \frac{1}{R}\frac{\partial \psi}{\partial R} + \frac{\partial^2 \psi}{\partial z^2} + F(\psi) = 0, \tag{4.5}$$

where $F = G\frac{\mathrm{d}G}{\mathrm{d}\psi}$ is a function of ψ. The third term on the left-hand side can be neglected in the corona, under the assumption of negligible field line curvature, $\frac{\partial \psi}{\partial z} \approx 0$ (Browning & Hood 1989; Lothian & Hood 1989). As a first assumption, we considered the azimuthal velocity to be linear in z, since the twisting is equal in magnitude and opposite in direction at the two ends:

$$v_\phi = \omega(r) r \frac{z}{l}, \tag{4.6}$$

where l is a length scale that can be assumed to be equal to L, the half-length of the loop, in order that this equation matches the angular speed imposed on the boundaries. From the linearization of the ideal induction equation (Eq. 1.13), with $\eta = 0$, the azimuthal component of the magnetic field in the photosphere is easily linked to the given twisting angular velocity $\omega(r)$ (see Eq. 4.2):

$$\frac{\partial B_{\phi,\mathrm{phs}}}{\partial t} = \frac{\partial \left(B_z(r) v_\phi\right)}{\partial z} = \frac{B_z(r)\omega(r) r}{l} t = rG. \tag{4.7}$$

The vertical component at the photosphere, $B_{z,\mathrm{phs}}(r)$, is given by the superposition of a background magnetic field B_{bk} and a Gaussian function with amplitude B_0 and a characteristic width ς, that is:

$$B_{z,\mathrm{phs}}(r) = B_{\mathrm{bk}} + B_0 e^{-\frac{r^2}{\varsigma^2}} \tag{4.8}$$

so that:

$$\psi(r, \pm L) = \frac{1}{2} B_{\mathrm{bk}} r^2 - \frac{B_0 \sigma^2}{2}\left(e^{-r^2/\varsigma^2} - 1\right) \,. \tag{4.9}$$

The magnetostatic equilibrium of a coronal loop in response to slow twisting of the photospheric footpoints can be investigated in the corona by solving the Grad-Shafranov

equation:

$$B_{\phi,\text{coro.}}(R) = \frac{G}{R} \tag{4.10}$$

$$B_{z,\text{coro.}}(R) = \frac{1}{R}\frac{\partial \psi}{\partial R}\ . \tag{4.11}$$

In this way, we accounted for the flux tube expansion across the chromosphere just by assuming magnetic flux conservation throughout the loop volume and force-free condition in the corona. In particular, the volume-integrated magnetic energy of a single thread in the corona is given by:

$$E_{\text{mag.}} = 2\pi \cdot 2L \cdot \int_0^{y_M} \frac{B^2_{z\text{coro.}} + B^2_{\phi,\text{coro.}}}{8\pi}\, r\, \mathrm{d}r. \tag{4.12}$$

The volume-integrated kinetic energy can be roughly assessed by assuming the coronal loop to reach a steady state where the plasma is moved only by the magnetic field torsion:

$$E_{\text{kin.}} = 2\pi \int_L^{-L} \mathrm{d}z \cdot \int_0^{y_M} r\frac{1}{2}\langle\rho\rangle\Omega(r)^2 \left(\frac{z}{L}\right)^2 r^2\, \mathrm{d}r, \tag{4.13}$$

where Ω(r) is the angular velocity of the loop in the corona (the relation $\Omega(\psi) = \omega(\psi)$ holds) and $\langle\rho\rangle$ is the averaged coronal density.

In a cylindrically symmetric flux tube, the angular velocity produces the axial current density and the azimuthal magnetic field (see Eq. 4.2):

$$J_z = \frac{1}{r}\frac{\partial}{\partial r}\left(rB_\phi(r)\right) = \frac{c}{4\pi}\frac{2\omega_0 B_z t}{L} \times \begin{cases} 1 & r < r_{\text{max.}} \\ \frac{4r_{\text{max.}} - 3r}{2r_{\text{max.}}} & r_{\text{max.}} < r < 2r_{\text{max.}} \\ 0 & r > 2r_{\text{max.}} \end{cases}, \tag{4.14}$$

according to Eq.s 2.7, 4.2, 4.6, and 4.7. A rough but effective estimate of the maximum current density over the time is retrieved by evaluating the current density at the loop axis:

$$J_{\text{max.}} = J_z(r = 0, t) = \frac{c}{4\pi}\frac{2B_z(0)\omega(0)}{L} \times t. \tag{4.15}$$

As soon as the azimuthal component of the magnetic field increases linearly with time, magnetic energy should grow quadratically and the current density should grow linearly.

4.3.2 Energy equations

The temporal evolution of the four energy terms (i.e. magnetic, kinetic, internal, and gravitational energy) is driven by the energy sources and sinks (background heating and radiative losses, respectively) and several energy fluxes at the boundaries of the domain

(such as thermal conduction, Poynting flux, enthalpy flux, and kinetic and gravitational energy fluxes). In addition, energy transfer terms may link two different forms of energy. This is the case for Ohmic heating, which converts magnetic energy into heat, and work done per unit time by the Lorentz force, the pressure gradient, and gravity, which respectively convert kinetic energy into magnetic, thermal, and gravitational energy. The respective equations governing the evolution of magnetic, kinetic, internal, and gravitational energy are as follows:

$$\frac{\partial}{\partial t}\frac{B^2}{8\pi} + \nabla\cdot\left[-\frac{1}{4\pi}\mathbf{B}\,(\mathbf{v}\cdot\mathbf{B}) + \frac{B^2}{4\pi}\mathbf{v} + \frac{\eta}{c}\mathbf{j}\times\mathbf{B}\right] = -\frac{j^2}{\sigma} - \frac{\mathbf{v}}{c}\cdot(\mathbf{j}\times\mathbf{B})\,, \tag{4.16}$$

$$\frac{\partial}{\partial t}\left(\frac{1}{2}\rho v^2\right) + \nabla\cdot\left(\frac{1}{2}\rho v^2\,\mathbf{v}\right) = -\mathbf{v}\cdot\nabla P + \frac{\mathbf{v}}{c}\,(\mathbf{j}\times\mathbf{B}) + \rho\,\mathbf{v}\cdot\mathbf{g}, \tag{4.17}$$

$$\frac{\partial(\rho\epsilon)}{\partial t} + \nabla\cdot\left[\frac{\gamma}{\gamma-1}P\,\mathbf{v} + \nabla\cdot\mathbf{F}_c\right] = \mathbf{v}\cdot\nabla P + \frac{j^2}{\sigma}, \tag{4.18}$$

$$\frac{\partial(\rho g h)}{\partial t} + \nabla\cdot(\rho g h\,\mathbf{v}) = -\rho\,\mathbf{v}\cdot\mathbf{g}. \tag{4.19}$$

The sum of the four equations gives the energy equation (Eq. 2.5) discussed in Sec. 2.2. Terms on the left-hand sides include rates of change in energy (the derivatives with respect to time) and energy fluxes (i.e. surface terms, which appear here as divergences). Energy transfer terms, sources, and sinks are on the right-hand sides.

4.4 Results

4.4.1 Continued driving: Evolution before the instability

The box size is 6.2 Mm in the z direction. The chromosphere extends for 0.7 Mm on both sides, and the corona (including the transition region) is in the middle $2L = 5\times10^9$ cm. In the following, we cautiously restricted our analysis to the inner domain between $z = \pm2\times10^9$ cm in order to avoid any possible undesired contributions from expected changes in transition region height. Since boundary conditions are periodic at the side boundaries of the box, fluxes were only evaluated at the upper and lower boundaries of the sub-domain (i.e. at $z = \pm2\times10^9$ cm).

Initially, the two flux tubes were slowly twisted at a speed much slower than the Alfvén speed. As a consequence, the initial evolution of the magnetic structure is through quasi-steady states. In particular, an azimuthal magnetic field component grows almost linearly with time. The magnetic torsion is transmitted to the coronal part of the magnetic tube (i.e. at $|z| < 2\times10^9$ cm) after two hundred seconds, in accordance with the time estimated for a magnetic signal to cross the chromospheric layer.

Fig. 4.2 shows the rate of change of the total energy, which is given as the sum of magnetic, kinetic, thermal, and gravitational energy. The total energy is not constant

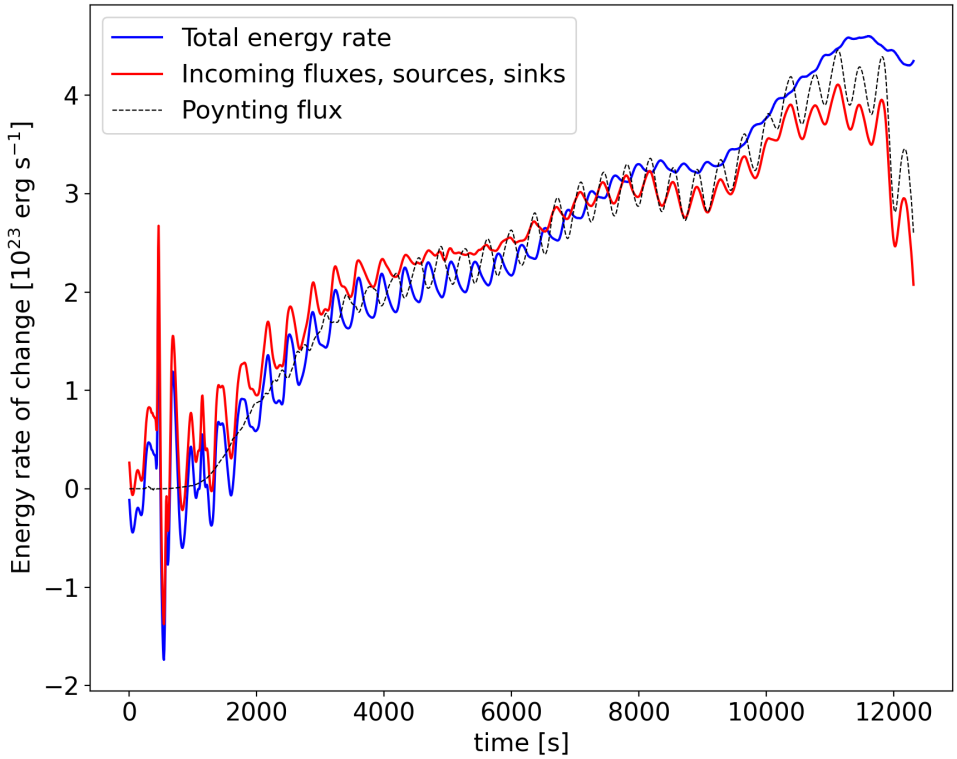

Figure 4.2: Evolution of the rate of change of the total energy, incoming fluxes, sources, and sinks for the reference simulation. The blue curve indicates the change in total energy over time, given by the sum of internal, kinetic, magnetic, and gravitational energies of the system, plotted as functions of time, before the onset of the instability. The red curve represents the sum of the total fluxes, energy sources, and sinks as a function of time before the onset of the instability. The closeness of the blue and red curves demonstrates the approximate energy conservation in the domain. The dashed black curve depicts the Poynting flux, which is the dominant flux and adds to the magnetic energy.

inside the coronal volume as a result of incoming fluxes at the chromospheric boundaries of the domain (such as Poynting flux, kinetic energy flux, enthalpy flux, gravitational energy flux, and thermal conduction), energy sources (background heating), and sinks (radiative losses). The total energy in the system, accounting for incoming and outgoing fluxes (see Eq. 2.5), is approximately conserved throughout the numerical experiment. Amongst all the external contributions, the Poynting flux is dominant during the build-up

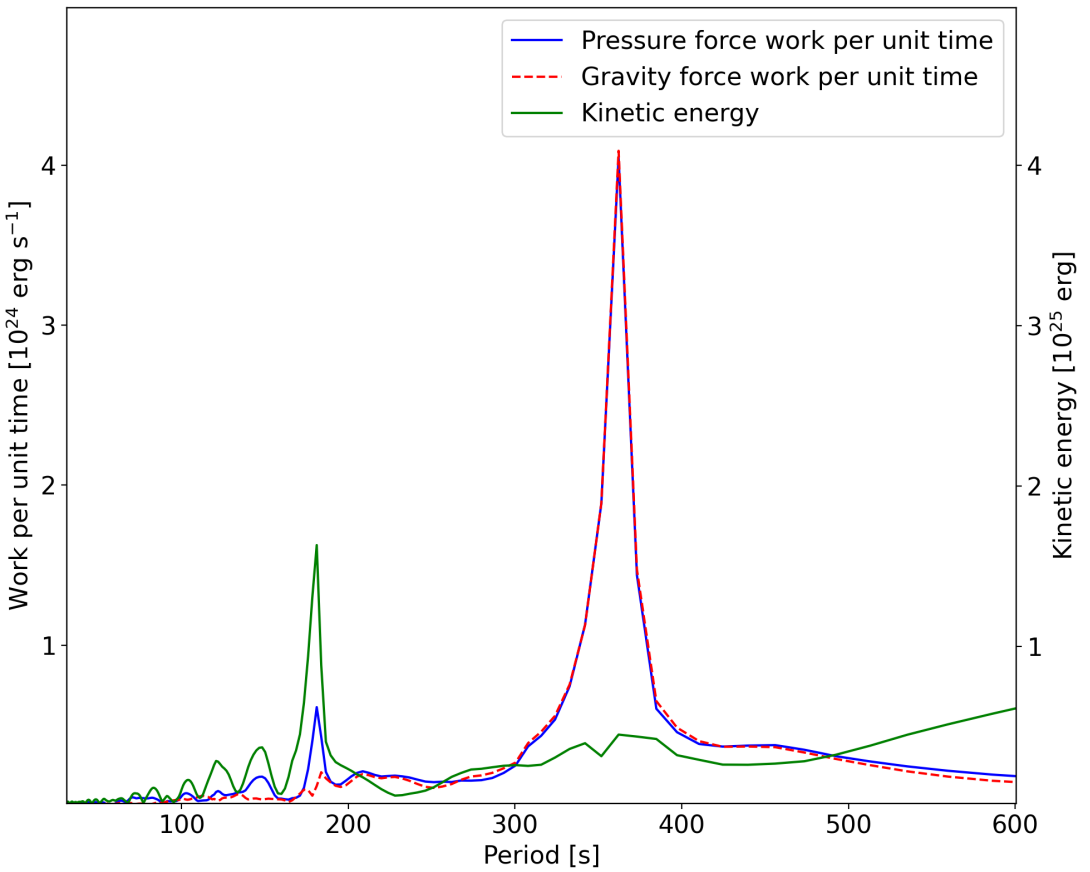

Figure 4.3: Fourier transform of pressure work, gravity work, and kinetic energy rates. The blue curve indicates the Fourier transform of the work done by pressure gradients per unit time, before the onset of the instability. The red curve represents the Fourier transform of the work done by gravity force per unit time, before the onset of the instability. Both curves show a peak around $T \approx 365$ s (identified by eye). The green curve depicts the Fourier transform of the kinetic energy before the onset of the instability. It shows a peak around 180 s.

of the twisting.

The initial evolution of the system might be seen as the superposition of a long-lasting and steady tube twisting (where magnetic energy and current density slowly grow as a consequence of the field line torsion) and a wave-like response to the induced dynamics (where oscillations of short characteristic timescales are damped with time).

In particular, long-period oscillation ($P \approx 360$ s) is clearly visible in Fig. 4.2 and in Fig. 4.3, the latter of which shows the work done by the pressure gradient and the

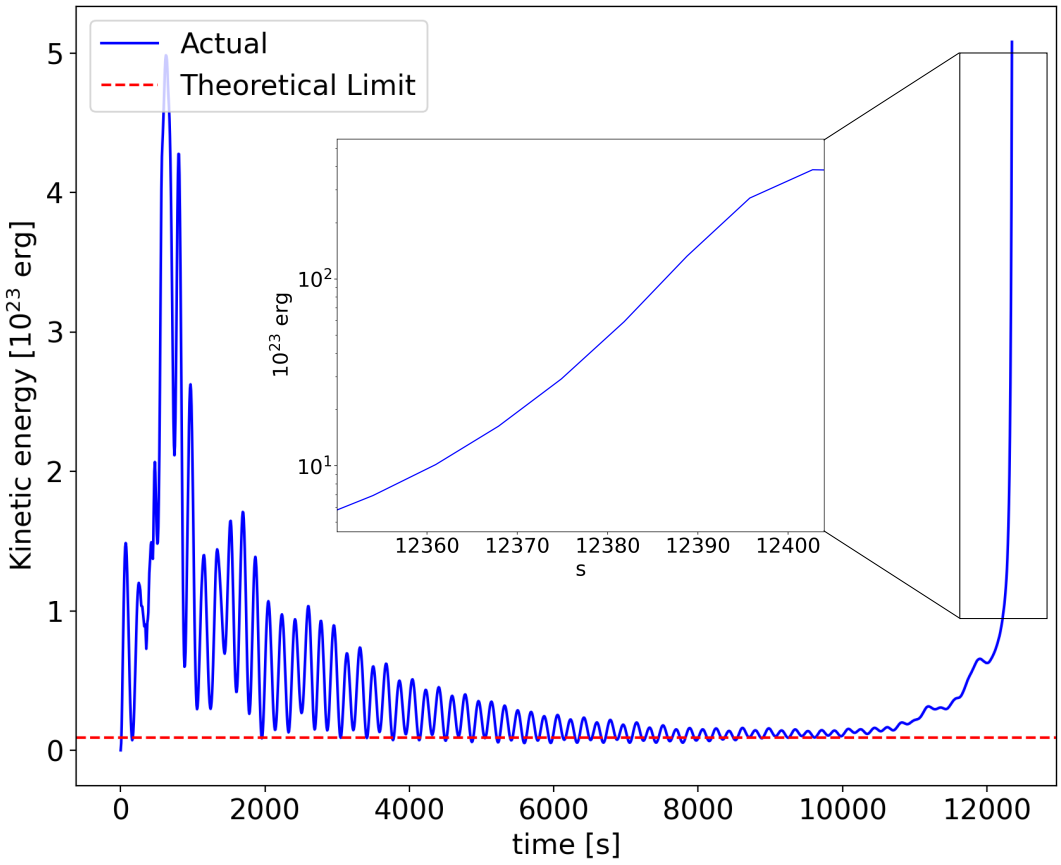

Figure 4.4: Kinetic energy damping before the instability onset. In blue is the total kinetic energy, plotted as a function of time, in the time leading up to the instability. The last exponential rise shows the time at which the first thread is disrupted. In dashed red is a theoretical estimation of the steady state based on the model described in Eq. (4.13). As waves are progressively damped, the total kinetic energy is expected to tend towards this theoretical steady state prior to the instability.

work done by gravity as functions of time. Given the length of the loop (50 Mm) and the typical coronal sound speed (150 km s^{-1}), a standing slow wave would also have a period around 400 s. Alfvén waves appear in each thread as azimuthal modes with a period of nearly 50 s.

In Fig. 4.4, the kinetic energy reaches a steady state value around a time of 6000 s and remains there until about $t = 11000$ s, when it exponentially increases as the first kink instability occurs. The theoretical limit, computed from Eq. (4.13) and shown as a

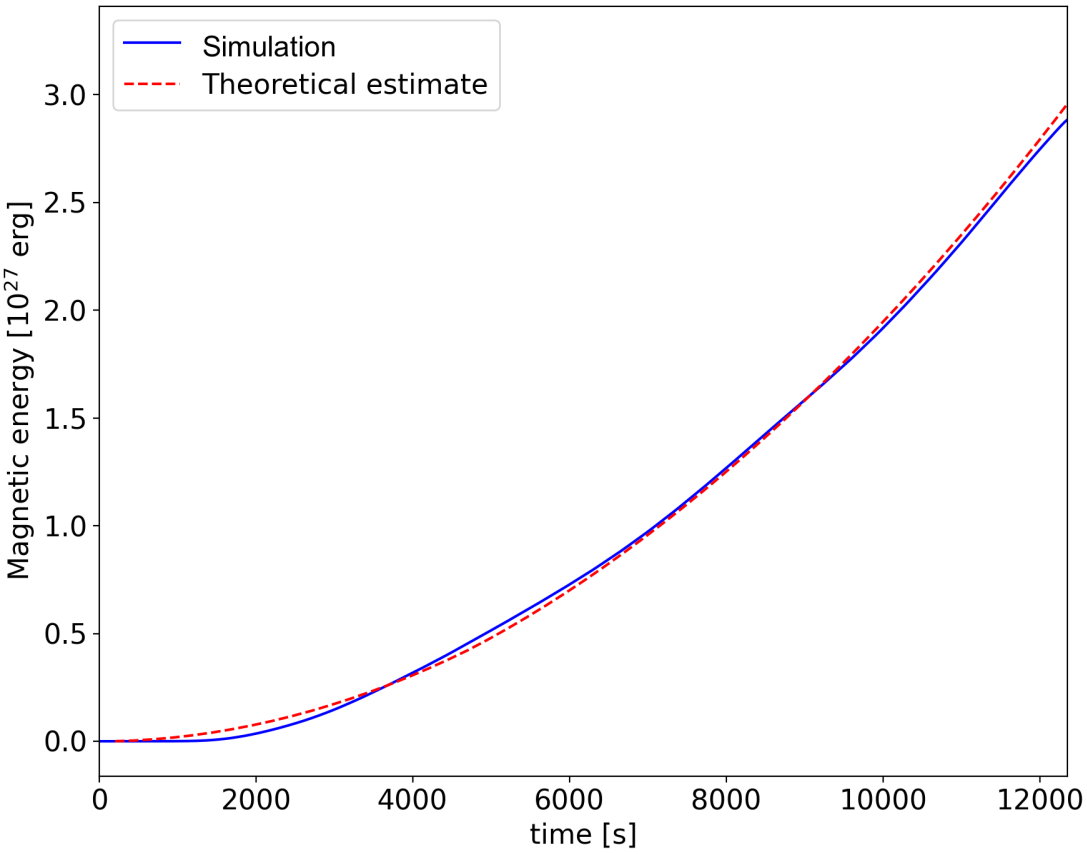

Figure 4.5: Evolution of the volume integrated magnetic energy prior to the instability. In blue is the total magnetic energy before the onset of the instability, plotted as a function of time. In dashed red is a theoretical estimate based on the model described in Sect. 4.3, which grows through the energy input by photospheric driving.

red dashed line, agrees with the actual volume-averaged kinetic energy. The oscillations in kinetic energy have a period of approximately $t = 180\,\mathrm{s}$ (see. Fig. 4.3) and are the result of magnetosonic waves. Moreover, the growth of the kinetic energy during the onset of the ideal kink instability is, as expected, exponential with time. This is shown in the internal panel of Fig. 4.4. In particular, the slope of the exponential increase matches with the theoretical value $\tau = 0.1 \times 2L/v_A$, where v_A is the Alfvén velocity (Van der Linden & Hood 1999; Hood et al. 2009).

Fig. 4.5 shows that the magnetic energy determined from the simulation is very close to the prediction of the theoretical model presented in the previous section. The

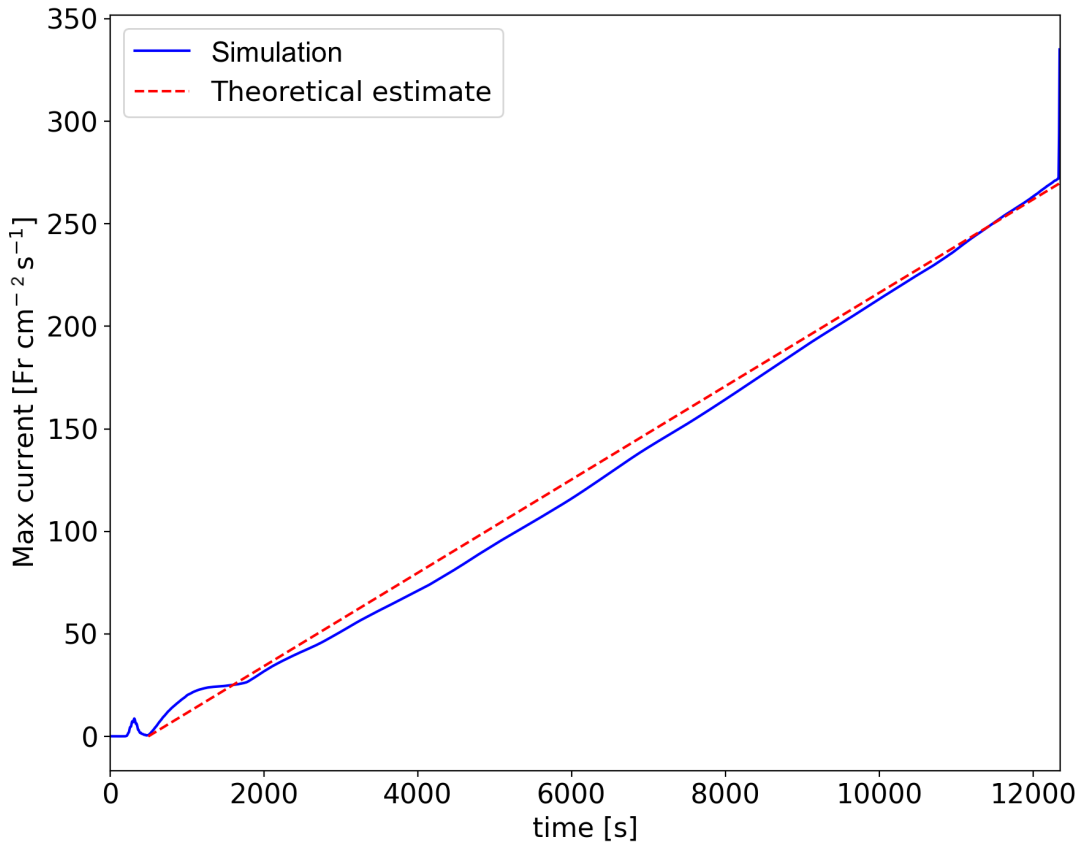

Figure 4.6: Evolution of the maximum current density. The solid, blue curve represents the maximum current intensity, before the onset of the instability, as a function of time. In dashed red is the theoretical estimate based on the model described in Sect. 4.3.

quadratic increase of the magnetic energy is determined by the linear growth of the azimuthal component of the magnetic field during the twisting.

The vertical component of the current density dominates over the other ones. It also grows linearly in time as a consequence of the magnetic tube twisting (see Fig. 4.6). As assumed in Eq. (4.15), the maximum current intensity is along the axis of each flux tube As shown in Fig. 4.7, the axial current remains positive around the centres of the strands. On the outer edge, there is a neutralizing negative current, ensuring the net axial current remains zero.

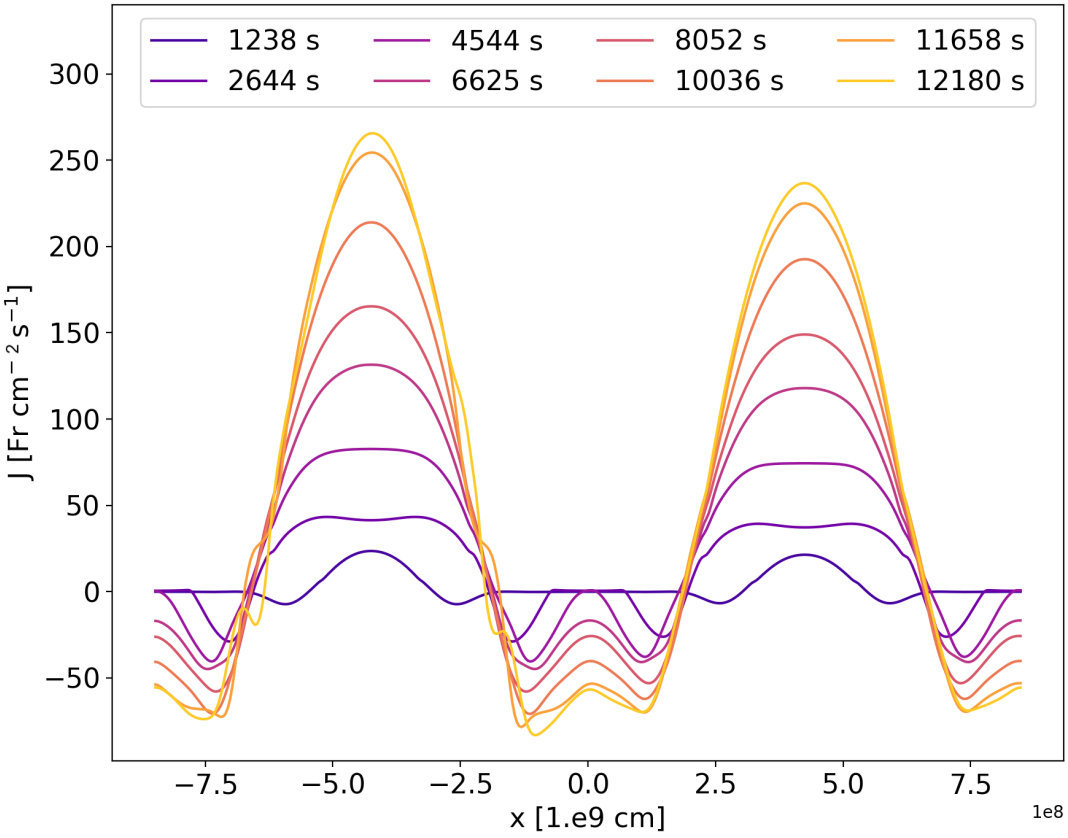

Figure 4.7: Profiles of the apex current intensity along the x-axis ($y = 0$) at different times.

4.4.2 Onset of the instability

The first tube becomes unstable after around 12400 s. We estimated the amount of twist, defined as $\Phi = 2\pi N$ (with N the number of twists in the unstable strand), at the time of the kink instability. We considered both the maximum tangential photospheric velocity v_ϕ and an averaged value $\langle v \rangle = \int_0^{2r_{\max.}} v_\phi r dr / \int_0^{2r_{\max.}} r dr$. In the first case, the $\Phi \approx 10$, while in the second one it is smaller by a factor of two. In both cases, Φ is of the same order of magnitude as previous results, such as the Kruskal-Shafranov condition ($\Phi_{KS} = 3.3\,\pi$) (Priest 2014).

The onset of the first kink instability and the subsequent MHD cascade can be followed by inspecting the current density and velocity evolution. For instance, Fig. 4.8 shows the current density distribution (first column) and the velocity field (second column) over the loop mid-plane at four different times. In the first panel ($t = 12400$ s),

the onset of the first kink instability is shown: the unstable flux tube begins to flex owing to the growing magnetic pressure imbalance. Consequently, a single current sheet forms at the edge of the loop, and the velocity grows at its sides. Then, in the second panel ($t = 12500$ s), the current sheet fragments in a turbulent way (see the velocity map) into smaller current sheets, and the entire structure expands to interact with the neighbouring loop. This causes the second strand's instability. The third ($t = 12550$ s) and fourth ($t = 12600$ s) panels show the evolution of the MHD cascade (i.e. second loop disruption) triggered by the first kink instability. Throughout the process, zones of high plasma velocity on the horizontal mid-plane spread over regions of high current density. This is expected since plasma is mostly accelerated by magnetic forces where magnetic field gradients are higher.

The average temperature peaks 100 s after the onset of the avalanche process, while the average density and radiative losses reach the maximum value after a further period of 800 s (see first panel of Fig. 4.9). The turbulent evolution of the system is difficult to follow, but quantitative information on its dynamics can be obtained from the maximum current, temperature, and velocity evolution shown in Fig. 4.9. The three plots show the same qualitative behaviour with some high peaks around $t = 12500$ s; that is, during large heating events corresponding to dissipation of relatively large current sheets. In particular, the first group of peaks occurs during the onset of the first kink instability. The second and third groups correspond to the times when the second loop is destabilized and when it is finally disrupted, respectively. Another peak in the current intensity occurs at $t = 13000$ s and is followed by a moderate enhancement in the loop temperature and velocity. It is produced by the formation and subsequent dissipation of a big current sheet induced by the continuous driving at the boundaries.

The dissipation of the multi-threaded loop into smaller current sheets can be traced by following the magnetic field lines connectivity over time. The third column of Fig. 4.8 shows the end points of some field lines on the upper boundary plane $z = z_{\max.}$. Red dots correspond to field lines connected at the bottom to the left footpoint (i.e. $z = -z_{\max.}$). Conversely, blue dots refer to field lines connected at the bottom to the footpoint on the right. Field lines were traced from the bottom side of the box and mapped into the upper one using a second-order Runge-Kutta integration scheme. The location of the starting points at $z = -z_{\max.}$ were updated according to the imposed rotation, while the points at the opposite side were expected to change as the field lines move or change by reconnection. It is easy to see that the field line connectivity changes as soon as the MHD cascade takes place and that magnetic reconnection has occurred in the meantime. Indeed, during the avalanche process, field lines from each strand become entangled and eventually cross the lateral boundaries of the domain. The same thing is likewise evident in Fig. 4.10, where field lines in the box are shown in full-3D rendering. The field lines were computed using a fourth order Runge-Kutta scheme, and colour was attributed depending on where on the photosphere the starting points were placed. As

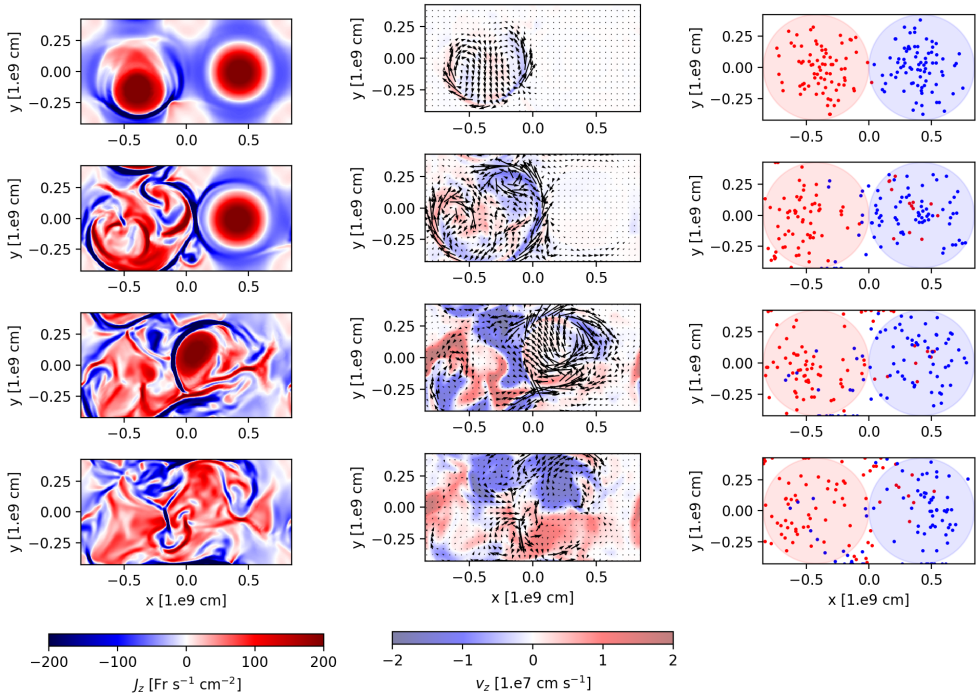

Figure 4.8: Onset and evolution of the MHD avalanche. First column: Horizontal cut of the current density across the mid-plane at times (from the top) $t = 12400$ s (onset of first kink instability), $t = 12500$ s, $t = 12550$ s (second strand's disruption), and $t = 12600$ s. Second column: Horizontal cut of the velocity across the mid-plane at the same four times. The arrows show the orientation of the velocity field. The colour maps evaluate the intensity of the vertical component of the velocity field. Third column: Terminal locations ($z = L$) of the sample field lines at the same four times. The red field lines (spots) depart from the $z = -L$ footpoint on the left (red shaded region), and the blue field lines depart from the right (blue shaded region). Initially, the red and blue field lines are randomly distributed inside the blue and red circles, respectively. Subsequent starting locations at the lower boundary points were determined at later times by tracking their locations in response to the photospheric motions.

the twisting triggers the kink instability, field lines reconnect with each other. At the end of the process, some light blue and purple lines connect different loop footpoints.

The energetics of the numerical experiment reflect the physical processes that drive the system dynamics. Fig. 4.11 shows the evolution of the four energy components (i.e. magnetic, kinetic, thermal, and gravitational energy). The magnetic energy dominates over the other components during the initial, smooth evolution of the system. As mentioned above, the main source of energy derives from the Poynting flux (see Fig. 4.2). The net effect of thermal conduction, radiative losses, and background heating is neg-

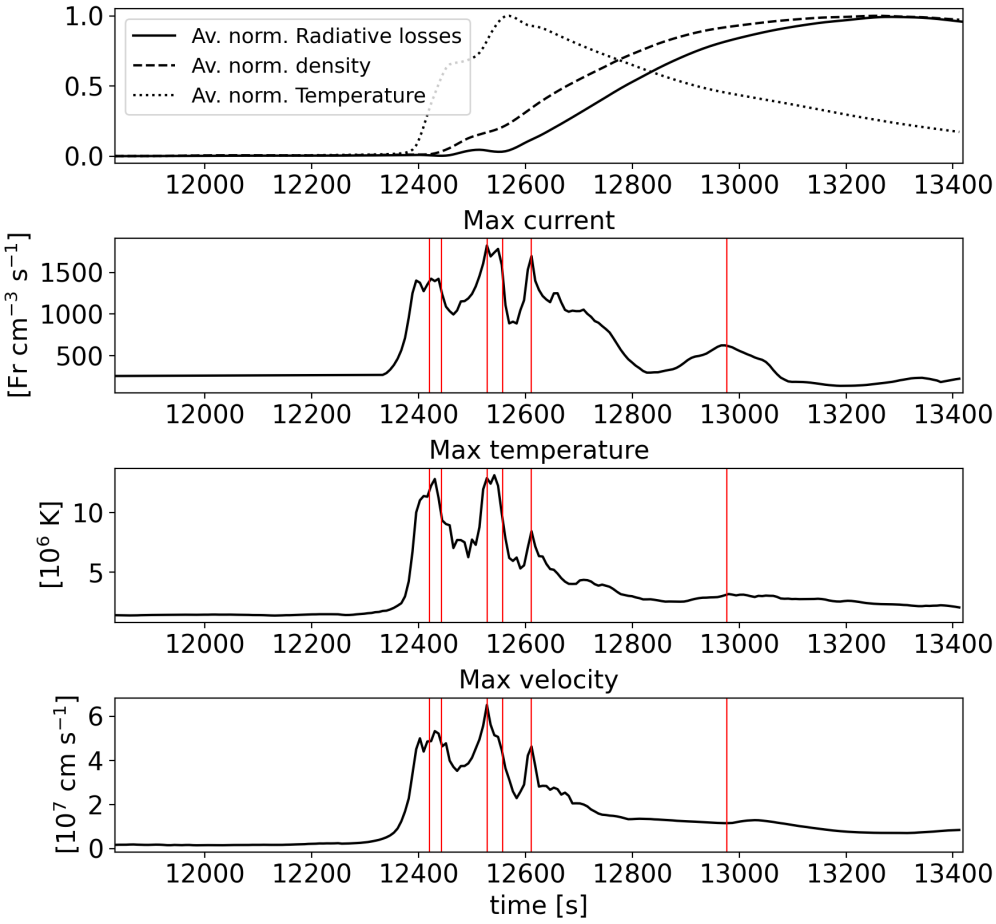

Figure 4.9: Global evolution of the MHD avalanche. From top to bottom: Average normalized radiative losses, density and temperature in the corona, maximum current density, maximum temperature, and maximum velocity against time. The red vertical lines mark the times of large heating events.

ligible provided that the magnetic field changes are slow compared with the radiative and conductive timescales. In Fig. 4.14, the sum of the time-integrated thermal flux, radiative losses, and uniform heating is practically zero, while the thermal conduction dominates over the radiative losses, as expected in typical coronal conditions.

After the onset of the MHD avalanche, the magnetic energy rapidly drops. The kinetic energy increases exponentially but remains at least one order of magnitude smaller than the magnetic energy. Most of the magnetic energy gained, through footpoint driving, is converted into heat, and the steep rise in thermal energy follows the plasma acceleration. This may be attributed to the accelerated conversion of kinetic energy into internal energy during the instability, which cascades energy to smaller scales where it can be

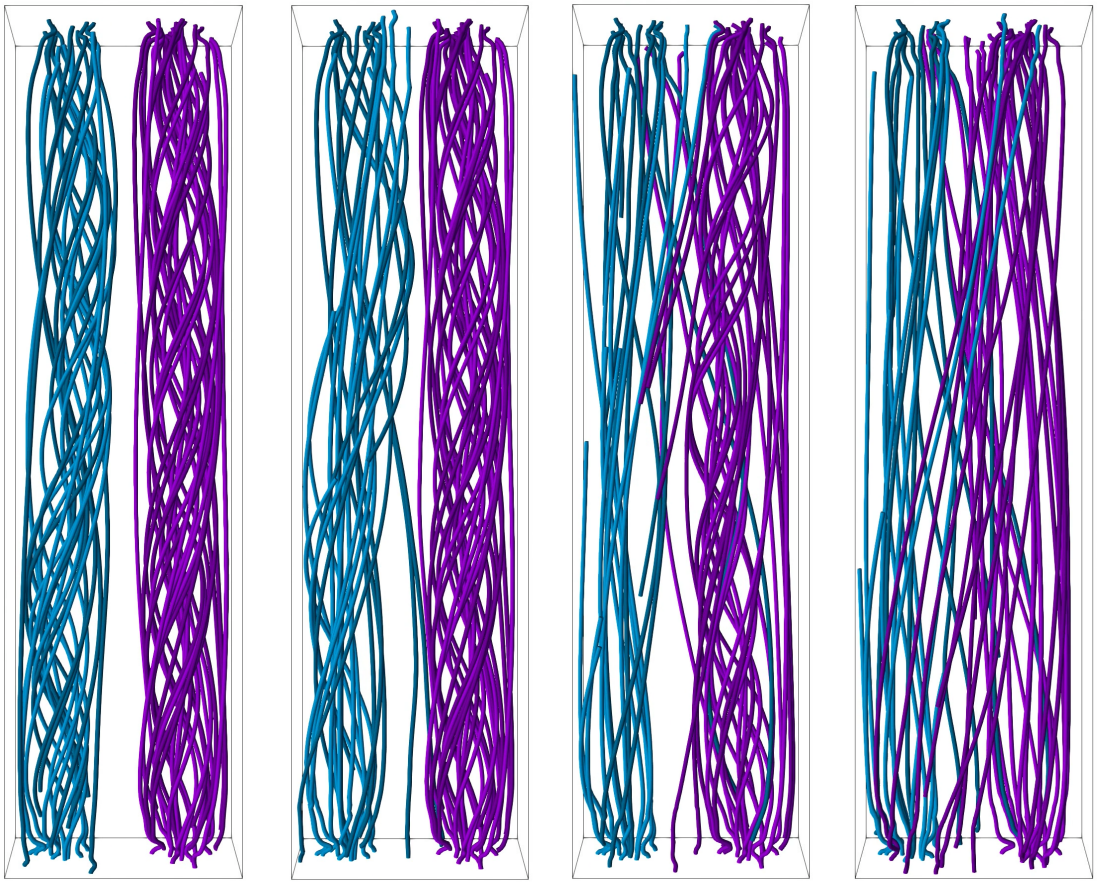

Figure 4.10: Three-dimensional rendering of the magnetic field lines in the box around the two flux tubes at different times. Far left panel: Field lines at $t = 12400\,\mathrm{s}$ (onset of first kink instability). Middle left panel: Field lines at $t = 12500\,\mathrm{s}$. Middle right panel: Field lines at $t = 12550\,\mathrm{s}$ (second loop disruption). Far right panel: Field lines at $t = 12600\,\mathrm{s}$. The change in the field line connectivity during the evolution of the MHD cascade is highlighted by the different colours.

dissipated more efficiently through numerical dissipation.

Fig. 4.12 shows how the rate of change in magnetic energy matches the instantaneous Ohmic heating and how it, in turn, influences the rate of change in heating.

Several heat pulses released after the multiple magnetic reconnection events enhance the thermal conductive flux towards both transition regions (see Fig. 4.14). The heat flow was then slowed down in the chromosphere because conduction is less efficient at cooler temperatures. As a consequence, an excess of pressure accumulates in the transition region and the top of the chromosphere. This creates the pressure gradient

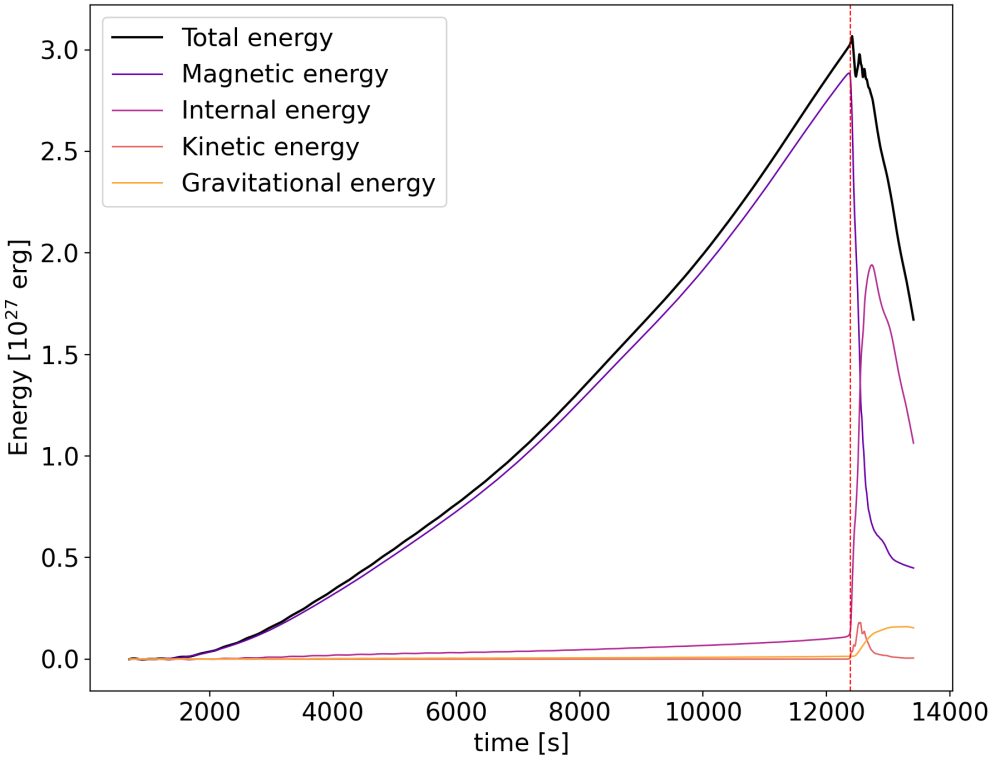

Figure 4.11: Magnetic (purple), internal (pink), kinetic (orange), and gravitational (yellow) energies as functions of time. The black is the total energy given as the sum of the four energy terms. The onset of the avalanche is marked with a vertical red dashed line.

that causes the evaporative upflow. The plasma expanding upwards, in turn, leads to an increase in the coronal density inside the magnetic structure.

The sudden growth of the gravitational potential energy traces this strong mass flow upwards, as shown in Fig. 4.13. After the beginning of the MHD avalanche, the gravitational energy increases as a consequence of the chromospheric plasma evaporation in the coronal volume. It supplied gravitational energy flux at the boundaries while the remaining contribution to the potential energy is given by the work done by the gravity force to distribute this denser plasma over the entire loop length.

Fig. 4.15 shows the average vertical thermal flux, radiative losses, density, and temperature as a function of time and height. The strongest thermal flux (first panel)

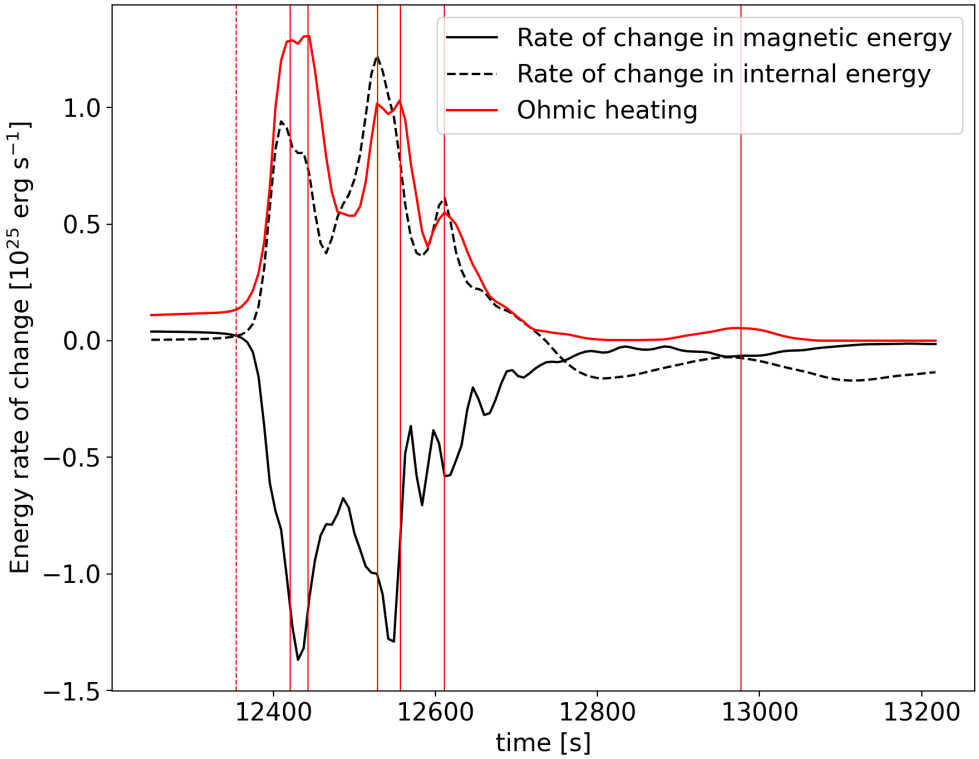

Figure 4.12: Rates of change in magnetic (solid black) and internal (dashed black) energies and Ohmic heating (red) as functions of time. The vertical red solid lines highlight times of large heating events. The onset of the avalanche is marked with a vertical red dashed line.

developed at the times when each loop is disrupted (i.e. when the temperature gradient is greatest). The heat flux propagates towards the upper and lower transition regions and was stronger in the corona. In contrast, the radiative losses (second panel) were stronger at later times, when the density (third panel) has increased by chromospheric evaporation. The biggest contribution is localised in the transition region where the rates exceed the coronal radiative losses by at least two orders of magnitude. As heating released during the MHD avalanche rapidly spread (in few tens of seconds) along the tube, temperature (fourth panel) rises uniformly. It then slowly decreases from 10 MK to 1 MK on a timescale of 1000 s.

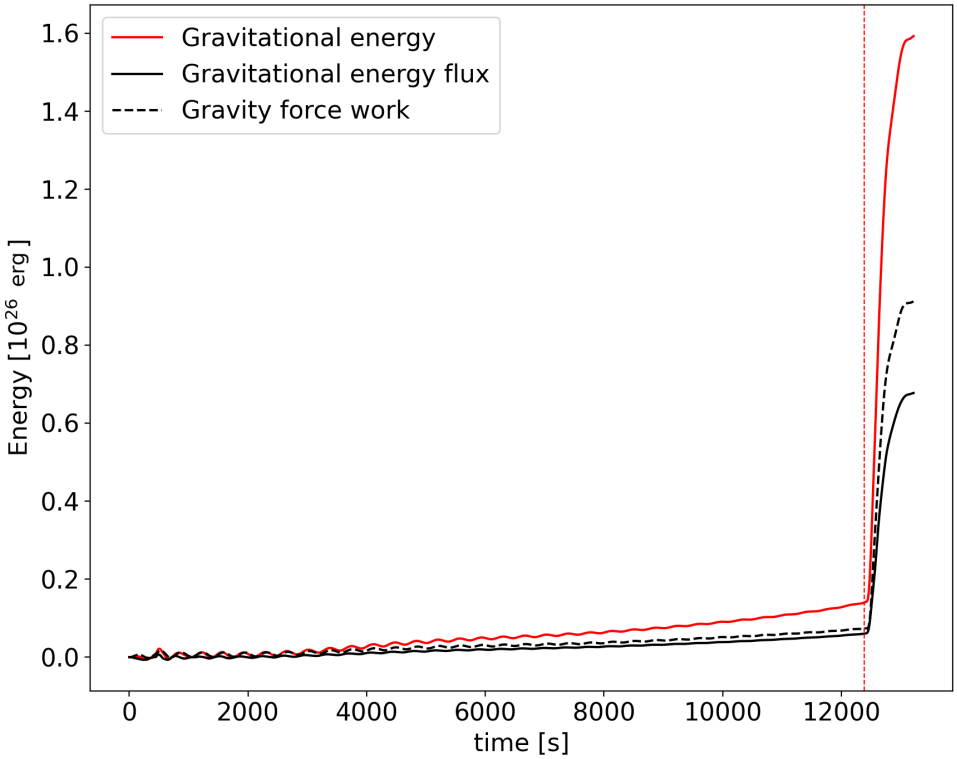

Figure 4.13: Gravitational energy (red), time-integrated gravitational energy flux (solid black), and work done by gravity (dashed black) as functions of time. The onset of the avalanche is marked with a vertical red dashed red line.

4.4.3 Three-stranded loop simulation

The propagation of the instability described so far is an avalanche process that can extend to increasing numbers of nearby flux tubes (Hood et al. 2016). To ensure this progression, we performed a second numerical experiment with three interacting strands within a coronal loop. The initial configuration of the magnetic structure is shown in the left panel of Fig. 4.16. As in the previous case, this magnetic structure is embedded in a stratified atmosphere with a cold ($T \simeq 10^4$K) chromospheric layer and a hot and tenuous corona ($T \simeq 10^6$K and $n \simeq 10^9$cm^{-3}). Equations (2.2 - 2.5) summarize the underlying physics driving the evolution of the system, as discussed in Sec. 5.2. As in the first case, one of the magnetic strands is twisted at its footpoint faster than the others and becomes kink unstable. The right panel of Fig. 4.16 shows the propagation

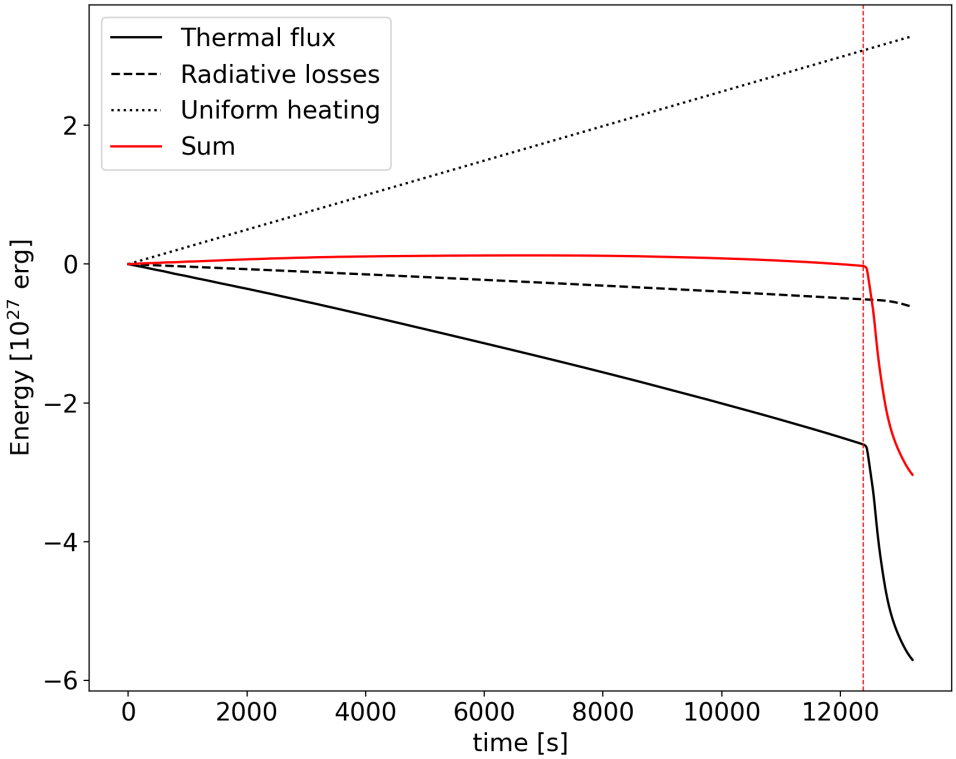

Figure 4.14: Time-integrated thermal flux (solid black), radiative losses (dashed black), and background heating (dotted black) as functions of time. The solid red curve is the sum of the three contributions. The onset of the avalanche is marked with a vertical red dashed line.

of the instability from a central, faster tube to the two adjacent tubes. As expected, the first unstable strand triggers the global dissipation of the magnetic structure into smaller current sheets. Heating by Ohmic dissipation is localised inside relatively small regions where the current density is higher. These current sheets develop and spread in a turbulent way throughout the entire extension of the domain.

4.5 Discussion

This work addresses the energy released impulsively in the corona under strong magnetic stresses. In particular, we have shown that MHD avalanches are efficient mechanisms for

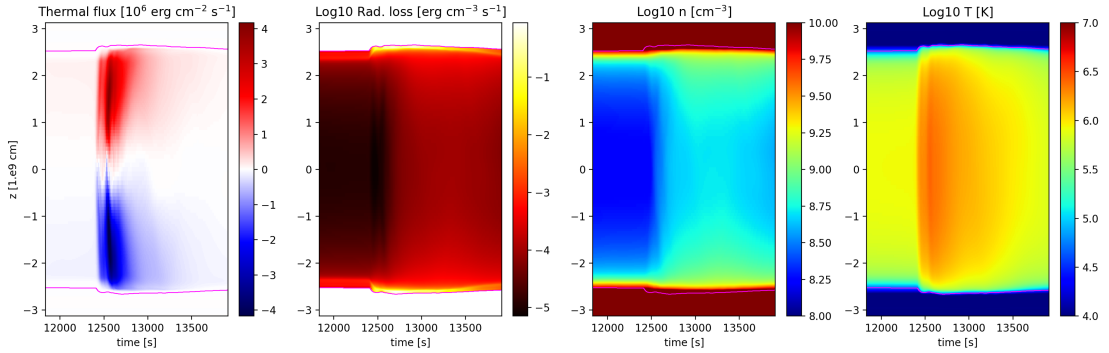

Figure 4.15: Average vertical thermal flux, radiative losses, plasma density, and temperature against time (on the horizontal axis) and height (z; on the vertical axis). The averaging is on the horizontal planes. The region of the domain where the temperature exceeds 10^4 K (i.e. transition region and corona) is bounded (magenta lines).

fast release of magnetic energy in the solar corona progressively stored by slow, uniform photospheric motions. We describe a system consisting of two neighbouring twisted flux tubes. These interacting flux tubes comprise a stratified atmosphere including chromospheric layers, a thin transition region to the corona, and an associated transition from high-β to low-β regions. Our model includes the effects of thermal conduction and of optically thin radiation. Rotation of the plasma at the upper and lower boundaries of our computational domain applies twisting to the magnetic flux tubes. Since line-tying of the field lines at the photospheric boundaries is expected to be maintained over time by high plasma beta values and a sufficient spatial resolution, each loop can develop high levels of twist, as the azimuthal component of the magnetic field increases. Above a certain stress threshold, the structure becomes kink-unstable and suddenly relaxes to a new equilibrium configuration (Hood et al. 2009). In particular, since one strand is twisted faster than the other, that strand will become unstable before the other and trigger the avalanche process that will, in turn, spread as it affects the neighbouring flux tube. Magnetic reconnection between unstable flux tubes causes bursty and diffuse energy release (similar to a nanoflare storm) and changes the field connectivity. Moreover, through repeated reconnection events, the system relaxes towards the minimum energy state. The system undergoes an initial dynamic phase where the plasma is rapidly accelerated. The initial helical current sheet progressively fragments in a turbulent way into smaller current sheets, which, in turn, dissipate magnetic energy via Ohmic heating. As soon as the steep rise in kinetic energy is damped in the corona, the released heating rapidly increases the coronal temperatures and, consequently, the pressure scale-height. As a consequence of that process, the steep rise in temperature is followed by a

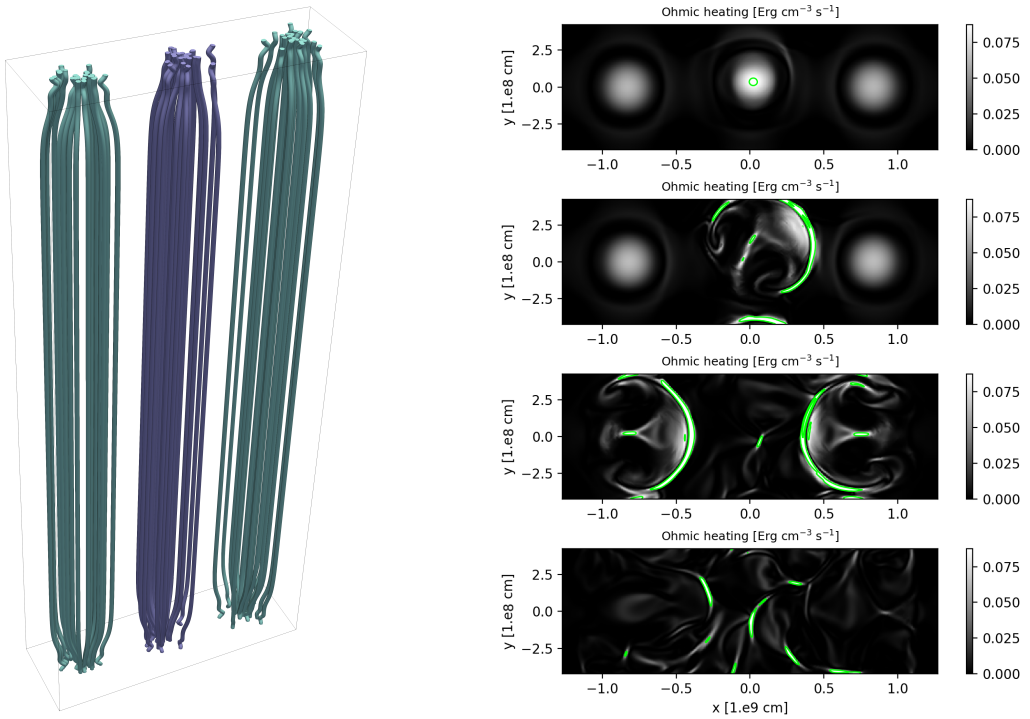

Figure 4.16: Three-threaded coronal loop simulation: initial condition and evolution of the MHD avalanche. Left panel: Three-dimensional rendering of the initial magnetic field configuration in the proximity of each coronal loop (for the second model, with three strands). The purple field lines were subjected to a faster twisting driver than the green ones. Right panel: Horizontal cut of the Ohmic heating per unit time and per unit volume at the middle of the box at different times. From the top down, these times are: $t = 11200$ s (onset of first kink instability), $t = 11400$ s, $t = 11800$ s (disruption of the second and third strands), and $t = 11900$ s. The green filaments indicate areas where the current density exceedes the threshold value for dissipation.

progressive coronal density enhancement due to chromospheric evaporation.

Results achieved in this work agree with those found by Hood et al. (2009), Hood et al. (2016), and Reid et al. (2018), but also go further and extend them. In particular, we demonstrate that even inside a stratified atmosphere, highly twisted loops with zero net current undergo the non-linear phase of the kink instability where reconnection in a single current sheet triggers the fragmentation of the flux tubes at multiple reconnection sites. In particular, once the first unstable strand is disrupted, it coalesces with the neighbouring strands, inducing an MHD cascade, as found in uniform coronal atmospheres (Tam et al. 2015; Hood et al. 2016; Reid et al. 2018).

As shown in Fig. 4.12, magnetic energy is released in discrete bursts as stable strands

are disrupted and single current sheets are dissipated. This bursty heating does not show evidence of reaching a steady state.

Thermal conduction is very effective in spreading heating along field lines, and this leads to the filamentary structuring in loop temperature. Also, as shown in Fig. 4.9, because of thermal conduction, the temperature grows to about 10^7 K, which is much cooler than the temperatures of approximately 10^8 K found in Hood et al. (2009). Peak temperatures of a few tens of millions of kelvin as well as variations in magnetic and internal energy of 10^{27} erg are found in our simulations. They agree with those measured from microflare observations (Testa & Reale 2020).

Radiation also has an important effect on the temperature distribution. Radiative losses are stronger across the transition region, where the plasma density is higher. As the upper atmosphere is heated, this layer acts as a thermostat for the corona since it tends to restore the initial coronal temperature. Indeed, it maintains the temperature gradient that allows heat to flow out of the corona.

A deep chromospheric layer is important to guarantee line-tying throughout the whole evolution of the coronal loop. With this layer in place, photospheric motions can slowly twist the magnetic flux tubes expanding across the chromospheric layer. At the same time, the chromosphere acts as a reservoir of dense plasma that can flow into the corona as a consequence of impulsive heating. Modelling the chromospheric evaporation and the resulting increase of the loop emissivity is fundamental to corroborate the results through comparison with EUV and X-ray observations of dynamic coronal loops.

As shown in Sect. 4.4.3, the propagation of the instability is an avalanche process that can extend to increasing numbers of nearby flux tubes (Hood et al. 2016). In conclusion, this work confirms, and constrains the conditions for, the propagation of a kink instability amongst a cluster of flux tubes, including a more complete, stratified loop atmosphere, as well as important physical effects, in particular thermal conduction and optically thin radiative losses. The avalanche can trigger the ignition and heating of a large-scale coronal loop with parameters not far from those inferred from the observations.

The reconfiguration of the magnetic structure and the resulting plasma dynamics have been found to occur at timescales on the order of 10 s and over spatial scales smaller than one arcsecond. The detection of these small scales involved in coronal heating release will be the target of high-resolution spectroscopic observations of future missions, such as MUSE (Cheung et al. 2022; De Pontieu et al. 2022) and SOLAR-C/EUVST (Shimizu et al. 2020).

5

Coronal heating by MHD avalanches: EUV line emission from a multi-threaded coronal loop

This chapter is structured based on the paper titled "Coronal heating by MHD avalanches II. EUV line emission from a multi-threaded coronal loop" (Cozzo et al. 2024).

Magnetohydrodynamic instabilities, such as the kink instability, can trigger the chaotic fragmentation of a twisted magnetic flux tube into small-scale current sheets that dissipate as aperiodic impulsive heating events. In turn, the instability could propagate as an avalanche to nearby flux tubes and lead to a nanoflare storm. The previous section was devoted to related 3D MHD numerical modelling, which included a stratified atmosphere from the solar chromosphere to the corona, tapering magnetic field, and solar gravity for curved loops with the thermal structure modelled by plasma thermal conduction, along with optically thin radiation and anomalous resistivity for 50 Mm flux tubes. Using 3D MHD modelling, this section addresses predictions for the extreme-ultraviolet (EUV) imaging spectroscopy of such structure and evolution of a loop, with an average temperature of 2-2.5 MK in the solar corona. We set a particular focus on the forthcoming MUSE mission, as derived from the 3D MHD modelling. From the output of the numerical simulations, we synthesized the intensities, Doppler shifts, and non-thermal line broadening in three EUV spectral lines in the MUSE passbands: Fe IX *171 Å, Fe* XV *284 Å, and Fe* XIX *108 Å, emitted by* ~ 1 MK, ~ 2 MK, *and* ~ 10 MK *plasma, respectively. These data were detectable by MUSE, according to the MUSE expected pixel size, temporal resolution, and temperature response functions. We provide maps showing different view angles (front and top) and realistic spectra. Finally, we discuss the relevant evolutionary processes from the perspective of possible observations. We find that the MUSE observations might be able to detect the fine structure determined by*

tube fragmentation. In particular, the Fe IX *line is mostly emitted at the loop footpoints, where we might be able to track the motions that drive the magnetic stressing and detect the upward motion of evaporating plasma from the chromosphere. In Fe* XV*, we might see the bulk of the loop with increasing intensity, with alternating filamentary Doppler and non-thermal components in the front view, along with more defined spots in the topward view. The Fe* XIX *line is very faint within the chosen simulation parameters; thus, any transient brightening around the loop apex may possibly be emphasized by the folding of sheet-like structures, mainly at the boundary of unstable tubes. In conclusion, we show that coronal loop observations with MUSE can pinpoint some crucial features of MHD-modelled ignition processes, such as the related dynamics, helping to identify the heating processes.*

5.1 Introduction

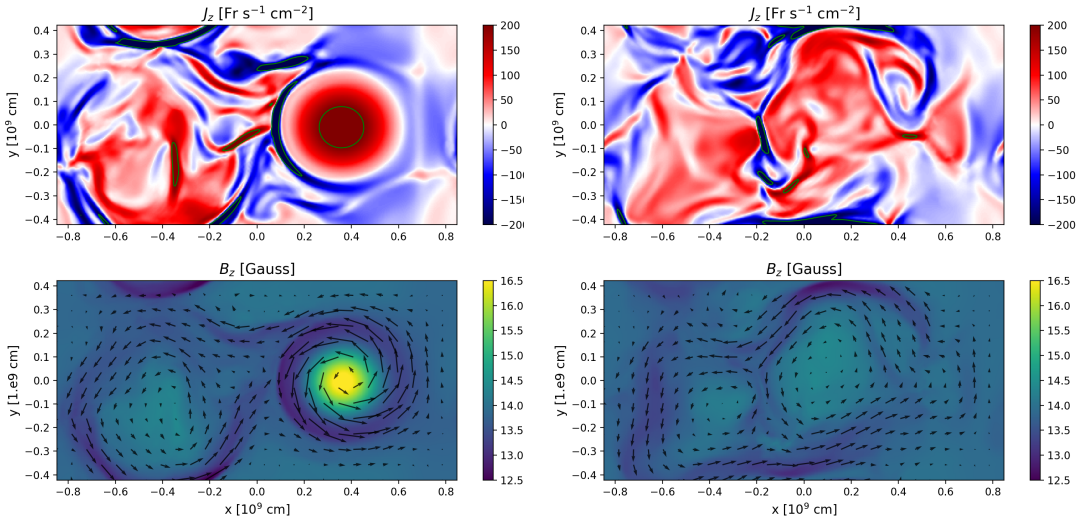

Figure 5.1: MHD avalanche 2D snapshots. Upper panels. Horizontal cuts of the current density across the mid plane at time $t = 180$ s (left) and $t = 285$ s (right). The green contours encloses the regions of the domain heated by Ohmic dissipation. Lower panels. Horizontal cuts of the magnetic field across the mid-plane at the same snapshot-times as before. The vector field is included.

The Multi-slit Solar Explorer (MUSE, De Pontieu et al. 2020; De Pontieu et al. 2022; Cheung et al. 2022) is an upcoming NASA MIDEX mission, featuring a multi-slit extreme-ultraviolet (EUV) spectrometer and an EUV context imager, planned for launch

Table 5.1: MUSE spectrometer emission lines.

Line	Wavelength [$\mathring{A}$]	$\log_{10}$ (T [K])
Fe IX	171	5.9
Fe XV	284	6.4
Fe XIX / Fe XXI	108	7.0 / 7.1

in 2027. MUSE is designed to offer high spatial and temporal resolution for spectral and imaging observations of the solar corona. One of the MUSE science goals is to advance the understanding of the heating mechanisms in the corona of both the quiet Sun and active regions, as well as of the physical processes governing dynamic phenomena like flares and eruptions. MUSE will provide fine spatio-temporal coverage of coronal dynamics, as well as wide field of view (FoV) observations, offering valuable insights into the physics of the solar atmosphere. In particular, it will obtain high resolution spectra ($\approx$ 0.38"), with wide angular coverage ($\approx$ 156" $\times$ 170"; resembling the typical size of an active region) and 12 s cadence. With its 35-slit spectrometer, MUSE will provide spectral observations, with unprecedented combination of cadence and spatial coverage, in different EUV passbands dominated by strong lines formed over a wide temperature range, enabling the testing of state-of-the-art models related to coronal heating, solar flares, and coronal mass ejections.

The main EUV lines in the MUSE passbands (171Å Fe IX, 284Å Fe XV, and 108Å Fe XIX and Fe XXI), are listed in Table 5.1 (for details, see De Pontieu et al. 2020; De Pontieu et al. 2022). Here, we focus on the new spectroscopic diagnostics provided by MUSE, but of course the findings can be extended to observations with other imaging and spectroscopic solar instruments observing at similar wavelengths, for instance, SDO/AIA (Pesnell et al. 2012; Lemen et al. 2012), Hinode/EIS (Culhane et al. 2007; Tsuneta et al. 2008), and the forthcoming Solar-C/EUVST (Shimizu et al. 2019).

To make meaningful predictions that can then be compared with solar observations, two critical developments are essential. Firstly, the modelling approach must encompass crucial physical components, including the thermodynamic response of the atmosphere, to derive realistic observational outcomes. Secondly, observational techniques must achieve sufficient temporal and spatial resolution within the pertinent spectral bands. The synergistic comparison between coronal observations and synthetic plasma diagnostics from numerical simulations can, on the one hand, significantly improve our interpretative power on real observational data. On the other hand, it can also help to refine the solar coronal modelling process.

This study focuses on extending the plasma diagnostics of the MHD avalanche model introduced by Cozzo et al. (2023b), also presented in Chap. 4, to observations with the forthcoming MUSE spectrograph. Although our analysis addresses plasma diagnostics from the MUSE spectrometer, the present work has a more general application to the plasma emission at representative coronal temperatures.

We extracted plasma diagnostics from a full 3D MHD simulation of a flaring coronal loop undergoing an MHD avalanche, as described in Cozzo et al. (2023b) and Chap. 4. In particular, we modelled the response of the MUSE spectrometer by using our simulated plasma output to synthesize line emission, intensity maps, Doppler shifts and non-thermal line widths, across the three spectral channels available with the instrument.

5.2 Model

The model setup is described in Sec. 2 and Sec. 4.2.3. The magnetised solar atmosphere is a 3D cartesian box of size, $-x_M < x < x_M$, $-y_M < y < y_M$, and $-z_M < z < z_M$, where $x_M = 2y_M = 8.5 \times 10^8$ cm, and $z_M = 3.1 \times 10^9$ cm.

The background atmosphere consists of a chromospheric and a coronal column separated by a thin transition region. In the corona, two flux tubes interact, each with a length 50 Mm and initial temperature of approximately 10^6 K, while the two chromospheric layers are $\sim$ 6 Mm wide each and 10^4 K hot. The transition region, $\approx$ 1 Mm wide, is artificially broadened using Linker–Lionello–Mikić method (Linker et al. 2001; Lionello et al. 2009; Mikić et al. 2013).

Two rotational motions at the footpoints twist each of the flux tubes. The two rotating regions have the same radius ($R \approx 1$ Mm), but one has an angular velocity that is higher than the other by 10% ($\approx 10^{-3}$ rad s^{-1} vs. $\approx 0.9 \times 10^{-3}$ rad s^{-1}), so that the faster strand becomes unstable first, triggering the avalanche process. As a reference time, deemed $t = 0$ s, we chose the time when the faster flux tube is nearly kink-unstable. Then, this kink-unstable tube rapidly disrupts the other one ($t = 285$ s). A 3D rendering of the two flux tubes and of their interaction as a result of the instability is shown in Fig.5.2. Here, we focus on the evolution after the first kink instability.

The left panels of Fig. 5.1 shows a cross-section at the mid-plane of the computational box at time $t = 180$ s, after the beginning of the instability, when the flux tube on the left ($x < 0$) has already become unstable and fragmented, and is about to trigger the instability of the flux tube on the right ($x > 0$). The current density map (top left panel) clearly shows on the left the thin, intense current sheets, around which magnetic reconnection occurs and magnetic energy dissipates. On the right of the map, we see the other flux tube, still not involved in the instability. In the lower-left panel, we show the magnetic field intensity: where the left-hand flux tube was, the field is more blurred, dispersed, and irregularly distributed as a consequence of the instability. The flux tube on the right is still compact and coherent. The twisting is emphasized by the vector

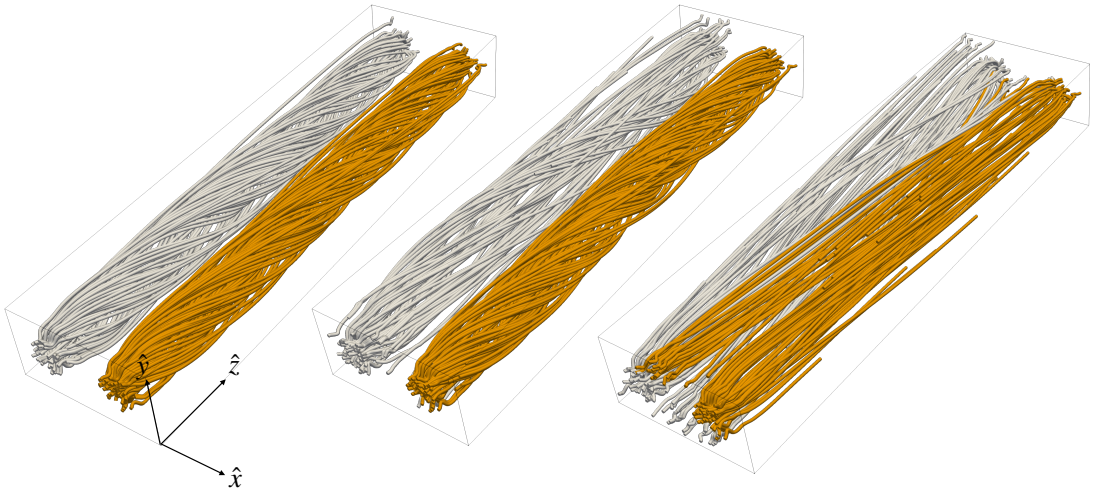

Figure 5.2: 3D rendering of the magnetic field lines inside the box at times (from left to right): $t = 0$ s (initial condition), 180 s, (first loop disruption), and 500 s. The change in the field line connectivity during the evolution of the MHD cascade is emphasized by the colors.

field of the component parallel to the plane. The right panels of Fig. 5.1 show the same quantities as do those on the left, but at a later time ($t = 285$ s), when the flux tube on the right has also been disrupted.

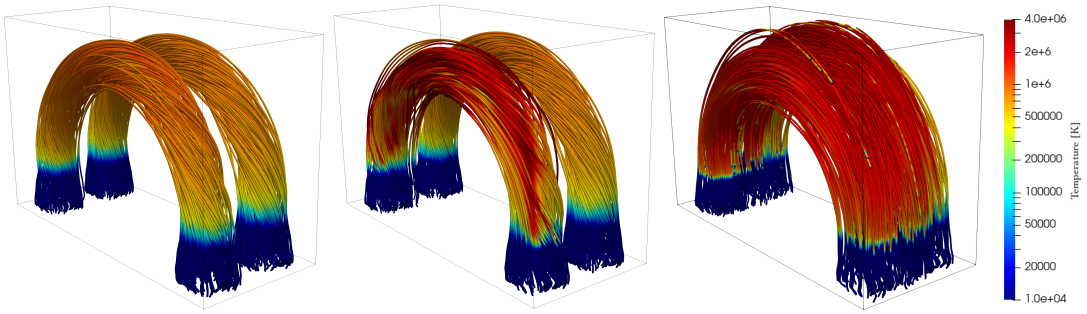

Figure 5.3: 3D rendering of the magnetic field lines inside the box at the same times shown in Fig.5.2. Magnetic field lines are color-coded according to the plasma temperature.

The emission intensity I (Boerner et al. 2012) from the modelled (optically thin)

plasma expected to be measured with MUSE is:

$$I(x, y) = \int_0^\infty \Lambda_f(T)\,\mathrm{DEM}(T)\,dT, \tag{5.1}$$

where $\Lambda_f(T)$ is the temperature response function per unit pixel for the line, f, and $\mathrm{DEM}(T) = n_H n_e \frac{dz}{dT}$ is the differential emission measure (with n_e the free electron density). Then, $\Lambda_f(T)$ combines the emission properties of the plasma with the response of the instrument:

$$\Lambda_f(T) = \int_0^\infty G(\lambda, T)\,R_f(\lambda)\,A_{\mathrm{pix}}\,d\lambda, \tag{5.2}$$

where $G(\lambda, T)$ is the plasma contribution function, $R_f(\lambda)$ is the spectral response of the f-th instrument channel, and A_{pix} is the area of a single MUSE pixel (0.167" × 0.4").

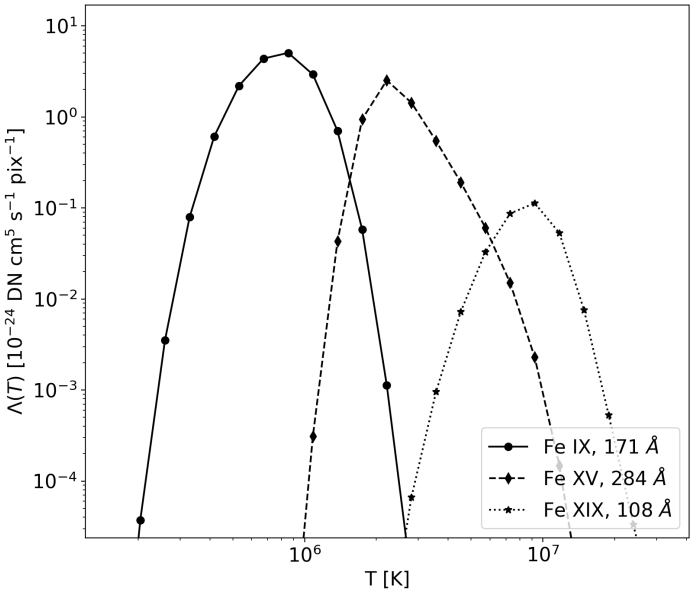

Figure 5.4: Response function $\Lambda_i(T)$ for the three MUSE emission lines (Fe IX, Fe XV, and Fe XIX) as a function of temperature.

5.3 Methods

5.3.1 Forward modelling

The temperature response functions for the three MUSE channels are shown in Fig. 5.4. They are calculated using CHIANTI 10 (Del Zanna et al. 2021) with the CHIANTI ion-

ization equilibrium, coronal element abundances (Feldman 1992), assuming a constant electron density of $10^9\,\mathrm{cm}^{-3}$, and no absorption considered. Each curve is multiplied by a factor to convert photons into data-numbers (DN). Each curve peaks approximately at the temperatures listed in table 5.1. The intensity of a single cell, labeled in the numerical grid by the indices i, j, k, in units of $\mathrm{DN\,s^{-1}\,pix^{-1}}$, is equal to (De Pontieu et al. 2022):

$$F_{i,j,k} = n^2_{e\,i,j,k}(T)\,\Lambda_f(T)\,\Delta z, \tag{5.3}$$

with $n_e \simeq \frac{\rho}{\mu\, m_H}$, where ρ is the mass density, m_H is the hydrogen mass, and Δz is the cell extent along a specific line of sight (LoS), such as $\hat{z}$. We assume a Gaussian profile for each line, at a fixed temperature and density. Therefore, each cell, with a local velocity of $v_{i,j,k}$ along the LoS, contributes to the overall line spectrum with the following single-cell line profile:

$$f_{i,j,k}(v) = \frac{F_{i,j,k}}{\sqrt{2\pi\sigma_T^2}} \exp\left[-\left(\frac{v - v_{i,j,k}}{\sigma_T}\right)^2\right], \tag{5.4}$$

where

$$\sigma_T = \sqrt{\frac{2\,k_b\,T}{m_{\mathrm{Fe}}}} \tag{5.5}$$

is the thermal broadening and m_{Fe} is the iron atomic mass, since we will look only at iron lines. The synthetic instrument response, namely, the integrated emission along the LoS is computed as:

$$I_0^{i,j} = I_{i,j} = \sum_k F_{i,j,k}\,. \tag{5.6}$$

MUSE will measure the line profiles, from which we can derive the line Doppler shifts and the line widths. We can compute the first moment of the velocity distribution along the LoS:

$$I_1^{i,j} = v_{i,j} = \frac{\sum_k F_{i,j,k} v_{i,j,k}}{I_0}, \tag{5.7}$$

which can be compared to the Doppler shifts measured along the LoS. We can derive the non-thermal contribution to the line width (measured after subtracting the thermal line broadening, σ_T, and instrumental broadening) from the second moment of the velocity:

$$I_2^{i,j} = \Delta v_{i,j} = \sqrt{\frac{\sum_k F_{i,j,k}(v_{i,j,k} - I_{1i,j})^2}{I_0}}. \tag{5.8}$$

5.4 Data interpolation

To resemble the typical, semicircular, coronal loops shape, the original simulation results have been remapped and interpolated onto a new cartesian grid (see Fig. 5.5). In particular, points (x, y, z) in the original grid corresponds to points $(\tilde{x}, \tilde{y}, \tilde{z})$ defined by equations (5.9) for the corona and (5.10) for the chromospheric layer.

Specifically, the coronal region of the domain ($z \in [-L, L]$) is transformed into a half cylinder shell with characteristic radius $R_0 = 2\,L/\pi$:

$$\begin{cases} \tilde{x} = R \sin\theta, \\ \tilde{y} = x, \\ \tilde{z} = R \cos\theta. \end{cases} \qquad \text{for} \quad z \in [-L, L] \tag{5.9}$$

with $R = R_0 + y$ and $\theta = \frac{\pi}{2}\frac{z}{L}$.

The chromospheric layers are instead threaded as two parallel parallelepipeds of height $z_{\max} - L$:

$$\begin{cases} \tilde{x} = y, \\ \tilde{y} = x, \\ \tilde{z} = L - |z|, \end{cases} \qquad \text{for} \quad |z| > L. \tag{5.10}$$

New vectors components $(\tilde{v}_x, \tilde{v}_y, \tilde{v}_z)$, such as velocity and magnetic field, are obtained from the former (v_x, v_y, v_z) using the following rule:

$$\begin{bmatrix} \tilde{v}_x \\ \tilde{v}_y \\ \tilde{v}_z \end{bmatrix} = \begin{bmatrix} 0 & -\sin\theta & \cos\theta \\ 1 & 0 & 0 \\ 0 & -\cos\theta & \sin\theta \end{bmatrix} \cdot \begin{bmatrix} v_x \\ v_y \\ v_z \end{bmatrix} \tag{5.11}$$

where both triads $\tilde{v}_i$ and v_i are functions of $(\tilde{v}_x, \tilde{v}_y, \tilde{v}_z)$. In general, the correspondence between the former set of coordinates and latter is that the gravity vector $\mathbf{g}$ points uniformly along $\tilde{z}$. Magnetohydrodynamic quantities are interpolated in the new geometry at high resolution, compatible with the original cell sizes. Synthetic observables are first extracted with such resolution, i.e. the dimension of the cells edges perpendicular to the LoS, and then rebinned to the given instrument resolution. In particular, the grid pixel size will be equal to 170 km × 290 km, corresponding to 0.167” × 0.4” i.e. the angular extension of the instrument’s pixel (parallel and perpendicular to the slits orientation).

Figure 5.3 shows the resulting field line configuration colored by temperature in the new geometry at the three times already shown in Fig. 5.2.

5.5 Results

To replicate the typical, semicircular, coronal loops shape better, the original data have been remapped and interpolated onto a new cartesian grid. The method is discussed in

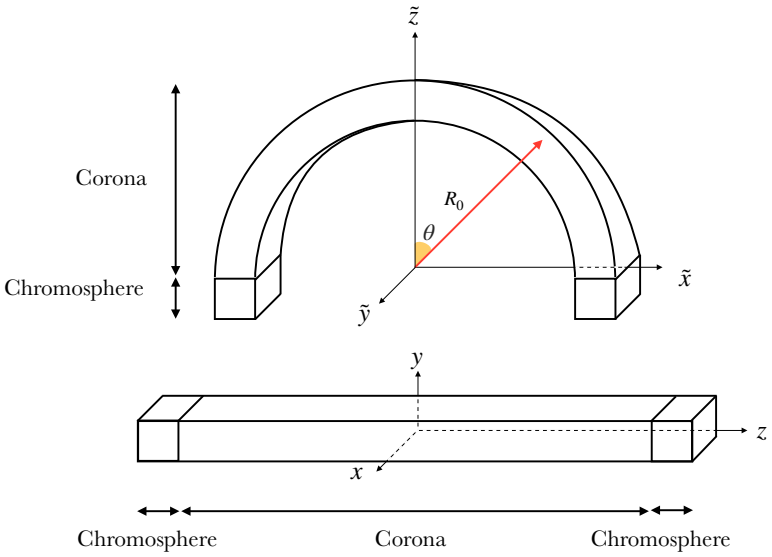

Figure 5.5: Original and interpolated box geometry. Lower picture: schematic representation of the 3D box containing the computational domain of the simulation. Upper picture: geometry of the interpolated domain mapping the straight flux tube into a curved one.

Sec. 5.4. Fig. 5.3 shows the 3D rendering of magnetic field lines in the new geometry, at the same snapshot times used for Fig. 5.2. Magnetic field lines are color-coded according to the plasma temperature, ranging from 10^4 K in the chromosphere (blue-layer in the lower part of the box) up to 4×10^6 K in the upper corona. The sequence clearly shows that both flux tubes are progressively heated from about 1 MK to more than 2 MK in the coronal part.

5.5.1 Side view

Figure 5.7 shows a side view of the loop in the MUSE passbands, obtained from the PLUTO 3D MHD model of the kink-unstable, multi-threaded coronal loop (discussed in Section 5.2) at the time $t = 180$ s (as in Fig. 5.1). The top three rows show the possible positions of the MUSE slits (dashed vertical lines). Each column for the MUSE line (Fe IX, Fe XV, and Fe XIX) shows the intensity, Doppler shift, non-thermal line broadening, current density, and the emission measure integrated along the LoS and in a temperature range the line is most sensitive to. Here, we show MUSE observables only where the line intensity exceeds 5 % of the peak, as we address the main emission features. Regarding the Fe XIX line, we have decided to equally show emission features in this line for completeness, even though this line hardly reaches an acceptable level for detection with MUSE for this specific simulation, both because the response function

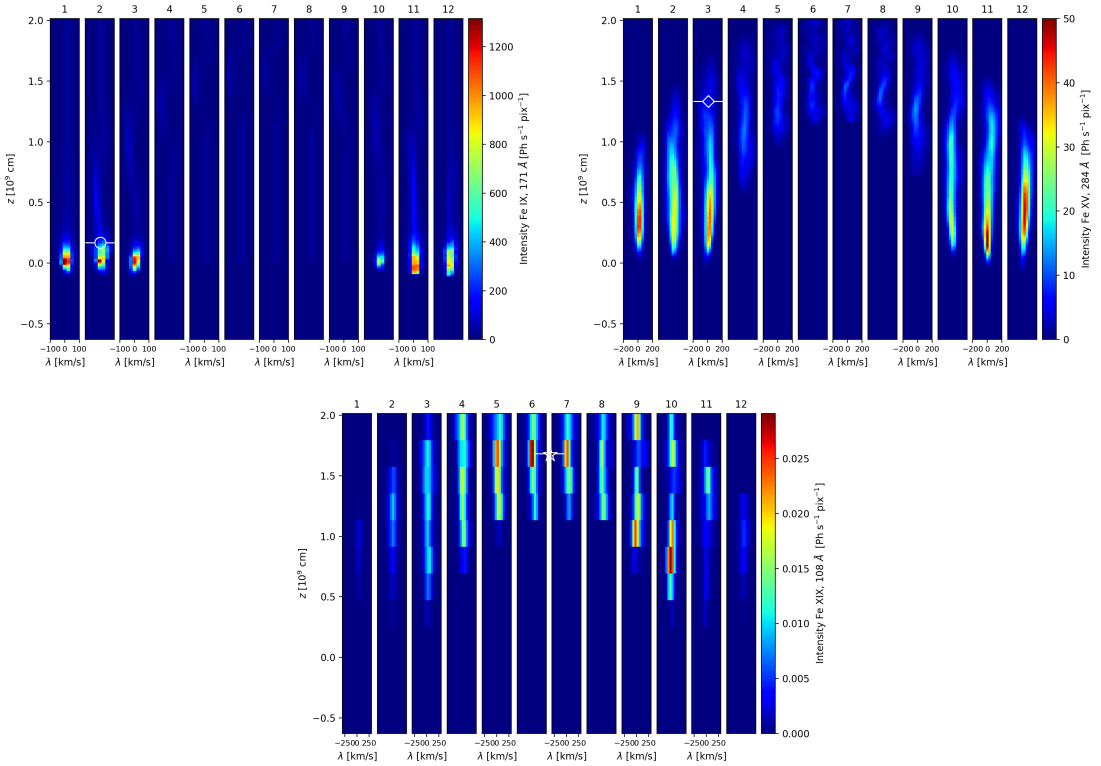

Figure 5.6: MUSE synthetic line profiles for Fe IX, Fe XV and Fe XIX emission line, as a function of height, z, slit number, and Doppler shift velocity, as seen in Fig. 5.7. The spectral bins here are $\Delta v = 25\,\mathrm{kms}^{-1}$ for Fe IX, $\Delta v = 30\,\mathrm{kms}^{-1}$ for Fe XV, and $\Delta v = 40\,\mathrm{kms}^{-1}$ for Fe XIX. The angular pixel along z is 0.4", equivalent to 290 km (see Sec. 5.4) for Fe IX and Fe XV lines and 2.7" for Fe XIX. The positions of the profiles shown in Fig. 5.11 are marked (circle, diamond and star).

is quite lower than the other two and because the densities are also lower at these temperatures. We expect more emission in this line for more energetic simulations, for instance, with a higher background magnetic field.

As shown in Fig. 5.4, the emission in the Fe IX line peaks around 1 MK. Figure 5.3 shows that the bulk of the flux tubes is soon heated to higher temperatures. As a consequence, the emission in this line mostly comes from the transition region at the footpoints, where the temperature steadily remains around 1 MK. On the other hand, the Fe XV line is emitted higher in the flux tubes, although the loop is still not entirely bright at this time.

For the hot Fe XIX line, we show the emission maps rebinned on macropixels (0.4" × 2.7"), increasing the level of emission closer to the detection level (De Pontieu et al.

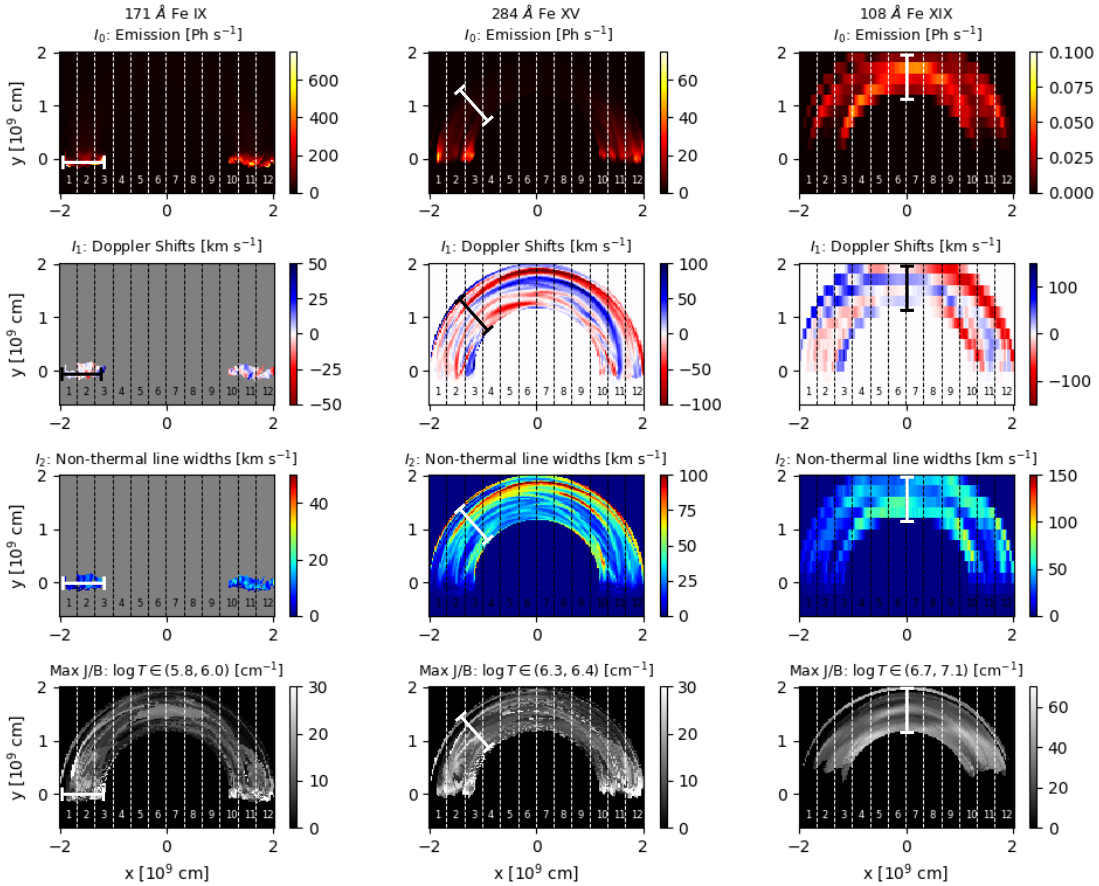

Figure 5.7: MUSE synthetic maps, from PLUTO 3D MHD model of the multi-threaded magnetic flux tube discussed in Section 5.2. Here we show the tube structure at time $\sim$ 180 s after the onset of the instability and with the loop in off-limb configuration (LoS along the $\hat{y}$ direction). From the top, the first row shows the intensity of Fe IX, Fe XV, and Fe XIX emission lines. Second row shows the related line shifts instead. Third row shows the non-thermal line broadenings. In the the Fe IX Doppler shifts and widths, we only show the pixels where the line intensity exceeds the 5% of its peak ($I_0 > 0.05\, I_0^{\max}$). We show Fe XIX observables rebinned on macropixels (0.4" $\times$ 2.7"). Fourth row shows the maximum of the current density-magnetic field ratio (per each pixel plasma column) in three temperature bins, around the temperature peak of each line (see Movie 1).

2020). We acknowledge that the emission in this line would come mostly from the region around the loop apex, where the temperature can reach around 10 MK.

The second row of Fig. 5.7 shows the Doppler shifts maps obtained as the first moment of the velocity distribution along the LoS (see Eq. 5.7). For the Fe IX line,

we show only the regions where the emission is within 5% of the maximum intensity, because we focus our attention on the brightest, low part of the loop. The overlapping velocity patterns along the LoS similar to those shown in Fig.5.1 (bottom left) designate an irregularly alternate Doppler shift pattern at the footpoints visible in the Fe IX line, generally below 25 km s^{-1}, complicated by the starting instability.

The Fe XV line captures the emission from most of the loop and emphasizes the chaotic filamentary (cross-section on the order of 1000 km) pattern of alternating blue-red shifts ($\leq$ 50 km s^{-1}), due to the initial MHD instability. Within the limitations above, we might infer a similar pattern (with higher speeds to about 100 km s^{-1}) also in the Fe XIX line, although the structuring does not overlap with the Fe XV one, because of different contributions along the LoS.

The third row shows maps of the second moment of each line, which is a proxy of the non-thermal line broadening. As a reference, we mention that the thermal line broadenings as defined in Eq. 5.5, at the line peak temperatures, namely, $T = 0.9$ MK for the Fe IX line, $T = 2.5$ MK for the Fe XV line, and $T = 10$ MK for the Fe XIX line, is 16 km s^{-1}, 27 km s^{-1}, and 54 km s^{-1}, respectively. The non-thermal broadening describes co-existing velocity components in different directions along the LoS. In very elongated structures, the thermal and non-thermal components are comparable; however, for the Fe XV (and Fe XIX) line in outer shells, the latter can exceed the former significantly, with a chaotic structure resembling that of the Doppler shifts. In the Fe XV line, there is a long strip around the loop apex where the non-thermal broadening exceeds 75 km s^{-1}. The fourth row shows the maximum of the current density-magnetic field ratio (per each pixel plasma column) in three temperature bins, around the temperature peak of each line, to locate the regions where reconnection is most likely to occur.

Figure 5.6 shows the synthetic line profiles for the Fe IX, Fe XV, and Fe XIX lines, as a function of height z, slit number, and Doppler shift velocity, in a slit-like format, similar to the expected direct output of the spectrometer (e.g., De Pontieu et al. 2022, Fig.4). These profiles account for both the thermal and non-thermal line broadening since they have been obtained from the integration of the single-cell Gaussian profiles (see Eq. 6.4) along the LoS and the angular coverage of each slit. The Fe IX line, bright at the footpoints only, does not show significant overall Doppler shift. The Fe XV line, brighter low in the loop, shows some distortion when moving to the upper and fainter regions. In the faintest top region we also see an oscillatory trend.

Regarding the Fe XIX line, we might say (solely in generical sense) that we could expect to see some Doppler shifts that are more on the blue side, but only if we had enough sensitivity in the top loop region. In general, having multi-slit allows us to see all these features across the loop in these three lines in the same instance.

5.5.2 Top view

Figure 5.8 shows the MUSE synthetic images from a different perspective, with the LoS along $\hat{z}$ (i.e.m the loop is observed from the top) at times of $t = 285$ s, when the emission intensity is high in all three lines. Also in this case, the maximum current density (weighted for the strength of the magnetic field) in the three lines temperature bins is shown in the fourth row, as in Fig. 5.7.

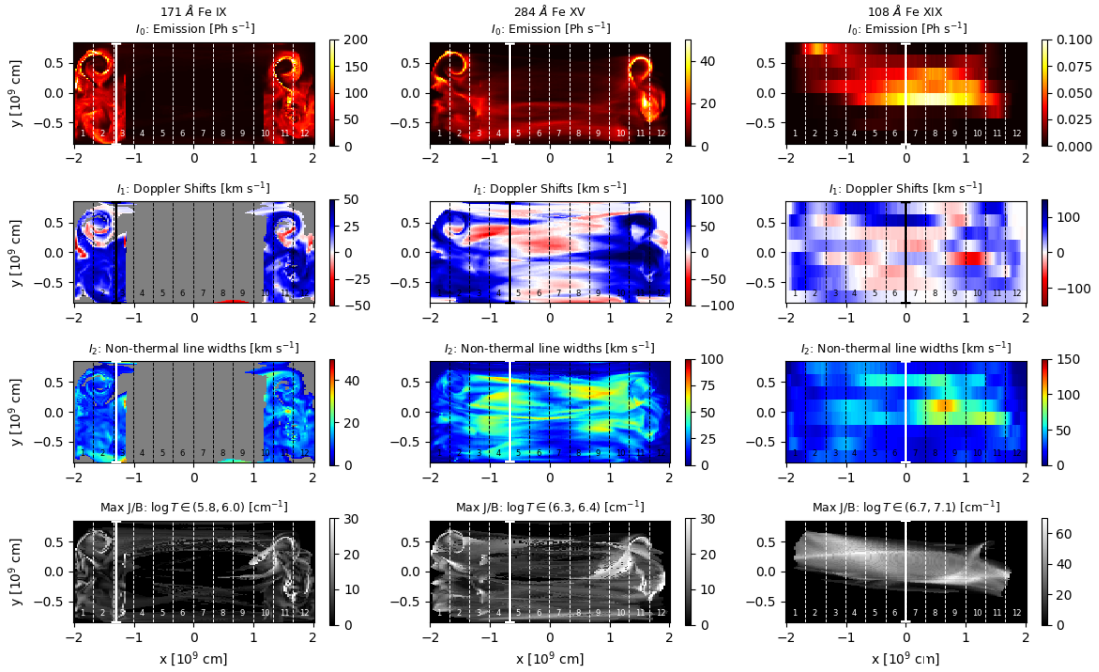

Figure 5.8: MUSE synthetic maps at time $\sim$ 285 s and with the LoS along the $\hat{z}$ direction (the loop is observed from the top). From the top, the first row shows the intensity of Fe IX, Fe XV, and Fe XIX emission lines. Second row shows the Doppler line shifts. Third row shows the non-thermal line broadenings. In the the Fe IX Doppler shifts and widths we show only pixels where the line intensity exceeds the 5% of its peak ($I_0 > 0.05\, I_0^{\max}$). We show Fe XIX observables rebinned on macropixels (0.4" $\times$ 2.7"). We also show the Fe XIX observables rebinned on macropixels (0.4" $\times$ 2.7"). The fourth shows the maximum of the current density (per each pixel plasma column) in three temperature bins, around the temperature peak of each line. The 12 dashed vertical lines mark the position of the MUSE slits. 12 dashed vertical lines mark the position of the MUSE slits (see Movie 2).

In Fig. 5.8, as expected, the Fe IX line intensity map shows bright footpoints at the sides, with no emission in between. In particular, helical patterns map the footpoint

rotations of the two flux tubes. The upper tube is better defined because not involved in the kink instability yet. The related Doppler map shows mostly blue shifts of up-moving plasma, driven by the heating. At the footpoints, the non-thermal broadening is noisy and mostly below 20 km s^{-1}. Overall, it maps the current density pattern rather well.

The Fe XV line is bright along most of the loop, but more so in the lower, kink-unstable loop than in the upper kink-stable loop. Significant blue-shifts at about 100 km s^{-1} are present low in the loop legs, marking bulk upflows. An alternation of blue and redshifts are present high in the loop. Non-thermal broadening above 50 km s^{-1} is located at intermediate heights it and maps the structuring of the current density quite well.

Also, from this perspective, the hot Fe XIX line is at its brightest around the loop apex and, in particular, at the boundary between the two flux tubes (in the mid plane). The Doppler shift pattern is diluted by rebinning, except for a couple of spots of redshift and non-thermal broadening.

5.5.3 Time evolution

In Fig. 5.7, we mark the cross-sections along the loop where each line is bright and we use them to analyse the time evolution of the lines emission. In Fig. 5.9, we show the same quantities as in the top three rows of Fig. 5.7, but considering three single slits (marked in Fig. 5.7) as a function of time. The time of Fig. 5.7 (t = 180 s) is marked.

The Fe IX line, sampled at one loop footpoint, starts to brighten quite early ($t \sim 100$ s) overall and, in particular, in correspondence to the outer shell of the loop. While it does not occur uniformly, the brightness increases progressively over time. Conversely, the Doppler shift and the non-thermal broadening show higher values earlier in the evolution, around 150-200 s. Both of them have a patchy pattern, with alternating red and blue Doppler shifts and high small-line broadening, respectively.

The Fe XV line brightens significantly after t = 200 s, which is quite later than the Fe IX line, because of the time taken by dense plasma to come up from the chromosphere. The brightening is more uniform than that seen for the Fe IX line and it already gets to its peak, in part of the loop, at about t = 300 s. Also in this case we have more significant dynamics at early times (between t = 100 s and t = 300 s), with Doppler shifts declining well below 50 km s^{-1} and broadenings below 20 km s^{-1} by the time the intensity peak is reached. However, the predicted intensities are already high enough (De Pontieu et al. 2020) at the time of peak shift or broadening to detect those line properties. In the Doppler-shift maps, we see more defined alternating red and blue patterns both in terms of the time and along the slit.

While it is quite faint, the Fe XIX line, emitted at the loop top, brightens very early ($t \sim 100$ s), for a short time and with an irregular pattern, marking the time interval when the heating from reconnection is most effective (because the density is still relatively low) and the temperature has a peak (see Fig.9 in Cozzo et al. 2023b). In the interval

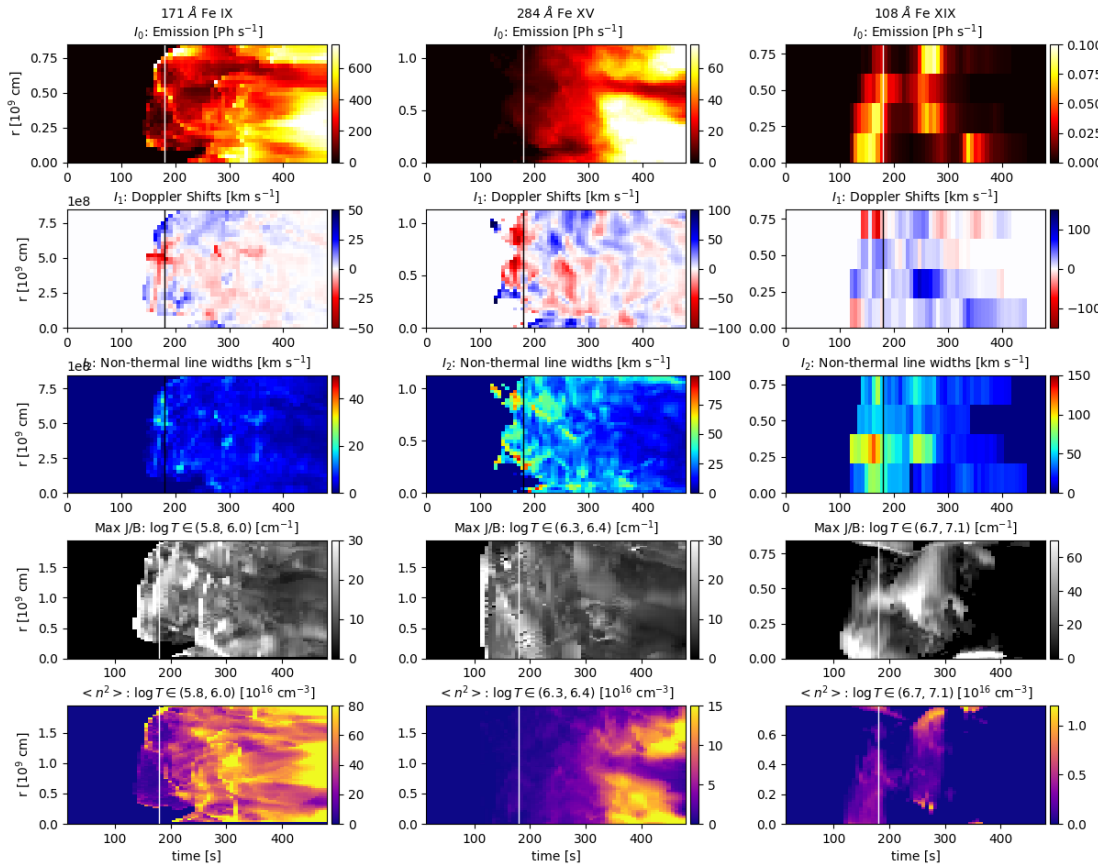

Figure 5.9: Same as in Fig. 5.7, but considering the three single slits marked in Fig. 5.7, as a function of time and of the distance from the loop's inner radius r. Times from Fig. 5.7 are shown as solid vertical lines.

between 100 s and 300 s we also see a bright spot of blue shift (100 km s^{-1}) and one of line broadening (100 km s^{-1}.)

Figure 5.10 is similar to Fig. 5.9, but the evolution is taken along a line in the XY plane, with a LoS that is parallel to the Z-direction (top view). Also, in this case, we see an increasing line luminosity in the Fe IX and Fe XV lines and flashes in the Fe XIX line. The evolution of the Doppler shifts cut shows clearly the presence of strong and long-lasting upflows from the loop footpoints (Fe IX).

Movie 1 [1] shows the system evolution in the side view of Fig. 5.7, from the onset of the instability to 500 s, when the system is close to a steady state.

Significant currents appear first in the low temperature bin and around the loop apex at the onset of the instability and then again after 1 min in the other temperature

[1]Link to Movie 1: https://www.aanda.org/articles/aa/olm/2024/09/aa50644-24/aa50644-24.html

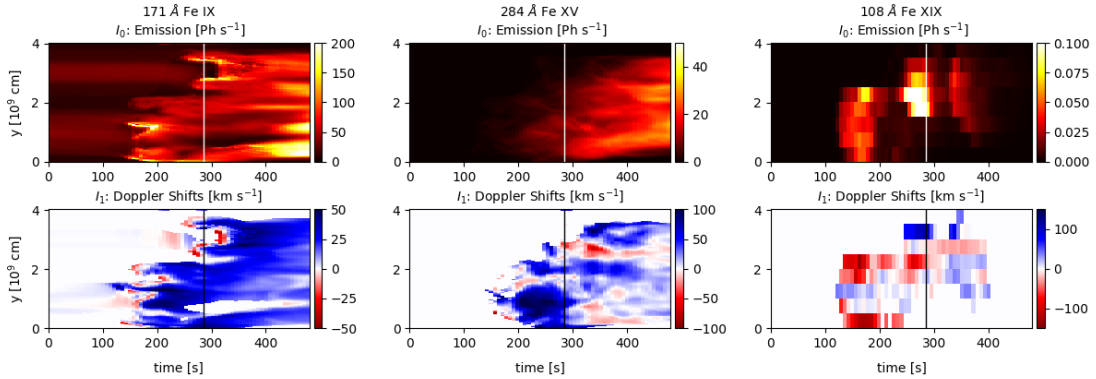

Figure 5.10: Same details as in the top two rows of Fig. 5.8, but considering three single slits (slit numbers 2, 4, and 6 in Fig. 5.8, for the Fe IX, Fe XV, and Fe XIX lines, respectively), as a function of time and y. The time of Fig. 5.8 is marked (solid vertical lines).

bins. After about 2 min, when the plasma suddenly reaches 10 MK, we see some faint emission at the top in the Fe XIX line, which rapidly extends down along the loop. At about $t = 150$ s we start to see emission also in the other two lines, starting from the loop footpoints, and then propagating upwards in the Fe XV line only. At $t = 300$ s the whole loop appears illuminated in this line, while the Fe XIX line rapidly disappears completely. In the Fe XV line, we clearly see bright fronts moving up and down and also that the brightness is not uniform across the loop, but with a filamented structuring which changes in time.

The Doppler shift images have quite well defined patterns around $t = 170$ s (blue on the right, red on the left in the Fe XV line), alternating wide strips in the Fe XIX line. These patterns rapidly become finely structured and chaotic by $t \sim 200$ s in both lines. In the first 2 min, we also see large intense (red) spots of non-thermal broadening in the same two lines, which become filamentary later on, until they decrease significantly below 50 km s^{-1} after about 5 min. The movie confirms that there is some level of correspondence between the evolution and structuring of the non-thermal broadening in the Fe XV line and those of the current density.

When looking more closely at the single lines, the Fe XIX line shows a brightening strip at the onset of the first instability (130 s $< t <$ 160 s) at the low boundary around the apex of the curved tube. There we can also see some blue-shift, more to the left, a spot of non-thermal broadening ($>$ 100 km s^{-1}) and intense current density. These features are produced by the folding of elongated structures which align along the LoS. We see an analogous effect at the onset of the second instability (250 s $< t <$ 290 s), this time involving more the top boundary. The evolution of the Fe XV line emission is more independent of the onset of the instabilities. In this side view, the loop starts

to brighten from the footpoints after $t = 150$ s and is filled in about 100 s. Then, its intensity increases more or less uniformly and progressively. Irregular Doppler-shifts and non-thermal broadening patterns are more intense at some times but progressively fade out. The Fe IX line shows irregular patterns, which are difficult to discern as they are very flat at the footpoints.

Movie 2[2] shows the system evolution (analogously to movie 1) from the top view of Fig. 5.8. Again we clearly see the first brightening in the Fe XIX line in a thin strip at the boundary between the two rotating tubes ($t = 125$ s). Then the first unstable loop brightens up in all lines at the same time. At $t = 153$ s, bright helices appear at the footpoints in both Fe XV and Fe IX lines and a broad oblique band extending over the whole loop length in the Fe XIX line. The Fe XV and Fe IX brightenings rapidly extent to the other flux tube, with two definite helices. The helices rapidly blur and fade away in the Fe XV line, while the emission gradually bridges over the whole loop region. Initially, it is brighter in the first unstable tube. In the Fe XIX line, there are rapid faint flashes of few tens of seconds involving different, but relatively large coronal regions: the first unstable tube earlier and the other one later. Regarding the Doppler shifts, this view clearly shows the expected strong upflows as the flux tubes initiate the instability, from $t \sim 200$ s. We see strong blueshifts in the first unstable tube at the footpoints in the Fe IX line, propagating to the body of the loop in the Fe XV line, and continuing with redshifts in the Fe XIX line flows, moving from one side to the other.

Also, from this view, we see the strongest non-thermal broadenings soon after the instabilities are triggered in both flux tubes, with a structuring similar to the one shown by the current density, especially in the Fe XV and Fe XIX lines. In particular, the Fe XIX line confirms the large non-thermal broadening when the line is more intense. Looking in more detail at each line, in the Fe XIX line emission boundary strips brighten again, due to the folding of emission sheets that overlap along the LoS. At the same time, there are significant downflows and line broadening, downstream, or close to the areas of intense current density.

The Fe IX emission shows the helical patterns clearly at the onset of the instability ($t > 150$ s, $t > 260$ s). Alternating blueshifts and redshifts are also present at the onset of the instability ($t = 167$ s, with velocity $v > 50$ km s^{-1}), then blue-shifts become dominant ($t > 200$ s). Transient non-thermal broadenings are present for $160\text{ s} < t < 330$ s (3 min, $\Delta v \sim 30$ km s^{-1}).

In the Fe XV line, we see the ignition of the lower part of the first unstable tube at $t = 167$ s, the whole tube is bright at $t = 264$ s. The other tube starts to brighten at $t = 264$ s, and is entirely bright at $t = 313$ s. Strong blueshifts appear at the footpoints early after each tube becomes unstable and extends upwards. Redshifts are present in area of weak emission, as well as large non-thermal broadenings.

[2]Link to Movie 2: https://www.aanda.org/articles/aa/olm/2024/09/aa50644-24/aa50644-24.html

5.6 Discussion

This chapter addresses how coronal loops, heated by an MHD avalanche process, would be observed with the forthcoming MUSE mission. It is an extension of the modelling-oriented work described in Cozzo et al. (2023b) and Chap. 4, and it delves into the synthesis of spectroscopic observations in Fe IX, Fe XV, and Fe XIX lines with the forthcoming MUSE mission, which will probe plasma at ~ 1 MK, ~ 2 MK, and ~ 10 MK, respectively, at high spatial and temporal resolution.

In this work, forward-modelling bridges theoretical investigation of loop heating through MHD instability (Hood et al. 2009; Cozzo et al. 2023b) with realistic observations in the EUV band. This approach represents a significant progress both because it is based on a non-ideal MHD model (see also Guarrasi et al. 2014, Cozzo et al. 2023a) and because it realistically accounts for future instrumental improvements (the MUSE mission). In particular, we provide specific observational constraints that are useful for testing the model and guide future modelling efforts. Forward-modelling for comparison with real observations requires a very detailed and complete physical description and including the space-time dependence at different spectral lines makes this task even more difficult. Historically, time-dependence has been possible using the 1D hydrodynamic modelling applied, for instance, to the light curves and line spectra of impulsively heated loops, (e.g., Peres et al. 1987; Antonucci et al. 1993; Testa et al. 2014). Constraints on the heating parameters of non-flaring loops were derived from comparing space-time dependent loop modelling with the brightness distribution and evolution observed with TRACE (Reale et al. 2000c,b) and SDO/AIA (Price et al. 2015). Collections of single loop models have been used to synthesize the emission and patterns of entire active regions (Warren & Winebarger 2007; Bradshaw & Viall 2016). Collections of 1D loop models have been used also to describe the emission of multi-stranded loops (Guarrasi et al. 2010).

Regarding proper multi-D MHD loop modelling, Reale et al. (2016) showed the synthetic emission of a coronal loop heated by twisting in two EUV (SDO/AIA 171 $\mathring{A}$ and 335 $\mathring{A}$, Lemen et al. 2012; Pesnell et al. 2012) channels and in one X-ray (Hinode/XRT Ti-poly, Lee et al. 2009) channel. Also in that case, only the transition region footpoints brighten in the 171 $\mathring{A}$ channel since the loop plasma is mostly at temperatures around 2–3 MK, at which the 335 $\mathring{A}$ channel is more sensitive. The central region of the coronal loop, at higher temperature plasma, is also bright in the X-ray band.

A list of preliminary applications of MHD forward-modelling to the MUSE mission is reported in De Pontieu et al. (2022) and Cheung et al. (2022). They show that Doppler shifts and line broadening are important tools to provide key diagnostics of the mechanisms behind coronal activity. Moreover, they point out the importance of coupling high-cadence, high-resolution observations with advanced numerical simulations.

The full 3D MHD model in Cozzo et al. (2023b) describes a release of magnetic

energy in a stratified atmosphere. It accounts for a multi-threaded coronal loop made up by two (or more) interacting magnetic strands, subjected to twisting at the photospheric boundaries. The global, turbulent decay of the magnetic structure is triggered by the disruption of a single coronal loop strand, made kink-unstable by twisting. Massive reconnection episodes are triggered and determine local impulsive heating and rapid rises in temperature. These are then tempered by efficient thermal conduction and optically-thin radiative losses. The overpressure drives the well-known chromosphere evaporation into the hot corona and consequent loop brightening in the EUV and X-ray bands.

The model allows for both space and time resolved diagnostics. In particular, we synthesized MUSE observations in the Fe IX, Fe XV, and Fe XIX emission lines, sensitive to a wide range of emitting plasma temperature, i.e., ~ 1 MK, ~ 2 MK, and ~ 10 MK, respectively.

The modelled loop is a typical active region loop of length 50 Mm with an average temperature of about 2.5 MK. As such, much of it its brightness is steadily in the Fe XV line, only at the footpoints in the Fe IX line, and (very faintly and transiently) at the apex of the Fe XIX line.

The loop is initially cold ($T \lesssim 1$ MK) and tenuous ($n \sim 10^8\,\mathrm{cm}^{-3}$), with faint emission only in the 171 $\mathring{A}$ channel of Fe IX. Rapid, high temperature peaks, with faint emission in the Fe XIX line, occur during the dynamic phase of the instability, but most of the radiation is emitted by Fe XV at a temperature of $\gtrsim 2$ MK (Fig. 5.3).

In Fig. 5.6, we show the overall distribution of lines intensity and shape at time ~ 180 s. In this case, line profiles show deviations from the Gaussian profile, such as an asymmetric shape and/or multiple peaks, as a consequence of the dynamic and impulsive behaviour of the instability. This is remarked also in Fig. 5.11 with three examples of Fe IX (solid), Fe XV (dashed), and Fe XIX (dotted) profiles at different slits and heights. The main peak of the Fe IX line is almost at rest, whereas Fe XV and Fe XIX show strong Doppler shifts (blue and red, respectively, at $|v| \gtrsim 50\mathrm{kms}^{-1}$). In all these cases, there is an increase of non-thermal width in locations where reconnection seems to occur. In particular, multi Gaussian components appear in Fe IX line (small, red-shifted peak at $v \sim 100\mathrm{kms}^{-1}$), in the Fe XIX line (small, blue-shifted peak at $v \sim -100\mathrm{kms}^{-1}$) and the Fe XV line (strong contribution at rest).

Testa & Reale (2020) show evidence of plasma heated at 10 MK during a microflare. In particular, they analysed the coronal (131 and 94 $\mathring{A}$ channels of AIA) and spectral (Fe XXIII 263.76 $\mathring{A}$ line of Hinode/EIS) imaging and compared observations with hydrodynamic 1D modelling of a single loop heated by a 3 min pulse up to 12 MK. Forward modelling from the simulations provides additional evidence of the coronal loop multistructuring into independently heated substrands.

We have obtained results in both a spatially resolved (Section 5.5.1) and a time-resolved (Section 5.5.3) fashion. In all cases, we conclusively show how the three

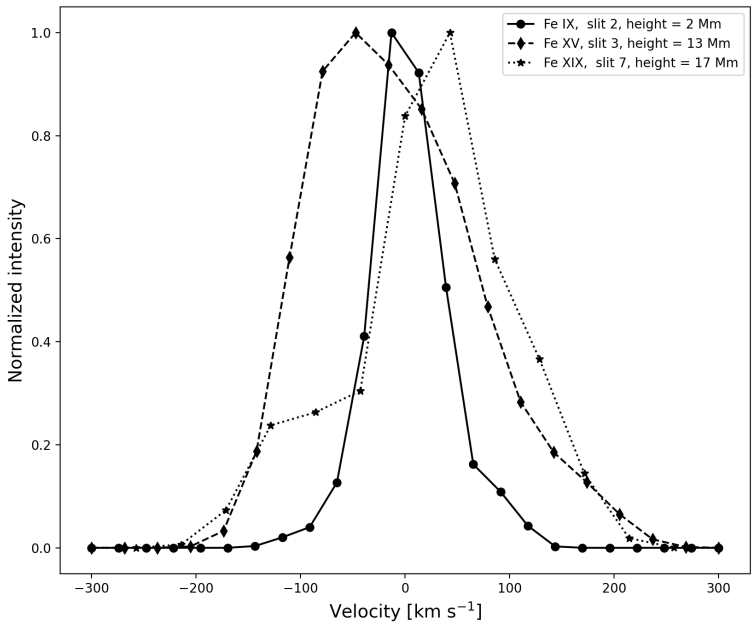

Figure 5.11: Detailed (normalized) profiles of the Fe IX (solid), Fe XV (dashed), and Fe XIX(dotted) lines at the positions marked in Fig. 5.6.

lines provide plasma information at different places, dynamical stages, and physical conditions. In particular, we have managed to efficiently disentangle the instability evolution into: (Fe IX) foot point response and plasma ablation in the transition region; (Fe XV) over-dense and warm plasma rising at intermediate heights; and, faintly in this case, (Fe XIX) hot flaring plasma inside current sheets.

Progressive brightening is expected in the cooler lines, while we expect that the hottest line might be bright only occasionally and with a lower count rate. This is due to the low densities at the loop apex and the small filling factor, namely, only a small plasma volume gets close to the Fe XIX line formation temperature. We might expect more emission for higher temperature loops, as produced, for instance, by a stronger background magnetic field. The hot Fe XIX shows faint emission here as soon as the flux tube becomes unstable, therefore, it may potentially become a signature of the initial phase of the instability. Fe XIX emission is expected to be short-lived and around the loop top, to be compared with recent evidence of traces of very hot plasma (e.g., Ishikawa et al. 2017; Miceli et al. 2012).

In this analysis, we have reproduced expected line profiles integrated along possible lines of sight (Fig. 5.6). In a limb snapshot view (Fig. 5.7), MUSE observations might show alternating red-blue patterns along the loop, especially in the Fe XV line. The non-thermal broadening might be also quite irregular with filamented structure.

The line profiles taken in a side view might show an irregular trend across the loop in the hot lines. The top view (Fig. 5.8) provides complementary information, helical patterns in the footpoints region, and systematic blue-shifts in the loop legs during the rise phase, but also possible faint one-way flows and filamented non-thermal patterns in the corona. More intense plasma dynamics from Doppler-shifts and non-thermal broadenings are expected during loop ignition, namely, just after the onset on the instabilities and avalanche process. Blue-shifts might be more persistent in the 1 MK line. Cross-structuring is ultimately linked to the assumptions on dissipation, in particular the resistivity determines the cross-size. The photospheric drive plays a role too close to the strands footpoints while it does not seem to influence cross-structuring in the upper corona. MUSE observations might provide crucial information. The instability propagates with a delay of about 2 min, the timing depends on some assumptions (thickness of the flux tubes/rotation radius, rotation rate, field intensity).

The Fe XIX line (if detectable) might be a fair proxy of strong and dynamic current buildups such as current sheets. They form and rapidly dissipate during the earliest, most violent phase of the instability. At the same time (i.e., at the time of the disruption of the threads), the Fe IX footpoint emission provides complementary information about the status of the magnetic structure (Fig. 5.1), suggesting a potential diagnostics role in terms of extrapolating information about the linear phase of the instability (Fig. 5.8), as it might outclass the observational restriction imposed by the small counts-rate obtained with Fe XIX line (De Pontieu et al. 2020).

After the early stages of the instability, Fe XV emission returns information about the evaporation process triggered by the avalanche. This is the only case in which almost the whole coronal loop structure becomes visible to the instrument.

Doppler shifts and non-thermal line broadening can provide additional information about the plasma dynamics, confirming the strongly turbulent behaviour of the avalanche process, which is otherwise difficult to grasp only from emission maps analysis. Doppler-shift maps also contribute complementary information on the strength of the chromospheric evaporation nearby footpoints (Fig. 5.8). Indeed, after the instability, the lines from the simulation broaden and strongly blue-shift, due to the strong chromospheric evaporation up-flows and in agreement also with Testa & Reale (2020) forward modelling of 1D microflaring coronal loop.

According to the estimated uncertainties in centroid and line width determination discussed in De Pontieu et al. (2020), minimum line intensities of $\sim 100/150$ photons for Fe IX/Fe XV, lines and ~ 20 photons for Fe XIX, are required to obtain the desired accuracy. In our simulations, Fe IX, and Fe XV, Doppler shifts, and non-thermal line broadening can be accurately estimated in the brightest regions (above 5% of the intensity peak) and with exposure times of $\gtrsim 5$ s. Emission in the Fe XIX MUSE line would perhaps be detectable only with particularly deep exposures (> 30 s) with our setup, but with shorter exposures for stronger magnetic field.

This work addresses in detail the observability of a 2 MK coronal loop system that is triggered by an MHD instability and described by a full 3D MHD model. To be specific, this forward-modelling approach is applied to the EUV spectrometry to be obtained with the forthcoming MUSE mission. Although calibrated on the high capabilities of this ambitious mission, our analysis is generally valid for observations made with instruments working in similar bands, such as present-day SDO/AIA, Hinode/EIS, Solar Orbiter SPICE (Anderson et al. 2020), and EUI (Rochus et al. 2020), or the forthcoming Solar-C/EUVST as well. The capabilities in terms of spatial, temporal, and spectral resolution of current observations (e.g., SDO/AIA, Hinode/EIS, Solar Orbiter SPICE and EUI) do not allow us to reach the diagnostic level shown by our analysis and further support the implementation of the MUSE mission.

6

Coronal heating by MHD avalanches: Identification of a reconnection nanojet

This chapter is structured based on the paper titled "Coronal heating by MHD avalanches III. Identification of a reconnection nanojet", submitted to A&A.

Nanojets are believed to be a possible signature of magnetic reconnection in the solar corona and specifically a way to detect the occurrence of ubiquitous small-angle magnetic reconnection. The aim of this work is to identify possible diagnostic techniques of nanojets in hot coronal loops with the Atmospheric Image Assembly (AIA) on-board the Solar Dynamics Observatory and the forthcoming MUltislit Solar Explorer (MUSE), in a realistically dynamic coronal loop environment in which an MHD avalanche is occurring. We consider a 3D MHD model of two magnetic flux tubes, including a stratified, radiative and thermal-conducting atmosphere, twisted by footpoint rotation (Cozzo et al. 2023b). The faster rotating flux tube becomes kink-unstable and soon involves the other one in the avalanche. The turbulent decay of this magnetic structure on a global scale leads to the formation, fragmentation, and dissipation of current sheets driving impulsive heating akin to a nanoflare storm. We captured a clear outflow from a reconnection episode soon after the initial avalanche and synthesized its emission as detectable with AIA and MUSE. The nanojet has maximum temperature around 8 MK*, an energy budget of* 10^{24} erg*, an outflow velocity of a few hundreds* km s^{-1}*, and a duration of less than 1 min. We show the emission in the AIA 94 Å channel (Fe* XVIII *line) and in the MUSE 108 Å Fe* XIX *spectral line. This nanojet shares many features with those recently detected at lower temperatures. Its low emission measure makes however its detection difficult with AIA, but Doppler shifts can be measured with MUSE. Conditions become different in a later steady state phase when the flux tubes are filled with denser and relatively cooler plasma.*

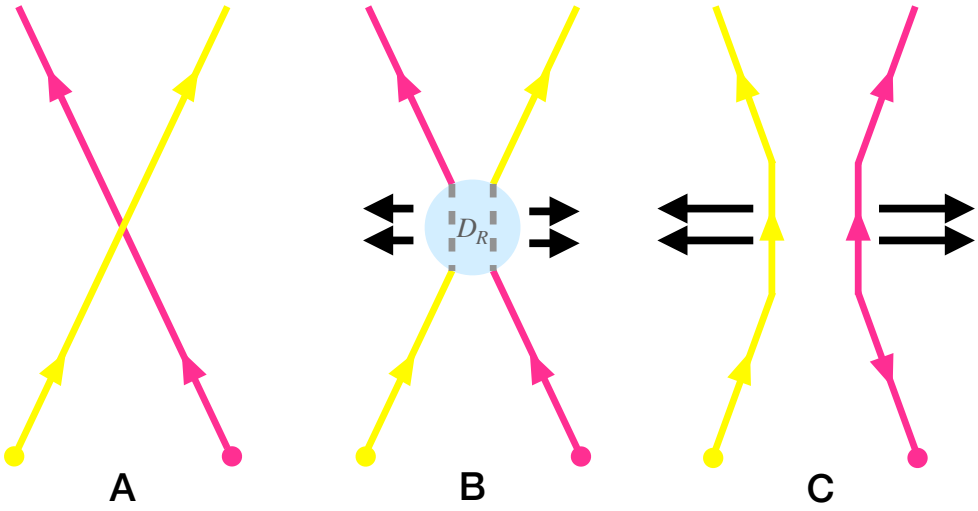

Figure 6.1: Schematic representation of guide field small-angle reconnection at three different stages. Step A: two field lines are tilted in opposite directions. Step B: field lines reconnect in the diffusion region D_R where currents are stronger. Step C: after the reconnection the field line connectivity has changed. The black arrows indicate the outflows.

6.1 Introduction

As already discussed in Sec. 1.5.7, recently, possible direct probes for nanoflare activity have been found to be the so-called 'nanojets': reconnection outflow jets generated by the "slingshot effect" of magnetic field lines during reconnection. They consist of the simultaneous ejection of plasma in opposite directions from the reconnection point, reaching Alfvénic speeds. They are considered a potential signature of reconnection-based nanoflares associated with the process of heating coronal loops.

A schematic description of the reconnection processes yielding the nanojet acceleration is shown in Fig. 6.1. As drifting magnetic field lines converge towards one another (A), the magnetic field component perpendicular to the guide field vanishes at the 'dissipation region' D_R, and it induces the field connectivity to change (B). It is a fully-3D reconnection process in the presence of non-vanishing magnetic field (see Sec. 1.3.6 for further details): the magnetic field reconnects inside the dissipation region (where $\mathbf{E} \cdot \mathbf{B} \neq 0$, Hesse & Schindler 1988; Schindler et al. 1988). The new field lines configuration induces a magnetic tension imbalance which in turns drives field lines to expand outwards (C). Outside of the dissipation region the plasma is frozen in the field, and is accelerated by the slingshot effect caused by the released magnetic tension.

High resolution observations of active regions (Antolin et al. 2021, Sukarmadji

et al. 2022, Patel & Pant 2022, Sukarmadji & Antolin 2024) have revealed a variety of small (500 − 1500 km), and transient (< 30 s) nanoflare-like EUV bursts followed by collimated nanojets, 100 to 300 km s^{-1} fast, sometimes driven by dynamic instabilities such as MHD avalanches (Antolin et al. 2021), Kelvin Helmholtz, and Rayleigh–Taylor instabilities (Sukarmadji et al. 2022). The forthcoming MUltislit Solar Explorer (MUSE, De Pontieu et al. 2019, also described in Sec. 1.2.4) will provide key diagnostics of nanojets, as shown in, e.g., De Pontieu et al. (2022). They predict MUSE synthetic observables from the 3D MHD model of Antolin et al. (2021). Distinctive signatures of the ongoing nanojet appear in Doppler shifts and non-thermal line widths (e.g., small Doppler velocity and enhanced non-thermal line broadening at the reconnection site, respectively).

Properties of such reconnecting plasma outflows were investigated via MHD numerical simulations (e.g., Antolin et al. 2021; Pagano et al. 2021; De Pontieu et al. 2022). Antolin et al. (2021) show a non-ideal MHD simulation of two interacting, gravitationally stratified coronal loops, the footpoints of which are slowly moved in opposite directions to create a small angle between the loops. As the x-type misalignment increases, the electric current between the loops increases as well, thus leading to magnetic field lines reconnection at the mid-plane. The enhanced magnetic tension in the reconnection region drives a transverse displacement of the plasma. A high-velocity (up to 200 km s^{-1}), collimated (widths of order of few Mm), bidirectional nanojet also results from the reconnection process. Beyond the work already done in basic models, it remains to be addressed if nanojets can occur in more realistic and dynamic scenarios and whether even in these circumstances they can be detected and observed with current instruments. To answer these questions, this work addresses the MHD and forward modelling of a nanojet, forming and evolving during an MHD Avalanche (Hood et al. 2016). We investigated the full 3D MHD simulation of an MHD-avalanche described in Cozzo et al. 2023b and Chap. 4, and checked the occurrence of nanojets-like events during the evolution of instability.

6.2 The model

We consider the 3D MHD simulation described in Cozzo et al. (2023b) and in Chap. 4 of an MHD avalanche in a kink unstable, multi-threaded coronal loop system (see also, Hood et al. 2016; Reid et al. 2018, 2020). In this case, small angle reconnection episodes result from the turbulent dissipation of the twisted magnetic field during the instability, rather than by regular photospheric motions, directly tilting the file lines, as in Pagano et al. (2021) and De Pontieu et al. (2022). Two identical magnetic flux tubes are embedded in a stratified solar atmosphere with a 1 MK corona anchored on both sides to a dense and cooler isothermal (10^4 K) chromosphere. The flux tubes are progressively twisted at different angular velocity by photospheric rotation motions at

their footpoints, mirrored with respect to the middle plane (Reale et al. 2016; Cozzo et al. 2023a), in a background magnetic field (B_{bkg} = 10 G). The time-dependent 3D MHD equations are solved with the PLUTO code (Mignone et al. 2007). The computational box has a size Δx = 16 Mm, Δy = 8 Mm, Δz = 62 Mm. Anomalous magnetic resistivity ($\eta_0 = 10^{14}$ cm^{-2} s^{-1}, Hood et al. 2009; Reale et al. 2016, and Sec. 2.2.7) turns on in the corona ($T > 10^4$ K) when and where the electric current density **j** exceeds the threshold value j_{cr} = 250 Fr cm^{-2} s^{-1}. The equations include radiative losses, thermal conduction and gravity component for a curved flux tube (closed coronal loop). Due to progressive twisting, the faster rotating flux tube becomes kink-unstable and rapidly fragments into a chaotic system with thin current sheets hosting small-size impulsive reconnection events. The instability soon propagates to the nearby slower tube, which then evolves in a similar way. The impulsive events cause local heating of the plasma to peaks above 10 MK.

6.3 Reconnection nanojet identification

Following the evolution of several magnetic fields lines in the aftermath of the MHD avalanche, we identified a few examples of nanojets, i.e. bundles of magnetic field lines whose evolution follows the patterns described in Fig.6.1. We selected one of them as a reference case resulting from the reconnection of two slightly misaligned magnetic filaments carried out by swirling plasma flows.

Figure 6.2 shows a localized reconnection event with the reference outflow. In the box (62 Mm long, and 4 Mm × 8 Mm cross section), the atmosphere is stratified, with two chromospheric layers at the top and lower sides and a 50 Mm corona. Field lines in the box are shown in full-3D rendering at three different times and from two different perspectives. They are computed using a fourth order Runge-Kutta scheme, while the colour is attributed depending on the starting points at the lower photospheric boundary, which move following photospheric twisting. On the left, a view from the top, along the coronal loop axis (z-axis), with a cut at the mid-plane of the box showing in blue the electric field component parallel to the magnetic field. Arrows mark the orientation and strength of the velocity field. On the right, a front view. We draw two reconnecting magnetic field lines. The sites of reconnection are localized as those where the electric field component parallel to the magnetic field is non-zero ($E_{\parallel}$, blue spots in the left panels, Hesse & Schindler 1988; Schindler et al. 1988; Reale et al. 2016, see also Fig. 6.3 for a full-3D rendering of D_R). The velocity field (arrows) illustrates the approaching flows and the collimated outflows diverging from the reconnection site. Movie 3[1] shows the evolution of the 3D rendering. Initially, the two field lines approach each other dragged by the chaotic dynamics of the MHD avalanche. The outflowing plasma is

[1] Link to Movie 3:
https://drive.google.com/drive/folders/1D2K1bjEp7AZyBOQ2WCRpCvMPwZhpEvNn?usp=sharing

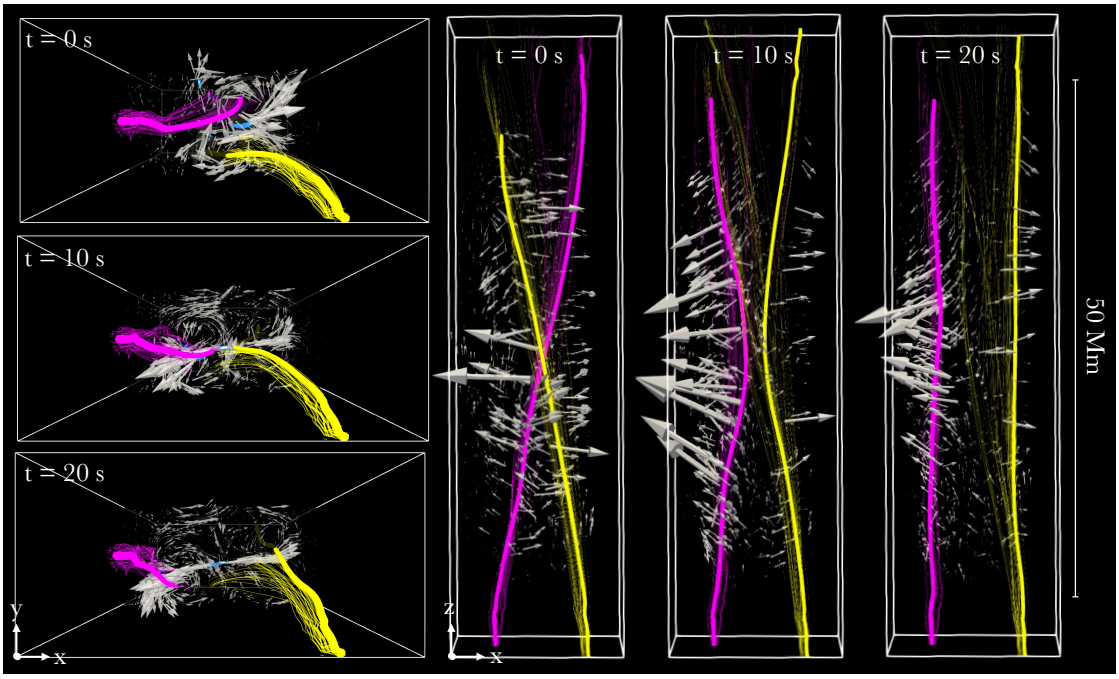

Figure 6.2: Magnetic reconnection and the outflow. Rendering 3D at 3 times since the beginning of the avalanche: $t = 0$ s (lines approaching), $t = 10$ s (lines reconnecting), and $t = 20$ s (new lines detaching). Left column, top view and cut at the middle plane: two reconnecting magnetic field lines (marked by yellow and magenta lines among two bundles), reconnection sites (blue spots close to the center of the plane), and velocity field (white arrows), which shows the collimated outflow departing from the reconnecting lines (see Movie 3). Right row: same reconnecting lines from a front view (the coronal part of the loop is 50 Mm long, see also Movie 4).

then accelerated (second panel) in the dissipation region near the mid-plane centre, i.e., where $E_{\parallel}$ becomes stronger. Afterwards (third panel) the reconnecting field pushes the plasma outwards where it eventually disperses in the ambient magnetic field. On the right (and in Movie 4[2]), the front view shows the reconnecting lines emphasizing the presence of the guide field, similar to Fig. 6.1. In the first panel, reconnecting magnetic field is starting to push the plasma outwards (as emphasized by arrows in few, high velocity spots near the reconnection site). The plasma velocity is mostly perpendicular to the field lines, with a small component along them. This transverse motion is stronger (middle panel) and longer lasting (third panel) around the middle of the flux tube.

Figure 6.3 shows the 3D rendering of the diffusion region (in solid cyan, see also Fig.

[2]Link to Movie 4:
https://drive.google.com/drive/folders/1D2K1bjEp7AZyBOQ2WCRpCvMPwZhpEvNn?usp=sharing

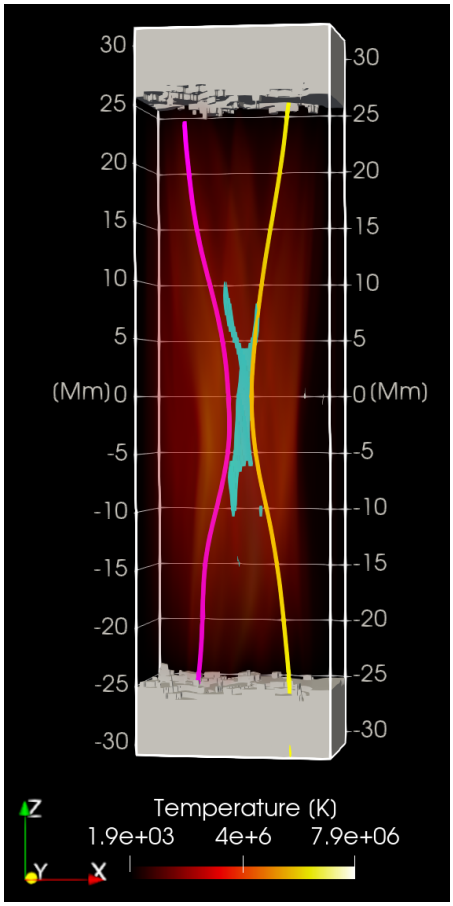

Figure 6.3: 3D rendering of the analyzed magnetic reconnection region. Field lines are the same as in the second panel of Fig. 6.2 ($t = 10\,\mathrm{s}$). The temperature (red color) is shown in the background. Here we also show the diffusion region D_R (pale blue, Fig. 6.1) defined by the region where where $\mathbf{E} \cdot \mathbf{B} \neq 0$. The solid blocks at the top and bottom are the footpoints in the chromosphere.

6.1) between two reconnecting field lines at $t = 10\,\mathrm{s}$ (as in Fig. 6.2). The thin diffusion region develops where the field lines meet and reconnect (i.e. close to the box center). It is elongated and oriented along the guide field, with short "branches" inclined with the magnetic field bundles to form an "X shape". Hot coronal plasma is in the proximity of the reconnection site. Field lines are embedded in the chromosphere, shown by solid blocks at the top and bottom sides on the box.

The evolution of the reference outflow in the midst of the first 300 s from the onset of the instability is shown in Fig. 6.4. To follow the evolution of the reference nanojet throughout the simulation we focused on a horizontal slice of size $\Delta x = 16\,\mathrm{Mm}$, $\Delta y = 4\,\mathrm{Mm}$ centered at the origin of the box. In the first two rows of figure 6.4 we show

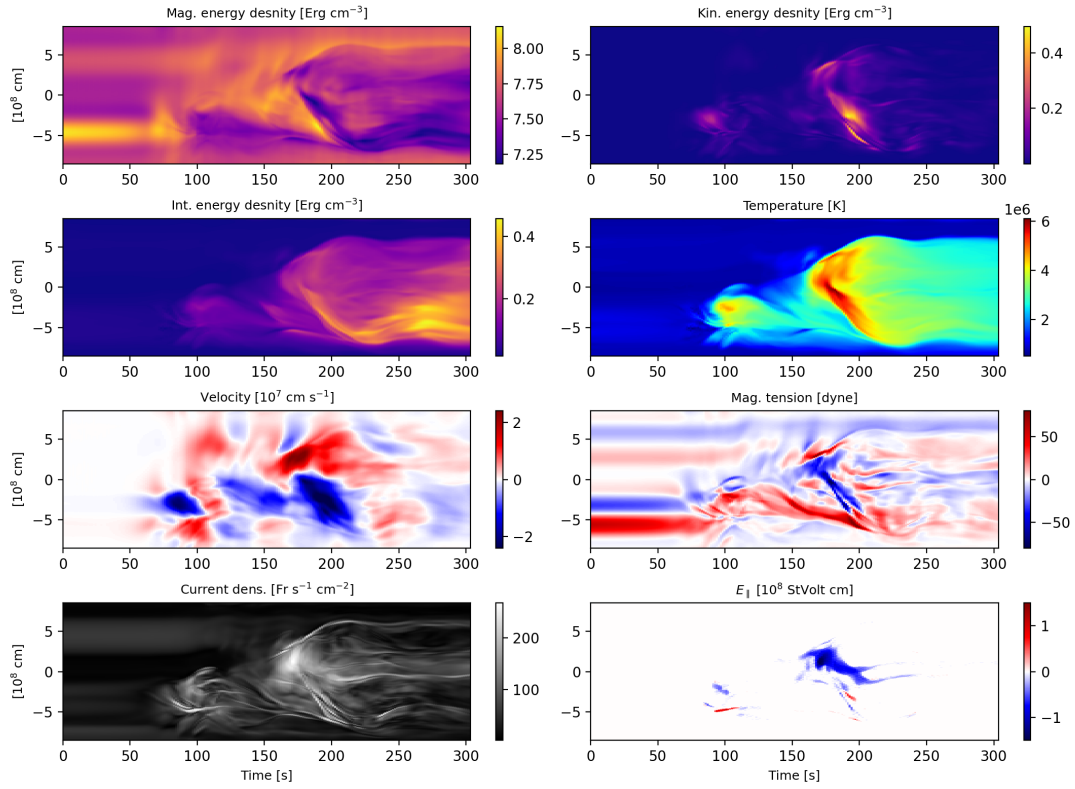

Figure 6.4: Evolution of the coronal loop inside a reference, horizontal slice of size $\Delta x = 1.6 \times 10^9$ cm, $\Delta y = 0.5 \times 10^9$ cm centered at the origin of the box. From the top left to the bottom right: magnetic energy density, kinetic energy density, internal energy density, temperature, x-component of the velocity, x-component of the magnetic tension, current density, and the component of the electric field parallel to the magnetic field. All the quantities are averaged over Δy and expressed as a function of x and time.

(from the top left) the evolution of the magnetic energy density, kinetic energy density, internal energy density, and temperature, averaged over the width Δy of the reference box. At time $t \simeq 170$ s the nanojet acceleration starts. As a consequence of that, kinetic energy abruptly grows up, following the field line trajectory. Internal energy increases as well, with temperature peaking close to the acceleration sites. As far as the nanojet expands, magnetic energy density drops down, as expected by energy conservation. In the third row of figure 6.4 the averaged x-components of velocity (left) and magnetic tension (right) are shown as a function of time. These maps hint at the role of magnetic tension in accelerating the outflow to a few hundreds of kilometers per second. Finally, in the fourth row of figure 6.4 the averaged current density (left) and parallel component

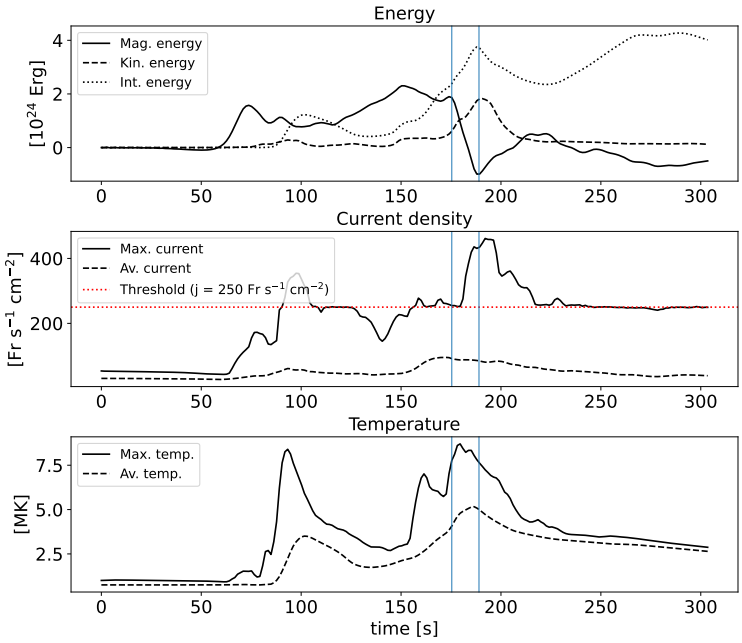

Figure 6.5: Evolution of the coronal loop inside a reference volume of size $\Delta x = 1.6 \times 10^9$ cm, $\Delta y = 0.5 \times 10^9$ cm, $\Delta z = 0.5 \times 10^9$ cm centered at the origin of the computational box. From top to bottom: total magnetic, kinetic, and internal energy changes as function of time; maximum and averaged current density against time; maximum and averaged temperature against time. Blue, vertical lines encapsulate the time lapse when the nanojet is accelerated. The red, dashed, horizontal line in the second panel indicates the threshold value for dissipation.

of the electric field to the magnetic field are displayed. The last quantity is different than zero only in the zones interested by magnetic dissipation i.e. where the current density exceeds the threshold value for dissipation. The velocity stays high ($\gtrsim 200\,\mathrm{km\,s^{-1}}$) for about 30 s, then the jet slows down, the current density dissipates, and the plasma smoothly cools down. We can therefore estimate as ~ 30 s the outflow overall duration. The two opposite jets propagate (toward positive and negative $\hat{x}$, respectively) with different velocities (as also remarked by the different front slopes in the firt panel of Fig. 6.4). In particular, the bidirectional jet, after $\Delta t = 30$ s the reconnection takes place, has expanded by about 10 Mm, with $\sim 40\%$ of asymmetry between the two parts.

During the event, a magnetic energy amount of $\sim 10^{24}$ erg is converted into kinetic and internal energy, as shown by the top panel of figure 6.5. It plots the evolution of the total magnetic, kinetic, and internal energy over the entire elapsed time of the MHD avalanche in the slab where the outflow dynamics is stronger, namely a reference volume of size of size $\Delta x = 10$ Mm, $\Delta y = 4$ Mm, $\Delta z = 10$ Mm, centered at the origin of the

computational box. This energy budget is compatible with the nanoflare energy predicted by Parker (1988). Within the box, an excess of magnetic energy initially increases, but then rapidly drops (below its initial level) upon activation of the anomalous resistivity. Concurrently, both the thermal and kinetic energies rise at similar rates. Magnetic and thermal energy variations are larger compared to kinetic one: plasma compression concurs in heating at the expense of the kinetic energy, localized near the centre of the reconnection (where the plasma is accelerated to $\sim 200\,\mathrm{km\,s^{-1}}$). The peak in kinetic energy lasts about 30 s, compatibly with the estimated duration of the outflow. The second and third panels of figure 6.5 shows the evolution of the averaged and maximum current density and temperature, respectively. During the occurrence of the nanojet (i.e between the two blue, vertical lines) the current density grows up abruptly, far beyond the threshold for dissipation (indicated by a horizontal, dotted, red line). The maximum temperature of the jet overcomes 7 MK although it occurs locally, both in space and time. The averaged temperature indeed does not exceed 5 MK.

In Fig. 6.6 we illustrate details of the selected nanojet. The three columns show the velocity component perpendicular to the magnetic field, current density and temperature maps, on the mid-plane perpendicular to the z vertical axis and at the same times as Fig. 6.2. Movie 5[3] shows the evolution of same quantities. The velocity maps $v_\perp$ emphasize where the plasma is accelerated by the magnetic field tension (as the Lorentz force acts always perpendicular to $\mathbf{B}$) or where the plasma drags the magnetic field lines. As expected, the velocity field diverges from the central reconnection site, near $x = 0$ Mm and $y = -1$ Mm in two strong, subalfvénic collimated jets. Its duration is of the order of a few tens of seconds. The current maps show an intense sheet in the central reconnection region (middle panel), where the magnetic field clearly reverses its direction on the midplane. The current density in the sheet exceeds the threshold for dissipation into Ohmic heating imposed in the simulation ($J_{\mathrm{cr}} = 250\,\mathrm{Fr\,cm^{-2}\,s^{-1}}$). The current density is rather weak at the beginning, it becomes more intense at the D_R, and it finally becomes intense and fragmented in the region around the collimated jets. The temperature maps confirm the dissipation of the reconnection current sheets into heat although rapidly decreasing because of the effect of dynamics and thermal conduction. In particular, as the strongest current deposits around the reconnection center, high-temperature spots ($T \sim 8$ MK) reside within these dissipation regions, indicating that Ohmic dissipation likely plays a role in heating the surrounding plasma. The reference nanojet itself is actually at these high temperatures while the density does not exceed $n \sim 10^9\,\mathrm{cm^{-3}}$.

The simulated solar atmosphere consists of a chromospheric and a coronal column separated by a thin transition region. Specifically, field aligned gravity, thermal conduction, optically thin radiative losses, heating by anomalous magnetic resistivity, and a background heating structures a 5 Mm long coronal loop, while its chromospheric

[3]Link to Movie 5:
https://drive.google.com/drive/folders/1D2K1bjEp7AZyBOQ2WCRpCvMPwZhpEvNn?usp=sharing

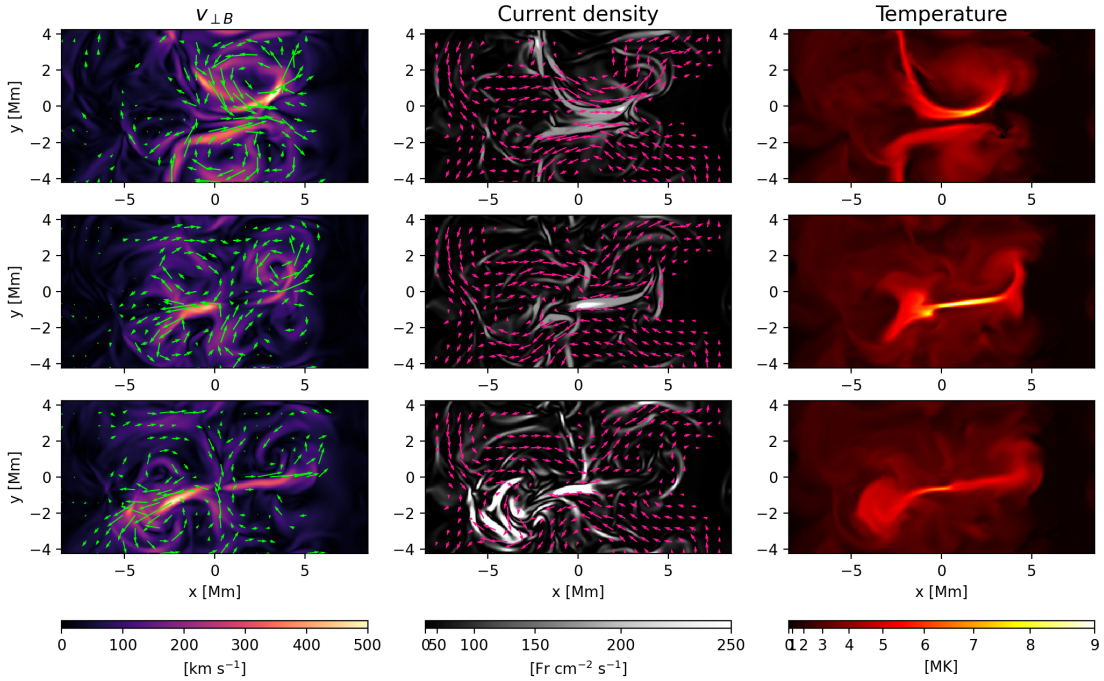

Figure 6.6: Dynamics of the nanojet. First column: horizontal mid-plane map of the value of the velocity component perpendicular to the magnetic field at the same three times shown in Fig. 6.2, i.e., $t = 0$ s (top, current sheet formation), $t = 15$ s (middle, nanojet acceleration), and $t = 30$ s (bottom, nanojet deceleration). The velocity field in the plane is also shown (arrows). Second column: horizontal mid-plane map of the current density. The map saturates where the current density exceeds the threshold value for dissipation. The magnetic field in the plane is also shown (arrows). Third column: horizontal mid-plane map of the temperature. (See Movie 5.)

footpoints are ~ 6 Mm wide each and 10^4 K hot (Reale et al. 2016; Cozzo et al. 2023b). Figure 6.7 shows the temperature and density stratification along a column of pixels passing through the nanojet center (coordinates: $x = y = 0$ Mm). Before the avalanche (black curve), the atmosphere is tenuous ($n \sim 10^8$ cm^{-3}) and cold ($T < 1$ MK). After the instability, when the nanojet is formed, plasma is soon heated (solid, orange line, $t = 0$ s) and temperature rise up to 10 MK (red line, $t = 15$ s), and subsequently cools (orange line, $t = 30$ s). Density (dashed lines) increases as well, approaching, but never exceeding, $n \sim 10^9$ cm^{-3}.

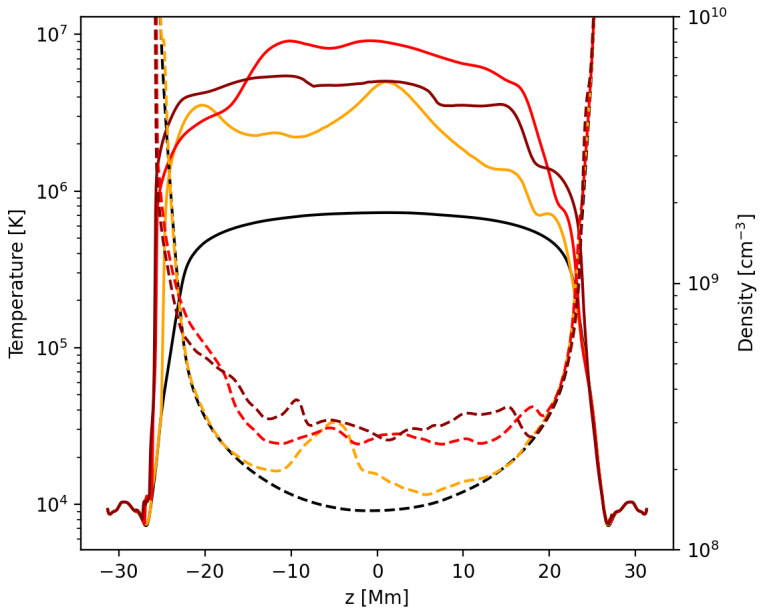

Figure 6.7: Atmospheric plasma stratification. The plot shows the temperature (solid line) and density (dashed) stratification along a pixels column crossing the nanojet center (coordinates: $x = y = 0$ Mm) at the time before the instability (black curve) and at times $t = 0$ s (orange) $t = 15$ s (red), $t = 30$ s (dark-red).

6.4 Forward modelling

In the previous section we have described the dynamics of a nanojet event occurring in a tenuous atmosphere heated up to 10 MK. In this section we discuss the result concerning the synthetic plasma diagnostics we extracted from the simulation results, described so far. In order to test the possibility to detect such reconnection events in the solar corona, we synthesise the emission lines of highly ionized iron atoms which have a formation temperature close to the one found during the nanojet reconnnection in the MHD simulation.

6.4.1 Methods

In order to compare with the familiar semicircular shape of coronal loops, the original simulation outputs were remapped and interpolated onto a new cartesian grid. In this process, the initially straight coronal section of the domain was curved into a half-cylinder shell with a characteristic radius of $R = L/\pi$ with $L = 50$ Mm, the loop's coronal length. On the other hand, the chromospheric layers were modeled as two

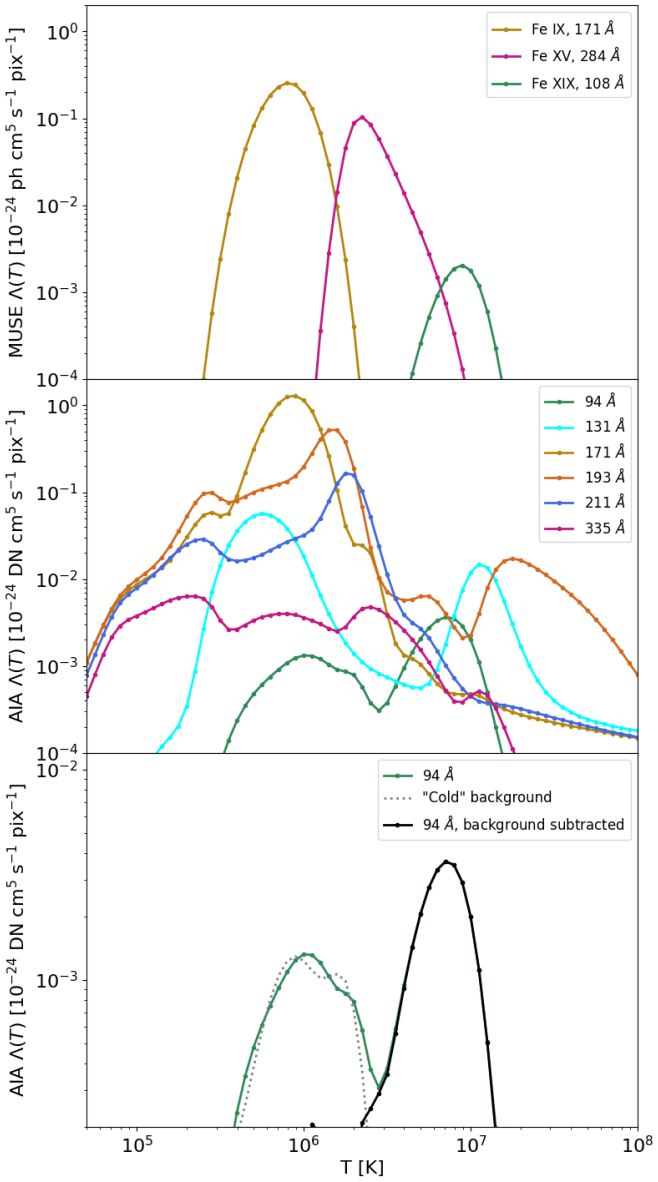

Figure 6.8: Temperature response functions $\Lambda_i(T)$ for the AIA and MUSE channels. Top: MUSE spectrometer lines: Fe IX 171 Å, Fe XV 284 Å, and Fe XIX 108 Å. **Middle**: AIA 94 Å (containing Fe XVIII line), 131 Å, 171 Å, 193 Å, 211 Å, and 335 Å channels. Bottom: expected response function of the 94 Å AIA channel (black line) after the subtraction of the cold component (dotted line) obtained by combination of 131 Å, 171 Å, 193 Å, 211 Å, and 335 Å AIA channels from the the total one(light green).

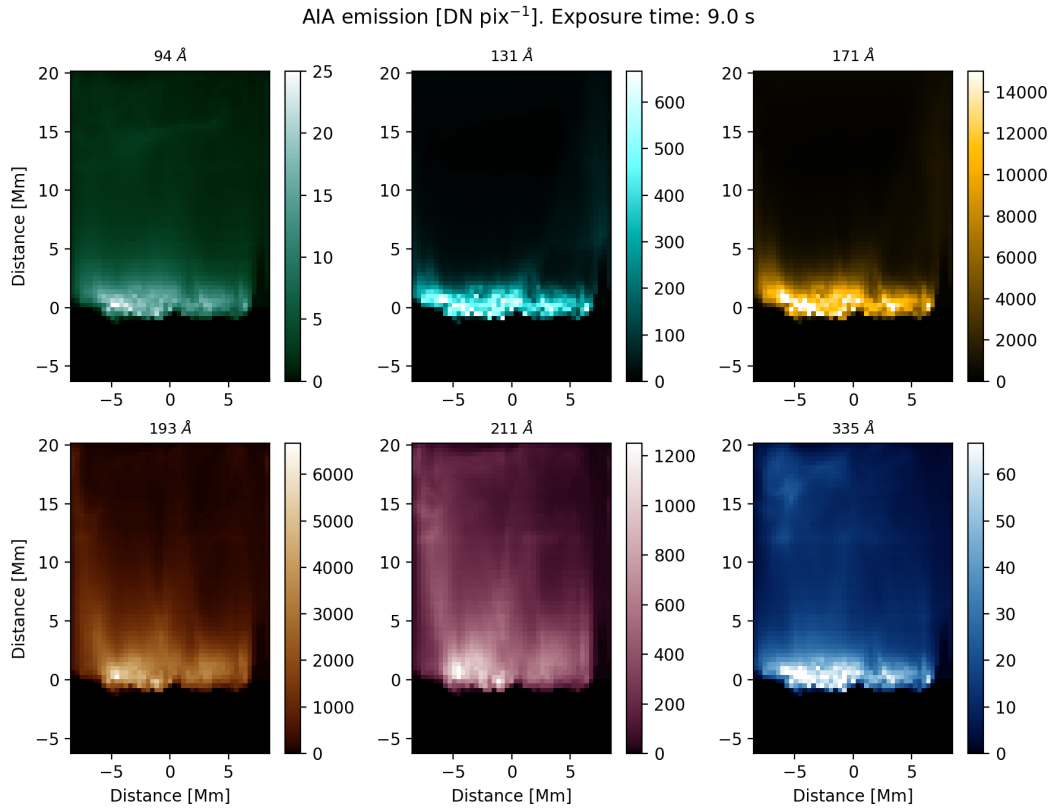

Figure 6.9: Synthetic maps of AIA emission integrated along a line of sight from a side view of the curved loop system for 94 Å, 131 Å, 171 Å, 193 Å, 211 Å, and 335 Å channels, respectively (see Movie 6).

parallel parallelepipeds, as described in Cozzo et al. (2024).

To remap on observation-like images, we computed line emission I_0 from the pixel i, j, by integrating cells intensity $F_{i,j,k}$ (in units of ph s^{-1} pix^{-1}) along the line of sight (as in De Pontieu et al. 2022; Cozzo et al. 2024):

$$I_0^{i,j} = \sum_k F_{i,j,k}, \tag{6.1}$$

with:

$$F_{i,j,k} = n_e^2(\tilde{x}, \tilde{y}, \tilde{z}; T)\, \Lambda_f(T)\, \Delta z, \tag{6.2}$$

where n_e is the free electron density, $\Lambda(T)$ is the instrument temperature response function, and Δz is the cell width. Instrument temperature response functions are calculated using CHIANTI 10 (Del Zanna et al. 2021) with the CHIANTI ionization equilibrium, coronal element abundances (Feldman 1992), assuming a constant electron density of 10^9 cm^{-3}, and no absorption considered.

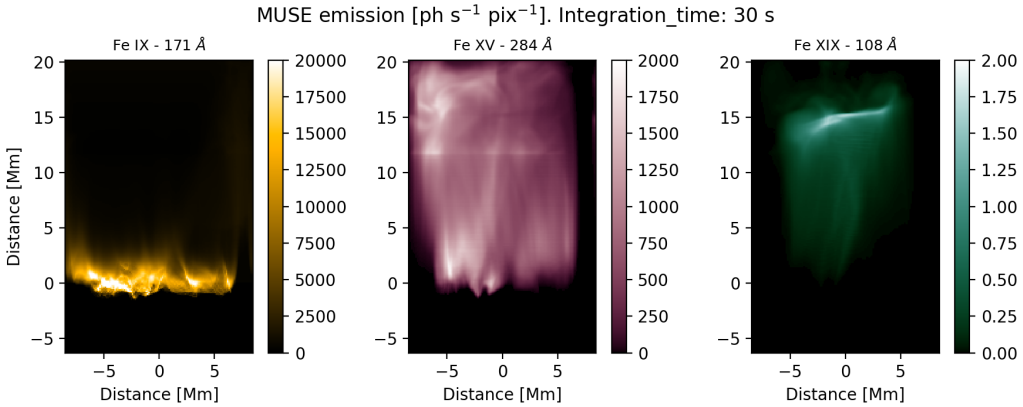

Figure 6.10: Synthetic maps of MUSE emission integrated along a line of sight from a side view of the curved loop system for the Fe IX 171 Å, Fe XV 284 Å, and Fe XIX 108 Å lines, respectively (see Movie 7).

In Fig. 6.8 we show the temperature response functions $\Lambda(T)$ of the three MUSE EUV lines: Fe IX 171 Å, Fe XV 285 Å, and Fe XIX 108 Å (De Pontieu et al. 2020); and of the six AIA EUV channels at 94 Å, 131 Å, 171 Å, 193 Å, 211 Å, and 335 Å, respectively (Boerner et al. 2012).

In Fig. 6.9 we show synthetic AIA emission maps from 9 s effective exposures across a 30 s observing window. Each panel shows the side view of the intensity distribution integrated over the entire filterband of the six EUV channels in Fig. 6.8. Emission in 131 Å, and 171 Å channels is dominated by a realtively cool ($\lesssim$ 1 MK) plasma component just above the transition region ($<$ 5 Mm in height); 193 Å, 211 Å, and 335 Å channels show evidence of warmer plasma (2 – 4 MK) at intermediate height ($\gtrsim$ 5 Mm). A faint feature from hot ($\gtrsim$ 5 MK) plasma shows up around the loop top ($\sim$ 15 Mm) in the 94 Å channel (containing the 'hot' Fe XVIII line), although most of the intensity comes from the cooler plasma background. Movie 6[4] shows the evolution of the coronal loop emission as imaged by the six AIA channels (Fig 6.8), and contributing to the integrated emission of Fig. 6.9. The atmosphere appears roughly steady in all the channels, with some noisy gleaming in the lower, cooler corona, and slow variations in the atmospheric structuring of the warm plasma at intermediate heights. Only the hot plasma jet at the loop top evolves dynamically, and expands outward until its emission vanishes in the background.

The synthetic emission as sampled by the three MUSE channels (Fig. 6.8) is shown in Fig. 6.10. We assumed a 30 s exposure time and line of sight from a side view of the curved loop. MUSE lines (Fe IX 171Å, Fe XV 284Å, and Fe XIX 108Å) detect

[4]Link to Movie 6:
https://drive.google.com/drive/folders/1D2K1bjEp7AZyBOQ2WCRpCvMPwZhpEvNn?usp=sharing

plasma emitting mostly around ∼ 1 MK, ∼ 2 MK, and ∼ 10 MK plasma, respectively. In particular, the Fe IX line is emitted mostly at the loop footpoints; in the Fe XVline we see the bulk of the loop; the Fe XIX line shows a transient brightening around the loop apex. Similarly to Movie 6, Movie 7[5] shows the evolution of the loop in the MUSE lines when the jet is visible. No evidence of the jet is found in the cooler MUSE channels. In the hot 108Å line the bright feature stretches into a strongly elongated structure.

Fig. 6.8 shows also the temperature response function $\Lambda(T)$ for the AIA filter at 94 Å (light green curve, Boerner et al. 2012) The figure also shows the same response function after subtraction of the cool component (dotted line) obtained by a combination of the other AIA responses (131 Å, 171 Å, 193 Å, 211 Å, and 335 Å). More in particular, we derived the background-subtracted emission maps $\tilde{I}_0^{94\mathring{A}}$ for the AIA filter at 94 Å as follows:

$$\begin{aligned}\tilde{I}_0^{94\mathring{A}} &= I_0^{94\mathring{A}} - I_0^{\rm bkg} \\ I_0^{\rm bkg} &= (2.3\, I_0^{131\mathring{A}} + 0.8\, I_0^{171\mathring{A}} + 1.0\, I_0^{193\mathring{A}} + \\ &\quad + 2.6\, I_0^{211\mathring{A}} + 30.1\, I_0^{335\mathring{A}}) \times 10^{-3}\end{aligned} \tag{6.3}$$

where $I_0^{\rm bkg}$ is the cooler background image we obtain from the other AIA filters (Reale et al. 2011; Warren et al. 2012; Cadavid et al. 2014; Antolin et al. 2024). In this way we manage to isolate better the emission in the hot Fe XVIIIline.

To compute the line profiles (Fe XIX line), we assumed at fixed temperature, density and plasma velocity, a Gaussian profile:

$$f_{\rm cell}(v) = \frac{F_{\rm cell}}{\sqrt{2\pi\sigma_T^2}} \exp\left[-\left(\frac{v - v_{\rm cell}}{\sigma_T}\right)^2\right] \tag{6.4}$$

where $\sigma_T = \sqrt{\frac{2k_B T_{\rm cell}}{m_{\rm Fe}}}$ is the thermal broadening, $m_{\rm Fe}$ is the Fe atomic mass and $v_{\rm cell}$ is the plasma velocity parallel to the line of sight in a single cell. MUSE Fe XIX spectral bin is $\Delta v = 40\,{\rm km\,s^{-1}}$ (De Pontieu et al. 2020). We assumed a spectral bin twice as large, $\Delta v = 80\,{\rm km\,s^{-1}}$, to increase the photon-counts. We account for both thermal and non-thermal broadening.

Finally, we rebinned MUSE Fe XIX observables on macropixels (0.4" × 2.7") that collect more photon counts, closer to the detection level (De Pontieu et al. 2020); AIA 94 Å channel intensity is shown with the original pixel size (0.6" × 0.6").

We have also convolved all the emission maps at the original resolution for the instrumental Point-Spread-Functions (PSFs) and then re-binned them to the instrument pixel size. MUSE PSF is modeled by a Gaussian with FWHM of 0.45". AIA PSFs are described in, e.g., Poduval et al. (2013).

[5]Link to Movie 7:
https://drive.google.com/drive/folders/1D2K1bjEp7AZyBOQ2WCRpCvMPwZhpEvNn?usp=sharing

6.4.2 Results

Having described the physical mechanism that leads to a nanojet in our MHD avalanche simulation, we then test the detectability of such an event. Specifically, whether the nanojet can be detected in EUV channels which contain spectral lines emitted by such hot plasma. We considered the 94 $\mathring{A}$ channel of the Atmospheric Imaging Assembly (AIA, Lemen et al. 2012) on-board the Solar Dynamics Observatory (SDO, Pesnell et al. 2012), including a Fe XVIII line emitted at $\log T \sim 6.8$, and the 108 $\mathring{A}$ Fe XIX spectral line, formed around $\log T \sim 7.0$, which will be observed by the forth-coming Multi Slit Solar Explorer (De Pontieu et al. MUSE, 2022; Cheung et al. MUSE, 2022; see Fig. 6.8 in the former Sec. 6.4.1, which also describes how the synthetic observables are calculated).

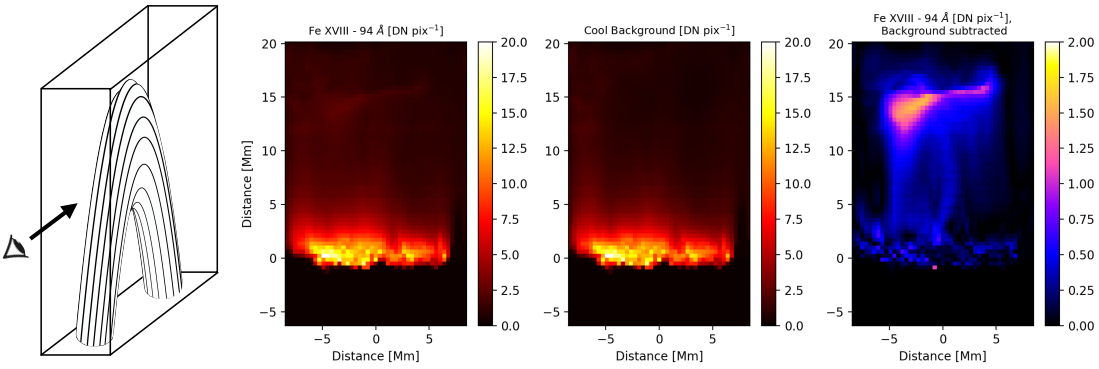

Figure 6.11: Synthetic maps in the AIA 94 $\mathring{A}$ channel integrated along a line of sight from a side view of the curved loop system. In this geometry the top of the loop is high in the image, as shown in the left panel. Second panel: intensity map in the entire filterband. Third panel: intensity map of the cool component ($\sim$ 1 MK). Fourth panel: map of the hot (Fe XVIII) component only, after subtracting the middle from the left.

In the synthetic maps, for a more realistic representation, the flux tube box is remapped onto a curved loop-like geometry (as in Cozzo et al. 2024, ans Sec. 5.4). Figure 6.11 presents how we would detect the emission in the AIA 94 $\mathring{A}$ channel integrated along a line of sight from a side view of the loops. The model has been remapped and oriented along the selected line-of-sight to maximize the brightness of observational signatures at the apex. The overlapping magnetic field lines at the loop top align the hot plasma along the line-of-sight within a compact region, thereby increasing the emission filling factor.

Under nominal operations, AIA exposure times are up to 2.9 s while the basic time step between to snapshots is set to 12 s (Lemen et al. 2012). We assume an exposure time of $\sim$ 9 s, to sample an event $\lesssim$ 36 s long (3 $\times$ 12 s merged observing windows) from

$t = 0$ s. On the left we show the emission map in the whole filterband. The low dense and cooler regions of the image are very bright because the filterband includes other intense 1 MK lines (Testa & Reale 2012; Boerner et al. 2014).

The hot nanojet emission is already visible, but very faint, high ($z \sim 15$ Mm) in the image. To enhance its contrast, we subtracted the cooler component (middle panel of Fig. 6.11) as obtained from other properly rescaled AIA channels (Reale et al. 2011; Warren et al. 2012; Cadavid et al. 2014; Antolin et al. 2024, and Eq. 6.3). The result is shown in the right panel. The signature of the nanojet is the horizontal elongated feature (about 10 Mm long) high in the image with a bright spot on the left. The brightest emission (above 50% of the peak). In this synthetic image, the emission from the hot nanojet plasma leads to counts about 4 times higher than the rest of the image, but nevertheless arguably barely detectable without rebinning.

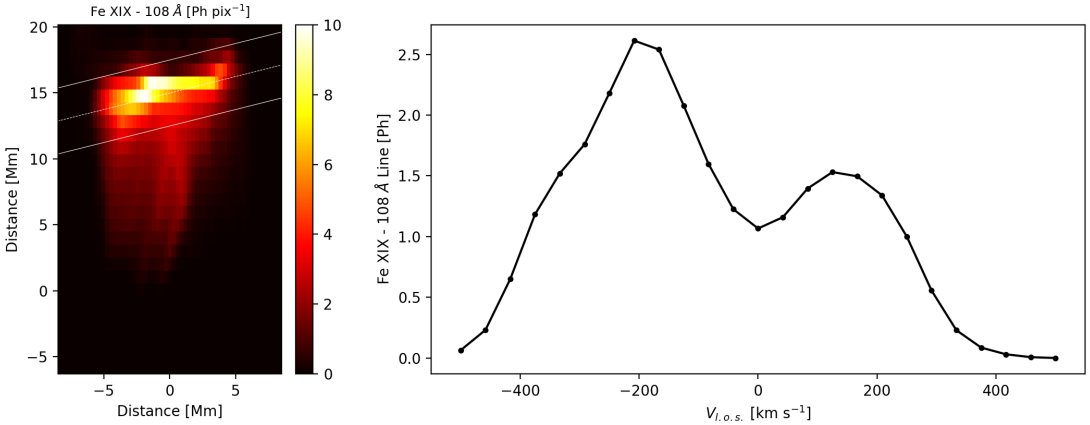

Figure 6.12: MUSE synthetic map and spectrum (line of sight shown in the fig. 6.11). Left: the Fe XIX 108 Åline emission map as in Fig.6.11. The emission is integrated over macro-pixels of size $\Delta_h = 0.28$ Mm, $\Delta_v = 1.89$ Mm (0.4" × 2.7"). Right: Fe XIX line spectrum obtained integrating the emission along the volume marked in the map on the left (white solid lines, cross section 5×5 Mm). The spectral bin is $\Delta v = 40\,\mathrm{km s^{-1}}$. We account for thermal, non-thermal and instrumental broadening.

In Fig. 6.12, we present the corresponding synthetic emission for the MUSE Fe XIX 108 Å spectral line. We considered an observing mode with long exposure time of 30 s from $t = 0$ s. This exposure time envelopes the event completely, although the bulk of the emission is contained in a shorter time. To improve for photon statistics closer to the detection level (De Pontieu et al. 2020), we rebin the map on macro-pixels (0.4" × 2.7"). The Fe XIX emission map is very similar to the "hot" 94 Å map on the right of Fig.6.11, and it highlights the bipolar jet about 500% more clearly, and the hot emission is better isolated in this single line. Also in this case the brightest emission

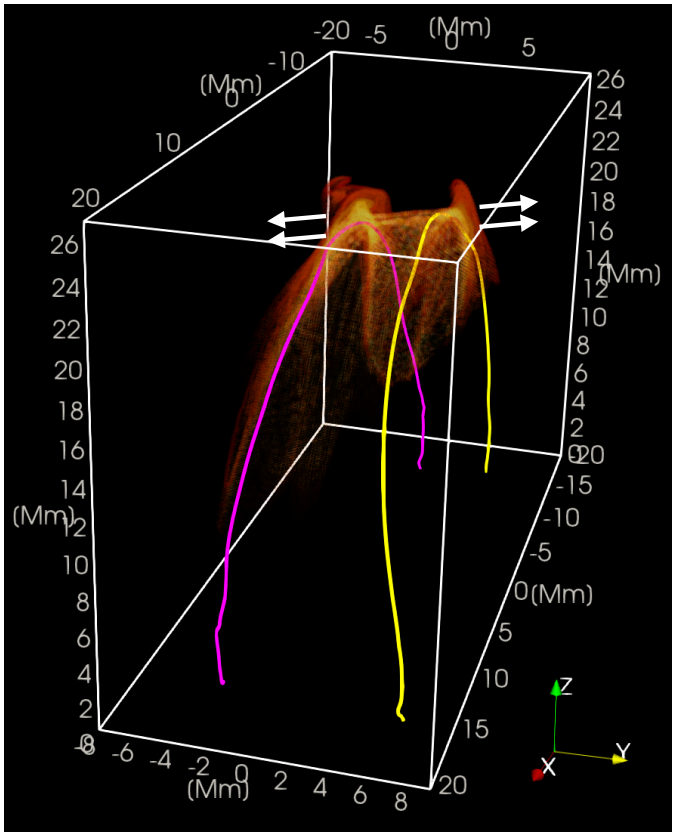

Figure 6.13: 3D rendering of the MUSE Fe XIX line emission at $t = 10$ s. In the 3D box, we show two field lines remapped in curved geometry for reference. The arrow point in the direction of the jet propagation.

(above 50% of the peak) has an elongated shape, about 10 Mm long. The Fe XIX line profile (on the right) is obtained by integrating over an area 5×5 Mm^2 large and inclined by 10 degrees (schematically highlighted on the right, and between the white lines of the mid panel). The surface is oriented exactly along the jet, and in this way we emphasize the plasma motion along the line of sight. The double-sided jet determines the presence of a clearly-defined double peak in the line profile, with peaks located at $v \approx \pm 200$ km s^{-1} (the Alfvén velocity is about 1000 km s^{-1}).

In Fig. 6.13, the 3D rendering in curved geometry clearly shows the jet emission in the MUSE Fe XIX channel at 108$\mathring{A}$ to be perpendicular to the guide field (represented by the drawn field lines). This can be compared to observed nanojets as in Antolin et al. (2021). Specifically, the brighter plasma (yellow volume) envelopes the jet at the loop top, but "tails" of hot plasma (redder parts), propagating along the field, also stands out in the EUV Fe XIX line emission. They form because thermal conduction efficiently spreads heat from the reconnection site.

6.5 Discussion

In this work we studied the serendipitous formation and evolution of a nanojet within the complex background of a coronal flux tube system, which fragments into smaller current sheets with random reconnection episodes. We analysed what kind of detection we might expect both with current instruments, such as the AIA imager, and with the forthcoming MUSE spectrometer. This outflow is the result of a reconnection event, of nanoflare size, and comes out perpendicular to the flux tube guide field. It shares therefore many features with observed small size jets, named nanojets (Antolin et al. 2021).

Previous 3D MHD simulations had addressed the issue of nanojets acceleration with ad hoc setups where field lines are tilted by photospheric motions (Antolin et al. 2021) or where their misalignment is provided from the begin, by initial conditions (Pagano et al. 2021). They provide a clear description of nanojet acceleration in terms of occurrence of magnetic reconnection and release of magnetic field tension perpendicularly to the guide magnetic field. Cozzo et al. (2023b) 3D MHD model (see Chap. 4) describes the turbulent, large-scale energy release of multiple magnetic strands within a stratified atmosphere, twisted by footpoints motions. This model provides an excellent opportunity to study the development of nanojets, and their possible detection, where they are dispersed in a more realistic situation. In other words, in this work we single out one magnetic reconnection event based on the heating and plasma acceleration that it causes, in the midst of the dynamic and thermally evolving loop structures. The described event is localized. It involves the thick field lines in Fig. 6.2, which are driven to cross each other and then detach again with a different topology. Although the configuration is not ideal as in plane parallel cases, there are all signatures of reconnection, including localized heating, and perpendicular flows. The $E_{\parallel}$ component can be different from zero only in non-ideal plasma condition (reconnection) and shows very high values half way down the loop, where the filed lines initially cross each other, and much small nearby, as emphasized in Fig.6.3 showing the extension of the dissipation region ($E_{\parallel} \neq 0$) in full 3D. Similarly to Antolin et al. (2021) observations, the jet is observed after the initial MHD avalanche.

The outflow event is generated as a result of the formation and dissipation of a current sheet, induced by the chaotic motion of plasma and magnetic field lines during the MHD avalanche. Magnetic field lines evolution is remarkably similar to schematic picture shown in Fig. 6.1. This event exhibits typical signatures of nanojets as anticipated by previous theoretical and numerical investigations, and observations (e.g., Antolin et al. 2021; Sukarmadji et al. 2022) such as, typical lateral dimension of few thousand kilometers and typical velocity of few hundreds of kilometers per second. It also takes place at the top of the loop, as many nanojets observed by Antolin et al. (2021); Sukarmadji et al. (2022); Sukarmadji & Antolin (2024). The magnetic energy released

during this event approximates 10^{24} erg, in agreement with Parker (1988), and the observational results discussed by e.g., Antolin et al. (2021). A significant fraction of this energy is converted into heat, increasing the plasma temperature above 8 MK, while the remaining energy propels the outflow. The jet originates from a localized reconnection event that is the dominant source of plasma heating. Field lines overlapping, when the system is mapped into a curved geometry, increases the plasma filling factor and, therefore, the signatures in the forward modelling. Fig. 6.11 shows that the outflow described here is very difficult to detect with present-day capabilities (AIA). Specifically, the AIA 94 $\mathring{A}$ channel is in principle sensitive to such hot plasma but its detection is made difficult both by the low emission measure of these events and by the presence of a strong cool component in the same filterband. The subtraction of this cool component is an approximation that does not work perfectly and introduces an extra source of noise (on top of photon noise, readout noise, digitization noise). Such noise related to the subtraction is likely significantly larger than the other sources of noise, and not properly quantifiable because the individual contributions of the different spectral lines within the broad AIA passbands cannot be accurately determined.

The MUSE spectrometer is instead able to isolate the Fe XIX line which is specifically sensitive to hot plasma only. In consideration of the low emission measure of these events, MUSE thus offers significant advantages over AIA given its sensitivity to the high temperature signal and its capability of detecting the predicted bidirectional Doppler shifts. The characterization of these events will be made even stronger by the peculiar expected bidirectional Doppler shift which MUSE is tailored to capture.

It is arguable that a stronger magnetic field, or denser loops, can lead to events easier to detect. In fact, higher heat capacity c (due to high averaged density) need higher magnetic energy budgets ΔE_B to keep the temperature high, i.e., in the Fe XVIII-Fe XIX temperature range, according to:

$$c\, n\, \Delta T = \Delta \left(\frac{B^2}{8\pi} \right), \tag{6.5}$$

indicating that $\Delta T \propto B^2/n$. With such a scaling pattern, the dissipation of a magnetic field just $\sqrt{10}$ times stronger (e.g. $\sim$ 30 G) heats up a 10 times denser plasma (e.g. $\sim$ 10^{10} cm^{-3}) to million degrees (up to $\sim$ 10 MK), attaining a 10^2 larger emission measure (enough to be easily detected by MUSE at a cadence as short as 10 s). In our simulation, we considered a typical coronal magnetic field strength of 10 G (Long et al. 2017) with plasma density of about 10^9 cm^{-3}. Nevertheless, in active regions magnetic field can exceed 30 G (e.g. Van Doorsselaere et al. 2008; Jess et al. 2016; Brooks et al. 2021) while density that can reach 10^{10} cm^{-3} (Reale 2014). In these cases, higher emission is expected and, comparably, shorter exposure times would be needed to single out the outflow jet, making its evolution suitable to be inferred with short-cadence (10 s or less) observing modes (that will be available with MUSE). This scaling needs to be verified to pave the way for the detection of magnetic reconnection in the solar corona.

The event described has all the physical features predicted by the theory of reconnection and shows strong similarities with the theoretical model proposed by Antolin et al. (2021): they both originate from a small-angle reconnection event, and share the same orders of magnitude in terms of dimensions, velocity, and duration of the outflow jets. A detailed, physical analysis of the simulated event has also shown many features matching with Antolin et al. (2021) numerical model, including: the distribution and orientation of the velocity field (Fig. 6.2), the detailed evolution of the magnetic, kinetic, and thermal energy (Fig. 6.5), and the location and structuring of the dissipation region (Fig. 6.3). As significant deviation from the more idealized model by Antolin et al. (2021) (towards observation, e.g., Patel & Pant 2022), we have shown a bidirectional, but asymmetric jet. Although we do not account for magnetic curvature (Pagano et al. 2021) in the simulation, other factors, in particular local field line braiding and warping, and the non-uniform background plasma effectively make the propagation different on the two sides.

Antolin et al. (2021) model suggests the role of small-angle magnetic reconnection in accelerating (nano-) jets within a non-vanishing coronal loop magnetic field. This is supported by observational evidence of collimated jets, interpreted as the kinetic counterpart of nanoflare heating. Smoking guns of such nanoflare heating in the tenuous solar corona are difficult to catch because of the small emission measure, and the highly efficient thermal conduction, limiting the visibility of such events to their already short kinetic times scales. In this work we show that detection of nanoflare jets might be possible with MUSE, even at high temperatures, when the plasma is under-dense and fainter, thanks to the MUSE detailed EUV spectroscopic diagnostics, until now restricted to the UV band (De Pontieu et al. 2014).

The onset of the reconnection event is caused be the overlapping of two misaligned bundles of field lines, ultimately brought together by the residual dynamics of the MHD avalanche. This scenario supports the interpretation of Antolin et al. (2021), and Sukarmadji et al. (2022) observations, where it is argued that MHD instabilities can trigger reconnection and nanojets.

This study focusses on MHD events occurring around the MHD avalanche triggered by the kink instability. At that time the impulsive heating events have not been effective to fill the flux tubes with dense plasma yet. In these conditions of tenuous plasma the heat pulse is effective to determines a steep increase of the local temperature, and the outflowing jet is therefore hot as well, and faint because of the low density.

This period of the evolution probably represents a relatively short transient in the global evolution of a loop system. So such hot and faint jets are also probably unfrequent and fainter. In future work, we intend to study the formation and possible detection of reconnection jets in more steady state conditions, i.e., later in the loop evolution, when the flux tubes are filled with denser plasma coming up from the chromosphere, driven by the heating. Cooler and brighter nanojets are therefore expected later in this more

steady regime.

7

Work in progress: effects of radiative transport on coronal loop heating, and nanojets statistical properties

In this chapter we briefly discuss some further developments of the model presented in Chap. 4 and Cozzo et al. (2023b) addressing dynamics and heating of a multi-threaded coronal loop for a long time after the MHD avalanche.

In our model, a continuous driver (Reid et al. 2018) at the photospheric footpoints constantly injects magnetic energy into the corona. The already fragmented magnetic field facilitates the formation of current sheets, dissipating by Ohmic heating. The system eventually reaches a statistical balance between radiative losses, thermal conduction, and coronal DC heating, but no evidence of a steady state is predicted (Reid et al. 2020). A realistic, stratified solar atmosphere is fundamental to study the coronal and chromospheric plasma response to impulsive heating and to forward model the observational signatures to be compared with current (e.g., AIA/SDO and IRIS) and forthcoming (MUSE) observations (see Chap. 5 and Cozzo et al. 2023b). Reconnection induced outflow nanojets (Antolin et al. 2021) are expected to self consistently develop in MHD simulations of multi-threaded coronal loops (Chap. 6): the physical descriptions of single events are described in Antolin et al. (2021) and in chap. 6. A physics-based statistical description of these events is now timely to physically interpret the growing amount of nanojets observations (Antolin et al. 2021; Sukarmadji et al. 2022; Patel & Pant 2022; Sukarmadji & Antolin 2024). In this chapter we describe a new MHD model of multistrands coronal loop, accounting for detailed corona optically thin emission (Reale et al. 2016) and approximated chromospheric NLTE radiative transfer (Carlsson & Leenaarts 2012). Moreover we describe and test an algorithm for the automatic detection of nanojets in PLUTO simulations, showing preliminary results and future

prospects.

7.1 PLUTO simulations setup

We used a model of a magnetized solar atmosphere in a 3D cartesian box where interacting and twisted coronal loop strands undergo braiding at sub-arcsec scales, similar to the one presented by Cozzo et al. (2023b); Reale et al. (2016) and described in Sec.s 2.2 and 4. The simulations are performed using the PLUTO code (Mignone et al. 2007). The radiative loss values are taken from look-up tables (Carlsson & Leenaarts 2012). In particular, chromospheric radiative transfer and radiative heating are approximately treated as discussed in Sec.s 2.2.3 and 2.2.4. In particular, the chromospheric radiative energy balance is dominated by the strong lines, of neutral hydrogen (H I), singly ionized calcium (Ca II), and singly ionized magnesium (Mg II), formed out of LTE (Vernazza et al. 1981). The net effect of each transition process on chromospheric cooling is approximated as the product of a optically thin radiative loss function, an escape probability, and the ionization fraction for each element, all dependent on local quantities (Eq. 2.14 in Sec. 2.2.3, Carlsson & Leenaarts 2012). Heating production and transfer is split into three parts: a background coronal heating H_0; chromospheric heating from incident coronal radiation, as part of the radiative losses in the corona is absorbed by the chromosphere in the continua of helium and neutral hydrogen; heating by photospheric absorption that is the reversed process of chromospheric cooling (Carlsson & Leenaarts 2012). These simulations account for a typical active region stratified atmosphere with a high-beta chromosphere, a narrow transition region, and a tenuous magnetized corona. An example of the system evolution is described in Fig. 7.1. Specifically, in the corona, four straightened coronal loop strands interact, each with length 50 Mm, aspect ratio $\gg 1$, and initial temperature $\sim$ 1MK (first column, Fig. 7.1). The computational box is a 3D Cartesian grid, $-x_M < x < x_M$, $-y_M < y < y_M$, and $-z_M < z < z_M$, where $x_M = y_M = 14\,\mathrm{Mm}$, and $z_M = 31\,\mathrm{Mm}$, with a staggered grid, uniform along $\hat{x}$ and $\hat{y}$, with $\Delta x = \Delta y \sim 0.03\,\mathrm{Mm}$. Along $\hat{z}$ we use a non-uniform grid, with high resolution ($\Delta z \sim 0.03\,\mathrm{Mm}$) in the chromosphere and TR, while Δz logarithmicly increases with height in the corona. For the simulations we discuss here, we implemented the Transition Region Adaptive Conduction (TRAC) method (Johnston & Bradshaw 2019; Johnston et al. 2021, see also Sec. 2.2.5) to accurately capture the enthalpy exchange between the corona and transition region, without need of extremely high grid resolution. Each flux tube is rooted to the chromosphere by its footpoints, with maximum strength of few hundred G, and it expands approaching the corona, with background intensity of $\sim 10\,\mathrm{G}$ or more. The loop's magnetic field is line-tied to the photospheric boundaries, at the opposite sides of the domain, where rotational motions at the footpoints twist the flux tubes (similar to the setup of Cozzo et al. 2023a, Chap. 3, and Cozzo et al. 2023b, Chap. 4). The four rotating regions have the same radius ($\sim 1\,\mathrm{Mm}$) but one has

twisting velocity higher than the other by 10% ($v_{\max} = 2.2\,\mathrm{km/s}$). The kink instability, triggered in the fastest strand, makes the initially monolithic flux tube fragment into a turbulent structure of thinner strands (second column, Fig. 7.1). The initial helical current sheet fragments into smaller and smaller current sheets, which dissipate by magnetic reconnection. As a consequence, a sequence of aperiodic, impulsive heating events expand and propagate across the guide field towards the others, nearby stable, magnetic strands (third column, Fig. 7.1). The initial decay of the magnetic structure on a global scale leads to the formation, fragmentation, and dissipation of current sheets akin to a nanoflare storm. Afterwards, photospheric motions continue to induce magnetic field braiding in the corona and drive impulsive heating at a steady frequency (DC heating). The same setup is used for the other simulations we consider, to study the heating process in the presence of higher coronal magnetic field strength. For example, figure 7.2 compares two simulations with background magnetic field of 20 (blue lines) and 10 (red lines) G, respectively. Energy is stored throughout the first $\sim 1300\,\mathrm{s}$. Then, and in both cases, a MHD avalanche disrupts the magnetic structure, and energy is rapidly dissipated at small (spatial and temporal) scales within "turbulent" current sheets. After a short transient ($\sim 300\,\mathrm{s}$) plasma and current density, velocity, and temperature set around a constant level. In particular, plasma and current density, and temperature are systematically higher in the 20 G case than in the 10 G one, while the velocity sets to $\sim 20\,\mathrm{km\,s^{-1}}$ in both cases (Lorentz force, $\propto j$, and plasma inertia, $\propto n$, have opposite influence on v).

7.2 Methodology

In the simulations we investigate, small scale heating events caused by magnetic field line braiding occur, driven by photospheric motions. Nanojets resulting from magnetic reconnection can also be found, as shown in previous work (e.g., Antolin et al. 2021, De Pontieu et al. 2022, and Chap. 6).

To investigate the potential of nanojets as diagnostic tools for coronal heating, our initial step involves developing a way to detect nanojets within simulations and ascertain their characteristics, allowing us to examine their correlations with heating properties. Toward this objective, we have formulated an automatic detection algorithm capable of identifying nanojets in the 3D MHD numerical simulations of the corona.

Nanojets automatic detection algorithm

The output quantities of the simulations include the plasma density (ρ) and pressure (p) or the internal energy (ϵ), and the velocity and magnetic vector fields (v_i & B_i, with $i = x\,y\,z$). From these primary variables, we can infer secondary variables such as: the current density $\frac{c}{4\pi}\nabla \times \mathbf{B}$ and the electric field $\mathbf{E} = -\frac{\mathbf{v}}{c} \times \mathbf{B} + \mathbf{j}/\sigma$, where $\sigma = \frac{c^2}{4\pi\eta}$ is the

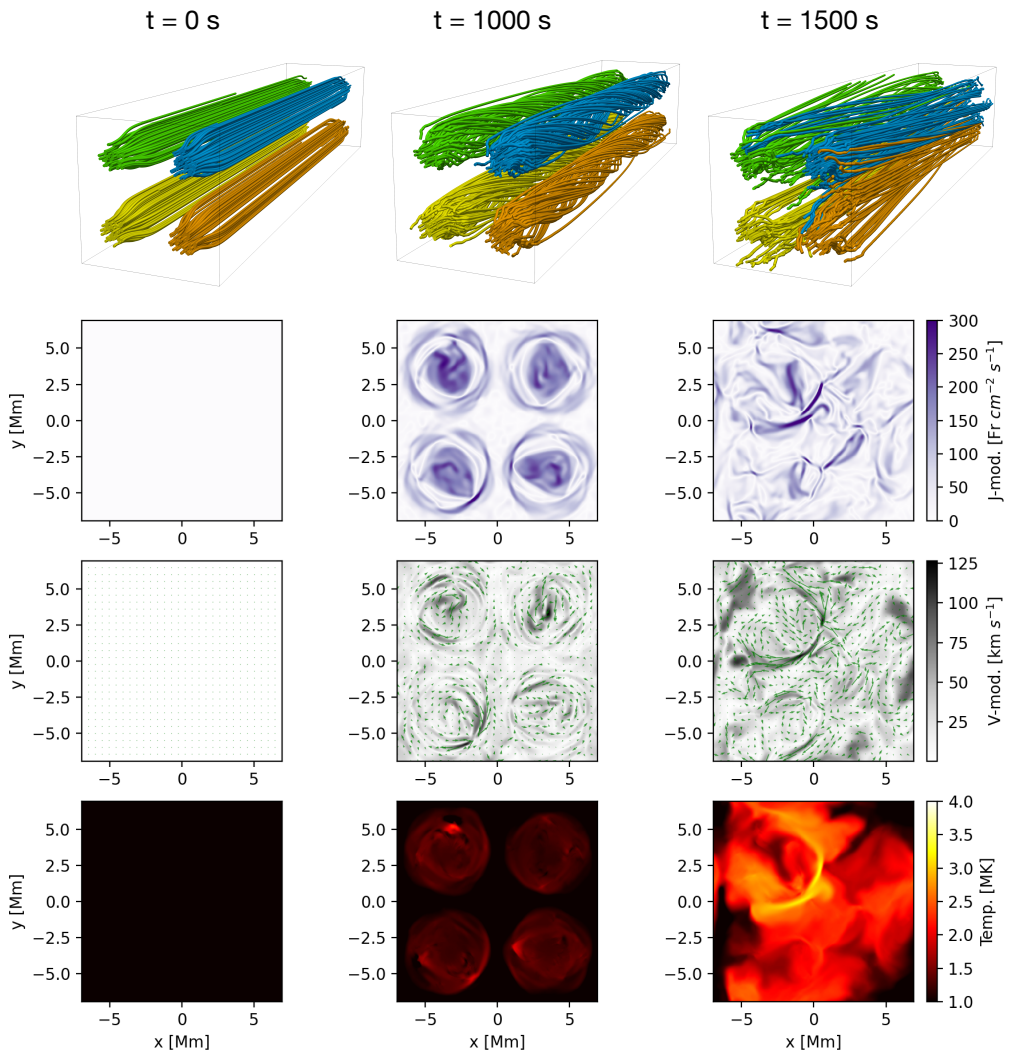

Figure 7.1: 3D MHD simulation with the PLUTO code modelling interacting coronal loops. Here we show a model of four flux tubes evolving and interacting, due to a rotation imposed at their footpoints (see text for details). For three times during the evolution – top to bottom: t = 0s (initial conditions), 1000s (first strand disruption), and 1500s (fourth strand disruption) – we show (left to right) a 3D rendering of the magnetic field lines in the box around the four modelled flux tubes (the change in the field line connectivity during the evolution of the MHD cascade is highlighted by the different colors); horizontal cuts of the current density; velocity modulus and orientation (green arrows); and plasma temperature across the mid plane.

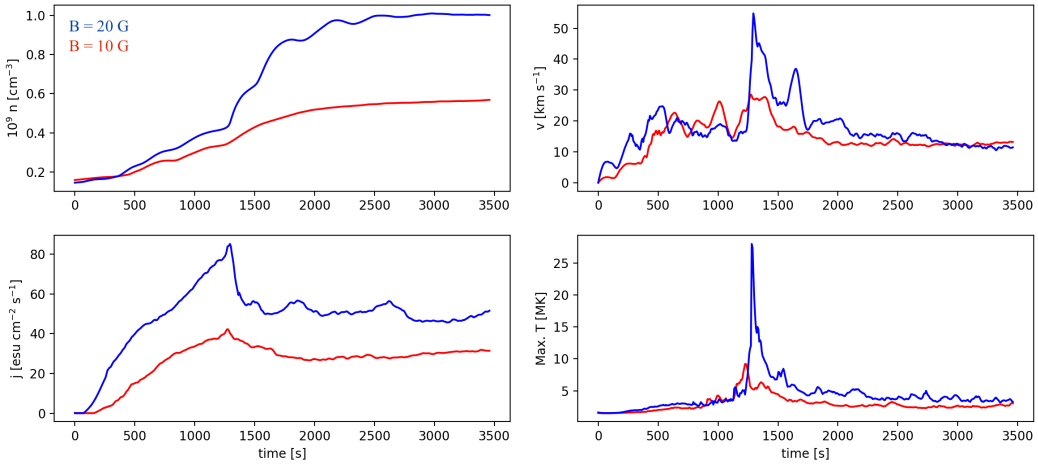

Figure 7.2: Temporal evolution of two multi-threaded coronal loops subjected to continuous footpoints twisting with guide magnetic field strength of 10 (red) and 20 (blue) G. The plots describe the averaged coronal ($T > 1$ MK) density (top-left), velocity (top-right), electric current density (bottom-left), and maximum temperature (bottom-right) evolution as function of time.

electrical conductivity, η the magnetic resistivity, and c the speed of light.

To automatically detect nanojets in the simulations, we base our criteria on specific properties of velocity, magnetic, and electric fields. In particular, we first extract a booleans 4D-cube (space and time) to cluster the plasma volume involved in reconnection outflow events. As described below and illustrated in Figure 7.3, we then apply a (connected components) machine learning clustering algorithm (He et al. 2017) to the new cube, to separate different nanojets events in space and time (top-right panel).

We define a nanojet as rapid plasma outflow generated by the slingshot-effect of magnetic field lines after reconnection. We thus consider a region of plasma A (Eq. 7.1 below) characterized by an increase in the velocity field, and where the component of the velocity perpendicular to the magnetic field exceeds a certain threshold value (for e.g., 100 km s^{-1}; top-left panel in Figure 7.3). We also account for a region of space B (Eq. 7.2 below) where magnetic dissipation region occurs, that can be identified where the electric field component parallel to the magnetic field is different than zero.

$$A = \begin{cases} v_\perp = \mathbf{v} - \frac{\mathbf{v}\cdot\mathbf{B}}{|B|}, \\ |v_\perp| > 100\,\mathrm{km\,s^{-1}}, \\ \nabla^2 |v_\perp| < 0; \end{cases} \quad (7.1) \qquad B = \begin{cases} E_\parallel = \frac{\mathbf{E}\cdot\mathbf{B}}{|B|}, \\ E_\parallel \neq 0. \end{cases} \quad (7.2)$$

The nanojet is identified as the union of A and B but only when their intersection is not an empty set: $A \cup B \neq \emptyset$, $A \cap B \neq \emptyset$. This way, we can identify volumes

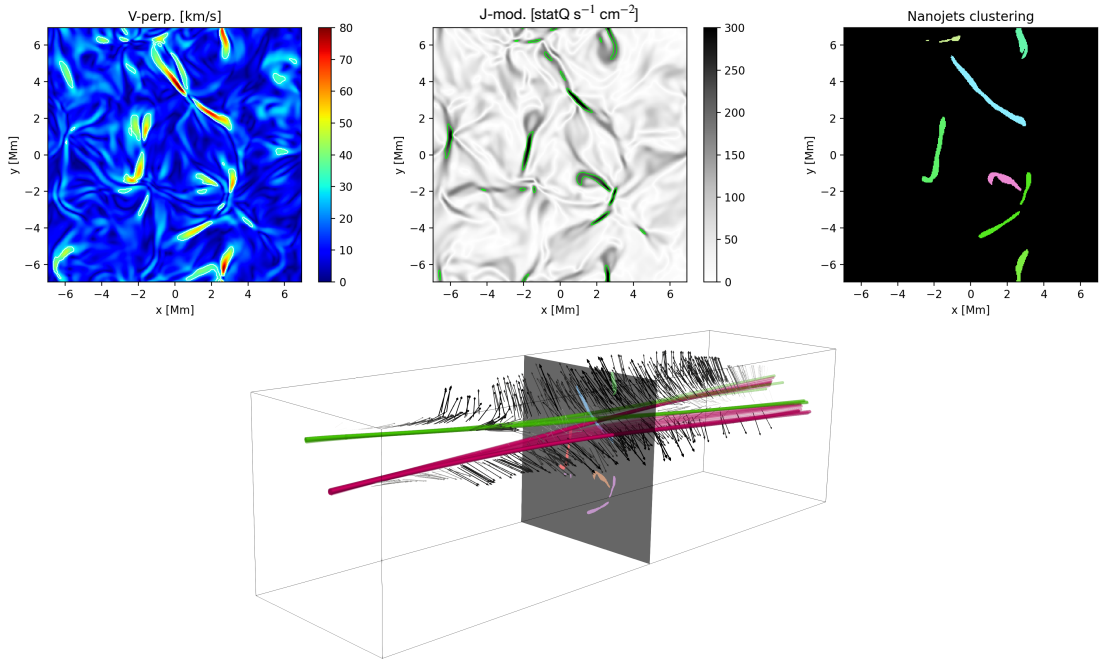

Figure 7.3: Example of automatic detection code of nanojets in 3D MHD simulations. We show the application of the automatic detection code to the PLUTO simulation shown in Figure 7.1. Top row: horizontal cut of the velocity magnitude perpendicularly to the magnetic field across the midplane and at time $t = 2000$ s (left panel); cut of the current density magnitude (middle panel), in which we highlight in green where the current exceeds the value for magnetic dissipation; and, cut of the nanojets clustering as a result of the automatic detection method (right panel). Lower panel: 3D rendering of magnetic field lines in the proximity of a nanojet reconnection region. Green and magenta field lines show connectivity change close to the light-blue nanojet cluster at the midplane. Arrows show strength and orientation of the velocity field in the proximity of the magnetic field lines.

of space where the plasma is accelerated by the magnetic field, as a consequence of released magnetic tension during reconnection. By clustering, we could also track the temporal evolution of each nanojet, allowing for statistical analysis of the results in terms, for instance, of released magnetic/internal/kinetic energy; correlations between temperature, velocity, and current density (first row, Fig. 7.4); geometrical properties (such as volume and circularity) and their relation with other physical quantities (second row, Fig. 7.4).

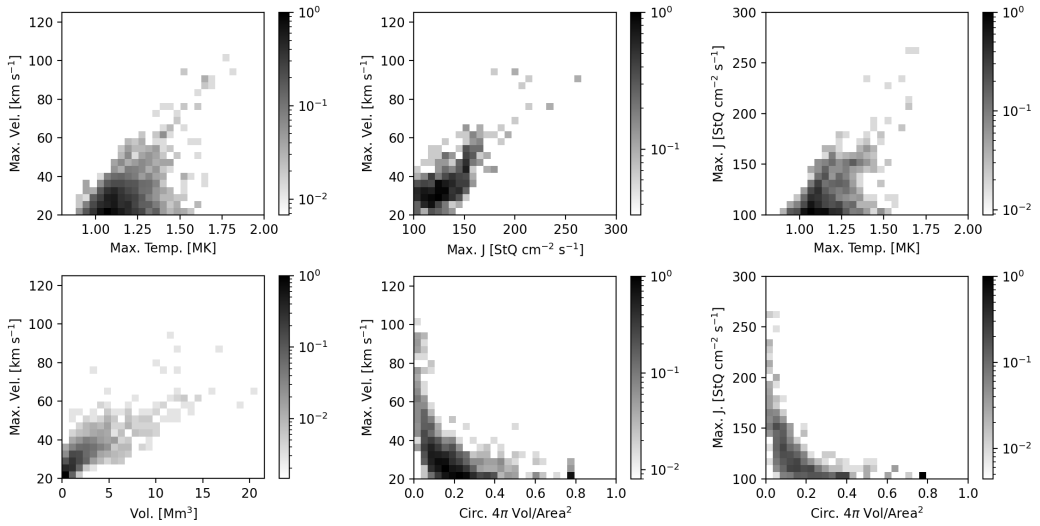

Figure 7.4: Example of statistics of nanojets properties that can be derived from the simulation. We show 2D histograms of the nanojets properties from the PLUTO simulation in Figure 7.1, highlighting possible correlations. Top row (from left): nanojets maximum velocity v.s. maximum temperature; maximum velocity v.s. maximum current density; and maximum current density v.s. max temperature. Bottom row (from left): nanojets maximum velocity, v.s. volume; maximum velocity v.s. circularity; and maximum current density v.s. circularity.

Statistical Analysis of Nanojets Properties in Simulations

The nanojet events, as identified and catalogued via the application of the above described automatic algorithm, can be analysed in detail and statistically across different models, codes, and synthetic observables. We can investigate properties such as: emission measure for different spectral lines, velocity perpendicular and parallel to the field lines, currents, temperatures, morphological properties (e.g., length, width), and duration. In Figure 7.4 we show examples of 2D histograms of pairs of variables, to investigate possible correlations, from the simulation shown in Figure 7.1. For instance, these histograms suggest correlations of maximum velocity and temperature in the nanojet with current density value, and that the highest speeds are found for larger and more elongated jets.

Discussion

This ongoing investigation is particularly timely as it addresses a the newly observed phenomenon of nanojets, that might significantly impact, as a direct nanoflares diagnostic tool, our understanding of coronal heating from magnetic reconnection. Investigating

nanojets with state-of-the-art 3D MHD models, where the physical variable are known, has multiple benefits including better understanding the nature of nanojets (e.g., by studying correlations of nanojets properties with the physical processed at work), and therefore putting the interpretation of the data on firmer grounds. In fact, synthetic observables can be derived from the physical parameters of the models (as in e.g., De Pontieu et al. 2022; Testa & Reale 2012; Testa et al. 2016; Chen et al. 2021; Hansteen et al. 2023; Cozzo et al. 2024, and Chap. 6), including the optically thin emission in the coronal SDO/AIA passbands (94Å, 131Å, 171Å, 211Å, 335Å), and the IRIS imaging and spectral TR emission. We can analyse the synthetic observables as the observational data, and derive the properties of the nanojets "as observed", also investigating the detectability of the simulated nanojets with different observatories and testing the feasibility of plasma diagnostics. Another key aspect of this work is that we can compare the results from the various simulations and explore the dependence of nanojets properties on the different physical conditions modelled, as well as possibly on the different approaches and assumptions of different codes in modelling the relevant physics. This work can allow us to evaluate possible effects of different modelling approaches while providing robust results in our understanding of reconnection driven nanojets, including constraints on nanoflare coronal heating.

8 Summary and conclusions

The work discussed in this thesis addresses the energy release in the corona as a result of photospheric-driven twisting of single or interacting magnetic flux tubes.

The work contributes to the topic of multistranded coronal loop modelling (Fuentes & Klimchuk 2010), in which coronal loops are described as an assemblage of multiple intertwined flux tubes that can be twisted, tangled, or braided together by chaotic photospheric motions. Such magnetic configurations may lead to the intensification of electric currents in narrow current sheets, thereby triggering magnetic reconnection and impulsive heating. Multistranded MHD coronal loop models represent the state-of-the-art approach in simulating DC coronal heating. This work builds upon the foundational 1D-HD framework (e.g., Peres et al. 1982), where the evolution of each individual loop strand is simulated independently by modelling the plasma as confined inside a magnetic flux tube. These models can effectively simulate the plasma response within a single strand once heating has occurred (Klimchuk 2015). Ad hoc impulsive heating is applied in a realistic stratified atmosphere from the chromosphere to the corona. These models were successfully applied to light curves and line spectra of flaring (e.g., Peres et al. 1987; Antonucci et al. 1993; Testa et al. 2014), and non-flaring coronal loops (Reale et al. 2000c,b; Price et al. 2015). By combining results from single-strand simulations, one can model multi-stranded coronal loops (Klimchuk 2006; Guarrasi et al. 2010; Reale 2014), or even of entire active regions (Warren & Winebarger 2007; Bradshaw & Viall 2016).

Our approach is a conceptual extension of this track to 3D MHD, made possible by recent improvements of computing power, and aims at studying the physics of the solar corona without loosing the conceptual effectiveness of ideal MHD modelling: we addressed specific questions about coronal loops physics, therefore avoiding a complex and encompassing reproduction of the coronal activity as a whole. As in 1D-HD coronal loop modelling, we describe the response of a stratified solar atmosphere in a straightened

flux tube against impulsive coronal heating (Linker et al. 2001; Lionello et al. 2009; Mikić et al. 2013). On the other hand, MHD allows us to address self consistent plasma heating by magnetic reconnection making a strong assumption on anomalous magnetic resistivity (Benford 1983; Hood et al. 2009), which is an intrinsically 3D phenomenon. This has enabled us to further explore the effects of magnetic reconnection within a guide magnetic field, where small-angle tilting of magnetic field lines may power the formation of reconnection outflow jets (nanojets, Antolin et al. 2021) as a direct, observable aftermath of nanoflare heating. In general, growing magnetic stresses are stored in strongly non-potential, braided, and eventually MHD-unstable magnetic structures, where excess of magnetic energy is gathered within twisted flux tubes, tapering in the chromosphere (Guarrasi et al. 2014). Many parameters are constrained by, e.g., boundary conditions (such as the amount of Poynting flux injected by photospheric vortexes, or the aspect ratio of the flux strands), thus ultimately determining amount and rate of energy released.

As a preliminary step, we have extended the study done in Reale et al. (2016) by relaxing the assumption of symmetric twisting at footpoints (chapter 3 and Cozzo et al. 2023a). Observed isolated coronal loops usually do not display strong side-by-side asymmetries despite their footpoints are likely driven by different rotation drivers in the photosphere. The small plasma β in the corona could explain why such coronal loops preserve so well such symmetry properties. Therefore, we have addressed a coronal loop twisted by non-coherent photospheric motions and investigated its response by forcing strong asymmetries. We show that coronal loops are capable to maintain high degree of symmetry for long time against asymmetric twisting drivers at their footpoints. Indeed, in order to break the symmetry, a relatively high plasma beta ($\beta \sim 1$) is required. This regime is hardly reached in the corona and strong, long lasting twisting would anyway make coronal loops unstable against kink modes (Hood & Priest 1979b). In Cozzo et al. (2023a) we have only accounted for large scale, ordered drivers but irregular patterns on smaller scales may lead to field braiding, which may make any possible asymmetry unobservable on large scales. The MHD numerical experiments presented in Cozzo et al. (2023a) can be used as a benchmark model to study energy gain and release in magnetic flux tubes, twisted by photospheric motions. By addressing observed coronal loop features (such as their symmetry), we have ultimately explored the parameter space of the Reale et al. (2016) model focusing on the flux tube evolution against different boundary twisting profiles, including non-coherent photospheric motions.

Chapters 4 and 5 (see also Cozzo et al. 2023b, and Cozzo et al. 2024) addressed coronal energy release by twisted magnetic flux tubes above the threshold for kink instability and how coronal loops, heated through an MHD avalanche process, would be observed with the forthcoming MUSE mission (De Pontieu et al. 2022). In a scenario of several twisted magnetic threads close to each other, a single unstable flux strand can trigger a cascade of instabilities in the nearby tubes, even if they are not yet kink-unstable (Tam et al. 2015). In particular, we have shown that such MHD avalanches

(Hood et al. 2016) are efficient mechanisms for fast release of magnetic energy in the corona progressively stored by slow, uniform photospheric motions (Reid et al. 2018, 2020). Cozzo et al. (2024) move on to forward modelling spectroscopic observations in Fe IX, Fe XV, and Fe XIX lines with the forthcoming MUSE mission, diagnosing plasma at temperatures of about ~ 1 MK, ~ 2 MK, and ~ 10 MK, respectively, at high spatial and temporal resolution. In particular, we provided specific observational constraints, useful for testing the model and as a guide for future modelling efforts.

In Chapter 4 magnetic reconnection inside unstable flux tubes drives bursty energy release akin to a nanoflare storm, while altering magnetic field connectivity. Repeated reconnection events lead the system towards a minimum energy state (Bareford et al. 2016). The initial helical current sheet fragments into smaller sheets, dissipating magnetic energy through Ohmic heating (Hood et al. 2009) and driving a usual loop ignition including chromospheric evaporation (Reale 2014; Reale et al. 2016). Cozzo et al. (2023b) extend prior studies on uniform coronal atmospheres by (Hood et al. 2009; Tam et al. 2015; Hood et al. 2016; Reid et al. 2018, 2020, among others), to a stratified atmosphere, confirming that twisted loops with zero net current experience kink instability. Thermal conduction effectively spreads heating along field lines, resulting in a filamentary loop temperature structure (Botha et al. 2011). In the simulation peak temperatures reach about ten millions of Kelvin degrees, with enhancement of magnetic and internal energy around 10^{27} erg, consistent with microflare observations (e.g., Testa & Reale 2020).

The modelled loop shown in Chapter 5 is typical of active region loops outside of the core and displays steady brightness primarily in the Fe XV line, with transient faint emission in Fe IX and Fe XIX at the footpoints and apex, respectively. Fe IX, Fe XV, and Fe XIX emissions reveal distinct aspects of plasma behavior. The footpoints Fe IX emission and transition-region ablation tracks the early response of the loop plasma to the impulsive energy release, while the Fe XV tracks denser plasma at intermediate heights, and the Fe XIX traces the hottest plasma within current sheets. Doppler shifts and line broadening provide further plasma dynamics details, supporting the turbulent nature of the avalanche process and aligning with forward-modelled microflaring events (Testa & Reale 2020). Line profiles frequently deviate from Gaussian shapes, reflecting the impulsive and dynamic characteristics of the instability, with notable Doppler shifts in Fe XV and Fe XIX during chromospheric upflows.

Chapter 6 focuses on the spontaneous formation and evolution of a nanojet within the same coronal flux tube system. The study aims to understand potential observational signatures of nanojets with both current and forthcoming instruments, specifically comparing the AIA imager with the future MUSE spectrometer. Unlike prior simulations (Antolin et al. 2021; Pagano et al. 2021), which imposed specific magnetic field alignments, this study singles out a collimated outflow associated with a serendipitous reconnection event triggered by the chaotic dynamics of a thermally evolving loop struc-

ture. The outflow shares usual features with observed nanojets, namely, thousands of kilometers wide and reaching velocities of several hundred kilometers per second (Antolin et al. 2021; Sukarmadji et al. 2022; Sukarmadji & Antolin 2024; Patel & Pant 2022). The nanojet forms close to the loop apex, releasing approximately 10^{24} erg, with a substantial portion converted to heat, raising plasma temperatures above 8 MK. Although, in principle, the SDO/AIA 94 Å channel is able to detect such high-temperature plasma, the cool component in the same channel makes the detection very hard. MUSE can instead isolate the hot Fe XIX line. MUSE capability to capture the expected bidirectional Doppler shifts adds on for a clearer, more precise characterization of nanojet dynamics.

Finally, in chapter 7 we further investigate DC coronal heating in multi-stranded coronal loops. We addressed the effects of continuous footpoints rotation, keeping driving the strands footpoints for a long time after the onset of the avalanche, and allowing the system to achieve a statistical energy balance. We show preliminary results focusing on the role of the guide magnetic field strength. Moreover, a physics-based algorithm for automatic detection of nanojets is presented as promising tool to investigate the nanoflare phenomenon and its observational signatures. We apply the algorithm to a simulation to show statistical correlations between general nanoflare/nanojet physical and geometrical properties.

This thesis advances our understanding of solar and stellar atmosphere heating by employing detailed numerical experiments that enable in-depth study of magnetic energy conversion to heat. By simulating twisted magnetic flux tubes under realistic solar conditions, this work dissects key physical mechanisms, such as reconnection and plasma response, which govern coronal heating. A major contribution of this research is the forward modelling of signatures —like nanojets and EUV emissions- that allow us to trace energy release dynamics. These diagnostics not only aid in interpreting complex observations but also provide rigorous tests for validating and refining numerical models through direct comparison with observed phenomena. Furthermore, the findings contribute directly to the science case for future instrumentation, particularly the upcoming MUSE mission. By predicting observable features of magnetic reconnection events and other heating signatures, this study helps shape the observational goals to improve MUSE capability to probe coronal heating.

In conclusion, although limited by some strong assumption in the microphysics to make the numerical approach feasible, this thesis shows that 3D MHD modelling of interacting and unstable coronal flux tubes provides a powerful tool both to investigate coronal heating mechanisms and physics and to provide possible diagnostics for checking with forthcoming spectroscopic observations.

8.1 Future works

The work in this thesis opens the way to a broad range of extensions and applications. First of all there are developments already on-going, those described in Chapter 7 which are still to be finalized. These developments concerns again multistrands coronal loop modelling and reconnection driven DC heating, and in particular the further application of 3D MHD simulations to interpret the observations of nanojets. We will analyze several 3D MHD coronal simulations modelling with an exploration of the space of the parameters in order to investigate statistically the properties of MHD, steady-state DC heating, and nanojets, including their correlation with the reconnection-driven nanoflares.

The modelling illustrated in this thesis is also projected toward a long-term observational perspective. It will be very interesting to test the model predictions against the real observations to be obtained with the MUSE mission, whose launch is planned in 2027. Because of its simultaneously high temporal, spatial and spectroscopic resolution, this mission will allow for deep probing physical conditions and therefore represent a quantum leap in the diagnostics of the confined corona and of magnetohydrodynamic mechanisms.

A line of future investigation concerns nanojets and their heating diagnostics by additional extensive use of 3D MHD modelling of the solar corona. We also aim to maximize the science potential of IRIS data, fully taking advantage of its spatial, temporal, and spectral resolution, and using them as a unique tool for understanding coronal heating (despite mostly observing non-coronal plasma).

We will refine the automatic nanojet detection algorithm we devised to Pluto (Mignone et al. 2007), and apply it also to Bifrost (Gudiksen et al. 2011) and MURaM (Vögler et al. 2005; Rempel 2016) simulations, that model different coronal environments in which heating and dynamics are primarily caused by current dissipation driven by footpoint braiding. Several simulations are already available for the analysis: a (Bifrost) network region (Hansteen et al. 2019) and a plage region (Hansteen et al. 2023), a (MURaM) emerging (Chen et al. 2023) and a smaller bipolar active region (Rempel 2016). They all include the chromospheric layer and overlying coronal regions. Pluto simulations are described in Sec. 7.1 and are based on the model discussed in Cozzo et al. (2023b) and Sec. 4, extended to include approximate chromospheric radiative transfer (Carlsson & Leenaarts 2012). We will complement the forward modelling and synthetic plasma diagnostics with automated detection of nanojets, therefore allowing for a statistical analysis of the temporal, geometrical, and physical properties of these events, and investigate their possible correlations with the characteristics of the heating processes.

As a parallel effort, we aim to extend the statistics of observations from Antolin et al. (2021); Sukarmadji et al. (2022); Sukarmadji & Antolin (2024); Patel & Pant (2022) by analyzing additional coordinated IRIS/SDO nanojet observations. In particular, we

plan to select observations of coronal loops configurations that closely resemble the ones in the used simulations (e.g., magnetic network region, quiescent AR, more active AR) and carry out a quantitative comparison of the observed nanojet properties with the ones predicted by these numerical experiments. We will use coordinate SDO/HMI data to infer the magnetic field properties of the observed targets for a more appropriate comparison with models matching those conditions and we will extend the existing statistics from observations by analyzing additional IRIS and SDO/AIA datasets. We will finally compute IRIS and SDO/AIA synthetic observables of nanojets to directly compare them with the observations. The observed quantities could differ from the ones derived without taking into account the observability. For instance, the event duration, can be significantly affected by the sensitivity of the instrument and the observing mode, while the maximum velocity might occur at a time when the emission measure in the observed line is not sufficient to observe the event, or the integration times are long compared with the nanojet dynamic properties, significantly impacting the statistical properties. Therefore, it is important to analyze both the intrinsic properties of the nanojets in the simulations, and the ones folding the instrumental responses. We also note that this work is of great interest as well for future missions such as EUVST and MUSE (De Pontieu et al. 2022).

This future investigation is particularly timely as it addresses a the newly observed phenomenon of nanojets, that might significantly impact, as a direct nanoflares diagnostic tool, our understanding of coronal heating from magnetic reconnection. Investigating nanojets with state-of-the-art 3D MHD models, where the physical variable are known, has multiple benefits including better understanding the nature of nanojets and therefore putting the interpretation of the data on firmer grounds. Additionally, by studying the correlations of nanojets properties with the physical processed at work will allow us to infer diagnostics from observations and test their feasibility for specific instruments. Another key aspect of this work is that we will compare the results from the various simulations and explore the dependence of nanojets properties on the different physical conditions modelled, as well as possibly on the different approaches and assumptions of the different code in modelling the relevant physics. This work will allow us to evaluate possible effects of different modelling approaches while providing robust results in our understanding of reconnection driven nanojets, including constraints on nanoflare coronal heating.

It is to be mentioned that this work is also a launch pad in the wider perspective of space weather issues, and it has been included in the COSPAR International Space Weather (ISWAT) Action Team: “Origins of the Spectral Irradiance and its Intermediate Timescale Variability”, aimed at providing physical models for improved forecasts of the spectral irradiance and accurate nowcasts of gaps in wavelength coverage.

9 Formal(-ish) Acknowledgements

This concluding section of my doctoral thesis is intended not only to formally recognize all the people and institutions that have substantially contributed to my academic and professional development, but also, inevitably, to convey my sincere gratitude in a more personal way. Yet, as with any academic effort of this magnitude, a Ph.D. is far from a solitary pursuit.

First and foremost, this thesis work and the entire Ph.D. scholarship have benefited from funding and support provided by the University of Palermo, to which I extend my acknowledgements. I also acknowledge the esteemed referees for the honest review of this work, as well as for the thoughtful insights, and the prompt feedback I received, that allowed me to refining the content of this thesis.

The research described herein has often relied on advanced high-performance computing resources, in particular the MEUSA system, part of the Sistema Computazionale per l'Astrofisica Numerica (SCAN) at INAF–Osservatorio Astronomico di Palermo. I acknowledge the efforts of all those responsible for maintaining and administering these HPC infrastructures, an indispensable task that requires recognition.

I turn now to the colleagues who have surrounded me, both experienced scholars and younger peers, who together form a "academic family" that has supported my growth. To all of them, I extend my heartfelt thanks! Among these, I would like to single out my collaborator and friend, Mr. Edoardo Alaimo, with whom I have shared a substantial portion of both my professional experience and my daily life. A warm thanks also goes to the fellow travelers I had the pleasure of meeting during my activities abroad and at conferences. I sincerely hope for future opportunities to share time and experiences together.

I am equally grateful to the many professors who have guided me. In particular, I wish to thank Professor Marco Cannas, who heads the Ph.D. program in Physical and Chemical Sciences, and Professor Grazia Cottone, who introduced me to computational

methods in Physics and kindly involved me in numerous enriching activities. I sincerely thank them for their willingness to lend an ear whenever I found myself in need of guidance, and for always offering invaluable advices.

I am also grateful to Professor Ineke De Moortel and the entire community at the University of St. Andrews Mathematics Department for welcoming me into their group. In particular, I express profound appreciation to Professor Alan Hood and Dr. Jack Reid, who served as inspiring reference points throughout my time in Scotland. I treasure the lessons learned abroad—the keen attention to detail, the intellectual earnestness, and the persistent wonder at nature's complexity—that have shaped my approach to designing and interpreting MHD models and their numerical simulations. Their words, reminding me that "simulations are always wrong until proven otherwise," remain an enduring guide to scientific humility and rigor.

My journey was further enriched at Lockheed Martin Solar and Astrophysics Laboratory in Palo Alto, where I had the honor of working with Dr. Bart De Pontieu, Dr. Juan Martinez Sykora, and Dr. Viggo Hansteen. I extend my sincere thanks for the opportunity to contribute to the MUSE mission, also supported by ASI/INAF (agreement no. 2022-29-HH.0). My time in California proved invaluable, both professionally and personally. I owe a special debt of gratitude to Dr. Paola Testa, who formally and personally ensured that my colleague Edoardo and I were well looked after, and who extended to me the privilege of continuing along this promising trajectory as a Postdoctoral member of the Harvard & Smithsonian Center for Astrophysics, a great chance to further enrich my scientific horizon. I look forward to our future collaborations!

This thesis also serves as a springboard into the realm of space weather research. It has found its place within the COSPAR International Space Weather Action Team - the "Origins of the Spectral Irradiance and its Intermediate Timescale Variability" task force - aimed at developing improved forecasts for spectral irradiance and providing accurate nowcasts in regimes where wavelength coverage remains incomplete. I wish to acknowledge Dr. Jim Klimchuk, in particular, for inviting me to join the group.

Lastly, I return to those whose guidance and support have been the cornerstone of my entire doctoral journey: my supervisors. Indeed, "the last shall be first" in these acknowledgements. A truly exemplary supervisor encourages maturity, fosters professional awareness, and sets a standard that the student aspires to emulate. In this respect, I am genuinely proud to have been guided by Professor Fabio Reale and Professor Paolo Pagano. I wish to sincerely thank Professor Paolo Pagano, whose tireless presence throughout these three years has provided me with the essential tools for solid research and always wise and enlightening conversations. To Professor Fabio Reale, I extend my heartfelt gratitude for being a praiseworthy mentor -*a mentor as a mentor shall be*- who served as a point of reference not merely during these final doctoral years, but throughout my entire tenure at the University of Palermo. He charted the course of my future, afforded me the unique opportunity to broaden my intellectual

horizons, and ultimately has, through his example, helped me evolve into a more capable and (hopefully) discerning researcher. I am confident that what we have achieved all together thus far represents but the auspicious beginnings of a much longer and more fruitful collaboration.

In sum, to all who have graced my path, enriched my understanding, and supported me in countless and immeasurable ways, I offer my sincerest thanks.

10

Acronym Index

AIA = Atmospheric Imaging Assembly
CA = Cellular Automaton
DEM = Differential Emission Measure
EM = Emission Measure
ESA = European Space Agency
EUV = Extreme UltraViolet
EUVST = Extreme UltraViolet High-Throughput Spectroscopic Telescope
FIR = Far InfraRed
FoV = Field of View
HD = HydroDynamic
Hi-C = High Resolution Coronal Imager
HMI = Helioseismic and Magnetic Imager
HXR = Hard X-Rays
IR = InfraRed
IRIS = Interface Region Solar Imager
JAXA = Japan Aerospace eXploration Agency
LTE = Local Thermodynamic Equilibrium
MDI = Michelson Doppler Imager
MHD = MagnetoHydroDynamics
MUSE = MUltislit Solar Explorer
NASA = National Aeronautics and Space Administration
NIR = Near InfraRed
NIXT = Normal Incidence X-ray Telescope
SDO = Solar Dynamics Observatory
SMM = Solar Maximum Mission
SoHO = Solar and Heliospheric Observatory

SOT = Hinode/Solar Optical Telescope
STEREO = Solar Terrestrial Relations Observatory
TR = Transition Region
TRACE = Transition Region Coronal Explorer
UV = UltraViolet
XRT = X-Ray Telescope
XUV = Xray to UltraViolet

Bibliography

Abbett, W. P. & Fisher, G. H. 2012, Solar Physics, 277, 3

Acton, L. c.-a., Culhane, J., Gabriel, A., et al. 1980, Solar Physics, 65, 53

Alazraki, G. & Couturier, P. 1971, Astronomy and Astrophysics, Vol. 13, p. 380 (1971), 13, 380

Alexiades, V., Amiez, G., & Gremaud, P.-A. 1996, Communications in numerical methods in engineering, 12, 31

Alfvén, H. 1942, Nature, 150, 405

Alfvén, H. & Lindblad, B. 1947, Monthly Notices of the Royal Astronomical Society, 107, 211

Anders, E. & Grevesse, N. 1989, Geochimica et Cosmochimica acta, 53, 197

Anderson, M., Appourchaux, T., Auchère, F., et al. 2020, Astronomy & Astrophysics, 642, A14

Antiochos, S. K. 2013, The Astrophysical Journal, 772, 72

Antolin, P., Auchère, F., Winch, E., Soubrié, E., & Oliver, R. 2024, Solar Physics, 299, 94

Antolin, P., Okamoto, T. J., De Pontieu, B., et al. 2015a, The Astrophysical Journal, 809, 72

Antolin, P., Pagano, P., Testa, P., Petralia, A., & Reale, F. 2021, Nature Astronomy, 5, 54

Antolin, P. & van Der Voort, L. R. 2012, The Astrophysical Journal, 745, 152

Antolin, P., Vissers, G., Pereira, T., van der Voort, L. R., & Scullion, E. 2015b, The Astrophysical Journal, 806, 81

Antonucci, E., Dodero, M., Martin, R., et al. 1993, Astrophysical Journal, Part 1 (ISSN 0004-637X), vol. 413, no. 2, p. 786-797., 413, 786

Antonucci, E., Rosner, R., & Tsinganos, K. 1986, Astrophysical Journal, Part 1 (ISSN 0004-637X), vol. 301, Feb. 15, 1986, p. 975-980. CNR-supported research., 301, 975

Anzer, U. 1968, Solar Physics, 3, 298

Arber, T., Longbottom, A., Gerrard, C., & Milne, A. 2001, Journal of Computational Physics, 171, 151

Arber, T., Longbottom, A., & Van der Linden, R. 1999, The Astrophysical Journal, 517, 990

Archontis, V. & Hansteen, V. 2014, The Astrophysical Journal Letters, 788, L2

Arregui, I. 2015, Philosophical Transactions of the Royal Society A: Mathematical, Physical and Engineering Sciences, 373, 20140261

Aschwanden, M. J., Crosby, N. B., Dimitropoulou, M., et al. 2016, Space Science Reviews, 198, 47

Aschwanden, M. J. & Nightingale, R. W. 2005, The Astrophysical Journal, 633, 499

Aschwanden, M. J., Wuelser, J.-P., Nitta, N. V., Lemen, J. R., & Sandman, A. 2009, The Astrophysical Journal, 695, 12

Asgari-Targhi, M., Van Ballegooijen, A., Cranmer, S., & DeLuca, E. 2013, The Astrophysical Journal, 773, 111

Avrett, E. H. & Loeser, R. 2008, The Astrophysical Journal Supplement Series, 175, 229

Bak, P. 2013, How nature works: the science of self-organized criticality (Springer Science & Business Media)

Balsara, D. S. & Spicer, D. S. 1999, Journal of Computational Physics, 149, 270

Bareford, M., Browning, P., & Van der Linden, R. 2011, Solar Physics, 273, 93

Bareford, M. & Hood, A. 2015, Philosophical Transactions of the Royal Society A: Mathematical, Physical and Engineering Sciences, 373, 20140266

Bareford, M., Hood, A., & Browning, P. 2013, Astronomy & Astrophysics, 550, A40

Bareford, M. R., Browning, P., & Van der Linden, R. A. 2010, Astronomy & Astrophysics, 521, A70

Bareford, M. R., Gordovskyy, M., Browning, P., & Hood, A. W. 2016, Solar Physics, 291, 187

Batten, P., Clarke, N., Lambert, C., & Causon, D. M. 1997, SIAM Journal on Scientific Computing, 18, 1553

Baty, H. 2000, Astronomy and Astrophysics, v. 353, p. 1074-1082 (2000), 353, 1074

Baty, H. & Heyvaerts, J. 1996, Astronomy and Astrophysics, v. 308, p. 935-950, 308, 935

Belcher, J. W. & Davis Jr, L. 1971, Journal of Geophysical Research, 76, 3534

Bellan, P. 2018, Journal of Plasma Physics, 84, 755840501

Bellan, P. M. 2000, Spheromaks: a practical application of magnetohydrodynamic dynamos and plasma self-organization (World Scientific)

Benford, G. 1983, Astrophysical Journal, Part 1 (ISSN 0004-637X), vol. 269, June 15, 1983, p. 690-697., 269, 690

Benz, A. O. 2017, Living reviews in solar physics, 14, 1

Berger, M. A. 1984, Geophysical & Astrophysical Fluid Dynamics, 30, 79

Berger, T., De Pontieu, B., Fletcher, L., et al. 1999, Solar Physics, 190, 409

Bernstein, I. B., Frieman, E., Kruskal, M. D., & Kulsrud, R. 1958, Proceedings of the Royal Society of London. Series A. Mathematical and Physical Sciences, 244, 17

Betta, R., Peres, G., Reale, F., & Serio, S. 1997, Astronomy and Astrophysics Supplement Series, 122, 585

Betta, R., Peres, G., Reale, F., & Serio, S. 2001, Astronomy & Astrophysics, 380, 341

Beveridge, C., Longcope, D., & Priest, E. R. 2003, Solar Physics, 216, 27

Bineau, M. 1972, Communications on Pure and Applied Mathematics, 25, 77

Biskamp, D. 1982, Zeitschrift für Naturforschung A, 37, 840

Biskamp, D. 1986, The Physics of fluids, 29, 1520

Biskamp, D. 1994, Physics Reports, 237, 179

Boerner, P., Edwards, C., Lemen, J., et al. 2012, The Solar Dynamics Observatory, 41

Boerner, P., Testa, P., Warren, H., Weber, M., & Schrijver, C. 2014, Solar Physics, 289, 2377

Bogachev, S. & Erkhova, N. 2023, Solar-Terrestrial Physics, 9, 3

Bohlin, J. D., Frost, K. J., Burr, P. T., Guha, A. K., & Withbroe, G. L. 1980, Solar Physics, 65, 5

Borrero, J. M. & Ichimoto, K. 2011, Living Reviews in Solar Physics, 8, 1

Botha, G., Arber, T., & Hood, A. W. 2011, Astronomy & Astrophysics, 525, A96

Botha, G. J. J., Arber, T. D., & Hood, A. W. 2011, Astronomy and Astrophysics, 525

Bradshaw, S. J. & Cargill, P. J. 2013, The Astrophysical Journal, 770, 12

Bradshaw, S. J. & Klimchuk, J. A. 2011, The Astrophysical Journal Supplement Series, 194, 26

Bradshaw, S. J. & Viall, N. M. 2016, The Astrophysical Journal, 821, 63

Braithwaite, J. 2006, Astronomy & Astrophysics, 453, 687

Braus, M. 2019

Breu, C., Peter, H., Cameron, R., et al. 2022, Astronomy & Astrophysics, 658, A45

Brickhouse, N. S. & Schmelz, J. 2005, The Astrophysical Journal, 636, L53

Brooks, D. H. & Warren, H. P. 2009, The Astrophysical Journal, 703, L10

Brooks, D. H., Warren, H. P., & Landi, E. 2021, The Astrophysical Journal Letters, 915, L24

Brooks, D. H., Warren, H. P., & Landi, E. 2021, Astrophysical Journal Supplements Letters, 915, L24

Brooks, D. H., Warren, H. P., & Ugarte-Urra, I. 2012, The Astrophysical Journal Letters, 755, L33

Brooks, D. H., Warren, H. P., Ugarte-Urra, I., & Winebarger, A. R. 2013, The Astrophysical Journal Letters, 772, L19

Browning, P. 1988, Journal of plasma physics, 40, 263

Browning, P. 2003, Astronomy & Astrophysics, 400, 355

Browning, P., Cardnell, S., Evans, M., et al. 2015, Plasma Physics and Controlled Fusion, 58, 014041

Browning, P., Gerrard, C., Hood, A., Kevis, R., & Van der Linden, R. 2008, Astronomy & Astrophysics, 485, 837

Browning, P. & Hood, A. 1989, Solar physics, 124, 271

Browning, P. & Priest, E. 1984, Astronomy and Astrophysics (ISSN 0004-6361), vol. 131, no. 2, Feb. 1984, p. 283-290. Research supported by the Science and Engineering Research Council of England., 131, 283

Browning, P. & Priest, E. 1986, Astronomy and Astrophysics, 159, 129

Browning, P., Stanier, A., Ashworth, G., McClements, K., & Lukin, V. 2014, Plasma Physics and Controlled Fusion, 56, 064009

Brueckner, G. & Bartoe, J.-D. 1983, Astrophysical Journal, Part 1 (ISSN 0004-637X), vol. 272, Sept. 1, 1983, p. 329-348., 272, 329

Cadavid, A., Lawrence, J., Christian, D., Jess, D., & Nigro, G. 2014, The Astrophysical Journal, 795, 48

Cargill, P. & Klimchuk, J. 1997, The Astrophysical Journal, 478, 799

Cargill, P., Warren, H., & Bradshaw, S. 2015, Philosophical Transactions of the Royal Society A: Mathematical, Physical and Engineering Sciences, 373, 20140260

Cargill, P. J., Bradshaw, S. J., & Klimchuk, J. A. 2012, The Astrophysical Journal, 752, 161

Cargill, P. J. & Klimchuk, J. A. 2004, The Astrophysical Journal, 605, 911

Carlsson, M., Hansteen, V. H., & Gudiksen, B. V. 2010, arXiv preprint arXiv:1001.1546

Carlsson, M. & Leenaarts, J. 2012, Astronomy & Astrophysics, 539, A39

Carlsson, M. & Stein, R. F. 1992, Astrophysical Journal, Part 2-Letters (ISSN 0004-637X), vol. 397, no. 1, p. L59-L62., 397, L59

Carlsson, M. & Stein, R. F. 1994, arXiv preprint astro-ph/9411036

Carlsson, M. & Stein, R. F. 1997, The Astrophysical Journal, 481, 500

Carlsson, M. & Stein, R. F. 2002, The Astrophysical Journal, 572, 626

Charbonneau, P. 2020, Living Reviews in Solar Physics, 17, 1

Charbonneau, P., McIntosh, S. W., Liu, H.-L., & Bogdan, T. J. 2001, Solar Physics, 203, 321

Chen, F., Cheung, M. C., Rempel, M., & Chintzoglou, G. 2023, The Astrophysical Journal, 949, 118

Chen, Y., Przybylski, D., Peter, H., et al. 2021, Astronomy & Astrophysics, 656, L7

Cheng, C.-C., Oran, E., Doschek, G., Boris, J., & Mariska, J. 1983, Astrophysical Journal, Part 1, vol. 265, Feb. 15, 1983, p. 1090-1119. NASA-Navy-supported research., 265, 1090

Cheung, M. C., Martínez-Sykora, J., Testa, P., et al. 2022, The Astrophysical Journal, 926, 53

Chiuderi, C. & Velli, M. 2012, Fisica del Plasma: Fondamenti e applicazioni astrofisiche (Springer Science & Business Media)

Christe, S., Hannah, I., Krucker, S., McTiernan, J., & Lin, R. P. 2008, The Astrophysical Journal, 677, 1385

Close, R., Parnell, C. E., Longcope, D., & Priest, E. R. 2004, The Astrophysical Journal, 612, L81

Cockburn, B. & Shu, C.-W. 2001, Journal of scientific computing, 16, 173

Coleman Jr, P. J. 1968, Astrophysical Journal, vol. 153, p. 371, 153, 371

Compton, W. D. & Benson, C. D. 1983, Living and working in space. A history of Skylab, Tech. rep.

Connor, J. W., Hastie, R., & Taylor, J. B. 1979, Proceedings of the Royal Society of London. A. Mathematical and Physical Sciences, 365, 1

Cooper, F., Nakariakov, V., & Williams, D. 2003, Astronomy & Astrophysics, 409, 325

Cowie, L. L. & Mckee, C. F. 1977, The Astrophysical Journal, 211, 135

Cowling, T. 1958, in Symposium-International Astronomical Union, Vol. 6, Cambridge University Press, 105–113

Cozzo, G., Pagano, P., Petralia, A., & Reale, F. 2023a, Symmetry, 15, 627

Cozzo, G., Reid, J., Pagano, P., Reale, F., & Hood, A. W. 2023b, Astronomy & Astrophysics, 678, A40

Cozzo, G., Reid, J., Pagano, P., et al. 2024, arXiv preprint arXiv:2406.11701

Crosby, N. B., Aschwanden, M. J., & Dennis, B. R. 1993, Solar Physics, 143, 275

Culhane, J. L., Harra, L. K., James, A. M., et al. 2007, , 243, 19

Dahlburg, R., Einaudi, G., Taylor, B., et al. 2016, The Astrophysical Journal, 817, 47

De Moortel, I. & Galsgaard, K. 2006, Astronomy & Astrophysics, 451, 1101

De Moortel, I., McIntosh, S., Threlfall, J., Bethge, C., & Liu, J. 2014, The Astrophysical Journal Letters, 782, L34

De Moortel, I. & Nakariakov, V. M. 2012, Philosophical Transactions of the Royal Society A: Mathematical, Physical and Engineering Sciences, 370, 3193

De Pontieu, B., De Moortel, I., Martinez-Sykora, J., & McIntosh, S. 2017a, The Astrophysical Journal Letters, 845, L18

De Pontieu, B., Martínez-Sykora, J., & Chintzoglou, G. 2017b, The Astrophysical Journal Letters, 849, L7

De Pontieu, B., Martínez-Sykora, J., Testa, P., et al. 2019, The Astrophysical Journal, 888, 3

De Pontieu, B., Martínez-Sykora, J., Testa, P., et al. 2020, Astrophysical Journal, 888, 3

De Pontieu, B., Testa, P., Martínez-Sykora, J., et al. 2022, The Astrophysical Journal, 926, 52

De Pontieu, B., Title, A., Lemen, J., et al. 2014, Solar Physics, 289, 2733

Del Zanna, G. 2013, Astronomy & Astrophysics, 558, A73

Del Zanna, G., Dere, K., Young, P., & Landi, E. 2021, The Astrophysical Journal, 909, 38

Del Zanna, G. & Mason, H. E. 2018, Living Reviews in Solar Physics, 15, 5

Del Zanna, L., Landi, S., Papini, E., Pucci, F., & Velli, M. 2016, 719, 012016

Dennis, B. R. 1985, Solar physics, 100, 465

Dere, K., Landi, E., Mason, H., Fossi, B. M., & Young, P. 1997, Astronomy and Astrophysics Supplement Series, 125, 149

Díaz-Castillo, S., Fischer, C., Rezaei, R., Steiner, O., & Berdyugina, S. 2024, Astronomy & Astrophysics, 691, A37

Dixon, A., Berger, M., Priest, E., & Browning, P. 1989, Astronomy and Astrophysics (ISSN 0004-6361), vol. 225, no. 1, Nov. 1989, p. 156-166. Research supported by SERC and Culham Laboratory., 225, 156

Domingo, V., Fleck, B., & Poland, A. I. 1995, Solar Physics, 162, 1

Doschek, G., Warren, H., Mariska, J., et al. 2008, The Astrophysical Journal, 686, 1362

Drake, J. F. 1971, Solar Physics, 16, 152

Duck, R., Browning, P., Cunningham, G., et al. 1997, Plasma Physics and Controlled Fusion, 39, 715

Duijveman, A., Hoyng, P., & Ionson, J. A. 1981, Astrophysical Journal, Part 1, vol. 245, Apr. 15, 1981, p. 721-735., 245, 721

Dungey, J. W. 1961, Physical Review Letters, 6, 47

Edlén, B. 1943, Zeitschrift für Astrophysik, Vol. 22, p. 30, 22, 30

Fawcett, B., Peacock, N., & Cowan, R. 1968, Journal of Physics B: Atomic and Molecular Physics, 1, 295

Feldman, U. 1992, Physica Scripta, 46, 202

Fisher, G. H., Canfield, R. C., & McClymont, A. N. 1985, Astrophysical Journal, Vol. 289, NO. 1/FEB. 1, P. 434, 1985, 289, 434

Forbes, T. & Priest, E. 1987, Reviews of Geophysics, 25, 1583

Fuentes, M. L. & Klimchuk, J. 2010, The Astrophysical Journal, 719, 591

Fuentes, M. L. & Klimchuk, J. A. 2015, The Astrophysical Journal, 799, 128

Fuentes, M. L., Klimchuk, J. A., & Démoulin, P. 2006, The Astrophysical Journal, 639, 459

Fuentes-Fernández, J., Parnell, C. E., Hood, A. W., Priest, E. R., & Longcope, D. W. 2012, Physics of Plasmas, 19

Furth, H. P., Killeen, J., & Rosenbluth, M. N. 1963, The physics of Fluids, 6, 459

Gabriel, A. 1976a, Philosophical Transactions of the Royal Society of London. Series A, Mathematical and Physical Sciences, 281, 339

Gabriel, A. 1976b, Philosophical Transactions for the Royal Society of London. Series A, Mathematical and Physical Sciences, 339

Galsgaard, K. & Nordlund, Å. 1997, Journal of Geophysical Research: Space Physics, 102, 219

Garcia Briseno, D. & Ireland, J. 2023, in AAS/Solar Physics Division Meeting, Vol. 55, 54th Meeting of the Solar Physics Division, 107.09

Gary, G. A. 2001, Solar Physics, 203, 71

Gerrard, C., Arber, T., & Hood, A. W. 2001, Astronomy & Astrophysics, 373, 1089

Gerrard, C. & Hood, A. W. 2003, Solar Physics, 214, 151

Giacconi, R., Reidy, W., Zehnpfennig, T., Lindsay, J., & Muney, W. 1965, Astrophysical Journal, vol. 142, p. 1274-1278, 142, 1274

Gibson, E. G. 1977, Solar Physics, 53, 123

Gimblett, C., Hastie, R., & Helander, P. 2006, Physical review letters, 96, 035006

Giovanelli, R. 1947, Monthly Notices of the Royal Astronomical Society, 107, 338

Gizon, L. & Birch, A. C. 2005, lrsp, 2

Glesener, L., Krucker, S., Hannah, I. G., et al. 2017, The Astrophysical Journal, 845, 122

Godunov, S. K. & Bohachevsky, I. 1959, Matematičeskij sbornik, 47, 271

Gold, T. & Hoyle, F. 1960, Monthly Notices of the Royal Astronomical Society, 120, 89

Golub, L. & Herant, M. 1989, X-Ray/EUV Optics for Astronomy and Microscopy, 1160, 629

Golub, L. & Pasachoff, J. M. 2010, The solar corona (Cambridge University Press)

Gomez, D. O., Martens, P. C., & Golub, L. 1993, Astrophysical Journal, Part 1 (ISSN 0004-637X), vol. 405, no. 2, p. 767-781., 405, 767

Goossens, M., Andries, J., & Arregui, I. 2006, Philosophical Transactions of the Royal Society A: Mathematical, Physical and Engineering Sciences, 364, 433

Goossens, M., Andries, J., & Aschwanden, M. 2002, Astronomy & Astrophysics, 394, L39

Goossens, M., Erdélyi, R., & Ruderman, M. S. 2011, Space science reviews, 158, 289

Gordovskyy, M., Browning, P., Kontar, E., & Bian, N. 2013, Solar Physics, 284, 489

Gordovskyy, M., Browning, P., Kontar, E., & Bian, N. 2014, Astronomy & Astrophysics, 561, A72

Gordovskyy, M., Kontar, E., & Browning, P. 2016, Astronomy & Astrophysics, 589, A104

Grad, H. & Rubin, H. 1958, in Proceedings of the Second. United Nations International Conference on the Peaceful Uses of Atomic Energy, Vol. 31, 190–197

Grotian, W. 1939, Naturwissenschaften, 27, 214

Gryaznevich, M. & Sykes, A. 2017, Nuclear Fusion, 57, 072003

Guarrasi, M., Reale, F., Orlando, S., Mignone, A., & Klimchuk, J. 2014, Astronomy & Astrophysics, 564, A48

Guarrasi, M., Reale, F., & Peres, G. 2010, The Astrophysical Journal, 719, 576

Gudiksen, B. V., Carlsson, M., Hansteen, V. H., et al. 2011, Astronomy & Astrophysics, 531, A154

Gudiksen, B. V. & Nordlund, Å. 2005a, The Astrophysical Journal, 618, 1031

Gudiksen, B. V. & Nordlund, Å. 2005b, The Astrophysical Journal, 618, 1020

Handy, B., Acton, L., Kankelborg, C., et al. 1999, Solar Physics, 187, 229

Hannah, I., Christe, S., Krucker, S., et al. 2008, The Astrophysical Journal, 677, 704

Hansteen, V., Ortiz, A., Archontis, V., et al. 2019, Astronomy & Astrophysics, 626, A33

Hansteen, V. H., Hara, H., De Pontieu, B., & Carlsson, M. 2010, The Astrophysical Journal, 718, 1070

Hansteen, V. H., Martinez-Sykora, J., Carlsson, M., et al. 2023, The Astrophysical Journal, 944, 131

Hathaway, D. H. 2015, Living reviews in solar physics, 12, 4

He, L., Ren, X., Gao, Q., et al. 2017, Pattern Recognition, 70, 25

Hendrix, D. & Van Hoven, G. 1996, Astrophysical Journal v. 467, p. 887, 467, 887

Hesse, M. & Schindler, K. 1988, Journal of Geophysical Research: Space Physics, 93, 5559

Heyvaerts, J. & Priest, E. 1984, Astronomy and Astrophysics (ISSN 0004-6361), vol. 137, no. 1, Aug. 1984, p. 63-78., 137, 63

Heyvaerts, J. & Priest, E. R. 1983, Astronomy and Astrophysics, vol. 117, no. 2, Jan. 1983, p. 220-234., 117, 220

Heyvaerts, J., Priest, E. R., & Rust, D. M. 1977, Astrophysical Journal, Part 1, vol. 216, Aug. 15, 1977, p. 123-137., 216, 123

Hood, A., Browning, P., & Van der Linden, R. 2009, Astronomy & Astrophysics, 506, 913

Hood, A. & Priest, E. 1979a, Astronomy and Astrophysics, 77, 233

Hood, A. & Priest, E. 1981, Geophysical & Astrophysical Fluid Dynamics, 17, 297

Hood, A. W., Cargill, P., Browning, P., & Tam, K. 2016, The Astrophysical Journal, 817, 5

Hood, A. W. & Priest, E. 1979b, Solar Physics, 64, 303

Hornig, G. & Rastätter, L. 1998, Physica Scripta, 1998, 34

Howson, T., De Moortel, I., & Antolin, P. 2017, Astronomy & Astrophysics, 602, A74

Hudson, H. 1991, Solar Physics, 133, 357

Hudson, H. 2010, Heliophysics: space storms and radiation: causes and effects. Cambridge University Press, London. p, 123

Hudson, H. S. 2011, Space Science Reviews, 158, 5

Hughes, D., Paczuski, M., Dendy, R., Helander, P., & McClements, K. 2003, Physical Review Letters, 90, 131101

Hussain, A. 2018

Hussain, A., Browning, P., & Hood, A. 2017, Astronomy & Astrophysics, 600, A5

Ishikawa, R., Bueno, J. T., del Pino Alemán, T., et al. 2021, Science Advances, 7, eabe8406

Ishikawa, S.-n., Glesener, L., Krucker, S., et al. 2017, Nature Astronomy, 1, 771

Jackson, J. D. 2021, Classical electrodynamics (John Wiley & Sons)

Jakimiec, J., Sylwester, B., Sylwester, J., et al. 1992, Astronomy and Astrophysics (ISSN 0004-6361), vol. 253, no. 1, Jan. 1992, p. 269-276. Research supported by Polish Academy of Sciences, ASI, CNR, and MURST., 253, 269

Janhunen, P. 2000, Journal of Computational Physics, 160, 649

Jess, D. B., Reznikova, V. E., Ryans, R. S., et al. 2016, Nature Physics, 12, 179

Ji, H., Prager, S., & Sarff, J. 1995, Physical review letters, 74, 2945

Johnston, C. & Bradshaw, S. 2019, The Astrophysical Journal Letters, 873, L22

Johnston, C. D., Cargill, P. J., Hood, A. W., et al. 2020, 635, A168

Johnston, C. D., Hood, A. W., De Moortel, I., Pagano, P., & Howson, T. A. 2021, Astronomy & Astrophysics, 654, A2

Kahler, S. 1982, Journal of Geophysical Research: Space Physics, 87, 3439

Kaiser, M. L., Kucera, T., Davila, J., et al. 2008, Space Science Reviews, 136, 5

Katsukawa, Y. & Tsuneta, S. 2002, in COSPAR Colloquia Series, Vol. 13, Elsevier, 61–64

Kliem, B., Karlicky, M., & Benz, A. O. 2000, arXiv preprint astro-ph/0006324

Kliem, B., Lee, J., Liu, R., et al. 2021, The Astrophysical Journal, 909, 91

Kliem, B., Linton, M., Török, T., & Karlickỳ, M. 2010, Solar Physics, 266, 91

Kliem, B., Török, T., Titov, V. S., et al. 2014, arXiv preprint arXiv:1407.2272

Klimchuk, J., Patsourakos, S., & Cargill, P. 2008, The Astrophysical Journal, 682, 1351

Klimchuk, J. A. 2006, Solar Physics, 234, 41

Klimchuk, J. A. 2009, arXiv preprint arXiv:0904.1391

Klimchuk, J. A. 2015, Philosophical Transactions of the Royal Society A: Mathematical, Physical and Engineering Sciences, 373, 20140256

Klimchuk, J. A. 2017, arXiv preprint arXiv:1709.07320

Klimchuk, J. A. & Antiochos, S. K. 2021, Frontiers in Astronomy and Space Sciences, 8, 662861

Klimchuk, J. A., Fuentes, L., & Devore, C. 2006, in SOHO-17. 10 Years of SOHO and Beyond, Vol. 617

Klimchuk, J. A., Leake, J. E., Daldorff, L. K., & Johnston, C. D. 2023, Frontiers in Physics, 11, 1198194

Klimchuk, J. A., Lemen, J. R., Feldman, U., Tsuneta, S., & Uchida, Y. 1992, PASJ: Publications of the Astronomical Society of Japan (ISSN 0004-6264), vol. 44, no. 5, p. L181-L185., 44, L181

Kolmogorov, A. N. 1941, Numbers. In Dokl. Akad. Nauk SSSR, 30, 301

Kondrashov, D., Feynman, J., Liewer, P., & Ruzmaikin, A. 1999, The Astrophysical Journal, 519, 884

Kosugi, T., Matsuzaki, K., Sakao, T., et al. 2008, The Hinode Mission, 5

Kramar, M., Jones, S., Davila, J., Inhester, B., & Mierla, M. 2009, Solar Physics, 259, 109

Krieger, A., Paolini, F., Vaiana, G., & Webb, D. 1972, Solar Physics, 22, 150

Krucker, S., Christe, S., Glesener, L., et al. 2014, The Astrophysical Journal Letters, 793, L32

Kruskal, M. D., Johnson, J., Gottlieb, M., & Goldman, L. 1958, Physics of Fluids, 1, 421

Kudoh, T. & Shibata, K. 1999, The Astrophysical Journal, 514, 493

Kuridze, D., Mathioudakis, M., Kowalski, A., et al. 2013, Astronomy & Astrophysics, 552, A55

Landi, E. & Reale, F. 2013, The Astrophysical Journal, 772, 71

Landi, S., Del Zanna, L., Papini, E., Pucci, F., & Velli, M. 2015, The Astrophysical Journal, 806, 131

Lang, K. R. 2001, The Cambridge encyclopedia of the sun

Lazarian, A., Eyink, G., Vishniac, E., & Kowal, G. 2015, Philosophical Transactions of the Royal Society A: Mathematical, Physical and Engineering Sciences, 373, 20140144

Leamon, R. J., Canfield, R. C., Blehm, Z., & Pevtsov, A. A. 2003, The Astrophysical Journal, 596, L255

Lee, J.-Y., Leka, K., Barnes, G., et al. 2009, in The Second Hinode Science Meeting: Beyond Discovery-Toward Understanding, Vol. 415, 279

Lemen, J. R., Title, A. M., Akin, D. J., et al. 2012, Solar Physics, 275, 17

Lenz, D. D., DeLuca, E. E., Golub, L., Rosner, R., & Bookbinder, J. A. 1999, The Astrophysical Journal, 517, L155

LeVeque, R., Mihalas, D., Dorfi, E., & Müller, E. 1998, Lecture Notes 1997 of the Swiss Society for Astronomy and Astrophysics (SSAA)

Li, S. 2005, Journal of computational physics, 203, 344

Liang, Y., Gimblett, C., Browning, P., et al. 2010, Physical review letters, 105, 065001

Lim, D., Van Doorsselaere, T., Berghmans, D., et al. 2023, The Astrophysical Journal Letters, 952, L15

Lin, R., Schwartz, R., Kane, S. R., Pelling, R., & Hurley, K. 1984, Astrophysical Journal, Part 1 (ISSN 0004-637X), vol. 283, Aug. 1, 1984, p. 421-425. Sponsorship: Centre National d'Etudes Spatiales., 283, 421

Lin, R. P., Dennis, B. R., Hurford, G. J., et al. 2003, The Reuven Ramaty High-Energy Solar Spectroscopic Imager (RHESSI) Mission Description and Early Results, 3

Linker, J. A., Lionello, R., Mikić, Z., & Amari, T. 2001, Journal of Geophysical Research, 106, 25165

Linton, M., Dahlburg, R., & Antiochos, S. 2001, The Astrophysical Journal, 553, 905

Lionello, R., Linker, J. A., & Mikić, Z. 2009, Astrophysical Journal, 690, 902

Lionello, R., Velli, M., Einaudi, G., & Mikić, Z. 1998, The Astrophysical Journal, 494, 840

Lites, B. & Hansen, E. 1977, Solar Physics, 55, 347

Liu, R. 2020, Research in Astronomy and Astrophysics, 20, 165

Londrillo, P. & Del Zanna, L. 2004, Journal of Computational Physics, 195, 17

Long, D. M., Valori, G., Pérez-Suárez, D., Morton, R. J., & Vásquez, A. M. 2017, Astronomy & Astrophysics, 603, A101

Lothian, R. & Hood, A. 1989, Solar physics, 122, 227

Lu, E. T. & Hamilton, R. J. 1991, Astrophysical Journal, Part 2-Letters (ISSN 0004-637X), vol. 380, Oct. 20, 1991, p. L89-L92., 380, L89

Lu, E. T., Hamilton, R. J., McTiernan, J., & Bromund, K. R. 1993, Astrophysical Journal, Part 1 (ISSN 0004-637X), vol. 412, no. 2, p. 841-852., 412, 841

Lundquist, S. 1951, Physical Review, 83, 307

MacNeice, P. 1986, Solar physics, 103, 47

Magyar, N. & Van Doorsselaere, T. 2016, Astronomy & Astrophysics, 595, A81

Martínez-Sykora, J., De Pontieu, B., Hansteen, V. H., et al. 2017, Science, 356, 1269

Martínez-Sykora, J., Hansteen, V., & Carlsson, M. 2009, The Astrophysical Journal, 702, 129

Martínez-Sykora, J., Hansteen, V., & Moreno-Insertis, F. 2011, The Astrophysical Journal, 736, 9

McIntosh, S. W. 2012, Space science reviews, 172, 69

McIntosh, S. W., De Pontieu, B., Carlsson, M., et al. 2011, Nature, 475, 477

McKevitt, J., Jarolim, R., Matthews, S., et al. 2024, The Astrophysical Journal Letters, 961, L29

McLaughlin, J. & Ofman, L. 2008, The Astrophysical Journal, 682, 1338

Melrose, D. 1997, The Astrophysical Journal, 486, 521

Mendoza, M., Kaydul, A., De Arcangelis, L., Andrade Jr, J. S., & Herrmann, H. J. 2014, Nature communications, 5, 5035

Miceli, M., Reale, F., Gburek, S., et al. 2012, Astronomy & Astrophysics, 544, A139

Mignone, A. 2005, The Astrophysical Journal, 626, 373

Mignone, A., Bodo, G., Massaglia, S., et al. 2007, The Astrophysical Journal Supplement Series, 170, 228

Mignone, A., Flock, M., Stute, M., Kolb, S., & Muscianisi, G. 2012, Astronomy & Astrophysics, 545, A152

Mikic, Z., Schnack, D. D., & Van Hoven, G. 1990, The Astrophysical Journal, 361, 690

Mikić, Z., Lionello, R., Mok, Y., Linker, J. A., & Winebarger, A. R. 2013, Astrophysical Journal, 773

Moll, R., Cameron, R., & Schüssler, M. 2011, Astronomy & Astrophysics, 533, A126

Mondal, S. 2021, , 296

Morales, L. & Charbonneau, P. 2008, The Astrophysical Journal, 682, 654

Morton, R. & McLaughlin, J. 2013, Astronomy & Astrophysics, 553, L10

Morton, R., Tomczyk, S., & Pinto, R. 2016, The Astrophysical Journal, 828, 89

Müller, D., Cyr, O. S., Zouganelis, I., et al. 2020, Astronomy & Astrophysics, 642, A1

Murray, S. A., Bloomfield, D. S., & Gallagher, P. T. 2013, Astronomy & Astrophysics, 550, A119

Nakariakov, V., Anfinogentov, S., Antolin, P., et al. 2021, Space Science Reviews, 217, 73

Nakariakov, V., Arber, T., Ault, C., et al. 2004, Monthly Notices of the Royal Astronomical Society, 349, 705

Nakariakov, V. M. & Verwichte, E. 2005, Living Reviews in Solar Physics, 2, 3

Nandy, D., Hahn, M., CANfiELD, R. C., & Longcope, D. W. 2003, The Astrophysical Journal, 597, L73

Newcomb, W. A. 1960, Annals of Physics, 10, 232

Ng, C., Lin, L., & Bhattacharjee, A. 2012, The Astrophysical Journal, 747, 109

Northrop, T. G. 1963, The adiabatic motion of charged particles, Vol. 21 (Interscience Publishers)

Ofman, L. 2009, The Astrophysical Journal, 694, 502

Ofman, L., Nakariakov, V., & DeForest, C. 1999, The Astrophysical Journal, 514, 441

Ogawara, Y., Takano, T., Kato, T., et al. 1991, The Yohkoh (Solar-A) Mission, 1

Ohki, K., Takakura, T., Tsuneta, S., & Nitta, N. 1983, Solar physics, 86, 301

Okamoto, T. J., Antolin, P., De Pontieu, B., et al. 2015, The Astrophysical Journal, 809, 71

Orlando, S., Bocchino, F., Reale, F., Peres, G., & Pagano, P. 2008, The Astrophysical Journal, 678, 274

Orlando, S., Peres, G., Reale, F., et al. 2005, Astronomy & Astrophysics, 444, 505

Pagano, P., Antolin, P., & Petralia, A. 2021, Astronomy & Astrophysics, 656, A141

Pagano, P. & De Moortel, I. 2017, Astronomy & Astrophysics, 601, A107

Pagano, P. & De Moortel, I. 2019, Astronomy & Astrophysics, 623, A37

Pagano, P., De Moortel, I., & Morton, R. 2020, Astronomy & Astrophysics, 643, A73

Pagano, P., Pascoe, D. J., & De Moortel, I. 2018, Astronomy & Astrophysics, 616, A125

Parenti, S. 2014, Living Reviews in Solar Physics, 11, 1

Parker, E. 1972, Astrophysical Journal, vol. 174, p. 499, 174, 499

Parker, E. 1983, Astrophysical Journal, Vol. 264, P. 642, 1983, 264, 642

Parker, E. N. 1957, Journal of Geophysical Research, 62, 509

Parker, E. N. 1988, The Astrophysical Journal, 330, 474

Parker, E. N. 1994, Spontaneous current sheets in magnetic fields: with applications to stellar x-rays, Vol. 1 (Oxford University Press)

Parnell, C. E. & De Moortel, I. 2012, Philosophical Transactions of the Royal Society A: Mathematical, Physical and Engineering Sciences, 370, 3217

Parnell, C. E., Haynes, A. L., & Galsgaard, K. 2008, The Astrophysical Journal, 675, 1656

Pascoe, D. J., De Moortel, I., & McLaughlin, J. A. 2009, Astronomy & Astrophysics, 505, 319

Pascoe, D. J., Hood, A. W., De Moortel, I., & Wright, A. N. 2012, Astronomy & Astrophysics, 539, A37

Pascoe, D. J., Wright, A. N., & De Moortel, I. 2011, The Astrophysical Journal, 731, 73

Patel, R. & Pant, V. 2022, The Astrophysical Journal, 938, 122

Patsourakos, S., Vourlidas, A., & Stenborg, G. 2012, arXiv preprint arXiv:1211.7211

Patsourakos, S., Vourlidas, A., Török, T., et al. 2020, Space Science Reviews, 216, 1

Peres, G., Reale, F., Serio, S., & Pallavicini, R. 1987, Astrophysical Journal, Part 1 (ISSN 0004-637X), vol. 312, Jan. 15, 1987, p. 895-908. Research supported by the Ministero della Pubblica Istruzione and CNR., 312, 895

Peres, G., Serio, S., Vaiana, G., & Rosner, R. 1982, The Astrophysical Journal, 252, 791

Peres, G. & Vaiana, G. 1990, Società Astronomica Italiana, Memorie (ISSN 0037-8720), vol. 61, no. 2, 1990, p. 401-430., 61, 401

Pesnell, W. D., Thompson, B. J., & Chamberlin, P. 2012, The solar dynamics observatory (SDO) (Springer)

Peter, H. & Bingert, S. 2012, Astronomy & Astrophysics, 548, A1

Petschek, H. E. 1964, NASA SP., 425

Pinto, R., Gordovskyy, M., Browning, P., & Vilmer, N. 2016, Astronomy & Astrophysics, 585, A159

Pinto, R., Vilmer, N., & Brun, A. S. 2015, Astronomy & Astrophysics, 576, A37

Poduval, B., DeForest, C., Schmelz, J., & Pathak, S. 2013, The Astrophysical Journal, 765, 144

Polito, V., Testa, P., & De Pontieu, B. 2019, The Astrophysical Journal Letters, 879, L17

Pontin, D., Candelaresi, S., Russell, A., & Hornig, G. 2016, Plasma Physics and Controlled Fusion, 58, 054008

Pontin, D., Wilmot-Smith, A., Hornig, G., & Galsgaard, K. 2011, Astronomy & Astrophysics, 525, A57

Pontin, D. I. & Hornig, G. 2015, The Astrophysical Journal, 805, 47

Pontin, D. I. & Priest, E. R. 2022, Living Reviews in Solar Physics, 19, 1

Porter, L. J. & Klimchuk, J. A. 1995, Astrophysical Journal v. 454, p. 499, 454, 499

Powell, K. G. 1994, An approximate Riemann solver for magnetohydrodynamics (that works in more than one dimension), Tech. rep.

Powell, K. G., Roe, P. L., Linde, T. J., Gombosi, T. I., & De Zeeuw, D. L. 1999, Journal of Computational Physics, 154, 284

Price, D. J., Taroyan, Y., Innes, D., & Bradshaw, S. J. 2015, Solar Physics, 290, 1931

Priest, E. 1976a, Solar Physics, 47, 41

Priest, E. 1976b, Philosophical Transactions for the Royal Society of London. Series A, Mathematical and Physical Sciences, 281, 497

Priest, E. 2014, Magnetohydrodynamics of the Sun (Cambridge University Press)

Priest, E., Chitta, L., & Syntelis, P. 2018, The Astrophysical Journal Letters, 862, L24

Priest, E. & Forbes, T. 1986, Journal of Geophysical Research: Space Physics, 91, 5579

Priest, E. & Forbes, T. 1989, Solar physics, 119, 211

Priest, E., Parnell, C., & Martin, S. 1994, Astrophysical Journal, Part 1 (ISSN 0004-637X), vol. 427, no. 1, p. 459-474, 427, 459

Priest, E. R. 1985, Reports on Progress in Physics, 48, 955

Priest, E. R., Foley, C., Heyvaerts, J., et al. 1998, Nature, 393, 545

Priest, E. R., Heyvaerts, J. F., et al. 2002, The Astrophysical Journal, 576, 533

Priest, E. R., Longcope, D., & Heyvaerts, J. 2005, The Astrophysical Journal, 624, 1057

Purkhart, S. & Veronig, A. M. 2022, Astronomy & Astrophysics, 661, A149

Raadu, M. 1972, Solar Physics, 22, 425

Rachmeler, L. A., Winebarger, A. R., Savage, S. L., et al. 2019, Solar Physics, 294, 1

Raga, A. C., Mellema, G., & Lundqvist, P. 1997, The Astrophysical Journal Supplement Series, 109, 517

Rappazzo, A., Dahlburg, R., Einaudi, G., & Velli, M. 2018, Monthly Notices of the Royal Astronomical Society, 478, 2257

Rappazzo, A., Matthaeus, W., Ruffolo, D., Velli, M., & Servidio, S. 2017, The Astrophysical Journal, 844, 87

Rappazzo, A. & Parker, E. 2013, The Astrophysical Journal Letters, 773, L2

Rappazzo, A., Velli, M., & Einaudi, G. 2010, The Astrophysical Journal, 722, 65

Rappazzo, A., Velli, M., & Einaudi, G. 2013, The Astrophysical Journal, 771, 76

Rappazzo, A., Velli, M., Einaudi, G., & Dahlburg, R. 2008, The Astrophysical Journal, 677, 1348

Rappazzo, A. F., Velli, M., Einaudi, G., & Dahlburg, R. 2007, The Astrophysical Journal, 657, L47

Reale, F. 2007, Astronomy & Astrophysics, 471, 271

Reale, F. 2014, Living Reviews in Solar Physics, 11, 1

Reale, F., Guarrasi, M., Testa, P., et al. 2011, The Astrophysical Journal Letters, 736, L16

Reale, F. & Landi, E. 2012, Astronomy & Astrophysics, 543, A90

Reale, F., Orlando, S., Guarrasi, M., et al. 2016, The Astrophysical Journal, 830, 21

Reale, F. & Peres, G. 1999, The Astrophysical Journal, 528, L45

Reale, F., Peres, G., Serio, S., et al. 2000a, The Astrophysical Journal, 535, 423

Reale, F., Peres, G., Serio, S., et al. 2000b, The Astrophysical Journal, 535, 423

Reale, F., Peres, G., Serio, S., DeLuca, E., & Golub, L. 2000c, The Astrophysical Journal, 535, 412

Reid, J., Cargill, P., Hood, A. W., Parnell, C. E., & Arber, T. D. 2020, Astronomy & Astrophysics, 633, A158

Reid, J., Hood, A. W., Parnell, C. E., Browning, P., & Cargill, P. 2018, Astronomy & Astrophysics, 615, A84

Reid, J., Threlfall, J., & Hood, A. W. 2022, Proceedings of the International Astronomical Union, 18, 116

Reidy, W., Vaiana, G., Zehnpfennig, T., & Giacconi, R. 1968, Astrophysical Journal, vol. 151, p. 333, 151, 333

Rempel, M. 2016, The Astrophysical Journal, 834, 10

Rieutord, M. & Rincon, F. 2010, lrsp, 7

Ripperda, B., Porth, O., Xia, C., & Keppens, R. 2017a, Monthly Notices of the Royal Astronomical Society, 467, 3279

Ripperda, B., Porth, O., Xia, C., & Keppens, R. 2017b, Monthly Notices of the Royal Astronomical Society, 471, 3465

Ritchie, M., Wilmot-Smith, A., & Hornig, G. 2016, The Astrophysical Journal, 824, 19

Roberts, B. 2000, Solar Physics, 193, 139

Rochus, P., Auchere, F., Berghmans, D., et al. 2020, Astronomy & Astrophysics, 642, A8

Roe, P. L. 1986, Annual review of fluid mechanics, 18, 337

Rosner, R., Golub, L., Coppi, B., & Vaiana, G. 1978a, Astrophysical Journal, Part 1, vol. 222, May 15, 1978, p. 317-332. Research supported by the Smithsonian Institution;, 222, 317

Rosner, R., Tucker, W. H., & Vaiana, G. 1978b, The Astrophysical Journal, 220, 643

Ruderman, M. S. & Erdélyi, R. 2009, Space Science Reviews, 149, 199

Rutten, R. J. 2012, Philosophical Transactions of the Royal Society A: Mathematical, Physical and Engineering Sciences, 370, 3129

Sakurai, K. 1976, solar physics, 47, 261

Schindler, K., Hesse, M., & Birn, J. 1988, Journal of Geophysical Research: Space Physics, 93, 5547

Schmelz, J. & Winebarger, A. 2015, Philosophical Transactions of the Royal Society A: Mathematical, Physical and Engineering Sciences, 373, 20140257

Selwa, M. & Ofman, L. 2009in , Copernicus GmbH, 3899–3908

Serio, S., Peres, G., Vaiana, G., Golub, L., & Rosner, R. 1981, The Astrophysical Journal, 243, 288

Shafranov, V. D. 1958, 6, 545

Shafranov, V. D. 1963, Journal of Nuclear Energy. Part C, Plasma Physics, Accelerators, Thermonuclear Research, 5, 251

Sharykin, I., Kuznetsov, A., & Myshyakov, I. 2018, Solar Physics, 293, 34

Shestov, S., Nakariakov, V. M., Ulyanov, A., Reva, A., & Kuzin, S. 2017, The Astrophysical Journal, 840, 64

Shibata, K., Nozawa, S., & Matsumoto, R. 1992, Astronomical Society of Japan, Publications (ISSN 0004-6264), vol. 44, no. 3, 1992, p. 265-272. Research supported by Ishida Foundation., 44, 265

Shibata, K. & Tanuma, S. 2001, Earth, Planets and Space, 53, 473

Shimizu, T., Imada, S., Kawate, T., et al. 2019, in UV, X-Ray, and Gamma-Ray Space Instrumentation for Astronomy XXI, Vol. 11118, SPIE, 27–37

Shimizu, T., Imada, S., Kawate, T., et al. 2020, in Space Telescopes and Instrumentation 2020: Ultraviolet to Gamma Ray, Vol. 11444, SPIE, 113–119

Snow, B., Botha, G., Scullion, E., et al. 2018, The Astrophysical Journal, 863, 172

Sokolov, I. V., Van der Holst, B., Oran, R., et al. 2013, The Astrophysical Journal, 764, 23

Solanki, S. K. 1993, Space Science Reviews, 63, 1

Spitzer Jr, L. & Härm, R. 1953, Physical Review, 89, 977

Srivastava, A. & Dwivedi, B. 2010, Monthly Notices of the Royal Astronomical Society, 405, 2317

Stanier, A., Browning, P., Gordovskyy, M., et al. 2013, Physics of Plasmas, 20

Strugarek, A., Charbonneau, P., Joseph, R., & Pirot, D. 2014, Coronal Magnetometry, 371

Suematsu, Y., Tsuneta, S., Ichimoto, K., et al. 2008, The Hinode Mission, 143

Sukarmadji, A. R. C. & Antolin, P. 2024, The Astrophysical Journal Letters, 961, L17

Sukarmadji, A. R. C., Antolin, P., & McLaughlin, J. A. 2022, The Astrophysical Journal, 934, 190

Svestka, Z. & Cliver, E. 1992, in IAU Colloq. 133: Eruptive Solar Flares, Vol. 399, 1

Sweby, P. K. 1985, in Large-scale computations in fluid mechanics

Sweet, P. 1958, Il Nuovo Cimento (1955-1965), 8, 188

Tam, K. V., Hood, A. W., Browning, P., & Cargill, P. 2015, Astronomy & Astrophysics, 580, A122

Tanaka, K., Nitta, N., Akita, K., & Watanabe, T. 1983, Solar physics, 86, 91

Tanaka, Y. 1983, Solar physics, 86, 3

Taylor, J. 1986, Reviews of Modern Physics, 58, 741

Taylor, J. 2000, Physics of plasmas, 7, 1623

Taylor, J. B. 1974, Physical Review Letters, 33, 1139

Terradas, J., Arregui, I., Oliver, R., et al. 2008, The Astrophysical Journal, 679, 1611

Testa, P., De Pontieu, B., Allred, J., et al. 2014, Science, 346, 1255724

Testa, P., De Pontieu, B., & Hansteen, V. 2016, The Astrophysical Journal, 827, 99

Testa, P., De Pontieu, B., Martínez-Sykora, J., et al. 2013, The Astrophysical Journal Letters, 770, L1

Testa, P. & Reale, F. 2012, The Astrophysical Journal Letters, 750, L10

Testa, P. & Reale, F. 2020, The Astrophysical Journal, 902, 31

Testa, P. & Reale, F. 2024, in Handbook of X-ray and Gamma-ray Astrophysics (Springer), 3075–3112

Testa, P., Saar, S. H., & Drake, J. J. 2015, Philosophical Transactions of the Royal Society A: Mathematical, Physical and Engineering Sciences, 373, 20140259

Thornton, L. M. & Parnell, C. E. 2011, Solar Physics, 269, 13

Threlfall, J., Bourdin, P.-A., Neukirch, T., & Parnell, C. 2016a, Astronomy & Astrophysics, 587, A4

Threlfall, J., Hood, A., & Browning, P. 2018, Astronomy & Astrophysics, 611, A40

Threlfall, J., Neukirch, T., & Parnell, C. E. 2017, Solar Physics, 292, 1

Threlfall, J., Reid, J., & Hood, A. 2021, Solar Physics, 296, 120

Threlfall, J., Stevenson, J., Parnell, C., & Neukirch, T. 2016b, Astronomy & Astrophysics, 585, A95

Tian, H., Kleint, L., Peter, H., et al. 2014, The Astrophysical Journal Letters, 790, L29

Tiwari, S. K., Evans, C. L., Panesar, N. K., Prasad, A., & Moore, R. L. 2021, The Astrophysical Journal, 908, 151

Tiwari, S. K., Thalmann, J. K., Panesar, N. K., Moore, R. L., & Winebarger, A. R. 2017, The Astrophysical Journal Letters, 843, L20

Toro, E. F., Spruce, M., & Speares, W. 1994, Shock waves, 4, 25

Toro, E. F. et al. 1997

Török, T., Kliem, B., & Titov, V. 2004, Astronomy & Astrophysics, 413, L27

Tóth, G. 1996, Astrophysical Letters and Communications, Vol. 34, p. 245, 34, 245

Tousey, R., Bartoe, J., Bohlin, J. D., et al. 1973, Solar Physics, 33, 265

Tripathi, D., Mason, H. E., Dwivedi, B. N., Del Zanna, G., & Young, P. R. 2009, The Astrophysical Journal, 694, 1256

Tsuneta, S., Acton, L., Bruner, M., et al. 1991, Solar Physics, 136, 37

Tsuneta, S., Ichimoto, K., Katsukawa, Y., et al. 2008, Solar Physics, 249, 167

Tsuneta, S., Nitta, N., Takakura, T., et al. 1984, Astrophysical Journal, Part 1 (ISSN 0004-637X), vol. 284, Sept. 15, 1984, p. 827-832., 284, 827

Ugai, M. 1992, Physics of Fluids B: Plasma Physics, 4, 2953

Ulyanov, A., Bogachev, S., Reva, A., Kirichenko, A., & Loboda, I. 2019, Astronomy Letters, 45, 248

Vadawale, S. V., Mithun, N., Mondal, B., et al. 2021, The Astrophysical Journal Letters, 912, L13

Vaiana, G. 1981, in X-Ray Astronomy with the Einstein Satellite: Proceedings of the High Energy Astrophysics Division of the American Astronomical Society Meeting on X-Ray Astronomy held at the Harvard/Smithsonian Center for Astrophysics, Cambridge, Massachusetts, USA, January 28–30, 1980, Springer, 1–18

Vaiana, G., Davis, J., Giacconi, R., et al. 1973a, Astrophysical Journal, vol. 185, p. L47, 185, L47

Vaiana, G., Krieger, A., & Timothy, A. 1973b, Solar Physics, 32, 81

Vaiana, G., Reidy, W., Zehnpfennig, T., VanSpeybroeck, L., & Giacconi, R. 1968, Science, 161, 564

Vaiana, G. S. & Rosner, R. 1978, In: Annual review of astronomy and astrophysics. Volume 16.(A79-14551 03-88) Palo Alto, Calif., Annual Reviews, Inc., 1978, p. 393-428., 16, 393

Van Ballegooijen, A. 1985, Astrophysical Journal, Part 1 (ISSN 0004-637X), vol. 298, Nov. 1, 1985, p. 421-430. Research supported by Lockheed Independent Research Program., 298, 421

Van Ballegooijen, A., Asgari-Targhi, M., & Berger, M. 2014, The Astrophysical Journal, 787, 87

Van Ballegooijen, A., Asgari-Targhi, M., Cranmer, S., & DeLuca, E. 2011, The Astrophysical Journal, 736, 3

van der Holst, B., Sokolov, I. V., Meng, X., et al. 2014, The Astrophysical Journal, 782, 81

Van der Linden, R. & Hood, A. 1999, Astronomy and Astrophysics, 346, 303

Van der Linden, R. & Hood, A. W. 1998, Astronomy and Astrophysics, v. 339, p. 887-896 (1998), 339, 887

Van Doorsselaere, T., Andries, J., Poedts, S., & Goossens, M. 2004, The Astrophysical Journal, 606, 1223

Van Doorsselaere, T., Nakariakov, V. M., Young, P. R., & Verwichte, E. 2008, Astronomy & Astrophysics, 487, L17

Van Doorsselaere, T., Srivastava, A. K., Antolin, P., et al. 2020, Space Science Reviews, 216, 1

van Driel-Gesztelyi, L. & Green, L. M. 2015, Living Reviews in Solar Physics, 12, 1

Van Leer, B. 1974, Journal of computational physics, 14, 361

Vekstein, G. 2009, Astronomy & Astrophysics, 499, L5

Velli, M., Lionello, R., & Einaudi, G. 1997, Solar Physics, 172, 257

Venkataramanasastry, A., Tiwari, S., Panesar, N., et al. 2023in , 105–08

Vernazza, J. E., Avrett, E. H., & Loeser, R. 1981, Astrophysical Journal Supplement Series, vol. 45, Apr. 1981, p. 635-725., 45, 635

Verwichte, E., Foullon, C., & Nakariakov, V. M. 2006a, Astronomy & Astrophysics, 446, 1139

Verwichte, E., Foullon, C., & Nakariakov, V. M. 2006b, Astronomy & Astrophysics, 449, 769

Vesecky, J., Antiochos, S., & Underwood, J. 1979, The Astrophysical Journal, 233, 987

Viall, N. M. & Klimchuk, J. A. 2011, The Astrophysical Journal, 738, 24

Vlahos, L., Georgoulis, M., Kluiving, R., & Paschos, P. 1995, Astronomy and Astrophysics, v. 299, p. 897, 299, 897

Vlahos, L. & Georgoulis, M. K. 2004, The Astrophysical Journal, 603, L61

Vögler, A., Shelyag, S., Schüssler, M., et al. 2005, Astronomy & Astrophysics, 429, 335

Wang, T., Ofman, L., Yuan, D., et al. 2021, Space Science Reviews, 217, 1

Warmuth, A. & Mann, G. 2016, Astronomy and Astrophysics, 588, A115

Warren, H. P., Ugarte-Urra, I., Doschek, G. A., Brooks, D. H., & Williams, D. R. 2008, The Astrophysical Journal, 686, L131

Warren, H. P. & Winebarger, A. R. 2006, arXiv preprint astro-ph/0602052

Warren, H. P. & Winebarger, A. R. 2007, The Astrophysical Journal, 666, 1245

Warren, H. P., Winebarger, A. R., & Brooks, D. H. 2012, The Astrophysical Journal, 759, 141

Warren, H. P., Winebarger, A. R., & Hamilton, P. S. 2002, The Astrophysical Journal, 579, L41

White, S., Kundu, M., & Gopalswamy, N. 1991, Astrophysical Journal, Part 2-Letters (ISSN 0004-637X), vol. 366, Jan. 1, 1991, p. L43-L46., 366, L43

Widing, K. & Feldman, U. 1992, The Astrophysical Journal, 392, 715

Williams, D. R., Török, T., Démoulin, P., van Driel-Gesztelyi, L., & Kliem, B. 2005, The Astrophysical Journal, 628, L163

Wilmot-Smith, A. 2015, Philosophical Transactions of the Royal Society A: Mathematical, Physical and Engineering Sciences, 373, 20140265

Withbroe, G. L. & Noyes, R. W. 1977, In: Annual review of astronomy and astrophysics. Volume 15.(A78-16576 04-90) Palo Alto, Calif., Annual Reviews, Inc., 1977, p. 363-387., 15, 363

Woltjer, L. 1958, Proceedings of the National Academy of Sciences, 44, 489

Wragg, M. & Priest, E. 1981, Solar Physics, 70, 293

Yamada, M., Ono, Y., Hayakawa, A., Katsurai, M., & Perkins, F. 1990, Physical Review Letters, 65, 721

Yang, Z., Bethge, C., Tian, H., et al. 2020, Science, 369, 694

Yeates, A., Russell, A., & Hornig, G. 2015, Proceedings of the Royal Society A: Mathematical, Physical and Engineering Sciences, 471, 20150012

Yeates, A. R., Hornig, G., & Wilmot-Smith, A. L. 2010, Physical Review Letters, 105, 085002

Yokoyama, T. & Shibata, K. 1994, Astrophysical Journal, Part 2-Letters (ISSN 0004-637X), vol. 436, no. 2, p. L197-L200, 436, L197

Zhdankin, V., Boldyrev, S., Perez, J. C., & Tobias, S. M. 2014, The Astrophysical Journal, 795, 127

Zirker, J. B. 1993, Solar physics, 148, 43

Zweibel, E. G. & Yamada, M. 2009, Annual review of astronomy and astrophysics, 47, 291